**DTU Library**

**Optofluidic waveguide sensors for point-of-care applications**

**Zhou, Chen**

*Publication date:*
2018

*Document Version*
Publisher's PDF, also known as Version of record

[Link back to DTU Orbit](#)

*Citation (APA):*
Zhou, C. (2018). Optofluidic waveguide sensors for point-of-care applications. DTU Nanotech.

# Optofluidic waveguide sensors for point-of-care applications

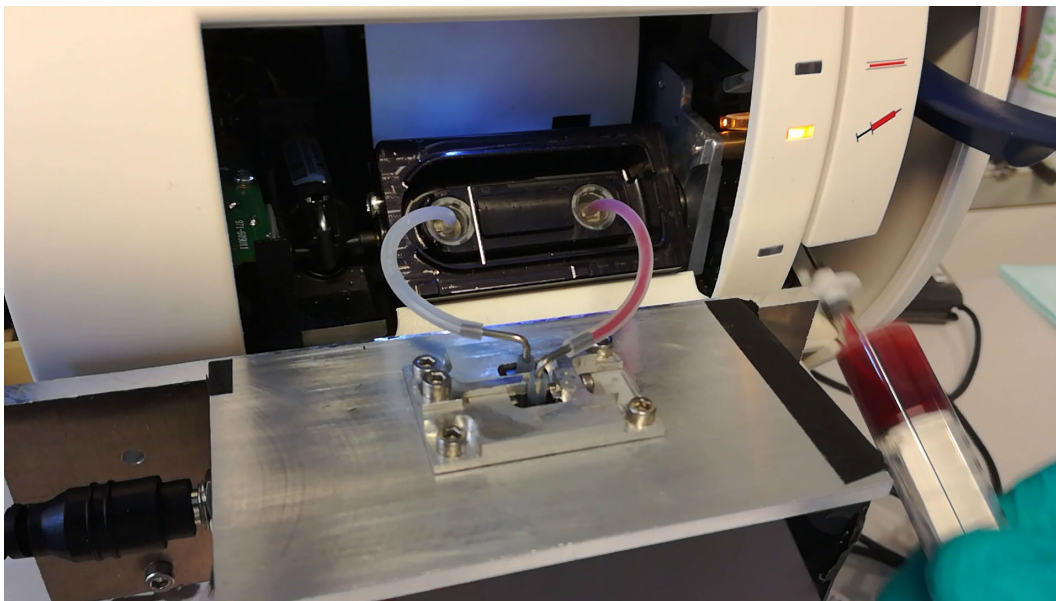Chen Zhou
PhD Thesis Oktober 2018

**DTU Nanotech**
Department of Micro- and Nanotechnology

**DTU Nanotech**
Institut for Mikro- og Nanoteknologi

# Optofluidic waveguide sensors for point-of-care applications



Chen Zhou

Kongens Lyngby 2018

DTU

# Summary

This Ph.D. thesis is concerned with optofluidic waveguide sensors for point-of-care (PoC) applications. The main objective is to demonstrate a hemolysis sensor that shows the potential of integration into state-of-the-art PoC blood gas analyzers. This project is conducted in collaboration with Radiometer Medical ApS.

Hemolysis is the rupture of the red blood cells in blood and has been a long-lasting global healthcare issue in clinics worldwide. In vivo hemolysis is an indication of serious medical condition and in vitro hemolysis interferes with other important blood parameters such as K+ and bilirubin. Currently, there is no method to detect hemolysis in a fast and reliable way since the separation of red blood cells and plasma require time-consuming procedure such as centrifugation. The novel sensor developed in this thesis presents innovative nano-filters on a single-mode optical waveguide, which enables evanescent absorption of free hemoglobin and simultaneous filtering of red blood cells. Thus, whole blood samples from patients can be directly measured with no sample preparation required. Sample volume of 65 µL is sufficient and measurement turn-around time of 1 minute is demonstrated. The sensor is successfully integrated in a modified PoC blood gas analyzer of Radiometer and shows excellent performance in repeatability, specificity, and long-term reliability.

Furthermore, in this thesis, a waveguide interferometer sensor is demonstrated which is capable of simultaneous detection of liquid refraction and absorption. The interferometer sensor is composed of a sensing waveguide and a reference waveguide, from which an interferogram is generated by interference of the light. The change in the real part of the refractive index (refraction) causes phase shift of the interferogram, while the change in imaginary part of the refractive index (absorption) causes signal attenuation. Size-exclusion function is added to the interferometer by using nano-filters as demonstrated in the hemolysis sensor. Nano-beads with diameter from 100 nm to 500 nm are measured with regard to their refractive index, where large nano-beads are filtered out and cause no signal change. Evanescent fluorescent excitation experiments further confirm the size-exclusion functionality.

# Dansk resumé

Denne ph.-d. afhandling drejer sig om optofluidiske bølgeleder sensorer til point-of-care (PoC) anvendelser. Hovedformålet er at udvikle en hæmolyse sensor, som kan integreres i de nyeste PoC blodgas analyseapparater. Dette projekt er udarbejdet i samarbejde med Radiometer Medical ApS.

Hæmolyse opstår når røde blodceller nedbrydes i blodet og har længe været et sundhedsproblem i klinikker over hele verden. In vivo hæmolyse indikerer en alvorlig medicinsk tilstand og in vitro hemolysis interfererer med andre vigtige blodparametre såsom K+ og bilirubin. På nuværende tidspunkt er der ikke nogen hurtig samt pålidelig metode til at registrere hæmolyse, da separationen af røde blodceller og blodplasma har behov for tidskrævende procedurer såsom centrifugering. I denne afhandling har vi udviklet en nyskabende sensor der kombinerer innovative nanofiltre med en single-mode optisk bølgeleder, hvilket giver mulighed for at detektere frie hæmoglobin gennem evanescent absorption og samtidig filtrere røde blodceller. Blodprøver fra patienter kan derfor undersøges direkte uden nogen form for prøveforarbejdelse. En prøvevolume på 65 µL er tilstrækkelig og vi demonstrerer en måletid på kun 1 minut. Vi har med succes integreret sensoren i et modificeret PoC blodglas analyseapparat udviklet af Radiometer, og sensoren viser fremragende ydelse i form af reproducerbarhed, specificitet, og langtidsvirkning.

Ydermere demonstrerer vi i denne afhandling en bølgeledersensor baseret på interferometri, der kan udføre samtidige målinger af både refraktion og absorption fra væsker. Interferometrisensoren er opbygget af en målebølgeleder og en referencebølgeleder, hvoraf et interferogram skabes ud fra interferensen af lys. Ændringer i den reelle del af brydningsindekset (refraktion) forårsager et faseskift, mens ændringer i den imaginære del af brydningsindekset (absorption) medfører dæmpning af intensiteten. Ligesom i hæmolysesensoren tilføjes nanofiltre til interferometrisensoren for at kunne lave størrelsessortering. Vi måler brydningsindekset af nanoperler med diametre fra 100 nm til 500 nm. De største nanoperler sorteres fra og kan derfor ikke detekteres. Eksperimenter baseret på evanescent excitation af fluorescensens bekræfter sortering af størrelser.

# Preface

This thesis is submitted in partial fulfillment of the requirements for obtaining the Philosophiae Doctor degree at the Technical University of Denmark. The work presented here has been carried out in the Optofluidics group at the Department of Micro- and Nanotechnology, and in the DTU Danchip cleanroom facilities.

# Abbreviations

| | |
|---|---|
| ADC | analog to digital converter |
| CVD | Chemical vapor deposition |
| DAC | digital to analog converter |
| DAG | directed acyclic graph |
| DC | direct current |
| DRIE | deep reactive ion etching |
| DSP | digital signal processor |
| EBL | electron beam lithography |
| ED | emergency department |
| GMRF | guided mode resonance filter |
| HI | hemolysis index |
| ICU | intensive care unit |
| IPA | iso-propanol |
| LoD | limit of detection |
| MCU | micro-controller |
| MK1 | waveguide sensor mark 1 |
| MK2 | waveguide sensor mark 2 |
| NA | numerical aperture |
| NIL | nanoimprint lithography |
| OWLS | optical waveguide lightmode spectroscopy |
| PBS | phosphate buffered saline |
| PCB | printed circuit board |
| PGMEA | Propylene glycol methyl ether acetate |
| RBC | Red blood cell |
| RIE | Reactive Ion Etching |
| RIU | refractive index unit |
| TE | transverse electric |
| TM | transverse magnetic |
| TPO | 2, 4, 6-trimethylbenzoyldiphenylphosphine oxide |
| USART | universal synchronous and asynchronous receiver-transmitter |
| WD | working distance |

# Contents

# Introduction

## 1.1  Motivation and objectives

Hemolysis is the rupture of the red blood cells (RBCs) with consequent release of their contents into blood plasma. So far, hemolysis is still the largest preanalytical error source in health care facilities and clinical laboratories around the world, accounting for 39-69% of all the unsuitable sample[86, 59]. Hemolysis can happen in both *in vivo* and *in vitro* conditions. In case of *in vivo*, there is a high likelihood that the patient is suffering from a serious medical condition, such as sickle cell disease[45], autoimmune disorder[35], and severe sepsis[33], which requires immediate treatment. On the other hand, hemolysis can occur *in vitro* by causes such as traumatic blood draw or mishandling of sample[59]. In these cases, hemolysis poses large threats in interfering other important blood test paramters. For instance, bilirubin determination can be strongly interfered[55], which affects the prevention of neonatal kernicterus[75]. Potassium (K+) results from a hemolyzed blood sample can falsely indicate or disgusie a life-threatening abnormality[26]. Parameters from immunoassay-based methods can also suffer from large abnormality in the presence of hemolysis[92]. Thus, in these cases, a new blood sample has to be taken, which delays the patient care and deteriorates overall healthcare quality[32]. Furthermore, for cardiac surgery undergoing cardiopulmonary bypass, hemolysis is nearly ubiquitous[90], eventually causing i.a. acute kidney injury[65]. Therefore, real-time monitoring of hemolysis level in whole blood is required to dynamically assess patient's condition.

An important reason that hemolysis remains such a global healthcare problem is due to the lack of a fast and reliable solution for hemolysis detection. A point-of-care (PoC) hemolysis detection tool that can deliver fast and reliable measurements directly from whole blood sample can thus be of significant value especially for neonatal units, intensive care units (ICU) and emergency departments (ED). However, a whole blood sample is very turbid, containing both RBCs and plasma. The determination of little amount of hemoglobin in the plasma is very difficult due to the large interference from the RBCs. The state-of-the-art hemolysis detection methods require centrifugation to separate blood plasma from RBCs, where the isolated blood plasma is further analyzed to quantify the hemoglobin level. Such method requires equipment that is normally located in central lab facilities, which is also time consuming and tends to give additional preanalytical errors. Therefore, the project "Hemolysis detection system for point of care blood gas analysers" (HemoPoc) is initiated with funding from Innovation Fund Denmark

to address the mentioned issues. Together with the commercial partner Radiometer Medical ApS (Denmark), we aim to develop and demonstrate a solution for fast and reliable detection of hemolysis with whole blood that can be integrated in future PoC blood gas analysers, namely Radiometer's ABL product family. Furthermore, the technology developed within the thesis is utilized for applications beyond hemolysis detection, which is also demonstrated in the thesis.

The main objectives for the thesis to be accomplished are as follows:

- Development of a detection method that can measure hemoglobin in free plasma from a small blood volume, i.e. collected in capillary tubes.

- Development of a plasma separation method that can separate RBCs from the blood plasma directly from the whole blood sample.

- Design and testing of a hemolysis detection system that can fulfill the strict requirements of Radiometer blood gas analyzer platforms.

More specifically, the following requirements should be met with the new design of sensor:

- hemoglobin detection limit $\leq 0.5$ g/L

- precision $\pm 0.1$ g/L

- specificity $> 95\%$

- sample volume $\leq 65$ µL

- detection time $\leq 35$ seconds

- turn-around time $< 1$ min

- sensor lifetime $> 1$ month

Thus, the development of the hemolysis sensor can be deviced into two phases. In phase I, different approaches are evaluated and the most promising method is selected for whole blood hemolysis detection. A waveguide sensor is demonstrated with imprinted nano-filters, which enable local filtering of RBCs from blood plasma and free hemoglobin detection in whole blood. The sensor is tested at Radiometer's R & D lab for long-term stability to verify the functionality and compatibility of the sensor with human whole blood and other calibration and rinse liquids from Radiometer. The result is published in paper I, as appended at the end of the thesis. In the phase II, the aim is to meet the new requirement of the integration with Radiometer's ABL product family, which has e.g. a strict space requirement for the sensor footprint. The cost aspect is also taken into consideration. The results are demonstrated mainly in **Chapter 5 Device prototyping and sensor integration** in this thesis.

Furthermore, methods and techniques developed during the hemolysis sensor have also led to further innovations. First one is the procedure of nano-structure transfer method by nanoimprint lithography, as shown in **Chapter 4 Materials and Fabrication**. Here, by utilizing the residue-free imprint method developed for the nano-filters of the hemolysis sensor, a reliable, low-cost, and large-scale pattern transfer method is demonstrated for master origination targeting for plasmonic color generation and meta-surface applications.

Another work that originates from the hemolysis sensor is the multi-functional waveguide interferometer sensor shown in the manuscript of paper II. To the date of the submission of this thesis, the paper II is under review process. Here, an integrated optical Young interferometer is demonstrated for sensing both refraction and absorption of a liquid sample. An interferogram is generated by the light coupled out from a sensing and a reference waveguide. The refraction is determined by the phase shift of the interferogram while the absorption is measured by the signal attenuation after low-pass signal filtering. Moreover, nano-filters are integrated to the sensing waveguide so that size-exclusive detection can be demonstrated. Nano-beads of different diameters (100 nm to 500 nm) are measured by phase shift signal as well as fluorescent emission. In general, similar to the development of the hemolysis sensor, the interferometer sensor here presents not only the possibility of sensitive refractive index and absorption detection but also the possibility of low-cost sensor fabrication, which can be scaled up easily in the future commercialization stage. Last but not least, the supporting hardware requirement (light source, readout, and alignment stages) has been designed to fit the size and cost consideration of PoC devices.

## 1.2   Thesis Outline

This thesis is concerned with the design and fabrication of waveguide sensors. The main objective is the demonstration of a hemolysis sensor and its experimental setup aiming at integration into Radiometer ABL products. Paper I in the appendix summarizes the main innovation of the thesis regarding hemolysis detection. Other chapters in the thesis are as follows:

- **Chapter 2 State of the art** reviews the state-of-the-art of hemolysis detection and other waveguide sensors.

- **Chapter 3 Theoretical background** provides both analytical analysis and numerical simulation regarding optical waveguide and sensitivity of the waveguide sensors.

- **Chapter 4 Materials and Fabrication** describes the fabrication methods developed to fabricate the waveguide sensors. Electron beam lithography is also described with regard to high throughput manufacturing. Imprint stamp origination and replication method is also shown and discussed.

- **Chapter 5 Device prototyping and sensor integration** demonstrates the design and fabrication of the prototype setup devic of the waveguide hemolysis sensor, aiming to demonstrate the potential of integration with Radiometer's product.

- **Chapter 6 Results and Discussion** summarizes the papers published on waveguide sensors and provides further details and discussions.

- **Chapter 7 Conclusion and Outlook** gives a summary, followed by an outlook for possible future work.

- **Appendix** includes the manuscripts and papers published on waveguide sensors developed within the thesis.

# State of the art

## 2.1 Hemolysis detection

Traditionally, hemolysis detection in clinical laboratories is made by visual inspection of centrifuged blood plasma samples, where the inspector judges the level of hemolysis by the color. This method is obviously subjective, unreliable and unrepeatable[85, 25]. Currently, more automated analytical platforms have replaced the visual inspection. In most cases, the free hemoglobin level is measured in optical way by evaluating the absorbance of hemoglobin at different wavelengths[41]. The common indicator used in clinics to describe the hemolysis level is the hemolysis index (HI), which is a quantitative value, of which the definition differs from manufacturer to manufacturer[41]. A consistent way for hemolysis detection and quantification that can serve as benchmark is still not developed worldwide[67]. There are in general two main categories of methods for free hemoglobin determination (from a centrifuged blood sample):

- Direct optical method. A photospectrometer is used here to measure the absorbance of the plasma sample. Sample is undiluted and compared to a phosphate buffered saline (PBS) or water blank signal to obtain the absorbance. Some methods use the 577 nm oxyhemoglobin to evaluate the hemoglobin level such as Cripps method[20], Kahn method[53], Porter method[72], and Shinowara method[84]. Other methods use *diluted* plasma sample to measure the absorption peak of hemoglobin at 415 nm such as Harboe method[40] and Fairbanks AII method[31]. The reason for the Harboe and Fairbanks AII method to use *diluted* sample lies in the fact that the hemoglobin absoprtion at 415 nm is much higher than at 577 nm (about 10 times larger in absorbance). Thus, it requires dilution for highly hemolyzed sample to avoid saturation. In the thesis, a modified Fairbanks AII method is used as reference measurement. In the origin Fairbanks AII method, the author used empirical absorbance values of hemoglobin, bilirubin and lipids at 415, 450, and 700 nm to polynomially fit the measured data. Here, the wavelength range is expanded from those 3 points to a broader range i.e. a range from 330 nm to 700 nm with 1 nm increment.

- Assay methods. Cyanmethemoglobin (HiCN) method is the most common hematological method for hemoglobin detection, which is also recommended by International Council for Standardisation in Haematology[97]. Here, blood plasma is diluted in Drabkin's solution which consists of potassium cyanide and potassium ferricyanide. Potassium ferricyanide converts hemoglobin to methemoglobin, which

is further converted by potassium cyanide to HiCN. The absorbance of the HiCN
solution can be measured at 540 nm wavelength. Despite the precision the method
provides, the complexity in preparation is high and analytical errors can be caused
during the pipetting and handling. Thus, it is mainly used as instrument calibration
but rarely as daily sample measurement routine.

So far, all methods shown here entails centrifugation as the sample preparation step
if one wants to measure hemolysis. Thus, the equipment for those detection method is
located in the central labs in clinics and is not appropriate for PoC applications. Only a
few works have been shown for *PoC* hemolysis detection in the literature:

- E. Archibong has demonstrated in her PhD thesis in 2015 a method of PoC hemol-
  ysis detection by means of a filtered fiber platform[5]. Similar to the previous
  work published by the author[6], a porous membrane is fabricated with patterned
  $Si_3N_4$ film (200 nm) and wet-etched Si substrate. Pores of 1–3 µm in diameter are
  fabricated to filter out cells. Au thin film is subsequently deposited on top of the
  $Si_3N_4$ membrane to provide reflection. To sense the hemoglobin level, a optical
  fiber senses the reflected signal from the back side. The setup is shown in Figure 2.1.
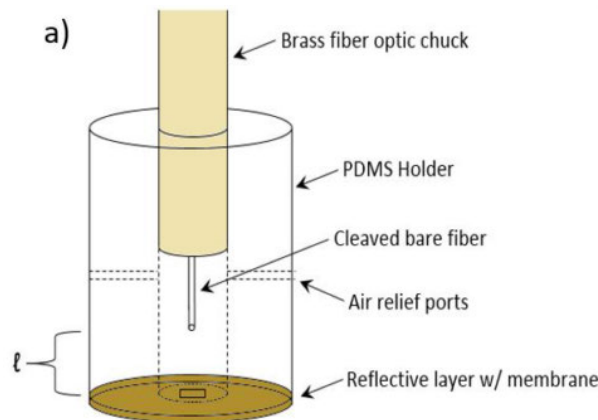


Figure 2.1: Proposed design for the spectroscopic probe with a filtered
fiber platform. The figure is adapted from Ref.[5].

The author thinks this work shows an interesting approach for hemolysis detection.
However, several drawbacks limit its application field: 1) liquid exchange is difficult
for such a membrane sensor. Since pores are perforated through the membrane,
pressure needs to be controlled on both sides to control the main flow and the
through-flow. 2) Cell clogging can be pronounced due to the presence of through-
flow. 3) The reflection from a perforated micro-porous membrane is complex
especially when it's measured with a optical fiber which has a certain angle spread
(numerical aperture (NA)).
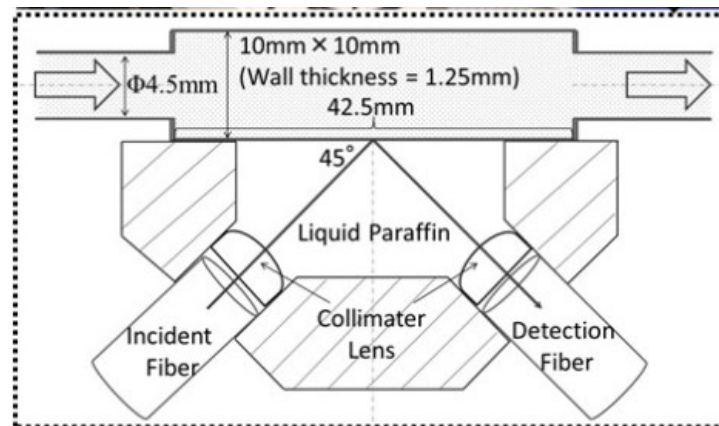
Figure 2.2: Experiemtal setup of the surface reflectance spectroscopy for hemolysis detection. The figure is adapted from Ref.[77].

- Sakota et al. has demonstrated a surface reflectance spectroscopic method for hemolysis detection[77]. As shown in Figure 2.3, the internal reflection at the interface to blood is detected. However, as shown in the paper, the absorption is dependent on both hematocrit (volume percentage of RBCs in blood) and hemolysis, which is not appreciated for measurement reliability. Nevertheless, due to the fact that there is a cell-free layer in sub-micrometer length at the wall (Fahraeus–Lindqvist effect[30]), the cell interference is limited in the region of the evanescent field. However, it was difficult to identify the absorption spectral fingerprint due to the large noise, which means other absorptive interference in plasma like bilirubin cannot be distinguished.

- A recent US patent from Instrumentation Laboratory Inc. describes an evanescent hemolysis sensor [81], which works similarly to the approach demonstrated by Sakota et al. Here, a prism is used to couple light, which interfaces the blood flow. The hemoglobin absorption peak at 415 nm can be identified. However, the sensitivity is not high, which is also difficult to be improved because of the absence of a controllable waveguide - there is a limited length for light-sample-interaction.

Conclusively, there is no solution in the literature that can fully fulfill the requirement of a fast PoC hemolysis sensor. However, some common features can be valuable for our consideratrion: 1) optical absorption measurement is the widely used for hemolysis detection. 2) evanescent sensing is promising because of the presence of a cell-free-layer at the wall, where the reliability is compromised. 3) Porous membrane can provide reliable mechanical filtering but requires pores under 2 µm size for effective RBC filtering.

## 2.2   Waveguide sensors

A brief review of the state-of-the-art of waveguide sensors is presented here. The main focus is targeted at dielectric waveguides. While surface plasmon sensors can also be

categorized as waveguides, they are not in focus of this thesis and will be solely compared as reference in some contexts. The governing physics of waveguide as a optical sensor can be described as follows: due to the contrast in refractive index between the core and cladding layers of an optical waveguide, light is guided through the device with help of total internal reflection. The guided light generates an evanescent field extending the sensor surface. Species within the evanescent field modulate the refractive index and thus the propagation properties of light in the waveguide, which can be attenuation in amplitude or modification in phase. Three categories of waveguide sensors will be discussed here.

## 2.2.1   Grating-based waveguide sensors
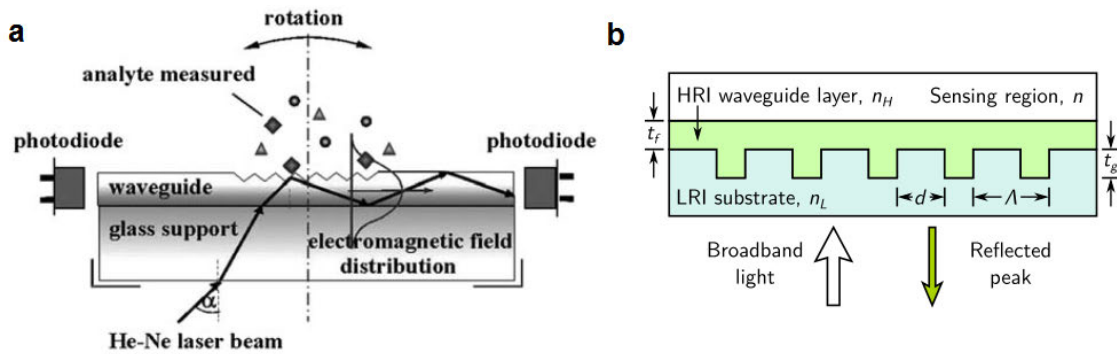


Figure 2.3: (a) Illustration of a sensor for optical waveguide lightmode spectroscopy (OWLS). The rotation angle is measured and evaluated. The figure is adapted from Ref.[88]. (b) Illustration of a guided mode resonance filter sensor (GMRF). The resonance wavelength is measured and evaluated. The figure is adapted from Ref.[46].

Due to the presence of periodic gratings, a waveguide can couple light in and out with a certain angle, which is dependent on the effective refractive index of the waveguide. Thus, sensors can be made by detecting the change of the coupling angle. This technique has been coined as optical waveguide lightmode spectroscopy (OWLS), where commercial products are already available such as OWLS platform from MicroVacuum Ltd[60]. $SiO_2$ substrate with appr. 200 nm $TiO_2$ layer provides the foundation for waveguiding. Using this platform, Kurunczi et al. have demonstrated label free detection of C-Reactive Protein with a limit of detection (LoD) of about 0.2 µg/mL[57]. Adanyi et al. have demonstrated detection of small molecule artemisinin by immunoassay in range of ng/mL[1]. Davila et al. have shown study of adsorption of proteins in mg/dL with OWLS[24]. OWLS has been also extensively used for monitoring of bacteria such as Legionella pneumophila[18] and Salmonella typhimurium[54], where a cell concentration (CFU/ml) of $10^3$ has been shown as the LoD[54].

Another class of grating-based waveguide sensors is the so called guided-mode resonance filter (GMRF). Here, instead of measuring the angle of coupling, the resonance wavelength is measured. A broadband light source is used and the normal incident angle is selected for the observation. Due to the change of the effective refractive index, the resonance wavelength is shifted, at which a guided mode is present in the waveguide. Cunningham et al. have shown detection of streptavidin with a LoD of 1 ng/mL[22]. Furthermore, due to the large size those grating can provide (by low-cost fabrication method like nanoimprint lithography), a two-dimensional scan is possible with the application of imaging the refractive index landscape[16, 15]. Protein-DNA binding activity can be monitored by GMRF system[14]. Furthermore, multiple resonances due to both transverse-electric (TE) and transverse magnetic (TM) modes can co-exist in a GMRF sensor. Magnusson et al. have demonstrated a GMRF sensor utilizing the relative resonance wavelength difference between two polarization states, where the common-mode error such as temperature fluctuation is suppressed[63]. Detection of 3.75 μg /mL protein calreticulin (cancer biomarker) is shown. Moreover, Hermannsson et al. presented a design of GMRF with organic-inorganic polymer as waveguide core instead of $TiO_2$ [46], which demonstrates a low-cost variation of fabricating waveguide in visible wavelength range.

## 2.2.2 Interferometric waveguide sensors

Waveguide interferometer sensor is a very sensitive sensing method as it combines two very sensitive disciplines, the waveguiding and interferometry technique. The ability to up-scale the waveguiding length and evaluate the change integrated over the total length provides the potential of larger signal generation compared to weakly guided modes in GMRFs. Moreover, another significant advantage of the interferometer sensor is its broad dynamic range. As comparison, surface plasmon resonance sensor and grating-based sensors have a trade-off between the dynamic range and resolution[19, 51]. There are different ways to categorize interferometers. One is based on their configurations. Two mostly used configurations for integrated planar waveguides are Young and Mach-Zehnder interferometers, of which the difference is illustrated in Figure 2.4.
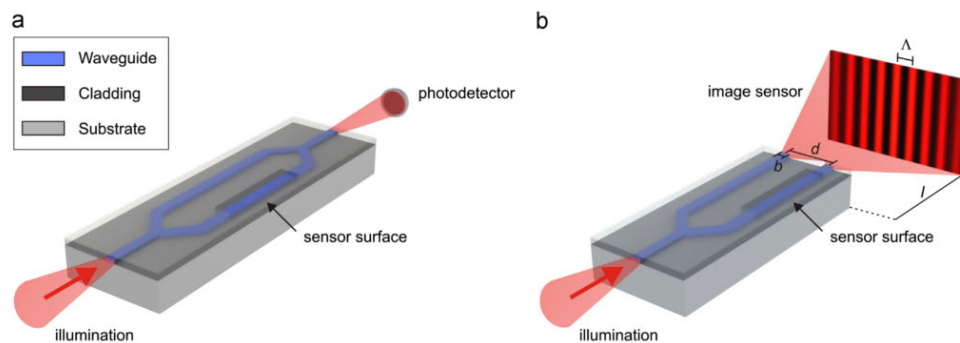


Figure 2.4: Typical (a) Mach-Zehnder and (b) Young interferometer configurations. The figure is adapted from Ref.[56].

For both interferoemters, the light in the waveguide is at first split into two beams, which propagates through the sensor arm and the reference arm. In case of Mach-Zehnder interferometer, the two beams are recombined into one single waveguide, as shown in Figure 2.4a. In case of a Young interferometer, two beams are projected onto a detector array, where the interference pattern is detected, as shown in Figure 2.4b. The spatial period is dependent on the spacing between the two output waveguides as well as the distance of the plane of sources and the detector.

**Mach-Zehnder interferometer**   In the early 90s, the first publications of integrated Mach-Zehnder interferometer sensor can be found. Heideman et al. have demonstrated detection of human chorionic gonadotropin (hCG) in µg/mL by a integrated Mach-Zehnder interferometer at 633 nm wavelength[44]. A resolution of $1 \times 10^2 \times 2\pi$ can be achieved, corresponding to a bulk refractive index change of $4 \times 10^{-6}$[43]. Prieto et al. demonstrated a Si-based Mach-Zehnder interferometer with ridge waveguides[74]. A LoD of $7 \times 10^{-6}$ was shown for bulk refractive index changes. However, due to the periodic nature of the output signal (subsequent dark and bright in $2\pi$ periodicity), Mach-Zehnder interferometer is susceptible to signal ambiguity and intensity fluctuation[23]. Those drawbacks can be solved by tuning the phase difference between the arms by electro-optical[58], acousto-optical[28], thermo-optical [29], and magneto-optical[83] modulation. However, the complexity of the sensor fabrication increases dramatically, which hampers the commercialization of such products.

**Young interferometer**   In contrast to the Mach-Zehnder interferometers, Young interferometer requires simpler design on chip but more complex readout such as a line camera. However, due to the large market of CMOS image sensors, the unit price of those image sensors especially line cameras becomes very low now. Thus, Young interferometer is potentially promising for industrial up-scaling. An early demonstration of integrated Young interferometer is shown by Cross et al. [21], where a humidity sensor realized. Brandenburg et al. demonstrated a Young interferometer based on silicon oxinitride waveguide with CCD line camera readout for measuring immunoglobulin G (IgG)[11]. 50 ng/mL concentration is shown, which corresponds to a refractive index change of $9 \times 10^{-8}$. Ymeti et al.[94] developed a four-channel integrated Young interferometer, where different distances between channel-pair are present, causing fringes of different periodicities. The additional information can contribute to drift compensation. A refractive index resolution of $8.5 \times 10^{-8}$ is shown.

Young interferometers made with polymeric waveguides have also gained great attention due to the potential of low-cost and large-scale fabrication. Young interferometer with vertically stacked slab waveguides made with OrmoCer materials (a organic-inorganic hybrid polymer [39]) has been demonstrated with a LoD of $10^{-5}$ refractive index unit (RIU)[91]. The configuration of the sensor is shown in Figure 2.5a. The same group has also demonstrated a Young interferometer made with OrmoCer waveguides with
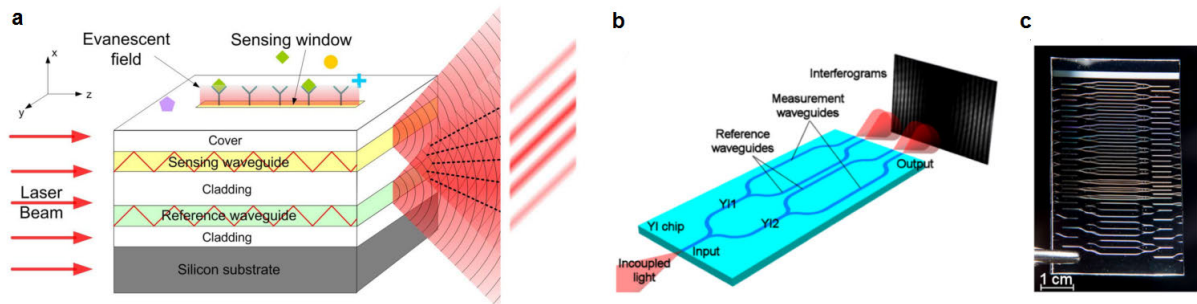
Figure 2.5: (a) Young interferometer made with OrmoCer materials. Sensign and reference waveguides are vertically aligned. The figure is adapted from Ref.[91]. (b)(c) Polymeric young interferometer made with roll-to-roll method. The figures are adapted from Ref.[3]

additional thin $Ta_2O_5$ layer for enhanced sensitivity, where a LoD of $10^{-7}$ RIU is achieved. Slot waveguides made with OrmoCer materials have been designed into Young interferometers, showing a LoD in range of $10^{-6}$ - $10^{-7}$ RIU[2, 47]. A noticeable attempt to mass product those polymeric interferometers has been shown with Aikio et al.[3]. Here, a four-channel Young interferometer is made with roll-to-roll technology, as shown in Figure 2.5b-c. A LoD of $10^{-5}$ - $10^{-6}$ RIU is demonstrated.

## 2.2.3   Waveguide absorption sensors
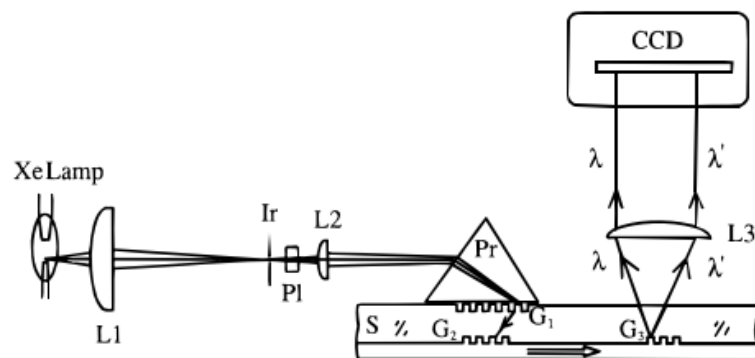


Figure 2.6: Schematic of a broadband waveguide spectrometer demonstrated by Mendes et al.[69]. Double graings and prism are used for achromatic coupling. Readout is made with a CCD camera. The figure is adapted from Ref.[69]

For absorbing molecules, measuring the absorption spectrum can be the simplest and fastest way to achieve specificity, since no immobilization assay is needed (like in most cases measuring the refractive index change) and the signal intensity is high

compared to e.g. Raman spectroscopy. Usually samples can be directly measured with a cuvette and a photospectrometer for absorption spectra. However, waveguide absorption sensor can provide additional confinement of the light and thus can deliver additional functionalities when combined with e.g. electrochemical modulation or microfluidics. Waveguide absorption spectroscopy was shown for heme protein [4], methylene blue[73], and bromothymol blue[76]. Bradshaw et al. demonstrated waveguide absorption spectroscopy with cytochrome c from 390 nm to 645 nm[10]. The broadband in-coupling is achieved with a prism while the out-coupling is utilized for spectral read-out with a CCD camera. Later, Bradshaw et al. used this platform to study spectro-electrochemical responses of redox-active molecules[9]. Wiederkehr et al.[93] have demonstrated UV absorption spectroscopy with an alumina waveguide. A wavelength range from 315 nm to 405 nm is demonstrated.

A more complex and efficient broadband coupling method is demonstrated by Mendes et al.[68, 69], as illustrated in Figure 2.6, where two grating areas are used to correction the first chromatic order and a prism for the second chromatic order. 70 nm bandwidth is thus demonstrated. This is to our knowledge the best performance in coupling bandwidth. However, the complexity in fabrication is not to be underestimated due to the need of alignment.

# Theoretical Background

## 3.1  Dielectric slab waveguides

Slab waveguide is the most essential form of optical waveguides[66]. Owing to their simple geometry, both guided mode and radiation mode can be expressed with simple mathematical expression. In reality, slab waveguide is also a simple way to implement an optical waveguide since no lateral confinement is needed. Here, the aim is to understand several fundamental properties of a slab waveguide, which serves as foundation for further optimizing the performance of the waveguide sensor.
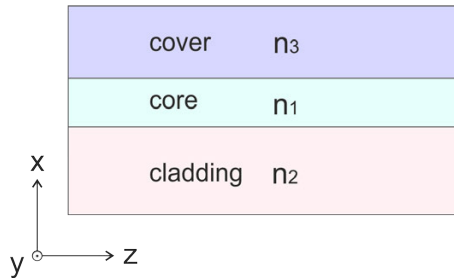


Figure 3.1: Illustration of a slab waveguide with the definition used in this thesis: cover, core, and cladding.

A dielectric slab waveguide is shown schematically in Figure 3.1. The core region of the waveguide possesses a refractive index $n_1$ . Underneath the core layer, the cladding is given with refractive index $n_2$. The refractive index of the cover is $n_3$. In the implementation of a polymeric waveguide in this work, the waveguide exhibits asymmetric behavior as follows:

$$n_1 > n_3 > n_2. \tag{3.1}$$

Since the cladding and substrate materials are not identical, different refractive index are shown. A complete description of the waveguide and its guided modes can be derived by solving Maxwell equation. Here, we assume nonmagnetic dielectric materials:

$$B = \mu_0 H, \tag{3.2}$$

and linear susceptibility in the Fourier domain:

$$D = \epsilon_0 \epsilon(\omega) E. \tag{3.3}$$

Thus, we obtain the frequency-domain Maxwell equation for our condition:

$$\nabla \times E = i\omega\mu_0 H, \tag{3.4}$$

$$\nabla \times H = -i\omega\epsilon_0\epsilon E, \tag{3.5}$$

$$\nabla \cdot (\epsilon E) = 0, \tag{3.6}$$

$$\nabla \cdot H = 0. \tag{3.7}$$

With the assumption that the waveguide is infinitely extended in the yz plane, $E$ and $H$ are y-independent and the z dependence of the mode fields is given with $\exp(-i\beta z)$. For Transverse-Electric (TE) modes, $E_z = 0$ and $E_x = 0$, thus we obtain:

$$-i\beta H_x - \frac{\partial H_z}{\partial x} = i\omega\epsilon_0 n^2 E_y \tag{3.8}$$

$$i\beta E_y = -i\omega\mu_0 H_x \tag{3.9}$$

$$\frac{\partial E_y}{\partial x} = -i\omega\mu_0 H_z \tag{3.10}$$

By applying eq. 3.9 and 3.10 into eq. 3.8, we can obtain the one-dimensional reduced wave equation for $Ey$ component:

$$\frac{\partial^2 E_y}{\partial x^2} + (n^2 k_0^2 - \beta^2)E_y = 0, \tag{3.11}$$

with $k_0^2 = \omega^2\epsilon_0\mu_0 = (2\pi/\lambda)^2$. Then, we apply the boundary conditions that the $E_y$ component vanishes at x = $\pm - \infty$ and the continuity of the tangential field component of $H$ and $E$ at the boundary at x = 0 and x = -d, so we obtain:

$$E_y = \begin{cases} Ce^{-qx} & x \geq 0 \\\\ C(cos(hx) - \frac{q}{h}sin(hx)) & 0 \geq x \geq -d \\\\ C(cos(hd) + \frac{q}{h}sin(hd))e^{p(x+d)} & -t \geq x \end{cases} \tag{3.12}$$

$$q = \sqrt{\beta^2 - k_0^2 n_3^2}, \quad p = \sqrt{\beta^2 - k_0^2 n_2^2}, \quad h = \sqrt{k_0^2 n_1^2 - \beta^2} \tag{3.13}$$

where $C$ is a constant. The eigenvalue equation for the TE mode is thus given as:

$$tan(hd) = \frac{p+q}{h(1 - \frac{pq}{h^2})}. \tag{3.14}$$

The eigenvalue equation gives the allowed values of the propagation constant $\beta$, which is the only unknown variable in eq. 3.11. $\beta$ practically defines the supported modes that can propagate in the waveguide. By applying the solved $\beta$ in to eq. 3.12, one can obtain

the field distribution in the slab waveguide. Furthermore, the term effective refractive index $n_{eff}$ is defined as:

$$n_{eff} = \frac{\beta}{k_0}. \tag{3.15}$$

It becomes clear that, if $n_{eff} < n_3$, the term $q$ in eq. 3.13 becomes imaginary - the evanescent field turns into radiation. At the border of $n_{eff} = n_3$, $q = 0$ and the field $E_y$ in eq. 3.12 becomes undiminished to infinite above the waveguide. This point gives the cut-off frequency of the waveguide.

Similarly, for the TM mode we have:

$$H_y = \begin{cases} -\frac{h}{q}Ce^{-qx} & x \geq 0 \\[2mm] C(-\frac{h}{q}cos(hx) + sin(hx)) & 0 \geq x \geq -d \\[2mm] -C(\frac{h}{q}cos(hd) + sin(hd))e^{p(x+d)} & -t \geq x \end{cases} \tag{3.16}$$

with the eigenvalue equation:

$$tan(hd) = \frac{n_3^2 n_1^2 p + n_2^2 n_1^2 q}{h(n_2^2 n_3^2 - n_1^4 \frac{pq}{h^2})}. \tag{3.17}$$

$$q = \sqrt{\beta^2 - k_0^2 n_3^2}, \quad p = \sqrt{\beta^2 - k_0^2 n_2^2}, \quad h = \sqrt{k_0^2 n_1^2 - \beta^2} \tag{3.18}$$

**Cut-off frequency**   In case of $n_1 > n_3 > n_2$ we can define the following parameters:

$$V = k_0 d\sqrt{n_1^2 - n_3^2} \tag{3.19}$$

$$\delta = \frac{n_3^2 - n_2^2}{n_1^2 - n_3^2} \tag{3.20}$$

where $V$ is a dimensionless parameter that indictes the number of supported mdoes, $\delta$ describes the degree of waveguide asymmetry. For the cut-off condition $n_{eff} = n_3$, we have $q = 0$. By applying the condition and parameters to the eigenvalue equations (eq. 3.14 and eq. 3.17), we get:

$$V_{cut,TE} = m\pi + \arctan\left(\sqrt{\delta}\right), \tag{3.21}$$

$$V_{cut,TM} = m\pi + \arctan\left(\frac{n_1^2}{n_2^2}\sqrt{\delta}\right), \tag{3.22}$$

where $m$ is an integer. Similarly, in case of a symmetric slab waveguide, where $n_2 = n_3$, i.e. $\delta = 0$. The cut-off frequency becomes:

$$V_{cut,TE} = m\pi. \tag{3.23}$$

This means that the lowest-order mode can propagate at arbitrarily low frequency, which in turn means that the core thickness can be made infinitely small. It enables the largest possible evanescent field, which is very advantageous for sensing application. However, for an asymmetric waveguide as used in the thesis, the asymmetry give rise to a cut-off condition, where the waveguide no longer supports any mode. For the design of the waveguide, this condition has to be considered for all wavelengths.

## 3.2 Guided modes in a polymer slab waveguide

In this section, the material properties are inserted into the equations to solve the mode condition for the real waveguide. At a wavelength of 450 nm, the refractive index of the polymer cladding (Efiron) is 1.418, the waveguide core (OrmoClear HI01) is 1.621, and the waveguide cover (OrmoComp) is 1.621. By solving the propagation constant $\beta$ for TE and TM modes, one can obtain the effective refractive index of different modes for the given waveguide. Figure 3.2 shows the results. The effective refractive indexes of different modes are plotted for different waveguide core thicknesses. The fundamental mode occurs in a core thickness range above 110 nm for the TE mode and 130 nm for the TM mode. The first order mode occurs above 550 nm and 580 nm for TE and TM mode, respectively. In the design for waveguide absorption sensor, one wants to avoid higher order modes, thus this result provides a guideline for the thickness selection.

Another important parameter is the cut-off thickness of the waveguide. As we will see later, the lower the core thickness, the higher the sensitivity that one can achieve for evanescent sensing. Thus, it's important to know the limit of the thickness. However, this cut-off thickness is strongly dependent on the wavelength. Thus, it's important to calculate the cut-off thickness over a broad range of wavelength. Figure 3.3 shows the cut-off thickness of the fundamental modes for the whole visible wavelength range. As we can see, the TE mode has a lower thickness requirement than the TM. The former is also selected for the waveguiding of the sensor. Conclusively, for a bandwidth from 400 nm to 500 nm, the waveguide should be at least 130 nm high to support the $TE_0$ mode propagation.
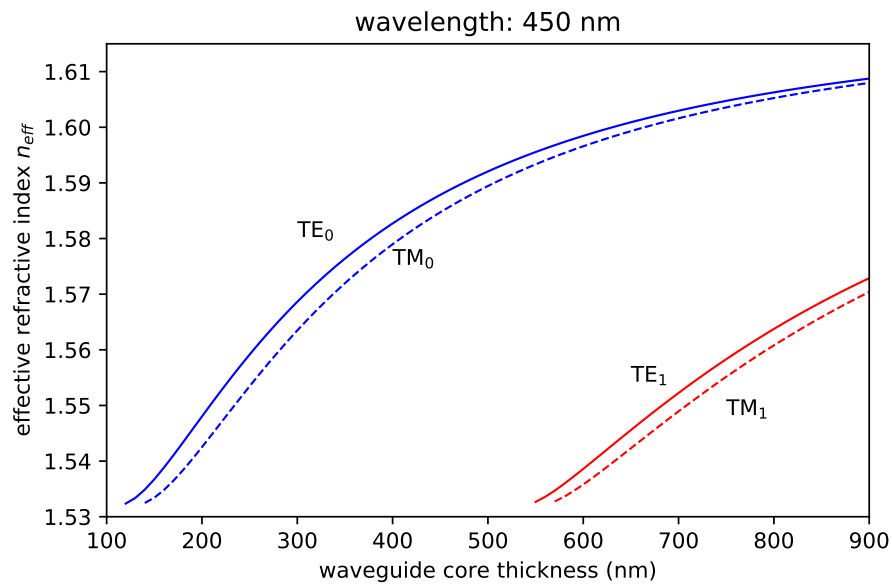
Figure 3.2: The effective mode index as a function of waveguide core thickness for a slab waveguide composed of a polymer substrate (Efiron) ($n_2 = 1.418$), a OrmoClear HI01 core ($n_1 = 1.621$), and OrmoComp ($n_3 = 1.532$) as the cover at a wavelength of $\lambda = 450$ nm
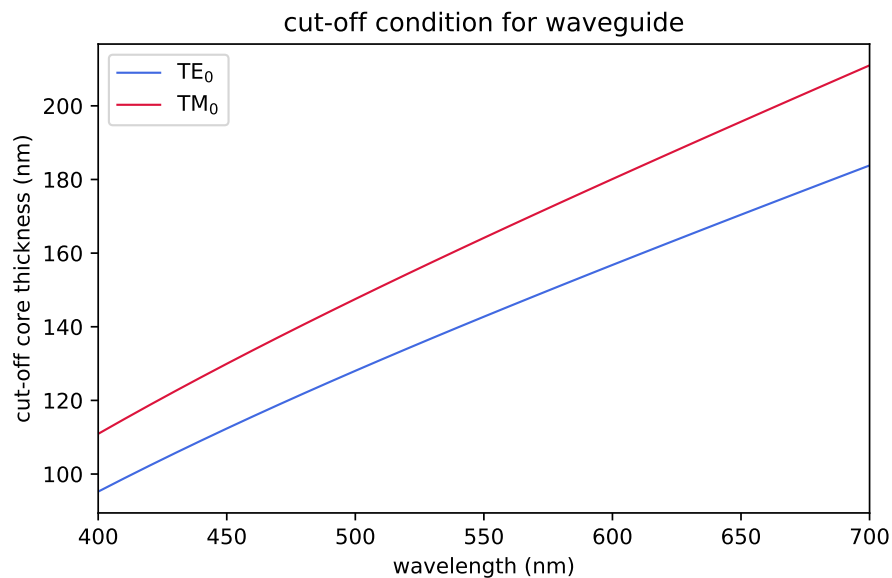


Figure 3.3: The cut-off thickness as a function of wavelength of the propagating light. There is no supported mode (TE or TM) at the given wavelength when the waveguide core is lower than the cut-off thickness.

# 3.3   Theory of grating couplers
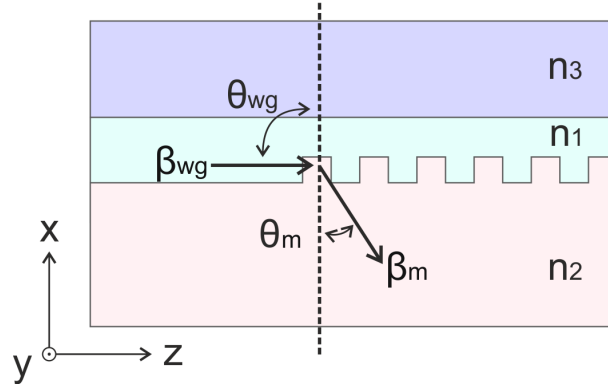


Figure 3.4: Illustration of the out-coupling from waveguide

## 3.3.1   The diffraction equation

The diffraction equation describes the coupling angle for a diffraction grating, which is a critical aspect in our polymer waveguide. In general, for coupling into a waveguide, it is necessary that the longitudinal components of the propagation constants are matched (for free-space coupled and guided waves), which is the z direction in our case, as shown in Figure 3.4, the phase matching condition is given:

$$\beta_{z,wg} = \beta_{z,m} + m\frac{2\pi}{\Lambda_z}, \tag{3.24}$$

where $\Lambda_z$ is the periodicity of the grating and $m$ the diffraction order. It can be further written as:

$$k_0 n_{eff} sin\theta_{wg} = k_0 n_2 sin\theta_m + m\frac{2\pi}{\Lambda_z}. \tag{3.25}$$

where $n_{eff}$ is the effective refractive index of the guided mode and $sin\theta_{wg}$, $sin\theta_m$ are the angles of the guided and out-coupled waves to the x direction, as defined in Figure 3.4. Clearly, $\theta_{wg}$ is 90 degree in this case, in which we have:

$$\frac{2\pi}{\lambda} n_{eff} = \frac{2\pi}{\lambda} n_2 sin\theta_m + m\frac{2\pi}{\Lambda_z}, \tag{3.26}$$

with $\lambda$ being the vacuum wavelength of the light. After simplification we have:

$$n_2 sin\theta_m = n_{eff} - \frac{m\lambda}{\Lambda_z}. \tag{3.27}$$

Since the free-space coupling angle is more of interest, which is the angle where the light is coming out of the substrate, the Snell's Law can be applied here with:

$$\frac{sin\theta_m}{sin\theta_{m,air}} = \frac{n_{air}}{n_2}, \tag{3.28}$$

where $n_{air}$ is the refractive index of air and is assumed to be one. By applying eq. 3.28 into eq. 3.27, we obtain:

$$\theta_{m,air} = arcsin(n_{eff} - \frac{m\lambda}{\Lambda_z}). \tag{3.29}$$

Only limited diffraction orders can exist, which have to satisfy that $|n_{eff} - \frac{m\lambda}{\Lambda_z}| \leq 1$. With the following condition, $\lambda = 420$ nm, $\Lambda_z = 368$ nm, and $n_{eff} = 1.555$ for the TE polarization, one can obtain e.g. the out-coupling angle of 24.4° for the given condition. Finally, the author is aware that the diffraction equation predicts only the diffraction orders and their angles, while the diffraction efficiency is not given. For this purpose, numerical simulations should be employed.

# 3.4 Grating couplers in a hybrid polymer waveguide

In this section, the hybrid polymer waveguide will be investigated with regard to their material parameters. The main objective of the investigation is to find design rules for grating couplers which are to be used for a broadband waveguide sensor. There are several input parameters one can vary:

- grating period,
- grating height,
- grating filling factor,
- total length of the gratings.

In contrast to many other studies of grating couplers with e.g. Si gratings for telecommunication application[27, 89], the situation is quite different in this work. First, the refractive index contrast of the materials is much smaller than e.g. $Si/SiO_2$ (3.48/1.44) with about 1.63/1.53. Second, broadband coupling is needed for absorption detection instead of single wavelength. Third, the in-coupling is achieved *without* a single mode fiber. The last point is critical since the most data on coupling efficiency that are shown in the literature are accomplished with the above-mentioned conditions. However, we want to prioritize the space-requirement and the cost of the system. Thus, free-space coupling is preferred, as one single mode fiber with alignment component can cost more than the whole setup.

The objective of the grating coupler design is to achieve efficient in-coupling, maximum out-coupling, and angle-resolved wavelength analysis. The main questions to be addressed are as follows:

- How large is the angle range when a broadband light is to be coupled?
- How is coupling angle related to the wavelength of the light when the grating period is fixed?

- What is the bandwidth that a waveguide with a certain thickness supports?
- How many gratings are needed to fully in- and out-couple the guided light?
- How is the energy distribution along the out-coupling gratings?
- What grating height should be used?
- Which filling factor of the gratings should be used?

In the following sections, the individual questions will be addressed with numerical simulations with CAMFR[13]. CAMFR implements an eigenmode expension method with perfect-matched-layer as boundary conditions and is widely used in studies regarding grating couplers[89].

## 3.4.1   Coupling angles

The essential parameter to be determined for designing a grating coupler is the grating period, which decides the in- or out-coupling angle of the guided light. There are several considerations regarding the coupling efficiency and other restrictions:

- One wants to avoid too large coupling angle, especially for out-coupling, since higher diffraction order can occur, as shown in eq. 3.29. There can be multiple values of $m$ that suffice the condition, leading to multiple diffraction orders and beams coming out at different angles.

- Zero degree vertical coupling is to be avoided at input. In such case, the input wave can propagate equally in both +z and -z directions. However, only one direction is needed for coupling into a waveguide. In the literature, most grating couplers are designed to couple in range of 3°-8°[27, 89], which avoids both higher order diffraction and zero degree vertical coupling.

- The hardware space requirement has to be taken into consideration. In the optical setup, we seek to use free-space coupled light source, which requires more space in the area near the sensor than a single-mode optical fiber. If we consider the following scenario: a 1 inch lens (ø 25.4mm) with f = 100 mm is used to focus the light, then the half angle of the light cone is 7.2°. Thus, it's practically unfeasible to place another set of optics for the output when the coupling angle is only 5°, especially when the in- and output gratings are very close to each other. In case of broadband coupling, this issue becomes more pronounced as a large range of angle is required for both excitation and collection. To avoid cross-talking of the input and output signal, an angle range from 15°-30° is desired. It gives more space for bulky components like camera or LED light source to be accommodated.

With those requirements in mind, the author investigated at first the angle range resulted from different grating periods, as shown in Figure 3.5. In general, higher coupling angle is obtained with increasing grating period. The wavelength plays another important role, when the wavelength is increased, $n_{eff}$ decreases due to lower refractive index of the
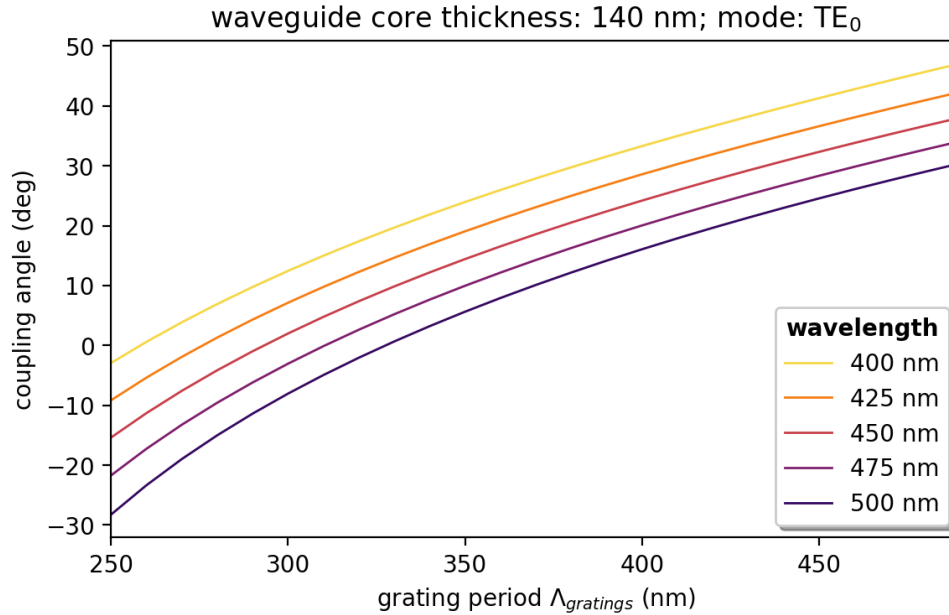
Figure 3.5: Influence of the grating coupler period on coupling angle. The waveguide core thickenss is fixed to be 140 nm. Only $TE_0$ mode is discussed. Wavelengths from 400 nm to 500 nm are plotted in different curves.

material, thus leading to also lower coupling angle. If 425 nm is chosen as the wavelength of interest, which is close to the maximum absorption peak of hemoglobin (415 nm), then we obtain 15° coupling angle for $\Lambda_{gratings} = 350$ nm and 25° for $\Lambda_{gratings} = 400$ nm, which is a practical range to work with.

In the waveguide sensor mark1 (MK1), 368 nm period is used as grating period, which was adopted from a previous sensor designed for guided-mode resonance filter. The author considers 368 nm to be a good value also for our application, as it spans a angle range from 5° - 25° for a wavelength range from 400 nm to 500 nm, as shown in Figure 3.5. Furthermore, for the MK1 sensor, the lowest waveguide core thickness was 200 nm, which leads to a higher $n_{eff}$ and, in turn, higher coupling angle in general. The choice of 368 nm gave thus a relevant coupling range from 10° - 30°. In the waveguide sensor Mark2 (MK2), which is the later version of the sensor, the waveguide core thickness was decreased to obtain higher sensitivity, which also decreased the overall coupling angles. In order to compensate the angle decrease, 390 nm was selected as the grating period. As shown in Figure 3.5, it has a coupling range from 12° - 28°.

After the grating period has been chosen, it's important to know the exact coupling angles for different waveguide core thicknesses, as the period cannot vary from batch to batch (as it's defined by the imprint stamp) but the thickness can be easily changed by different spin-coating conditions (the core layer is spin-coated and cured). Figure 3.6 shows the simulation results for a fixed grating period of 368 nm. The important aspects
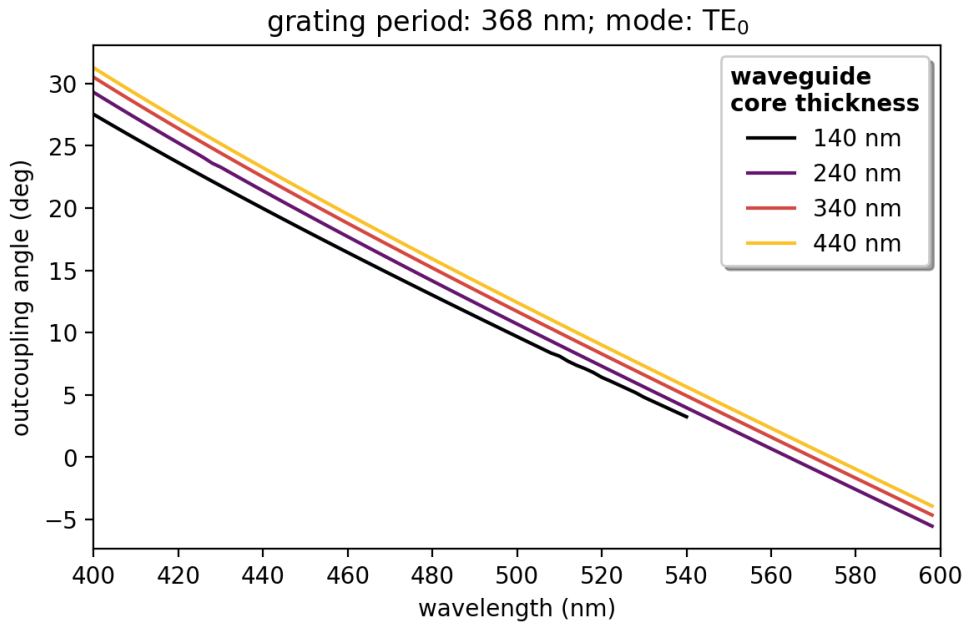
Figure 3.6: Calculated coupling angle for different wavelength. The grating period is fixed at 368 nm and only fundamental TE mode is considered. The thickness of the waveguide core is varied from 140 nm to 440 nm.

of the results are as follows:

- The change of the coupling angle is almost linearly scaled to the change of the wavelength.

- For the waveguide with 140 nm core thickness, 3°-28° is the range of coupling for a wavelength range from 400 nm to 540 nm.

- A cut-off wavelength (around 540 nm) occurs when the core thickness is low, as shown in the case of 140 nm. There is no mode available any more for higher wavelength. Thus, the bandwidth is limited, especially for a low core thickness, and the limit appears at high wavelength.

- The core thickness variation, which is inevitable during the fabrication process, will modify the coupling angle. However, with a 20 nm variation, the change of the angle is overall less than 1°, which is not critical if high numerical aperture is used for in-coupling and camera readout is used for out-coupling.

## 3.4.2   Length and height of the gratings

While the grating period determines the angle, the efficiency is strongly impacted by the geometry of the gratings. Here, the author intends to find a good height of the gratings to achieve maximum coupling efficiency. Furthermore, it's important to know the total

number of gratings needed to fully out-couple the light from the waveguide.
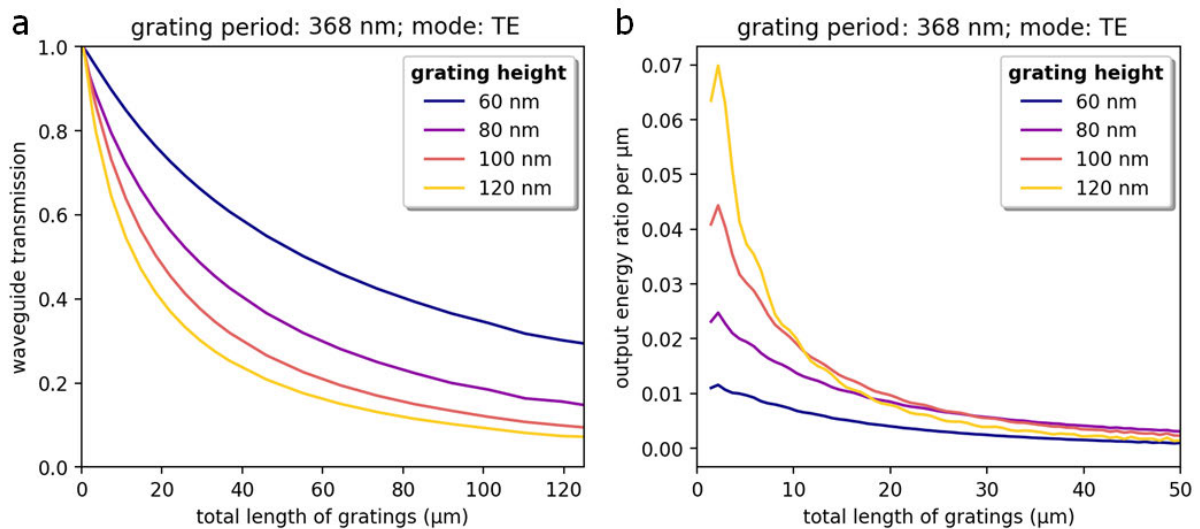


Figure 3.7: a) Simulated transmission in the waveguide after different length of gratings. At zero length of gratings, the energy is normalized to one. Grating period is fixed at 368 nm and polarization is TE. The waveguide core thickness is fixed at 140 nm with grating heights from 60 nm to 120 nm. b) Simulated output energy (both upwards and downwards) at different position of the gratings. Grating period is fixed at 368 nm and polarization is TE. The waveguide core thickness is fixed at 140 nm with grating heights from 60 nm to 120 nm.

Figure 3.7a shows the transmitted energy in the waveguide after different length of gratings. This plot helps visualizing the energy leakage in the waveguide due to the presence of gratings. Four different grating height from 60 nm to 120 nm are investigated. The height of the waveguide core is 140 nm and the grating period is 368 nm. Only $TE_0$ mode is considered. As we can see, when the total length of gratings is at zero, the energy is normalized and is always 1.0. After the guided light meets the gratings, out-coupling appears and the transmitted energy is attenuated. There is some important information from this figure:

- Low grating height leads to lower out-coupling efficiency. 60 nm gratings can out-couple 40% of the energy after 40 µm of gratings, while 120 nm gratings can out-couple about 80% of the energy with the same length.

- In order to couple 90% energy in the waveguide, at least 120 µm of gratings (100 nm height gratings) have to be placed.

Figure 3.7b shows energy that is being out-coupled at different position of the gratings. The number is normalized to the initial waveguide energy and shows the fraction of output in every µm. Not surprisingly, the gratings with 120 nm height are most efficient

in out-coupling, as the energy output is the highest after the wave enters the grating area. The peak that occurs in the first 5 µm indicates a minimum number of gratings that is required to achieve the maximum output. For 120 nm high gratings, the energy drops to 10% of the maximum after about 25 µm; in case of 60 nm high gratings, the length is 45 µm. In conclusion, higher gratings are more leaky; however, due to the fabrication process, in which the waveguide layer is spin-coated and cured from liquid phase to solid on top of the gratings, 120 nm high gratings can be hardly achieved for a core thickness of 140 nm with the configuration used in the simulation, since it allows only 20 nm difference between the the top of the grating and the waveguide. In reality, the difference is higher and the waveguide becomes wavy on top of the gratings, due to the dewetting process involved in the baking and curing.

### 3.4.3   Direction and filling factor of the gratings
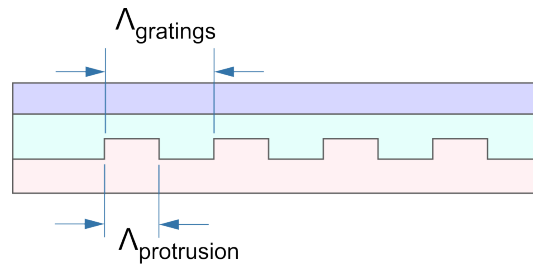


Figure 3.8: The definition of the filling factor is defined with the illustration, which is $\Lambda_{protrusion}/\Lambda_{gratings}$.

Here, another parameter of the grating is considered, which is the filling factor. Figure 3.8 illustrates the definition of the filling factor in our study, which is $\Lambda_{protrusion}/\Lambda_{gratings}$. Furthermore, two different configurations of the gratings are compared in the simulation, as shown in Figure 3.9. In design 1 (see Figure 3.9a), the protrusion is fabricated with the cladding layer and the core is cast on top. In design 2 (see Figure 3.9b), the gratings are formed with the core layer and extend into the cover. For the simulation, 120 nm grating height was used with a grating period of 368 nm; waveguide core is 140 nm; 30 gratings are taken into account. In both cases, directed scattering happens, as shown in Figure 3.9c-d. In case of the design 1, the waveguide has a small effective core thickness in region of the gratings as the gratings occupy the space. Strong scattering happens as shown in Figure 3.9c. In contrast, the design 2 (see Figure 3.9d) has an higher effective core thickness in the grating region and thus preserves the confinement better. However, in both case directed output wave can be seen in the air area, which also have the same angle - the grating period is the same in both case.

The total energy flux is integrated for both up and down direction, as plotted in Figure 3.9c and d. Moreover, the grating filling factor is varied from 0.1 to 0.9 to investigate the most efficient design. The results are shown in Figure 3.9e-f for design 1 and 2. For

design 1, the maximum out-coupling efficiency occurs at a filling factor of 0.33 for both upwards and downwards coupling. The difference in efficiency of both directions is little, while the absolute maximum of the coupling efficiency occurs in downwards coupling for 0.058. On the other hand, the design 2 gives more difference regarding the coupling direction. The highest efficiency occurs with upwards coupling for 0.045, which is lower than the case of design 1. Furthermore, the most efficient filling factor of the gratings is at 0.5 for design 2, which is usually anticipated for the highest leakage factor. The author considers the reasons to be as follows:

- Design 1 has a higher overall coupling efficiency, which is to be explained by the higher contrast of the refractive index of the grating and surrounding materials. In design 1, the gratings generate an alternation of refractive index between 1.63 and 1.43 (core and cladding). Design 2 has a lower contrast in refractive index - 1.63 and 1.53 (core and cover). The low contrast will lead to lower leakage for a given length (30 gratings in this case).

- The position of the gratings also decides the favored direction of coupling. If the protrusion is in the substrate layer, the coupling is more towards substrate i.e. downside. Analogously, if the protrusion is into the cover, the upward direction is favored.

- The most efficient coupling is impacted by both the filling factor and the geometry. If the protrusion replaces the space of the waveguide core, like in design 1, high leakage can be anticipated as the effective waveguide core is strongly reduced. Normally, 0.5 filling factor leads to the highest leakage of the gratings. However, asymmetry can happen if the core thickness is strongly influenced by the gratings. In the extreme case, when the filling factor is equal 1, the core thickness of design 1 is under the cut-off limit of the waveguide, forcing the wave to be scattered.
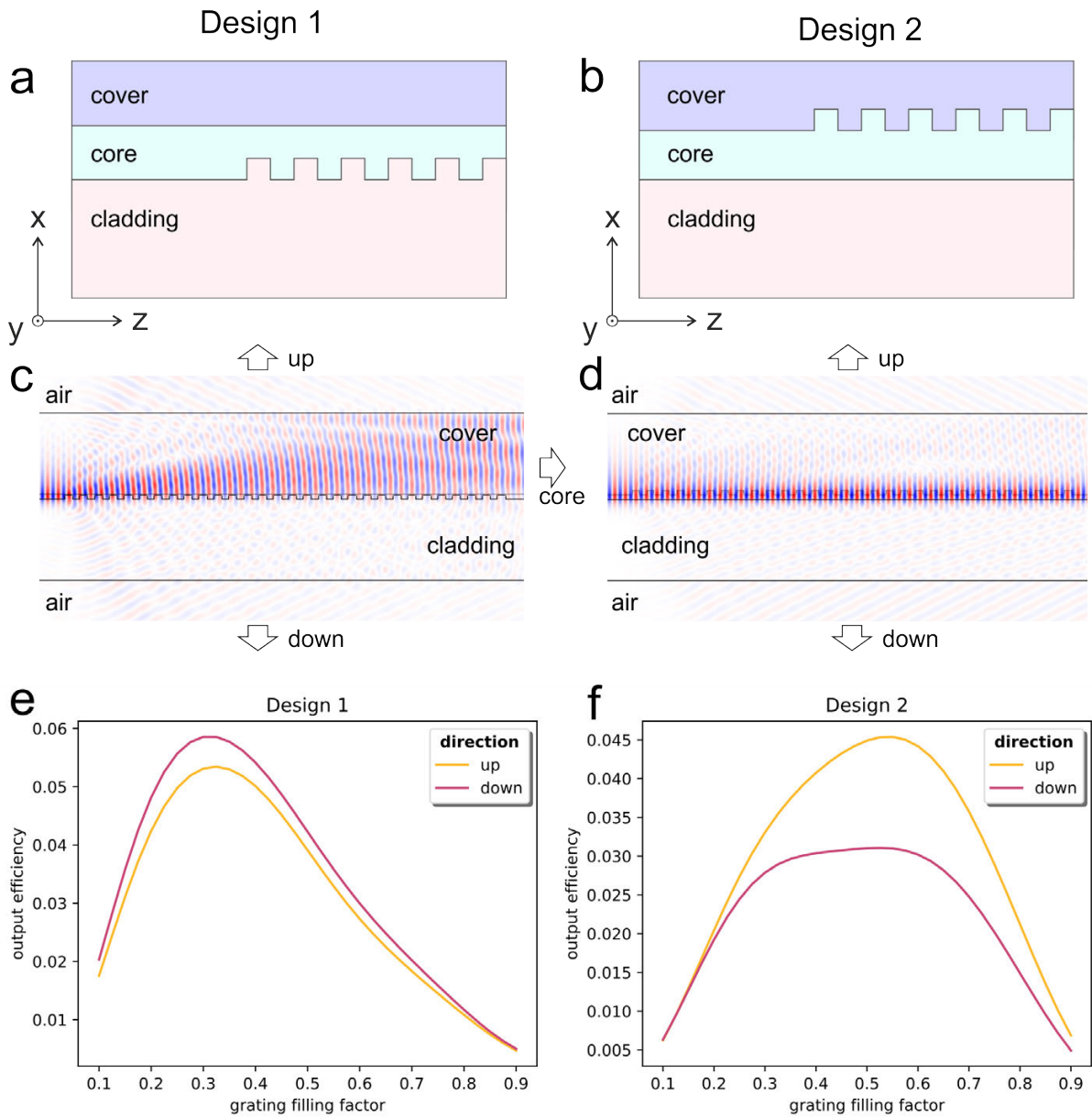
Figure 3.9: a) Illustration of the grating design 1. The gratings are extended from the surface of the cladding. b) Illustration of the grating design 2. The gratings are extended from the surface of the core. c) d) Simulation of electric field in the grating area for design 1 and 2. Air is defined as surrounding with perfect-matched-layer boundary condition. The out-coupled light is probed in both up- and down-direction. e) f) The out-coupling efficiency against different grating filling factors. Up- and down-directions are separately examined.

# 3.5   Sensitivity of waveguide sensors

## 3.5.1   Beer-Lambert Law

The law of Beer-Lambert describes the decay of light intensity $I$ in presence of absorbing medium. For a single absorbing molecule, the relation can be expressed as follows:

$$I = I_0 e^{-\sigma n l} = I_0 10^{-\epsilon c l} \tag{3.30}$$

where $I_0$ is the initial light intensity, $l$ the optical length, $\sigma$ the attenuation cross section, $n$ the number density of the attenuating species, $\eta$ the molar attenuation coefficient, and $c$ the species concentration. As we can see, for different bases, different sets of parameters can be used to describe the system. They are also interchangeable with the followingrrelation:

$$\varepsilon(\lambda) = \frac{N_A}{ln10}\,\sigma(\lambda), \tag{3.31}$$

$$c = \frac{n}{N_A}, \tag{3.32}$$

where $N_A$ is the Avogadro's number.

## 3.5.2   Sensing absorption with waveguide
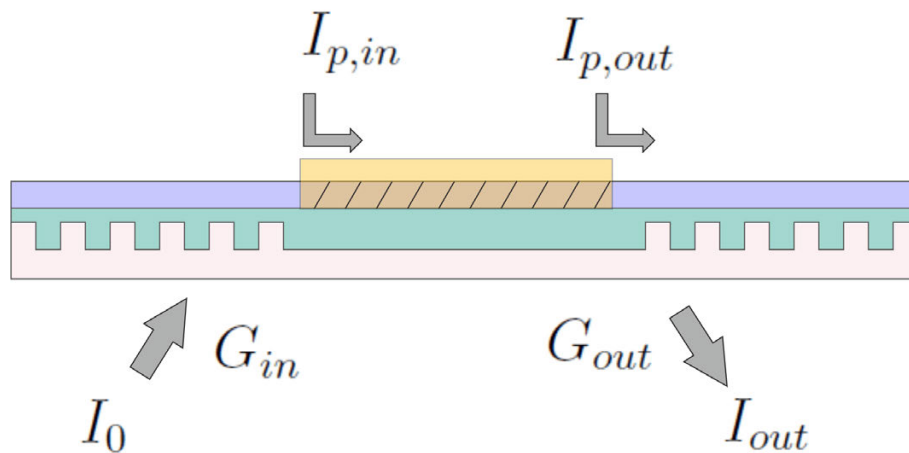


Figure 3.10: Illustration of the optical system for sensing absorption with an optical a planar waveguide

In this section, a system is described where the absorption of the analyte is measured by waveguide evanescent field. Different factors are investigated for their influence on the sensitivity. A waveguide with a sensing section (in this case a nano-filter region) is illustrated and annotated in Figure 3.10. In general, $I$ indicates the power of the light

and $G$ the optical transfer function. The input intensity $I_{p,in}$ of the waveguide mode is given by

$$I_{p,in}(\lambda) = G_{in}(\lambda)\,I_0(\lambda). \tag{3.33}$$

$I_0$ is the initial intensity of the light before entering the grating couplers, $G_{in}$ the efficiency of the coupling. Regarding the propagation loss within the region of the ridge-waveguide, we can define

$$I_{p,out}(\lambda, n, l) = I_{p,in}(\lambda)\,\exp(-\eta(\lambda)\,\sigma n l - \alpha_0 l), \tag{3.34}$$

where $I_{p,out}(\lambda, n, l)$ denotes the output power of the waveguide after a length of $l$. $\alpha_0$ is the intrinsic loss of the waveguide. Here, the power transmitted through the waveguide is attenuated by the absorption of the specimen in the liquid according to Lambert-Beer's law (the first term in the exponent) and the dielectric loss inside the waveguide (the second term). The latter should include scattering loss and material absorption loss inside the waveguide. A further parameter $\eta$ is defined as the evanescent mode overlap, which has been put into the consideration as not 100% energy is interacting with the absorbing species as assumed in the Lambert-Beer's law. It is defined as:

$$\eta = \frac{\iint_{evan} \mathbf{S} \cdot \mathbf{n}\; dx\, dy}{\iint_{tot} \mathbf{S} \cdot \mathbf{n}\; dx\, dy}, \tag{3.35}$$

where $\mathbf{S} = \mathbf{E} \times \mathbf{H}$ is the Poynting vector of the mode field in the waveguide and $\mathbf{n}$ is the normal vector to the cross-section of the waveguide.

For the output of the light, we obtain a similar relationship like the input side:

$$I_{out}(\lambda) = G_{out}(\lambda, \theta)I_{p,out}(\lambda). \tag{3.36}$$

Combing equations 3.33 to 3.36, we can obtain a description for the outcoming signal $I_{out}$ like the following expression:

$$I_{out}(\lambda) = I_0(\lambda)G_{in}(\lambda, \alpha)exp(-\eta(\lambda)\sigma n l - \alpha_0 l)G_{out}(\lambda) \tag{3.37}$$

In real measurements, it's imperative to always have a reference signal obtained and compared with the signal taken with the species of interest. Usually, it's taken immediately before or after the measurement with rinse. Here, we define an output signal $I_{out,ref}(\lambda)$ to refer to the reference measurement taken by signal acquisition with rinse fluid. The measurement and reference signal can be expressed as:

$$I_{out,mea}(\lambda) = I_0(\lambda)G_{in,mea}(\lambda)$$
$$exp(-\eta_{mea}(\lambda)\sigma_{mea}(\lambda)n_{mea}l - \alpha_{0,mea}(\lambda)l)G_{out,mea}(\lambda), \tag{3.38}$$

$$I_{out,ref}(\lambda) = I_0(\lambda)G_{in,ref}(\lambda)$$
$$exp(-\eta_{ref}(\lambda)\sigma_{ref}(\lambda)n_{ref}l - \alpha_{0,ref}(\lambda)l)G_{out,ref}(\lambda) \tag{3.39}$$

After taking the division of $I_{out,ref}$ and $I_{out,mea}$, following expression can be made:

$$\frac{I_{out,ref}(\lambda)}{I_{out,mea}(\lambda)} = \frac{G_{in,ref}(\lambda)G_{out,ref}(\lambda)}{G_{in,mea}(\lambda)G_{out,mea}(\lambda)}$$
$$exp((\eta_{mea}(\lambda)\sigma_{mea}(\lambda)n_{mea} - \eta_{ref}(\lambda)\sigma_{ref}(\lambda)n_{ref})l + (\alpha_{0,mea}(\lambda) - \alpha_{0,ref}(\lambda))l) \quad (3.40)$$

If we assume $G_{in,mea}(\lambda) = G_{in,ref}(\lambda)$ and $G_{out,mea}(\lambda) = G_{out,ref}(\lambda)$ as the grating couplers are excluded from the context of liquid interaction and $\sigma_{ref}(\lambda)n_{ref} \to 0$ for non-absorbing reference measurement, then we have:

$$\frac{I_{out,ref}(\lambda)}{I_{out,mea}(\lambda)} = exp(\eta_{mea}(\lambda)\sigma_{mea}(\lambda)n_{mea}l + (\alpha_{0,mea}(\lambda) - \alpha_{0,ref}(\lambda))l) \quad (3.41)$$

Furthermore, if we assume the intrinsic loss of the waveguide stays the same, $\alpha_{0,mea}(\lambda) = \alpha_{0,ref}(\lambda)$, then:

$$\frac{I_{out,ref}(\lambda)}{I_{out,mea}(\lambda)} = exp(\eta_{mea}(\lambda)\sigma_{mea}(\lambda)n_{mea}l) \quad (3.42)$$

or

$$ln(\frac{I_{out,ref}(\lambda)}{I_{out,mea}(\lambda)}) = \eta_{mea}(\lambda)\sigma_{mea}(\lambda)n_{mea}l \quad (3.43)$$

We can also use molar attenuation coefficient $\eta$ and species concentration $c$ replacing the attenuation cross section and number density:

$$\chi = \log_{10}(\frac{I_{out,ref}(\lambda)}{I_{out,mea}(\lambda)}) = \eta_{mea}(\lambda)\varepsilon_{mea}(\lambda)c_{mea}l. \quad (3.44)$$

Taking the derivative of the concentration, we obtain an expression of sensitivity:

$$S = \frac{\partial\chi}{\partial c} = \eta_{mea}(\lambda)\varepsilon_{mea}(\lambda)l. \quad (3.45)$$

**Short conclusion**   Here, we can conclude some important facts regarding the sensitivity:

- For a given analyte with known extinction coefficient, the sensitivity of the waveguide sensor is proportional to the mode-overlap ratio $\eta$ and the length of the waveguide.

- The change in refractive index of the media doesn't substantially influence the sensitivity since it alters the mode-overlap ratio $\eta$ only slightly.

- To obtain a better signal to noise ratio, one should maximize the signal $I_{out,mea}(\lambda)$, which can include strategies like 1) suppression of the intrinsic waveguide loss, 2) increase of the initial input optical, 3) improve the coupling efficiency.

- To be able to compare with the reference spectra that is taken by a cuvette and a photospectrometer, the dependence of the evanescent mode overlap $\eta$ has to be taken into account since $\eta$ changes strongly with the wavelength.

### 3.5.3   Refractive index measurement

In this section, the method of measuring refractive index change by a waveguide interferometer is described with regard to the sensing sensitivity.

The time-dependent phase difference $\Delta\widetilde{\phi}(t)$ between the sensing and reference arms is given as:

$$\Delta\widetilde{\phi}(t) \equiv \Delta\phi_{sen}(t) - \Delta\phi_{ref}(t)$$
$$= 2\pi\frac{L}{\lambda}\Delta\widetilde{n}_{eff}(t), \tag{3.46}$$

where

$$\Delta\widetilde{n}_{eff}(t) \equiv \Delta n_{eff,sen}(t) - \Delta n_{eff,ref}(t). \tag{3.47}$$

$\Delta\widetilde{n}_{eff}$ is the total refractive index difference between the sensing ($\Delta n_{eff,sen}$) and the reference arms ($\Delta n_{eff,ref}(t)$). $L$ is the length of the waveguide, and $\lambda$ the wavelength. In order to achieve a higher phase change, one can increase the length of the length of the waveguide or decrease the sensing wavelength. The refractive index difference between the sensing and the reference waveguide is also to be maximized, which, similarly to the absorption sensor, is dependent on the evanescent mode overlap $\eta$. In the literature, attempts have been shown to increase the mode-overlap by means of a slot waveguide[48, 2].

The main limitation of such an interferometer sensor is often the thermal influence, since tiny temperature fluctuation can change the refractive index of the waveguide materials. Thus, the temperature influence is analyzed here. The temperature variation is defined as $\Delta T$. The total refractive index change $\Delta\widetilde{n}_{eff}$ is thus influenced by both the change in bulk refractive index of the analyte $\Delta n_a$ and the temperature $\Delta T$ as:

$$\Delta\widetilde{n}_{eff}(t) = \left(\frac{\partial\widetilde{n}_{eff}}{\partial n_a}\right)\Delta n_a + \left(\frac{\partial\widetilde{n}_{eff}}{\partial T}\right)\Delta T. \tag{3.48}$$

The first term in equ. 3.48 describes the influence of the bulk refractive index of the analyte, which is the sensing capability of the sensor. The second term describes the thermal sensitivity of the waveguide materials, which can be further elaborated as[87]:

$$\frac{\partial\widetilde{n}_{eff}}{\partial T} = \frac{\partial\widetilde{n}_{eff}}{\partial n_c}\frac{\mathrm{d}n_c}{\mathrm{d}T} + \frac{\partial\widetilde{n}_{eff}}{\partial n_{wg}}\frac{\mathrm{d}n_{wg}}{\mathrm{d}T} + \frac{\partial\widetilde{n}_{eff}}{\partial n_{sub}}\frac{\mathrm{d}n_{sub}}{\mathrm{d}T} + \frac{\partial\widetilde{n}_{eff}}{\partial d_F}\alpha_F d_F, \tag{3.49}$$

where $n_i$, with $i = c, wg, sub$, is the refractive index of the waveguide cover, core, and cladding (substrate). Consequently, $\frac{\mathrm{d}n_i}{\mathrm{d}T}$, with $i = c, wg, sub$, denotes the thermo-optic coefficient of the waveguide cover, core, and cladding. The last term in eq. 3.49 describes the contribution of the thermal expansion of the waveguide thickness, where $\alpha_F$ is the thermal expansion coefficient of the waveguide thickness $d_F$. This term is negligible compared to the contributions of the thermo-optic effects[87].

For a complex waveguide with nano-filters atop, the exact solution requires numerical simulations. However, some approximations can be made to show the main factor of the thermal influence. Here, we assume that all waveguide materials have the same thermo-optic coefficient as OrmoComp, which is $-1.27 \times 10^{-4}$ °C$^{-1}$[78]. Also, the impact from the waveguide core and cladding is the same for reference and sensing waveguide, i.e. $\frac{\partial \widetilde{n}_{eff}}{\partial n_{wg}} = \frac{\partial \widetilde{n}_{eff}}{\partial n_{sub}} = 0$. Thus, eq. 3.49 can be simplified to:

$$\frac{\partial \widetilde{n}_{eff}}{\partial T} = \frac{\partial n_{eff}}{\partial n_c} \left( \frac{\mathrm{d}n_a}{\mathrm{d}T} - \frac{\mathrm{d}n_{OrmoComp}}{\mathrm{d}T} \right). \tag{3.50}$$

In this model, the most critical thermal influence is from the difference between the thermo-optic coefficients of the analyte ($dn_a/dT$) and the waveguide cover material ($dn_{OrmoComp}/dT$). If we assume water is used as medium for the analyte, then $dn_a/dT$ = $-0.9 \times 10^{-4}$ °C$^{-1}$[61]. We further assume the proportional impact of the cover to the effective refractive index $\partial n_{eff}/\partial n_c$ is in order of $10^{-1}$. Thus, it can be concluded that the total thermal influence of the waveguide $\partial \widetilde{n}_{eff}/\partial T$ is in order of $10^{-6}$ °C$^{-1}$. Thus, if one wants to reach a sensitivity in order of $10^{-8}$ RIU, the thermal control should ideally in order of 0.01 °C.

**Short conclusion**   The sensitivity of the interferometer is more complex than the absorption sensor. Larger waveguide length and lower wavelength is constructive for large phase signal. Higher evanescent-mode overlap also contributes to the sensitivity, while the exact influence should be numerically determined. The thermal influence of the waveguide is strongly influenced by difference of the thermo-optic coefficient between the analyte and reference cover material. A thermal control in 0.01 °C should enable a thermal interference in $10^{-8}$ RIU.

# 3.6   Mode analysis in a waveguide with nano-filters

As discussed in the previous sections, mode field of a waveguide is critical for the sensitivity of a waveguide sensor. In this section, different parameters are studied to investigate their influences on the mode field. In Figure 3.11a-d, a schematic definition of the most relevant parameters is given, including waveguide core thickness, filter height, and residual layer thickness. Furthermore, we define the energy fraction that is in the liquid to the total waveguide energy as the evanescent mode overlap, as shown in Figure 3.11c. This is the key parameter to study the sensitivity of the sensor for both absorption and refraction measurement. Another important parameter is the unfiltered ratio, which is defined as the ratio of energy above the liquid and the total energy in the liquid, as shown in Figure 3.11d. This parameter is used to quantify the ability of the filtration, since the area above the filters can be accessed by large particles in the liquid, like red blood cells. In the following sections, the results of simulations with FEM method (COMSOL multiphysics) are shown.



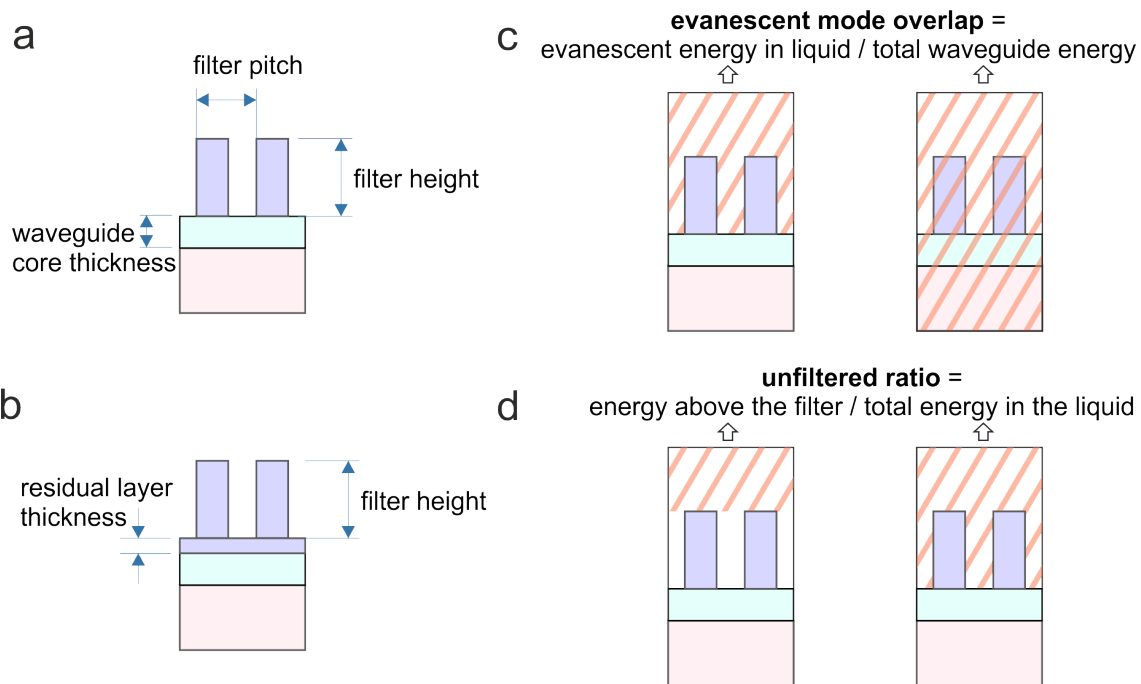Figure 3.11: a) Definition of the waveguide core thickness, filter pitch, and filter height. b) Definition of the residual layer thickness and filter height. c) Definition of the evanescent mode overlap, which is the ratio of evanescent energy in liquid to the total waveguide energy. d) Definition of the unfiltered ratio, which is the ratio of energy above the filter to the total energy in the liquid.

## 3.6.1   Waveguide modes and filtering function



Figure 3.12: a) Simulation of the evanescent mode overlap of for different combinations of waveguide core thicknesses and filter heights. Only TE modes are considered. Inserts above the images are the amplitude of the electrical field for different modes. Higher order modes occur when the value abruptly changes as indicated by the color change. b) Simulation of the unfiltered evanescent ratio for different TE modes. Inserts below the image indicate different TE modes, where the unfiltered ratio is high.

At first, the evanescent mode overlap for different waveguide core thickness and filter height is investigated. TE polarization is considered and the propagation light has a wavelength of 420 nm. In Figure 3.12a, the *highest* evanescent mode overlap (of all modes) is plotted for all combinations of waveguide core thickness and filter height. For some combinations of the two parameters, multiple modes can occur, which will also lead to different evanescent mode overlap as well as unfiltered ratio. Inserts are the amplitude of the electrical field of different modes with different parameter combinations. The important information for the figure is as follows:

- The map of the evanescent mode overlap is split into three main areas, which are caused by three different modes. With a low filter height ($<100$ nm), the first order mode occurs when the waveguide is thicker than 300 nm. With increased filter height, higher order modes occur at lower waveguide core thicknesses. With a filter

height of 500 nm, the first order mode appears already under 200 nm waveguide core thickness, and a second order mode is excited as well for a waveguide thickness larger than 420 nm, as shown in Figure 3.12a.

- Higher order modes generates higher evanescent mode overlap. As we can see from the inserts on top of the 2D graph, in fundamental modes ($TE_0$) the field is mainly confined inside the waveguide. The field is pulled out a little where the filter appears. When the thickness of the waveguide increases, another mode can propagate, which is located mainly inside the filter, as shown in $TE_1$ (middle) and $TE_2$ (right), these modes give high evanescent ratio in the liquid up to 0.26.

While the evanescent mode overlap increases the sensitivity, the filtering function can be compromised. In Figure 3.12b, the unfiltered ratio, which corresponds to the highest evanescent mode overlap in Figure 3.12a, is plotted. The important aspects are as follows:

- The highest unfiltered ratio always appears when the filter height is low. Under 100 nm filter height, the unfiltered ratio can reach 0.5, i.e. more than half the energy in on top of the filter.

- Higher order modes give rise to higher unfiltered ratio. When the modes reside in the filter (instead of the waveguide core), the unfiltered ratio is high, due to the field beyond the top of the filter.

- The mixture of the modes causes radically different evanescent mode overlap as well as filtering function. Due to the geometry of the waveguide, all modes have to be converted into a three layer slab waveguide before it reaches the grating couplers. Different modes will have different conversion efficiency with the slab waveguide modes. It is difficult to individually extract those modes, thus one will get a sensitivity which is a mixture of all available waveguide modes, which reduces the reliability and increases the sensor-to-sensor variation. In order to avoid this unreliability, only the fundamental mode should be excited, which can exclude the higher order modes.

- The transition lines in Figure 3.12a and b, where the values abruptly change, give the geometrical limits of the waveguide design regarding the core thickness and the filter height, if a single mode waveguide is desired.
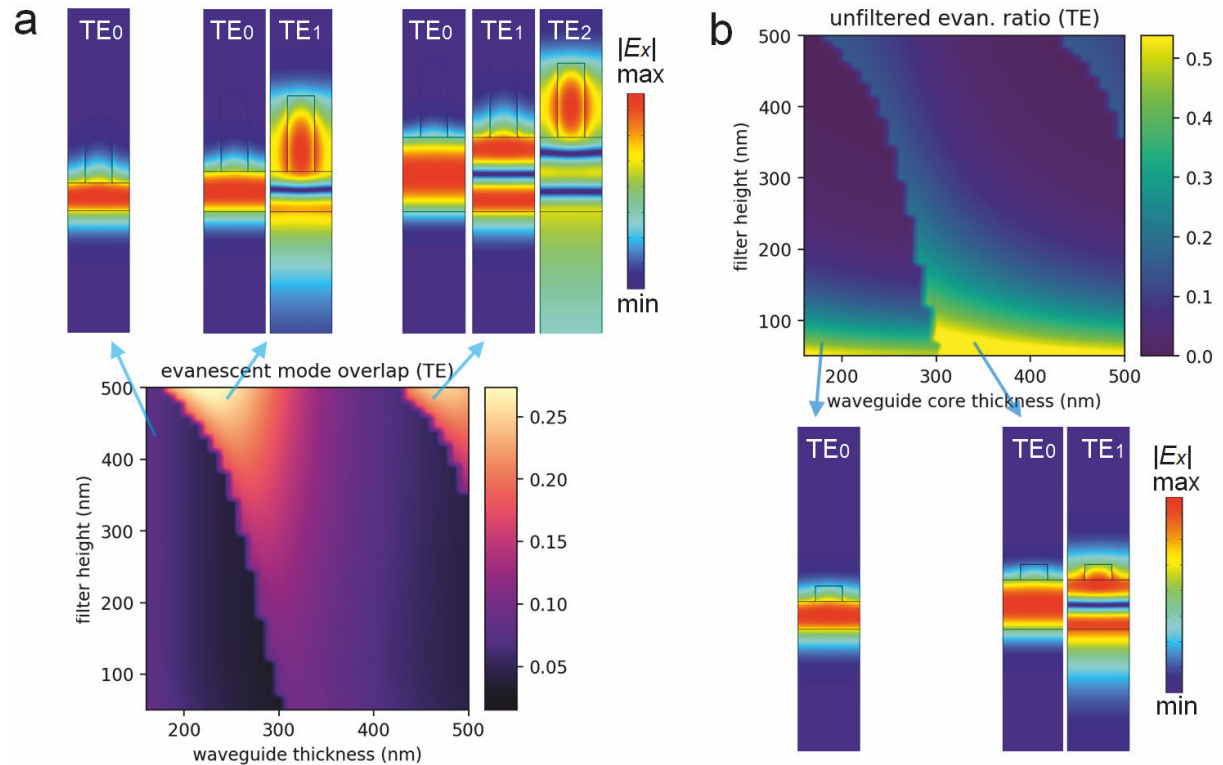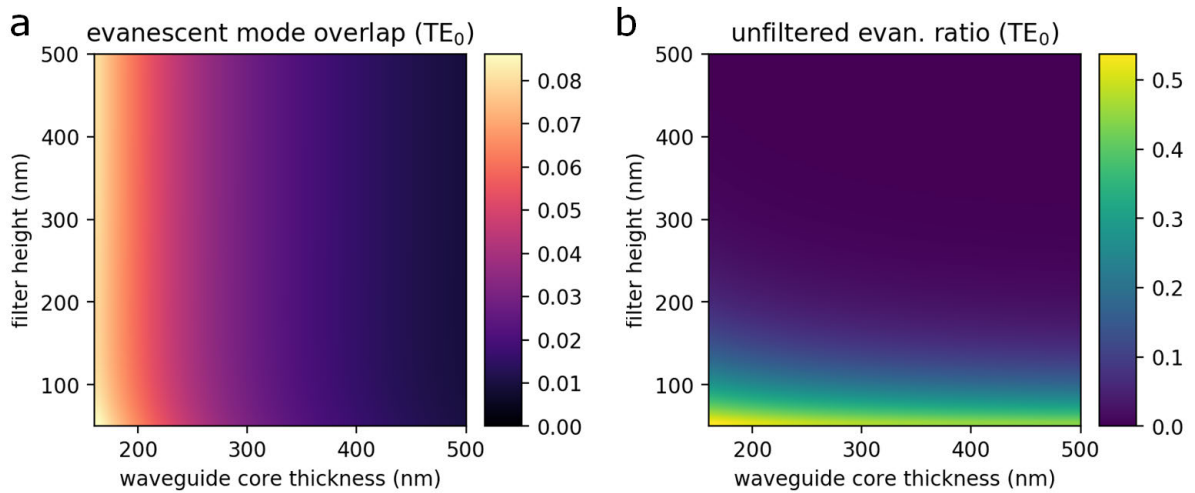
Figure 3.13: a) Simulation of the evanescent mode overlap of for different combinations of waveguide core thicknesses and filter heights. Only the *fundamental* TE mode (TE$_0$) is considered. b) Simulation of the unfiltered evanescent ratio for TE$_0$ mode.

In Figure 3.13a and b, the evanescent mode overlap and the unfiltered ratio of only the fundamental mode (TE$_0$) is plotted. In comparison to Figure 3.12, the distribution is clearer. The valuable information can be summarized as follows:

- For the evanescent mode overlap, lower waveguide core thickness leads to higher mode overlap. The influence from the filter height is little, which is attributed to the fact that the electrical field actually do not reach the top of the filter after about 300 nm, thus the additional height does not contribute to the field distribution. Only when the filter height is lower than 100 nm, this relation breaks because of the field extending the top of filters.

- For the unfiltered evanescent ratio, higher filter height clearly decreases the unfiltered ratio. For a unfiltered evanescent ratio of 0.5%, one needs about 400 nm filter height (waveguide core thickness 200 nm). Note that the simulation is done at a wavelength of 420 nm. For an increased wavelength, higher filter height will be needed for the same unfiltered ratio, due to the lower field confinement.

So far, we have obtained a picture of possible combinations for achieving a single mode waveguide with a balanced performance between sensitivity and filtering function. Now, the wavelength is added as a new parameter. As we have seen from the previous section, the wavelength plays a large role in coupling conditions. Its influence on the evanescent mode overlap and unfiltered evanescent ratio is studied in Figure 3.14a and b.
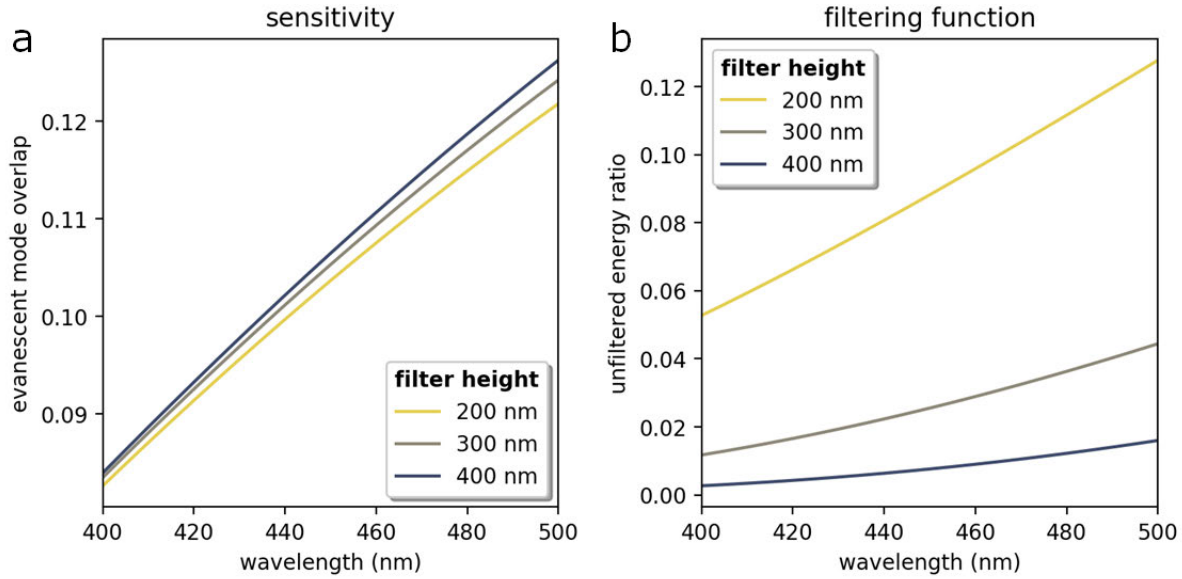
Figure 3.14: a) Simulation of the evanescent mode overlap with different wavelengths. Filter heights from 200 nm to 400 nm are included. Only $TE_0$ mode is considered. b) Simulation of filtering function for different wavelengths. Filter height from 200 nm to 400 nm are included for $TE_0$ mode.

- In Figure 3.14a, the relation of the wavelength on evanescent mode overlap (sensitivity) is pictured. Higher wavelength monotonously increases the mode overlap. An increase of circa 50% is shown for increasing wavelength from 400 nm to 500 nm, indicating significantly wavelength-dependent sensitivity.

- The filter height has little influence on the evanescent mode overlap. Higher filters generally increase the sensitivity because the mode field is pulled out of the waveguide towards the filter.

- Filtering function is strongly dependent on both wavelength and filter height, as shown in Figure 3.14b. A lower filter height radically increases the unfiltered evanescent ratio, which is amplified by the larger wavelength. More than 100% increase in the unfiltered ratio can be expected by increasing wavelength from 400 nm to 500 nm.

**Trade-off between sensitivity and bandwidth**  After the relation between the sensitivity and the geometry of the waveguide (core thickness and filter height) is investigated, the bandwidth will be also considered. As shown in the previous section, the evanescent mode overlap (sensitivity) is strong correlated with the core thickness. A thinner core leads to higher mode overlap, while a high filter height is constructive to both sensitivity and filtering functionality. However, a thin waveguide core will also lead to low cut-off wavelength, as already shown in Figure 3.6. There is thus a trade-off between sensitivity and bandwidth, if broadband coupling for absorption measurement is wished.
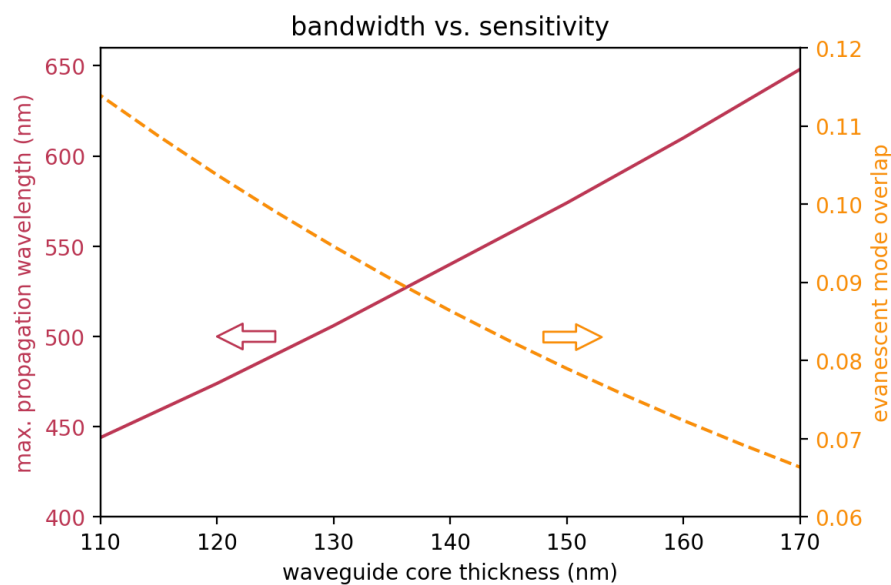


Figure 3.15: Plot of calculated maximum propagation wavelength (bandwidth) and simulated evanescent mode-overlap (sensitivity) against different waveguide core thickness. A trade-off is shown with bandwidth and sensitivity, as increased core thickness can support higher bandwidth but smaller sensitivity.

Figure 3.15 demonstrates the trade-off between the bandwidth and the sensitivity. The maximum propagation wavelength that is supported by the waveguide is plotted to the left axis. A higher bandwidth i.e. higher cut-off wavelength can be achieved by a higher waveguide core thickness. For a cut-off wavelength of 500 nm, a core thickness of 130 nm is required, while 600 nm wavelength can be supported when the core thickness reaches 160 nm. On the other hand, the sensitivity, which is given by the evanescent mode overlap, is plotted to the right axis. Here, we observe a decreasing sensitivity with an increasing waveguide core thickness. From 110 nm to 170 nm core thickness, a decrease of 70% in evanescent mode overlap can be seen.

To achieve a balanced performance of bandwidth and sensitivity, the cut-off frequency is set to be 550 nm, which corresponds to a core thickness of 140 nm. 550 nm is enough for

measuring two most relevant absorbing molecules in blood plasma, which are hemoglobin and bilirubin. An evanescent mode overlap of 0.085 is thus achieved by this core thickness.

## 3.6.2   Influence of the imprint residual layer



Figure 3.16: a) Simulation of the evanescent mode overlap for different residual layer thickness and waveguide core thickness. Only $TE_0$ mode is considered. The wavelength is 420 nm for the simulation. b) Simulation of the unfiltered evanescent ratio for different residual layer thickness and waveguide core thickness. Inserts illustrate the amplitude of the electrical field with high (top insert) and low (bottom insert) residual layer. In general, residual layer is detrimental for the sensitivity.

Ideally, the filters can be fabricated on top of the waveguide core without any residual in the nano-wells. However, during the fabrication, it is not always possible to fabricate these filters without leaving residue on the waveguide. Residual layer can remain after the imprint, which causes a transition layer between the waveguide core and the filter, as illustrated in Figure 3.11b. Knowing the influence of the residual layer is important for estimating the potential sensitivity variation from sensor to sensor. Numerical simulations were carried out to investigate the impact. The results are shown in Figure 3.16a and b. The residual layer thickness is varied in the y axis while the waveguide thickness is swept and plotted in the x axis. Here, 420 nm wavelength and fundamental $TE_0$ mode is considered. For the evanescent mode overlap shown in Figure 3.16a, both

waveguide core thickness and residual layer thickness are of importance. For a 30 nm residual layer, a 30% decrease of mode overlap is induced. Effectively, this is equivalent to an increase of the waveguide thickness of about 50 nm, which, as discussed earlier, reduces the sensitivity. As we can see from the insert on the top, a residual layer with a refractive index of 1.53 buffers the refractive index from waveguide (1.63) to sample (1.33) and accommodates the electrical field, thus reducing the interaction with the liquid.

The unfiltered evanescent ratio, shown in Figure 3.16b, shows similar relation with the evanescent mode overlap. Both higher waveguide core thickness and residual layer thickness can reduce the unfiltered ratio, as the confinement is enhanced by these two parameters. In general, the residual layer thickness has a smaller impact on unfiltered ratio than evanescent mode overlap, which can be attributed to the fact that the filter height is kept the same (400 nm) on top of the residual layer, which effectively keeps the unfiltered region away from the evanescent field.
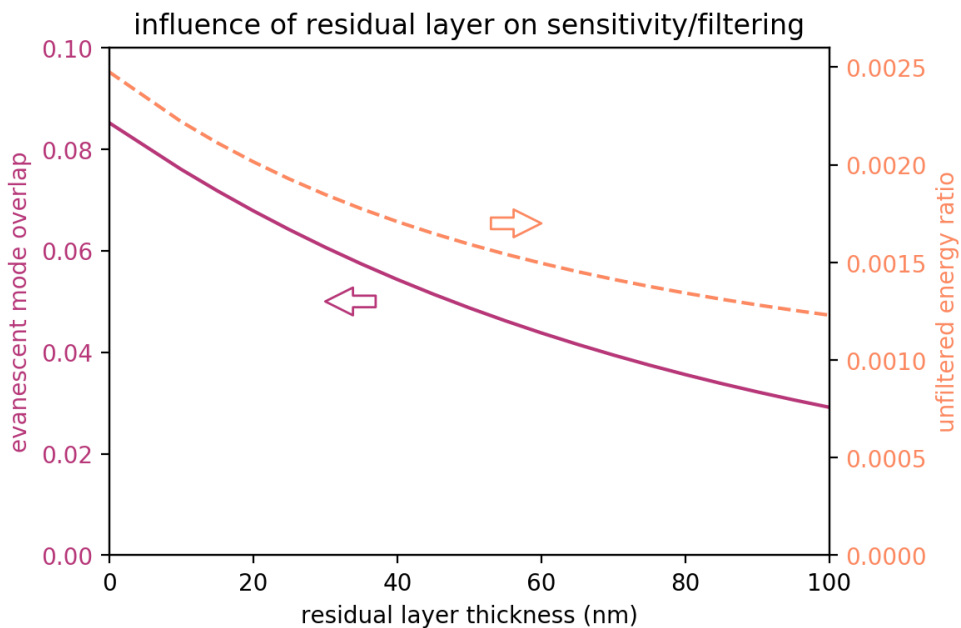


Figure 3.17: Simulation of the evanescent mode overlap and unfiltered ratio for different residual layer thicknesses. 50% decrease in evanescent mode overlap can be observed with 60 nm residual layer.

The impact of the residual layer thickness is further plotted in Figure 3.17 , in which the left axis denotes the evanescent mode overlap and the right axis the unfiltered evanescent ratio. Here, there is also a trade-off to be observed, as low residual layer increases the sensitivity but also increases the unfiltered ratio. However, since the unfiltered ratio for a 400 nm filter is under 0.0025 for zero residual layer, the filtering function is considered to be sufficient.
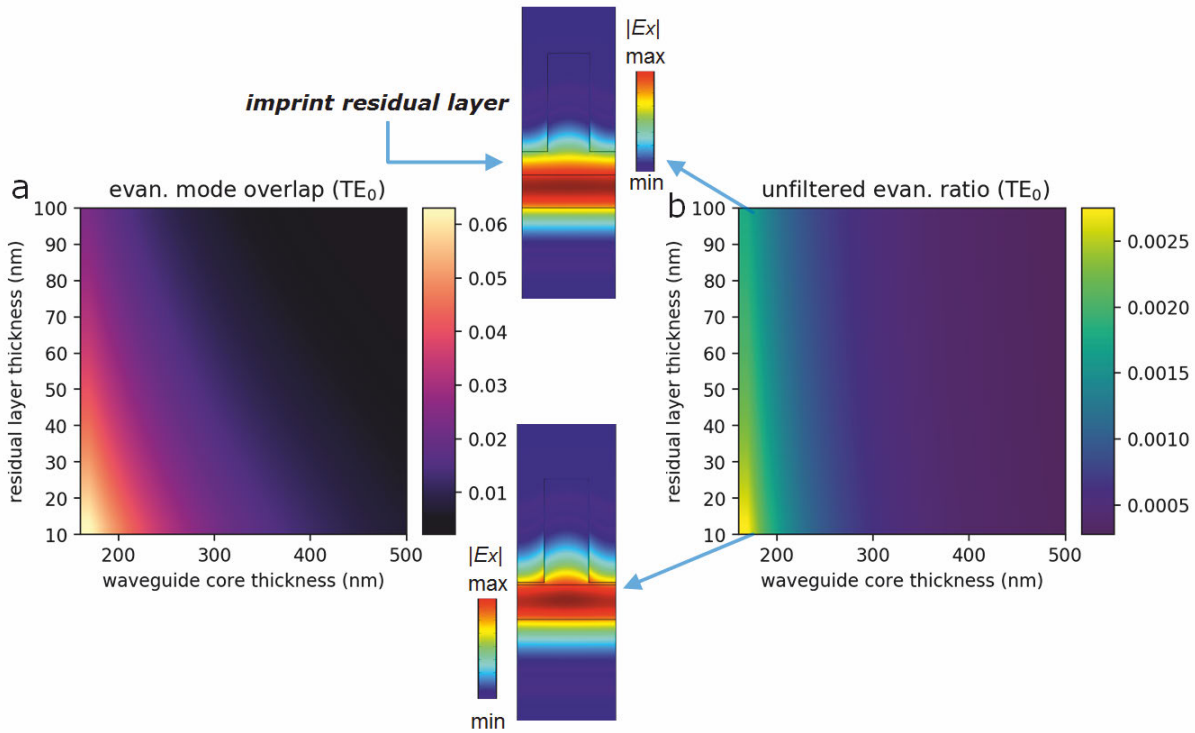
### 3.6.3   Influence of the pitch width
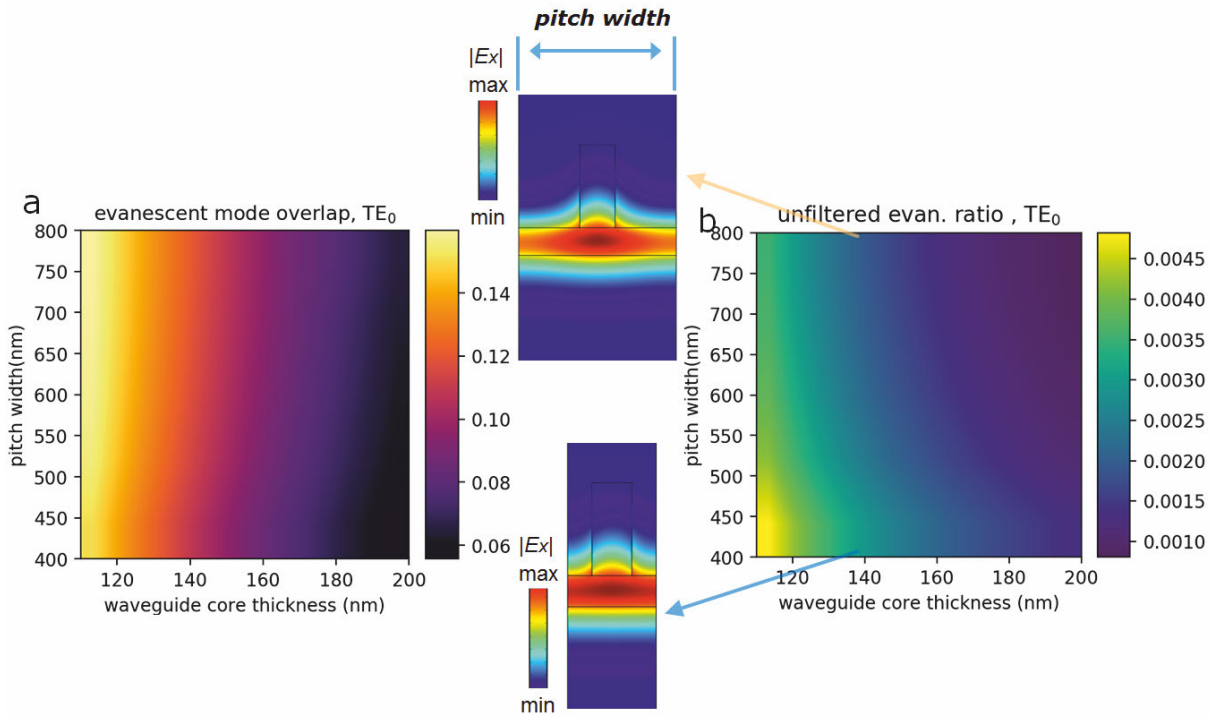


Figure 3.18: a) Simulation of the evanescent mode overlap for different pitch width and waveguide core thickness. Only $TE_0$ mode is considered. The wavelength is 420 nm for the simulation. b) Simulation of the unfiltered evanescent ratio for different pitch width and waveguide core thickness. Inserts illustrate the amplitude of the electrical field with 800 nm (top insert) and 400 nm (bottom insert) pitch width.

So far, we have kept the pitch width (period) of the filters the same (at 400 nm). However, different pitch widths can be used to realize different filtering functionality. With a pitch width of 400 nm, 180 nm was occupied by the filter ridge and leaving 220 nm opening for interaction between liquid and evanescent field. The main consideration of choosing the value was to ensure the filtering function for majority of the contents in blood plasma: lymphocytes (min. feature size: 7 µm), red blood cells (min. feature size: 2 µm), and platelets (min. feature size: 2 µm). However, it is not a fixed value. Actually, different pitch widths can be easily realized by using different imprint stamps. Here, the pitch width was swept as a parameter with a fixed filter width of 180 nm. The results are shown in Figure 3.18. In Figure 3.18a, the evanescent mode overlap of the $TE_0$ mode is plotted for different pitch widths and waveguide core thicknesses. Here, a reduced range of the core thickness is used to focus more on the most relevant area.

As we can see from 3.18a, a small waveguide core thickness leads to higher evanescent mode overlap, while a higher pitch width also induces higher mode overlap. An increase

of pitch width from 400 nm to 800 nm with a core thickness of 140 nm causes an increase of mode overlap of 0.2, which is equivalent to a decrease of the core thickness of 14 nm. This change is actually smaller than initially expected. Given the fact the wave propagates inside the filter does not contribute to the sensitivity, the change of the filling factor of filter ridges (the space occupied by the filters to the whole) should strongly influence the mode overlap, which is calculated only to the area between the filters, as illustrated in Figure 3.11. From 400 nm to 800 nm, the *filling factor* of the filter ridges changes from 0.45 to 0.225 (41% decrease). If we assume a situation where the filters do not perturb the field on top of the waveguide (e.g. filters have the same refractive index as liquid sample), then the change in the filling factor will also lead to an increase of 41% in evanescent mode overlap. However, the simulation shows an increase less than 20%. The author thinks that this effect is attributed to the fact that the strongest field in the liquid is located besides the filter, especially in the corner. The inserts in Figure 3.18 demonstrate this phenomenon: the largest field amplitude appears at the interface between the filter and the liquid. When the pitch width increases, the additional space occupied by the liquid has smaller contribution to the sensitivity, thus causing the non-linear relation.

On the other hand, the performance of the filtering is plotted in Figure 3.18b. Overall, for the 400 nm filter height that is used in the simulation, the unfiltered evanescent ratio is very low (under 0.5%). For lower pitch width like 400 nm, the field is more pushed into the liquid, thus causing higher unfiltered ratio. This effect is suppressed with increasing pitch width and gradually reaches the minimum at 800 nm. The elevated evanescent field with lower pitch width is in agreement with the assumption that, with a gap size small enough, a slot waveguide can be realized, where the mode resides mainly outside and between the high refractive index materials[48, 42, 2].

## 3.6.4   TE and TM modes

So far, we have investigated most relevant parameters of the nano-filtered waveguide design in TE polarization, where the electrical field is horizontally aligned in the cross-section of the waveguide. As shown in Figure 3.2, TM modes can also be exited inside the slab waveguide. As already indicated in Figure 3.2, TM modes have lower effective refractive index than TE modes, i.e. weaker confinement than TM modes. The evanescent mode overlap (sensitivity) is in general larger in TM than TE. Figure 3.19a illustrates the difference (in ratio) in evanescent mode overlap for fundamental TM mode ($TM_0$) and fundamental TE mode ($TE_0$). For a waveguide thickness lower than 400 nm, $TM_0$ exhibits higher sensitivity than $TE_0$. The largest difference appears at the lowest waveguide thickness with the highest filter height. Top inserts in Figure 3.19 show the electrical field of the $TE_0$ and $TM_0$ modes for a waveguide with 160 nm core thickness. It is obvious that, due to the boundary condition of Maxwell equation, the tangential component of electrical field is continuous at the material interface. Thus, when the electrical field is vertically applied (TM mode), no abrupt change occurs at the vertical wall between the
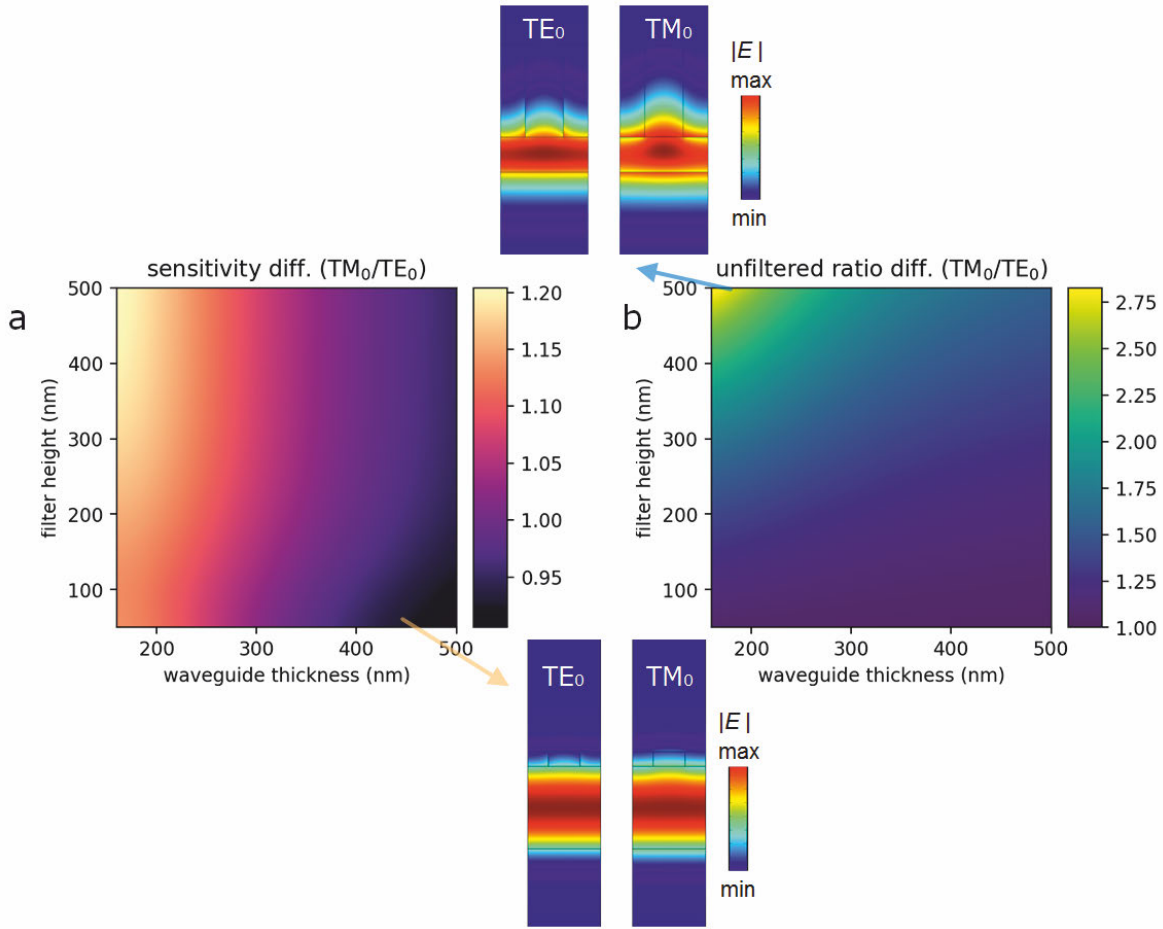
Figure 3.19: a) Simulation of the evanescent mode overlap for $TE_0$ and $TM_0$ modes. The wavelength is 420 nm for the simulation. b) Simulation of the unfiltered evanescent ratiofor $TE_0$ and $TM_0$ modes. Inserts illustrate the amplitude of the electrical field with a large filter height (top insert) and a low filter height (bottom insert).

filter and the liquid, whereas the horizontally polarized (TE) mode is discontinuous for vertical interfaces. The field intensity for TM mode is strongly extended into the liquid upwards, causing both higher evanescent mode overlap (20% more than TE) and higher unfiltered evanescent ratio (175% more than TE).
In case of high waveguide core thickness like 450 nm, the fundamental modes for TE and TM polarization are similar, as shown in the bottom inserts in Figure 3.19. The existence of the filter perturbs the field distribution minimally, as the field is strongly confined inside the core area.

## 3.6.5 Conclusion

- Different modes co-exist in the waveguide when the core thickness and the filter height are high enough.

- Higher order modes are to be avoided for the clarity of the sensitivity.

- For the fundamental mode, lower waveguide core thickness leads to higher sensitivity. Filter height should be at least 200 nm, ideally 400 nm.

- There is a trade-off between the sensitivity and the bandwidth that the waveguide can support. 140 nm thick waveguide core gives a good balance.

- Imprint residual should be avoided as much as possible.

- Larger pitch width gives higher sensitivity, which is however not directly proportional to the filling factor of the filter.

- TM mode gives higher sensitivity but also higher leakage out of the filter region.

# CHAPTER 4

# Materials and Fabrication

This chapter describes the fabrication methods that are developed to make polymer waveguides as well as large-scale stamp replications, which uses the techniques that are developed for the waveguide fabrication. Although different fabrication strategies have been used to enable the fabrication of waveguide devices, a central technology has been the nanoimprint lithography. Since we target for high resolution, high throughput, and low cost fabrication, nanoimprint lithography provides a replication process that can combine all the merits. Furthermore, some aspects of the electron beam lithography (EBL) are discussed, which has been extensively used to fabricate nano-structures on imprint stamps. Here, the chapter is divided into three main sections:

- **Fabrication of a polymeric slab waveguide.** Here, the method of making a simple slab waveguide with organic-inorganic hybrid polymer is described. Furthermore, characterization of the hybrid materials, especially regarding their optical properties, has been demonstrated and discussed.

- **Nanoimprint of filters on waveguide.** Here, a nanoimprint procedure for making nano-filters on top of a simple slab waveguide is presented.

- **Electron beam lithography for stamp generation and meta-surface applications.** EBL methods have been discussed. Two procedures are shown for fabricating imprint stamps and meta-surfaces. Furthermore, strategy used for high-throughput EBL is shown and discussed.

- **Large scale nano-structured stamp replication.** By using the technique of low-residue replication, the author demonstrates here wafer-scale replication of nano-dot array for plasmonic color generation application.

## 4.1 Fabrication of a hybrid-polymer slab waveguide

Nanoimprint lithography is used for low-cost fabrication of a hybrid-polymer slab waveguide. To achieve low loss in the waveguide, the process is optimized towards low surface roughness (of the waveguide) and low absorption in the waveguide material. Methods will be shown in the following sections.

## 4.1.1  Fabrication protocol
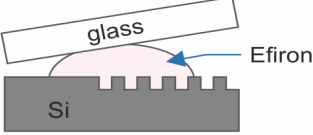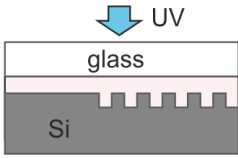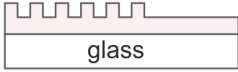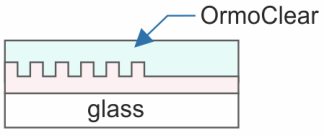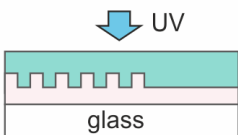
| Process | Procedure | Illustration |
|---|---|---|
| **1. Nanoimprint of grating couplers** | | |
| Cast-imprint cladding polymer | About 150 µL undiluted Efiron UVF polymer is cast onto Si stamp with glass substrate on the top side. Apply pressure for 1 min. Relaxation for 3 min. | |
| UV curing | 4 minutes exposure with broadband UV light (11 mJ/cm² at 365 nm) in $N_2$ atmosphere. | |
| Separation | Using razor blade to separate the substrate with the Si stamp. Polymer should stay on the glass substrate. | |
| **2. Casting waveguide core layer** | | |
| Spin-coating of core polymer | The polymer needs to be treated with $O_2$ plasma at first. OrmoClear HI01 polymer is diluted in PGMEA and spin-coated on top of the substrate. Prebake at 80° for 5 min. | |
| UV curing | Sample is cured under $N_2$ atmosphere for 4 minutes with a broadband UV light (11 mJ/cm² at 365 nm). Inspection is done with an ellipsometer to determine the thickness. | |

Table 4.1: Fabrication protocol of polymer slab waveguide with grating couplers and air cover.

**UV-curing cast imprint** Cast imprint is one variation in nano-imprint lithography, where the polymer is simply cast onto the substrate and imprinted with the stamp by pressure. Especially in combination with UV-curing, cast imprint is a powerful method for replication of micro- and nano-structures. The advantages of UV-curing cast-imprint are as follows:

- Simple and fast process. There is not need for spin-coating or spray-coating. The polymer is dispensed in the liquid phase to the substrate and being spread by the pressure applied. UV curing process is extremely fast in comparison to thermal imprint, where heating and cooling steps are inevitable and time-consuming.

- High replication fidelity and low defects. Since the polymer is cast in the liquid phase, the viscosity is very low compared with thermal imprint, which is constructive for replicating nano-structures. Furthermore, no vacuum is needed during the imprint to eliminate trapped air bubbles between the stamp and the substrate. If handled properly, the spreading of the polymer do not include any air void.

- Ecological process. Since no spin-coating is needed, the material usage is the low. In case of spin-coating, 90% or more materials are wasted.
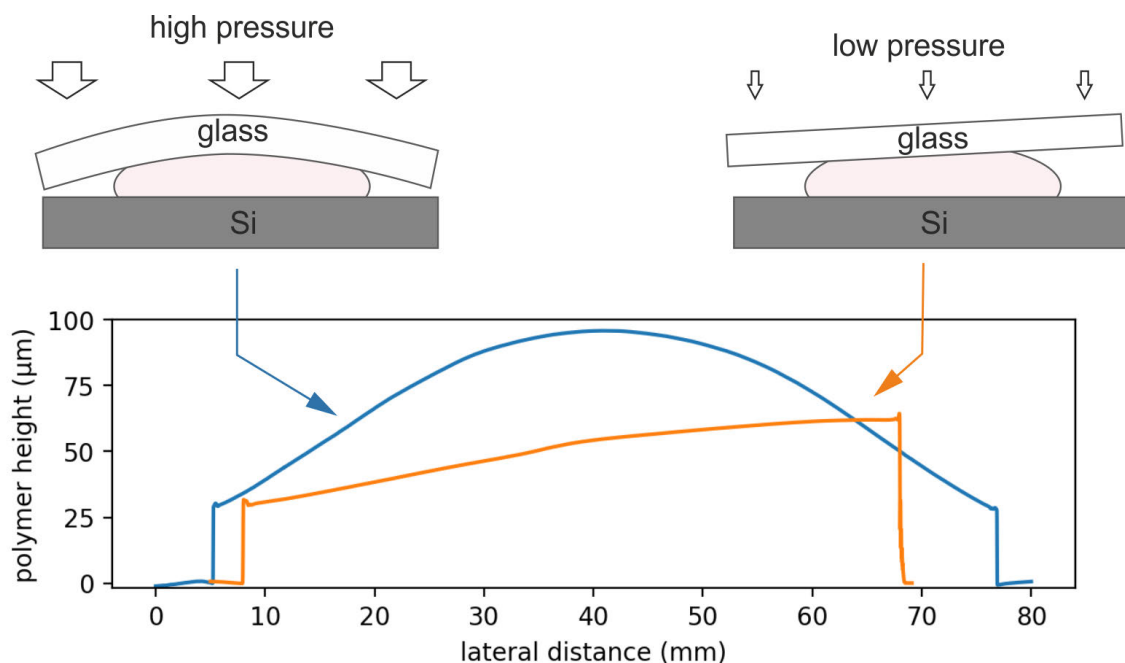


Figure 4.1: Profile of polymer on a glass substrate after UV-curing cast imprint. Bending of the stamp is caused and replicated by the polymer in case of high pressure imprint. With low pressure, smaller bending is caused with tilted surface.

However, together with the advantages of the UV-curing cast imprint, some compromises have to be met as well:

- High polymer thickness. If no solvent is used, the thickness is imprint is usually quite high, depending on the viscosity of the polymer used. In case of Efiron or OrmoComp, 30 µm-100 µm thick film is usually generated. If solvent is added, one can achieve a thickness lower than 10 µm. However, it inevitably causes material shrinking due to the evaporation of solvent.


- Bending of the imprint plane. Even though two flat surfaces are used for the imprint, stamp bending can be induced during the imprint process. Figure 4.1 shows the profile measured with a profilometer. In high pressure case, circa 1 kPa (gauge) pressure is applied by using a weight. We can see higher film thickness in the middle and lower at the edge. The height difference is 60 µm over 45 mm, which corresponds to 0.07°. However, it also means the the substrate height of sensors from different positions on the wafer will have $\pm$ 60 µm difference, which is not good for sensor-to-sensor variation. In low pressure case, no extra weight was used, the spreading can still take place with longer time required. The height difference is now only 25 µm over 60 mm i.e. a slope of 0.02°. In comparison to spin-coated samples, cast-imprinted samples will always show variance like this, if no further optimization is accomplished.


- Transparent stamp or substrate is required. Compared with thermal imprint process, UV-curing requires obviously UV transparent substrate or stamp so that the curing process can take place. In our case, a borosilicate glass substrate is used, which has good transparency in wavelength range of 300 - 400 nm - the most relevant range for the UV curing of Efiron and OrmoComp.


In conclusion, UV-curing cast imprint with low pressure is chosen for the imprint of the cladding polymer. High-throughput and replication fidelity can be achieved. Grating couplers with 368 nm periodicity (0.25 filling factor) are fabricated in the imprint process.


**Spin coating**   Spin coating is an essential process for the fabrication of the waveguides. It practically defines the core layer. The thickness of the core layer, as shown in the previous chapter, plays an important role in the sensitivity of the sensor. A thickness around 140 nm can be a good value for achieving high sensitivity while keeping a good bandwidth. The thickness of the final film can be varied by dilution, solvent, spin-coating velocity, time, and acceleration. For simplification, the time and the acceleration are kept constant at 30 s and 1000 rpm/s and the other parameters are varied. For thickness under 500 nm, PGMEA is used as solvent. Different dilutions and spin-velocities have been tested. The resulting thicknesses are plotted in Figure 4.2.
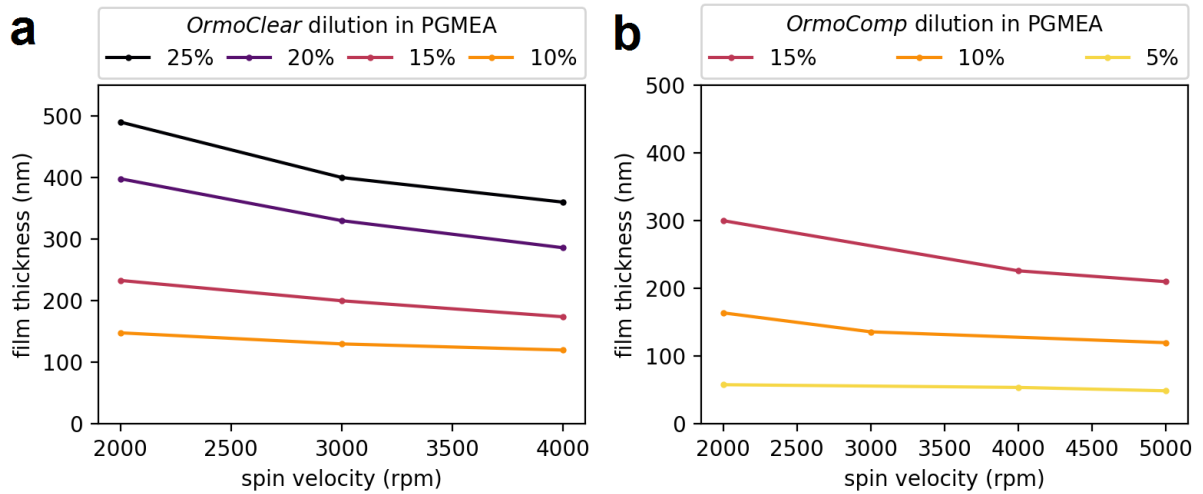
Figure 4.2: Spin-curves of OrmoClear (a) and OrmoComp (b) dilution in PGMEA solution.

To achieve 140 nm waveguide core layer, 10 wt.% Ormoclear in PGMEA was spin-coated at 3000 rpm for 30 s. For the filter layer, 160 nm OrmoComp layer is needed, which is achieved by spin-coating of 10 wt.% OrmoComp in PGMEA. For the same dilution and spin-coating parameter, OrmoComp shows higher layer thickness than OrmoClear, which is attributed to their different initial viscosities. Furthermore, for the thinnest homogenous layer that we have achieved, 5 wt.% OrmoComp in PGMEA results in 50 nm thickness with 5000 rpm. According to the manufacture, for a thicker layer ($>$ 500 nm), different solvent should be used. OrmoThin (propyl acetate) provided by *micro resist technology GmbH* is used for thicker dilutions. Since thick OrmoComp layers are solely used as the final passivation layer, for which the exact thickness is too critical, the author didn't make a separate spin-curve. Using 80 wt.% OrmoComp in OrmoThin, circa 10 µm thick final layer is achieved after curing.

**Prebake and UV curing**  Prebake is usually aimed for evoporating the remaining solvent, making the following curing process more consistent. However, OrmoCer polymers have complex properties regarding prebake. For example, they do not solidify with prebake like most photoresists (e.g. AZ resist), instead they remain viscous and liquid. The provider of OrmoCer polymers (micro resist technology GmbH) suggests 130°C and 10 mins for prebaking PGMEA diluted OrmoCer polymers like OrmoClear. However, as to be shown in the next paragraph, high temperature has a strong detrimental effect for the surface roughness of the waveguide, which is caused by the low thermal tolerance of the underlying cladding polymer. Here, different prebake conditions are investigated, especially with low temperatures, in order to find an appropriate condition for the waveguide fabrication.
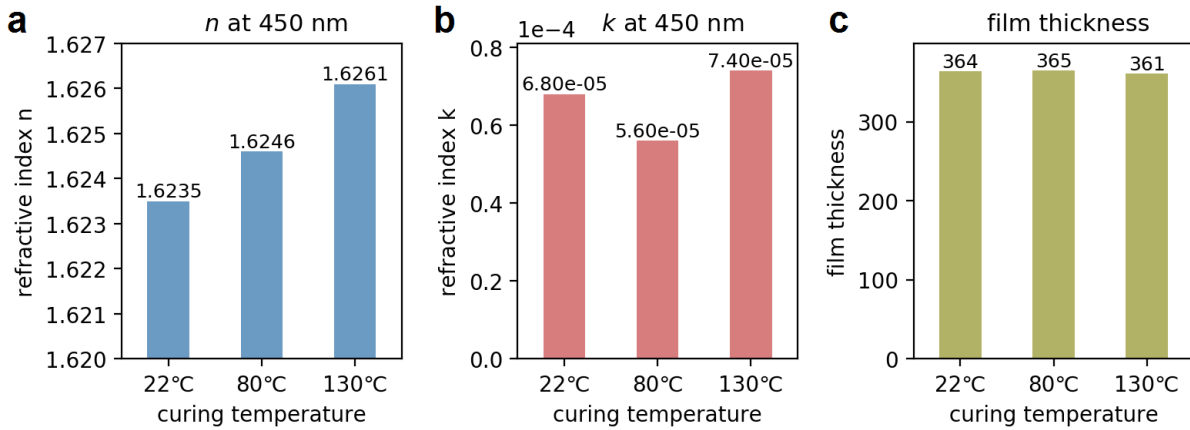
Figure 4.3: Optical properties and film thickness for cured OrmoClear HI01 with different curing conditions (22°C, 80°C, and 130°C). (a) The real part of the refractive index (n) at 450 nm. (b) The imaginary part of the refractive index (k) at 450 nm. (c) The thickness of the film is plotted. All data are obtained by an ellipsometer.

In Figure 4.3, 20% OrmoClear was spin-coated at 3000 rpm on a Si wafer. Different prebake temperatures were applied for 5 mins, followed by UV curing in nitrogen atmosphere. The films were subsequently examined with an ellipsometer for their optical properties. The real part of the refractive index (Figure 4.3a) of all temperatures have very close values around 1.624. The difference is only less than 0.2%. The higher baking temperature shows slightly higher refractive index (n), which can be attributed to the lower content of remaining solvent and slightly higher degree of cross-linking. The imaginary part of the refractive index (Figure 4.3b) is very low in $10^{-5}$ range, and the difference is not substantial. Furthermore, the thicknesses measured at all temperatures are consistent (see Figure 4.3c). Only 4 nm difference is shown as the largest difference, which is close to the precision that can be reached by an ellipsometer. Conclusively, low temperature prebake does not cause relevant change of the optical properties or physical thickness. The author considers the reason to be that the low film thickness allows effective solvent evaporation during the spinning and thus reduces the need of high temperature baking.

Another important parameter of curing OrmoClear, the waveguide core layer, is the oxygen inhibition, i.e. the photo-initiated cross-linking (curing) happens only when oxygen is depleted in the environment. For OrmoComp curing, oxygen inhibition is not an issue. The curing of OrmoClear is investigated subject to different environments. Figure 4.4 shows the results. Here, 25% OrmoClear is spin-coated onto a Si wafer, followed by prebake at 130°C for 5 min. Afterwards, one sample is UV-cured in $N_2$ atmosphere and the other in normal air atmosphere. 5 min UV exposure with 13.5 mW/cm$^2$ at 365 nm was applied for both samples. It was immediate to notice that the surface of the air-cured sample remains viscous. As suggested by the manufacturer, isopropanol (IPA) is used to rinse away the uncured layer. Then, the samples were investigated with an
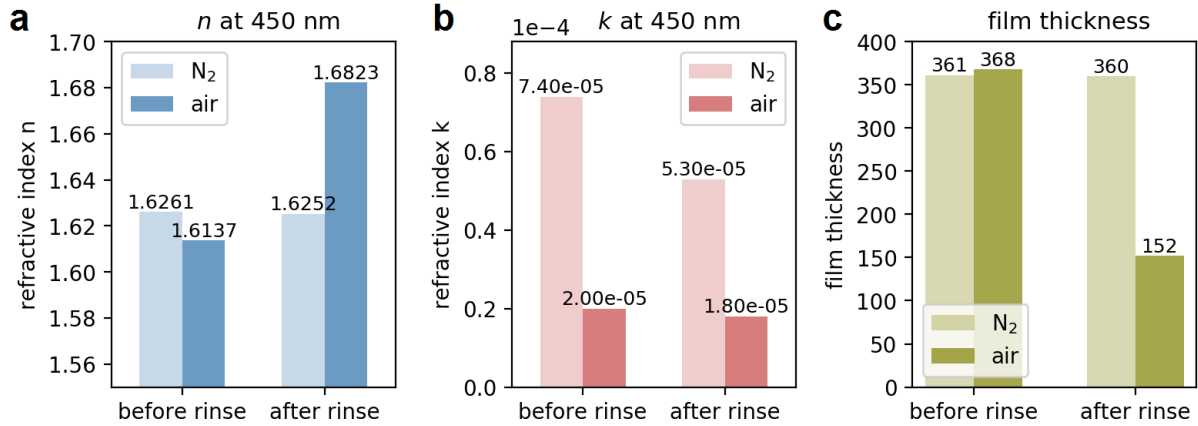
Figure 4.4: Optical properties and film thickness for air- and $N_2$-cured OrmoClear HI01 before and after IPA rinse. (a) The real part of the refractive index (n) at 450 nm. (b) The imaginary part of the refractive index (k) at 450 nm. (c) The thickness of the film is plotted. All data are obtained by an ellipsometer.

ellipometer for the film quality.

The real part of the refractive index is plotted in Figure 4.4a. Before the rinse, both samples have similar real refractive index, where the air-cured sample shows slightly lower value, also when compared with the samples cured with different temperatures (Figure 4.4). After the IPA rinse, the refractive index (n) of the air-cured samples increases substantially. However, as shown in Figure 4.4c, the thickness of the air-cured sample drops radically from 368 nm to 152 nm, while the $N_2$-cured counterpart exhibits no change. The imaginary part of the refractive index is shown in Figure 4.4b, the air-cured sample shows overall lower absorption both before and after rinse. The change of the optical properties is in good agreement with our assumption. Since the oxygen inhibits the cross-linking, the top layer of 200 nm is not cured, which is rinsed away by IPA. The uncured layer has also lower refractive index which reduces the overall refractive index level of the film. After the rinse, the thickness reduces dramatically. The remaining film displays a higher refractive index. The cause is not fully clarified, while the author presumes that the chemical change in the film plays a role here. The lower imaginary refractive index of the air-cured sample is presumably attributed to the lower surface roughness due to the liquid surface.

In conclusion, the air-curing method is possible but unappreciated because of the unreliable thickness shrinkage after rinse and refractive index change. $N_2$ or other inert gas atmosphere is necessary for the curing process of OrmoComp.

**Thermal influence**   OrmoClear and OrmoComp can easily withstand temperature up to 200°C. However, the cladding material has a lower temperature tolerance. Efiron polymer has a low glass transition temperature at 83°C. The influence of temperature to the
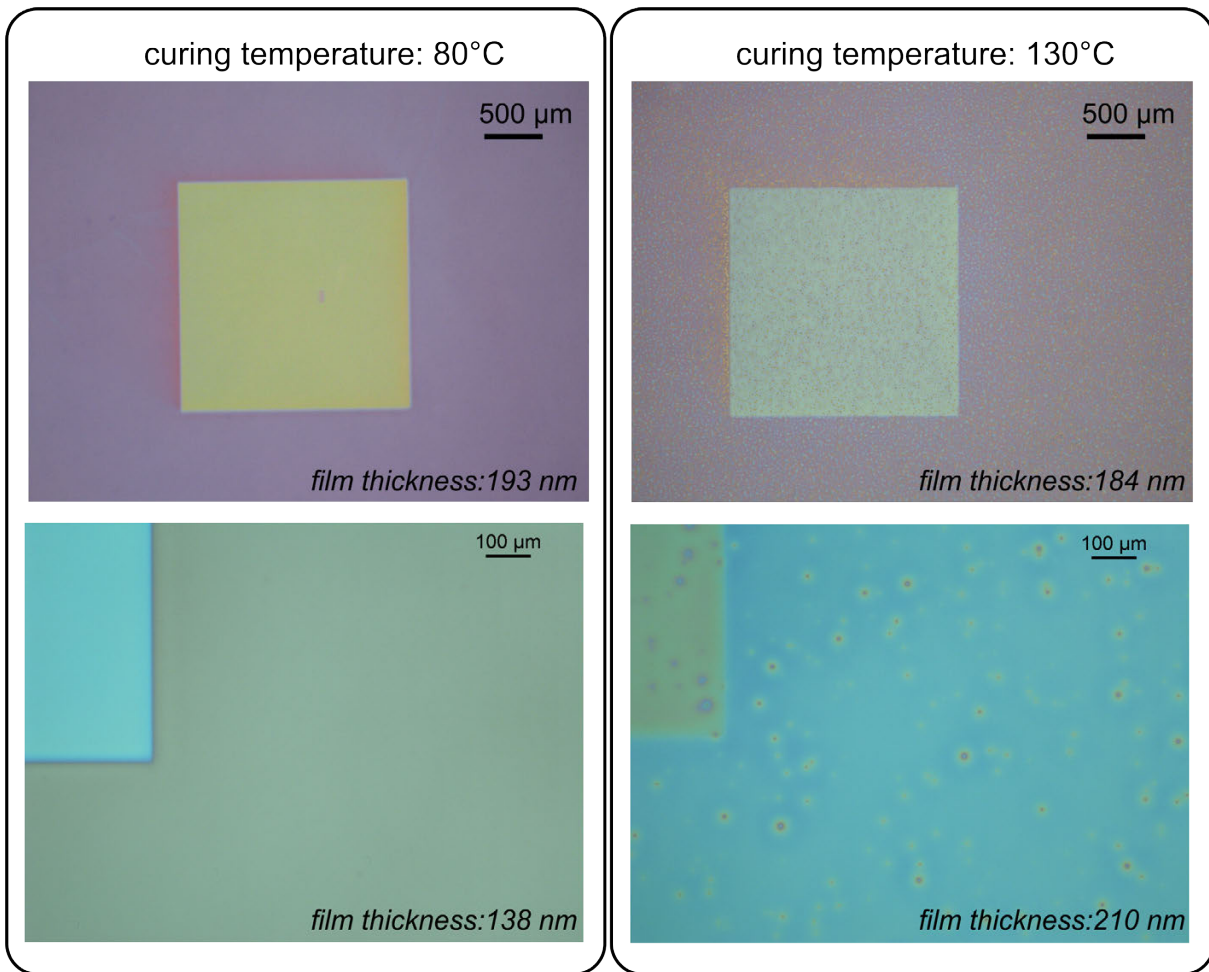
Figure 4.5: Optical microscope images of OrmoClear layer on Efiron. All layers are UV-cured. Squares are grating coupler regions. Two different temperatures (80°C, 130°C) were applied as prebake temperature. The thickness of samples were measured with an ellipsometer and annotated on images.

waveguide is investigated by changing the prebake temperature of the Ormoclear/Efiron composite. Figure 4.5 shows the optical images of the surfaces after curing the waveguide with different temperatures (80°C, 130°C). The large square area is the grating coupler region, which shows a different color due to the diffraction of the gratings.

With 130°C prebake temperature, we obtained the image shown on the right panel. It is obvious that the film quality is poor. Particle aggregations appear everywhere, which can cause large scattering loss of the guided light. The density of the defects scales up with lower film thickness. On the left panel, 80°C curing temperature was used, the defects disappear almost completely. The films appear homogeneous with a thickness down to 138 nm. Together with the results from Figure 4.3, it can be concluded that using a low prebake temperature is essential for the fabrication of the waveguide

device with Efiron as underlying cladding. No substantial change in optical or physical property is concluded for the decrease of the prebake temperature. Thus, throughout the fabrication process, the temperature should be kept low - ideally always lower than 80 °C.

## 4.1.2   Material properties

Both real and imaginary part of the refractive index are essential for the waveguide property. In general, the real part determines the confinement of the guided light while the imaginary part determines the absorption of the energy. Here, all polymers are characterized with regard to their absorption property. Using a polymer frame (as spacers) sandwiched by two thin borosilicate glass slices, a 1.12 mm thick cuvette is made for characterizing the polymer optical absorption. The absorption was measured for different polymers against a water reference sample to obtain the absorbance. Here, the optical absorption of water in range of 300 nm to 700 nm is assumed to be negligible.

In Figure 4.6a, the absorption of all three polymers in uncured liquid phase is plotted. The characteristic peaks appear at 368, 385, 395 nm for all samples. The absorbances of OrmoComp and OrmoClear are similar, while Efiron has a substantially higher absorbance in the UV range. All polymers show high transparency in wavelength range larger than 425 nm. By comparing the absorption characteristics with the literature, the author found out the photo-initiator used in all three polymers - 2, 4, 6-trimethylbenzoyldiphenylphosphine oxide (TPO). The TPO absorption curve given by a commercial manufacturer is shown in Figure 4.6b, which is in good agreement with the measured curves. Subject to UV exposure, photo-initiator like TPO forms free-radicals (see Figure 4.6c) that can react with monomers and initiate cross-linking. The conjugated $\pi$-system, which acts as a chromophore - causes the absorption of light, is reduced. The absorption shifts to the deeper wavelength range[49]. After 5 min broadband UV exposure, the absorption is measured again. In this case, the most TPO are cleaved and not absorbing in the near UV range. As Figure 4.6d shows, the characteristic peaks of TPO disappear, instead smooth increase in the absorption occurs with decreasing wavelength. Obviously, Efiron still has a much higher absorption in range lower than 400 nm, followed by OrmoClear. OrmoComp shows excellent transparency until 365 nm. In range of 400 nm to 500 nm, which is most important for the hemolysis absorption, the absorption of OrmoClear is the highest among three. Optically, we can see that cured OrmoClear becomes foggy, which is presumably due to scattering induced by the curing process. In conclusion, Efiron is the main source of material absorption within the waveguide. For a waveguide with a thin core layer like 140 nm, large part of the energy is distributed in the cladding layer. Thus, the high absorption of Efiron in wavelength range lower than 400 nm can hamper waveguiding of UV light.

Furthermore, the influence of the exposure dose on the transparency of the materials is investigated. 1 min, 5 min, and 15 min broadband UV exposure was applied to
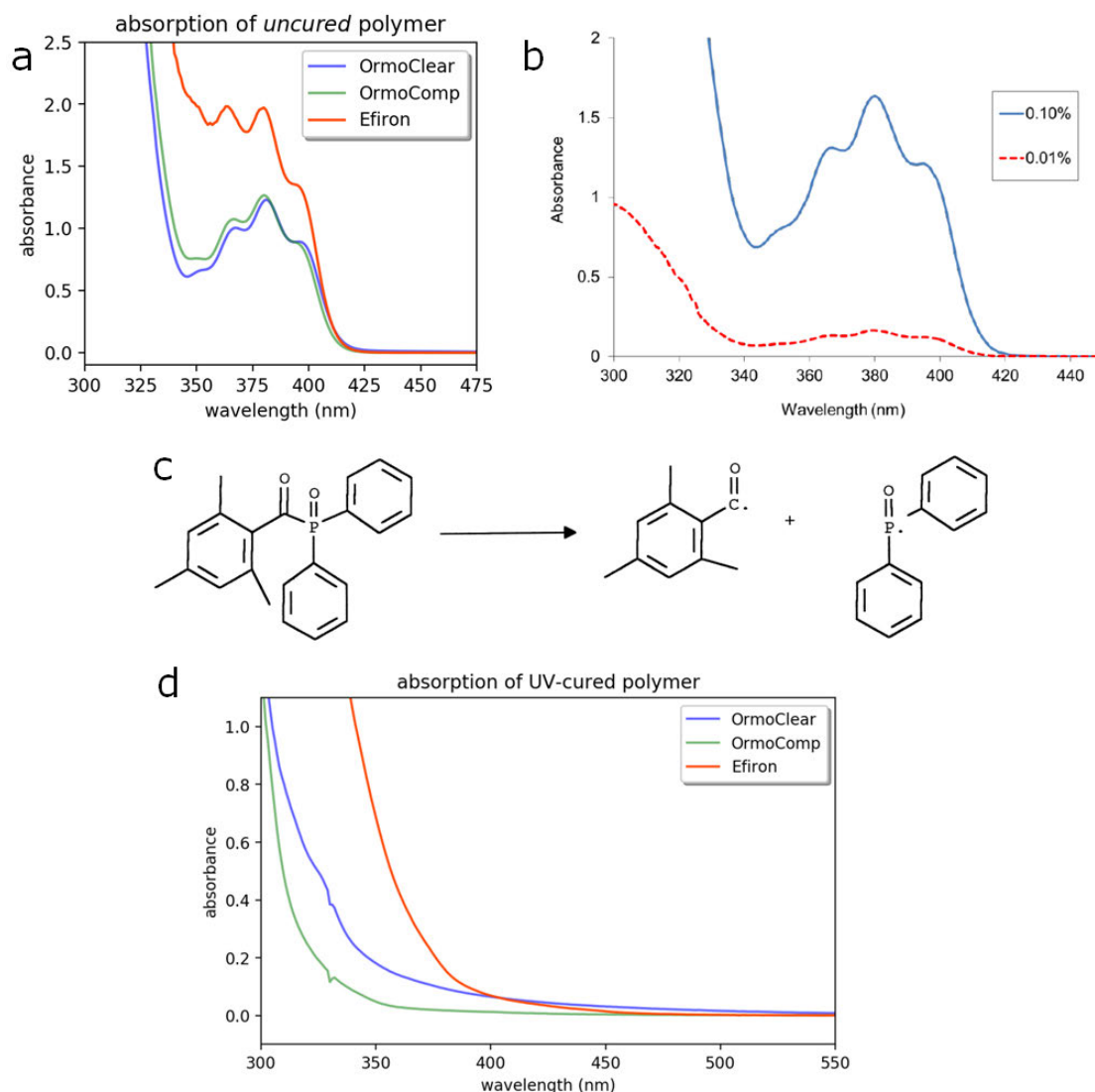
Figure 4.6: (a) Measured absorbance of *uncured* OrmoClear, OrmoComp, and Efiron polymers. (b) Absorption curve from data sheet of Irgacure® TPO from BASF[8]. (c) Reactgion of TPO upon absorption of light. Reprint from [82]. (d)Measured absorbance of 5 min UV-*cured* OrmoClear, OrmoComp, and Efiron polymers.

Efiron, OrmoComp, and OrmoClear. The absorption is measured with the 1.12 mm home-made cuvette as mentioned previously. Figure 4.7 shows the measured absorbance for all three polymers. On the right side of the figure, a zoomed area of wavelength from 400 nm to 450 nm is shown, which is the most important range for hemoglobin detection. With a 1 min exposure of 13.6 mW/cm$^2$ (measured at 365 nm) a total dose of 1140 mJ/cm$^2$ is applied. A large decrease of the absorption can be clearly observed, indicating the cleavage or bleaching of the photo-initiators, which is the phenomenon that the absorptive photo-initiators lose their original absorption property - the absorption
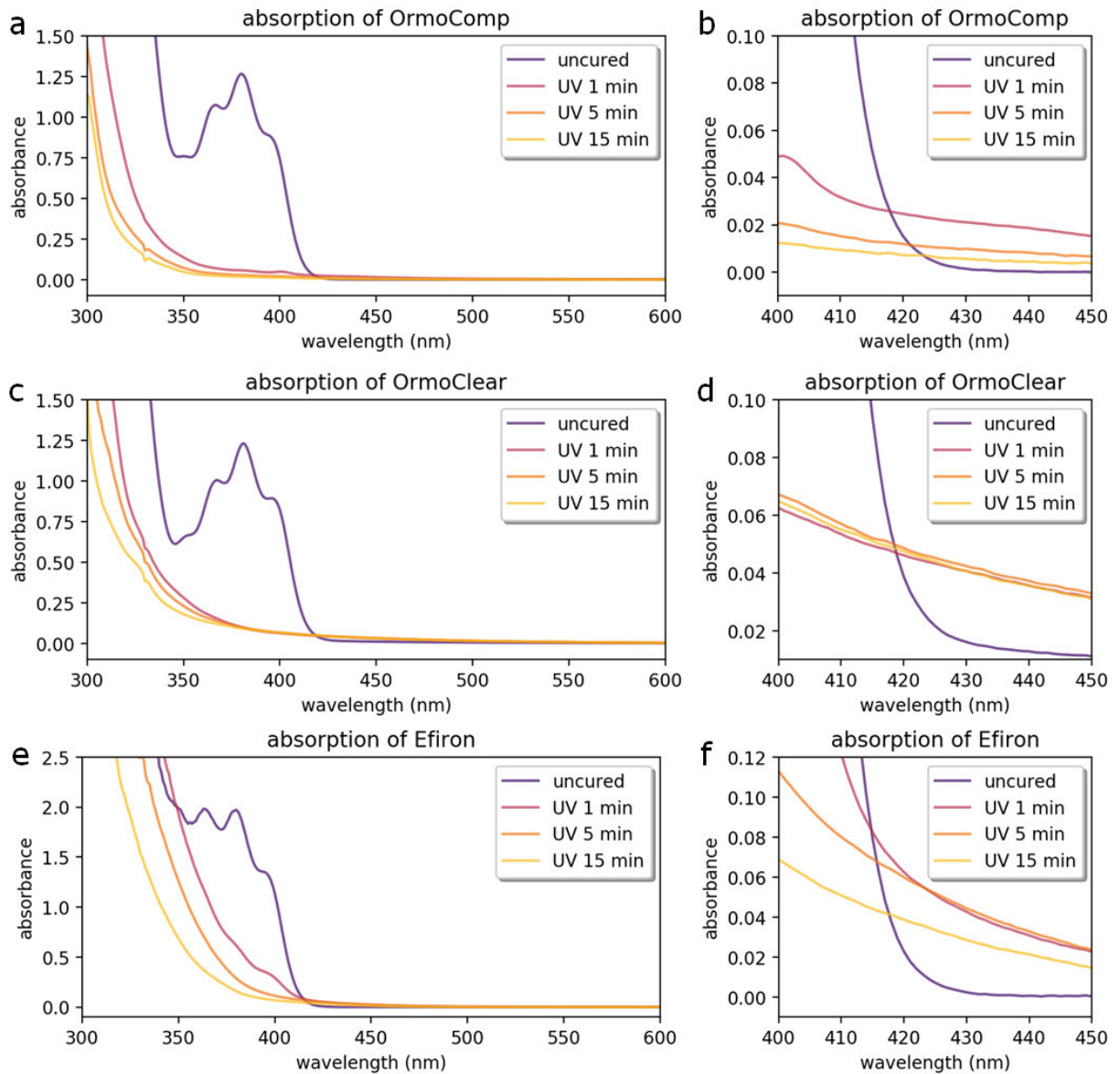
Figure 4.7: (a) Measured absorbance of OrmoComp subject to UV exposure. Smaller wavelength region is shown in (b). (c) Measured absorbance of OrmoClear subject to UV exposure. Smaller wavelength region is shown in (d). (e) Measured absorbance of OrmoClear subject to UV exposure. Smaller wavelength region is shown in (f).

shifts to lower wavelength range. However, characteristic peaks can still be observed in Efiron and OrmoComp, indicating incomplete cleavage of the photo-initiators. With 5 min UV exposure, absorption of all polymers further decreases, where the absorption peaks are not to be identified. An extensive exposure of 15 min leads to a further decrease of the absorption in the UV range (300 nm to 400 nm) in all samples. The dose influence on transparency is strongest for Efiron among all three, where no clear saturation in absorption is shown (more dose will certainly leads to more transparency),

while transparency of OrmoClear changes relatively little after 5 min exposure, as shown in Figure 4.7a.

Furthermore, we can observe the effect that the absorption after curing is strongly reduced for wavelength range lower than 420 nm, while the absorption is *increased* from 420 nm to 500 nm, as shown in Figure 4.7b, d, and f. The author considers that it comes from scattering caused by cross-linking process, which is induced by density fluctuation and compositional inhomogeneities[62]. The increase in absorption has a negative effect on the waveguide loss; however, high exposure dose still decreases the absorption overall, which should be used. In conclusion, high exposure dose is important for the cleavage of the photo-initiators to obtain high transparency in the near UV-range. However, one also does not want to introduce thermal effect by excessive exposure, which can cause increased roughness.

# 4.2   Nanoimprint of filters on waveguide

Nanoimprint lithography (NIL) has proven to be able to provide both high-throughput and high-resolution. In order to define nano-filter on top of the waveguide, a UV-NIL method is developed to achieve homogeneous patterning of nano-filters covering up to milimeter areas. The goal of this fabrication step is to achieve:

- **low residual layer thickness**, which will decrease the waveguide sensitivity,

- **homogeneous residual layer** over the whole filter area for avoiding sensitivity difference across the waveguide,

- **continuous filter lines** without interruption,

- **aspect ratio of 2-5** for narrow filter lines (circa 200 nm wide) to be able to block out cells,

- **maximum throughput** for potential industrial scale-up.

In the following sections, the final method and protocol, which can deliver the best quality, is presented at first. During the discussion, other methods and intermediate results are shown which contributed to the optimization process.

## 4.2.1   Nanoimprint with low residue

The protocol of low-residue nanoimprint is shown in Table 4.2. Here, one starts with the air-covered waveguide that is presented in the previous section. The important steps are discussed as follows:
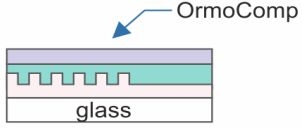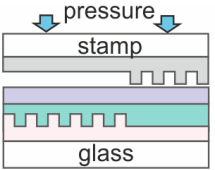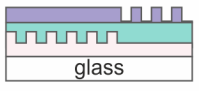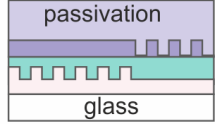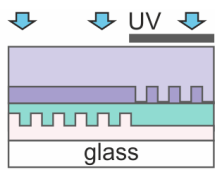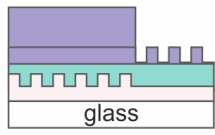
| Process | Procedure | Illustration |
|---------|-----------|--------------|
| *1. Nanoimprint of filters on waveguides* | | |
| Spin-coating the filter polymer | $O_2$ plasma is required at first to enhance the adhesion. OrmoComp is diluted in PGMEA and spin-coated on top of the substrate. Prebake at 80° for 5 min. | |
| UV-nanoimprint | The stamp and the substrate are aligned and then imprinted, where vacuum is applied at first, followed by 6 bar pressure (15 min). 2 min UV exposure (19 mW/cm² at 365 nm) is applied finally while the pressure is maintained at 6 bar. | |
| Separation | Using razor blade to separate the substrate with the stamp. | |
| *2. Passivation of non-waveguide areas* | | |
| Spin-coating of the passivation layer | The polymer needs to be treated with $O_2$ plasma at first. OrmoComp polymer is diluted in OrmoThin and spin-coated on top of the substrate. Prebake at 80° for 3 min. | |
| UV lithography | Sample is aligned with help of nano-structured alignment marks. Exposure dose is 1000 mJ/cm². | |
| Development | Sample is developed in OrmoDev for removing the windows on top of the waveguide, leaving the rest passivated. | |

Table 4.2: Fabrication protocol of polymer slab waveguide with grating couplers and air cover.

**Oxygen plasma surface treatment.**  The first critical step is the oxygen plasma treatment. The adhesion between cured OrmoClear and PGMEA-diluted OrmoComp is poor. Uniform coating can not be achieved without proper surface treatment. However, the author remarks that the intensity and time of the plasma treatment is crucial, as oxygen plasma can also induce porous structure in OrmoComp [7]. For the plasma oven used (Model 300 Semi Auto Plasma Processor from PVA TEPLA AG, Germany), plasma is generated by 2.45 GHz microwave and applied in the barrel-type ashing apparatus. A combination of 100 sccm oxygen gas with 200 W power for 2 min is shown to be appropriate.

**UV-NIL with OrmoStamp master stamp**  . A hybrid imprint master stamp made with OrmoStamp on borosilicate glass wafer is used as imprint master. The fabrication process of the hybrid imprint stamp is shown individually later in Table 4.3 and will be discussed in detail. Regarding the imprinting, an imprint tool developed by NIL Technology in Denmark (CNI v2.1) is used. The imprint tool provides three important features: vacuum in the imprint chamber (down to 0.1 mbar), pressure-air-driven membrane imprint up to 10 bar, and UV-LED at 365 nm, which can penetrate the transparent membrane used for pressing. The vacuum is important for excluding air between stamp and substrate. The membrane-based pressure system provides homogeneous pressure application. UV-LEDs can be used for UV-curing inside the chamber while the pressure is still on. However, the imprinter cannot provide alignment, which has to be done manually.

The alignment is required for two steps. First, the filters have to be aligned to the grating couplers. Since the waveguide is practically defined by the grating couplers (no lateral confinement is defined otherwise), the filters should be perpendicular to the grating. Conventional alignment is done with alignment marks made with thin metal films or other materials showing large optical contrast. However, the positioning of the grating couplers depends solely on the cast imprint step and no optical contrast can be easily made. Thus, a new design of alignment marks is created with periodic nanodots (500 nm pitch width, 200 nm diameter). Similar to the gratings, diffraction happens at the area of the nano-dot array, thus showing color contrast under microscope. An example can be found in Figure 4.10, where the alignment mark (bottom layer) is made by this way. Similar to the alignment with a mask aligner, there is a distance between the substrate and the mask (imprint stamp in our case) during the alignment. This is accomplished by placing several spacers at the edge of the imprint wafer, which make 40 μm height difference. The spacers are simply made with single-sided adhesive films cut into small pieces. The spacers are also important in another sense: they keep distance between stamp and substrate during the vacuuming step of the imprint. If no spacer is used, there will be a large risk that the nano-structures make contact with the substrate. In case of OrmoComp as imprint polymer, it is still liquid before the final UV curing. Thus, the contact will clearly deteriorate the imprint quality.

**Passivation of non-waveguide areas**   This step is necessary because the imprint OrmoComp imprint layer is too thin. The layer thickness is directly determined by the filter height to be targeted and cannot be chosen freely. In case of 400 nm filter height, the film thickness can definitely not exceed 400 nm (usually only 200-300 nm depending on imprint protrusion density). This thickness is not enough to completely accommodate the evanescent field in the cover layer. A higher layer should be used to exclude the influence of content atop areas where sensing is not wished (like grating couplers areas). The passivation is done with conventional photo-lithography. With OrmoComp diluted in OrmoThin (80% in weight), one can achieve 10 μm OrmoComp layer. The photomask thus defines the the sensing window of the waveguide. The alignment is done with matching the alignment marks in the photomask with the above-mentioned nano-structured alignment mark around the waveguide.

## 4.2.2   Transparent organic-inorganic hybrid stamp

The fabrication of the organic-inorganic hybrid stamp is shown in Table 4.3. The main steps are similar to the cast-imprint process of the waveguide cladding. However, there are two main differences that are important for making the stamp usable for imprinting:

- Adhesion promoter is needed for the demolding process. During the demolding, it is critical that the OrmoStamp stays with the stamp and not the waveguide. Thus, high adhesion is required between OrmoStamp and glass substrate of the stamp. Here, micro resist technology GmbH provides adhesion promoter OrmoPrime for this purpose[37]. Presumably, functional silane molecules have been utilized to enhance the adhesion between glass and OrmoStamp. OrmoPrime is be spin-coated onto the glass wafer that has been treated with oxygen plasma. The cast-imprint can follow on top of the OrmoPrime layer.

- The final imprint needs to be treated with anti-sticking molecule. In our case, FDTS is grafted onto OrmoStamp with its silane terminal group. The anti-sticking treatment is necessary for demolding when using OrmoStamp as a imprint stamp.

The fabricated organic-inorganic hybrid stamp has several advantages:

- Transparency in UV range. The feature is particularly useful when curing a UV-mediated cross-linking polymer, where either the substrate or the stamp has to be transparent.

- High thermal stability. The use of OrmoStamp for thermal imprint is possible for 190°C applications[71].

- High resolution. In our application, 100 nm feature size can be replicated without pattern distortion. Sub-100 nm imprints have been shown with UV-NIL[12].

- Release force is optimized with fluorine-based modification[38]. Assisted by surface-assembled anti-sticking molecules, the demolding process is strongly eased.
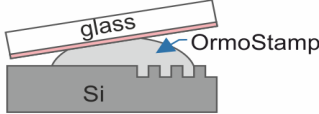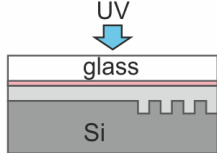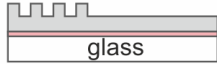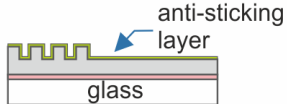
| Process | Procedure | Illustration |
|---------|-----------|--------------|
| *1. Nanoimprint of organic-inorganic hybrid stamp* | | |
| Priming of glass substrate | The borosilicate glass wafer is treated with $O_2$ plasma. OrmoPrime is spin-coated to the wafer. Prebake at 150°C for 5 min. |  |
| Cast-imprint cladding polymer | About 150 µL undiluted Efiron UVF polymer is cast onto Si stamp with glass substrate on the other side. Apply pressure for 1 min. Relaxation for 3 min. |  |
| UV curing | 4 minutes exposure with broadband UV light(11 mJ/cm$^2$ at 365 nm) in $N_2$ atmosphere. |  |
| Separation | Using razor blade to separate the substrate with the Si stamp. Polymer should stay on the glass substrate. |  |
| Anti-sticking treatment | 1H,1H,2H,2H-Perfluorodecyltrichlorosilane is grafted onto the surface in gas phase by a molecular vapor deposition machine. |  |

Table 4.3: Fabrication protocol of making transparent organic-inorganic hybrid stamp.

- Long life time. Brittle stamps are prone to crack, particularly because of their susceptibility to small defects and notching. Soft stamps can conform around those defects. One of the stamps is used for 30 imprints for the UV-NIL process. The author hasn't tested the maximum lifetime one stamp can reach. However, if the stamp is maintained with regular anti-sticking treatment, over 100 times of imprints should be possible.

## 4.2.3   Imprint results and discussion
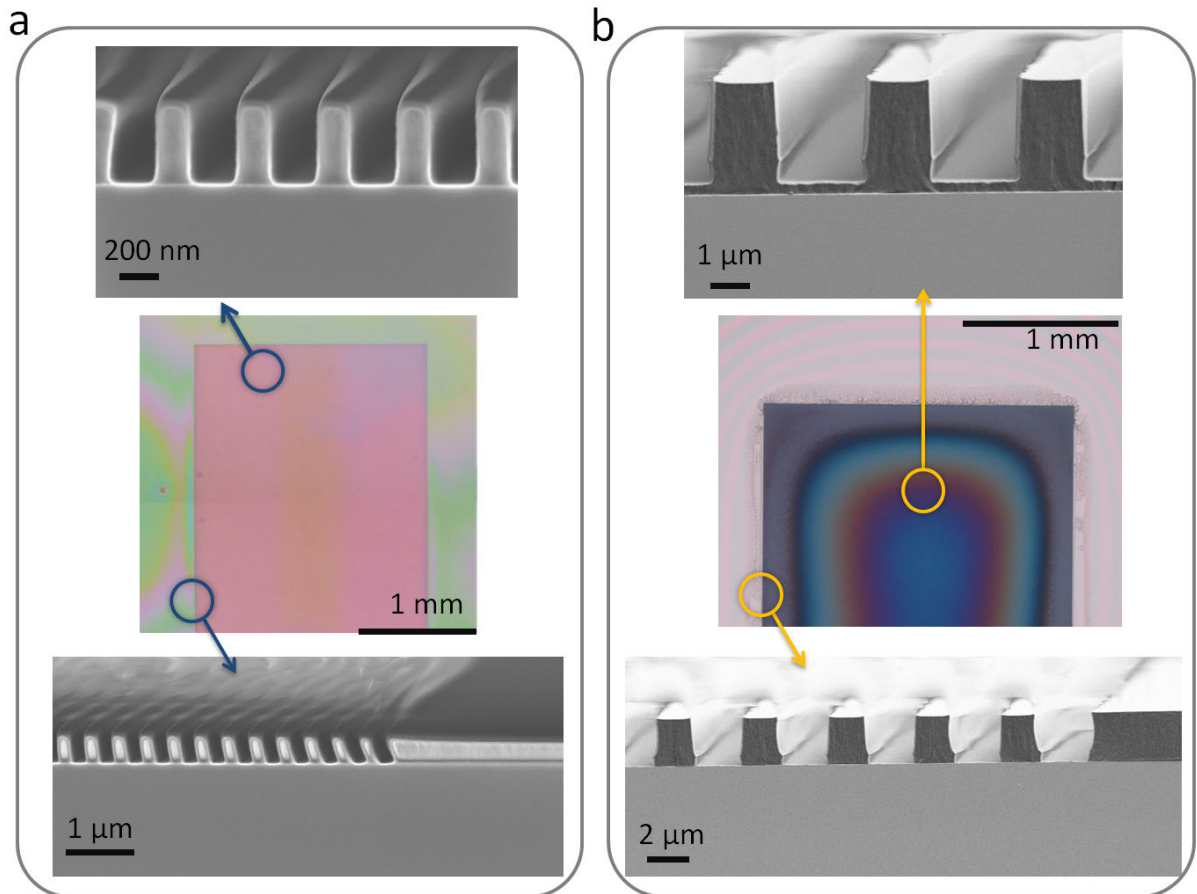


Figure 4.8: (a) OrmoComp imprint on Si wafer made with OrmoStamp hybrid stamp. Nano-filters with a feature size of 200 nm x 400 nm are imprinted for low residue. (b) OrmoComp imprint on Si wafer made with quartz stamp. Micro-filters with a feature size of 1.5 µm x 2 µm are imprinted, where inhomogeneous imprint residue is shown.

In Figure 4.8a, the result of the imprint with the process shown in Table 4.2 is shown. The total area was 2 mm x 6 mm, which is filled with nano-filters of 200 nm width and 420 nm height. As we can see from the optical image (middle) and the SEM images (top and bottom inserts), the result matches with our expectation:

- Negligible residual layer is shown after the imprint. As shown in top SEM image of Figure 4.8a, there is no visible residue left after the imprint. Both the middle and edge area of the imprint shows no identifiable residue.

- No significant defect occurs after the imprint. Once defects occur in the imprint, like the nano-ridge peeled off from the substrate in large scale, it is clearly visible with the color change. As we can see from the optical image, the pink color is pure, indicating the same periodicity for the whole area.

- Slight volume shrinkage is shown after the curing. OrmoComp has intrinsically low shrinkage after curing of about 3-5%, owing to its 3D cross-linking mechanism. In our case about 10% shrinkage is shown, as the width of the ridges reduce from 200 nm (define by the stamp) to about 180 nm. The author considers the reason to be the solvent residual in the OrmoComp layer. As mentioned before, the prebake temperature is reduced to avoid deterioration in the Efiron layer. However, the author also considers this volume shrinkage to be helpful for the demolding as smaller release force is required and the fragile nano-ridges can be preserved.

- Color gradients can be observed *around* the imprint area. It is attributed to the height difference caused by the contact of the stamp and the substrate. Since the layer thickness is low (400 nm) but not sub-wavelength, height difference of 20 nm can easily cause strong color shift, which is further amplified by the refractive index of the OrmoComp of circa 1.54.

To compare with the successful results shown in Figure 4.8a, an earlier process is shown where quartz stamp was used and larger feature size was designed. In Figure 4.8b, the result is shown. Here, the designed the ridges are 1.5 µm wide and 2 µm high. It is obvious that color gradient occurs from the center to the edge of the imprint. SEM images reveal the fact that different thicknesses of residual layer are shown at different positions, while the height of the ridges remains the same. Residal layer thickness up to 200 nm is shown in the middle of the imprint. The effect is caused by stamp bending, which is further caused by the squeeze flow of the polymer at different position where the protrusion density is different. In case of Figure 4.8b, the imprint lines are protrusion on top of a flat quartz wafer, which have the first contact with the polymer. For the relation between the imprint protrusion ratio and the imprint time, we have the equation shown below[79]:

$$t_f = \frac{\eta_0 s^2}{2p} \left( \frac{1}{h_f^2} - \frac{1}{h_0^2} \right),$$

(4.1)

where $t_f$ is the imprint time, $\eta_0$ the viscosity of the polymer, $s$ the protrusion density, $p$ is the applied pressure (assumed to be the same everywhere), $h_f$ the residual layer thickness, $h_0$ the initial layer thickness. As we can see, for a fixed $t_f$, the higher the protrusion density $s$, the higher is the residual layer thickness $h_f$. At the edge of the imprint stamp, the protrusion density $s$ outside the imprint area is zero, while the filter region has a $s = 0.5$. Thus, the edges sink effectively faster, which can be intuitively understood in the way that the squeeze flow can allocate more easily outside the stamp protrusion region. The pressure difference causes the stamp to bend and leads to higher residual layer in the middle.

To relief stamp bending, soft stamps are good alternatives. Quartz has a Young's Modulus of 73 GPa, while OrmoStamp has only 0.65 GPa. The effect of stamp bending can be significantly reduced by replacing quartz with OrmoStamp. Though we don't have the exact structure imprinted with a OrmoStamp stamp, the result shown in 4.8a demonstrates excellent imprint quality in sub-micron range. One drawback from the soft

stamp can also been seen in Figure 4.8a, where at the edges of the imprint distortion of
the stamp is caused by the high imprint pressure (6 bar). However, the tilting of the
ridges is not critical in our case.
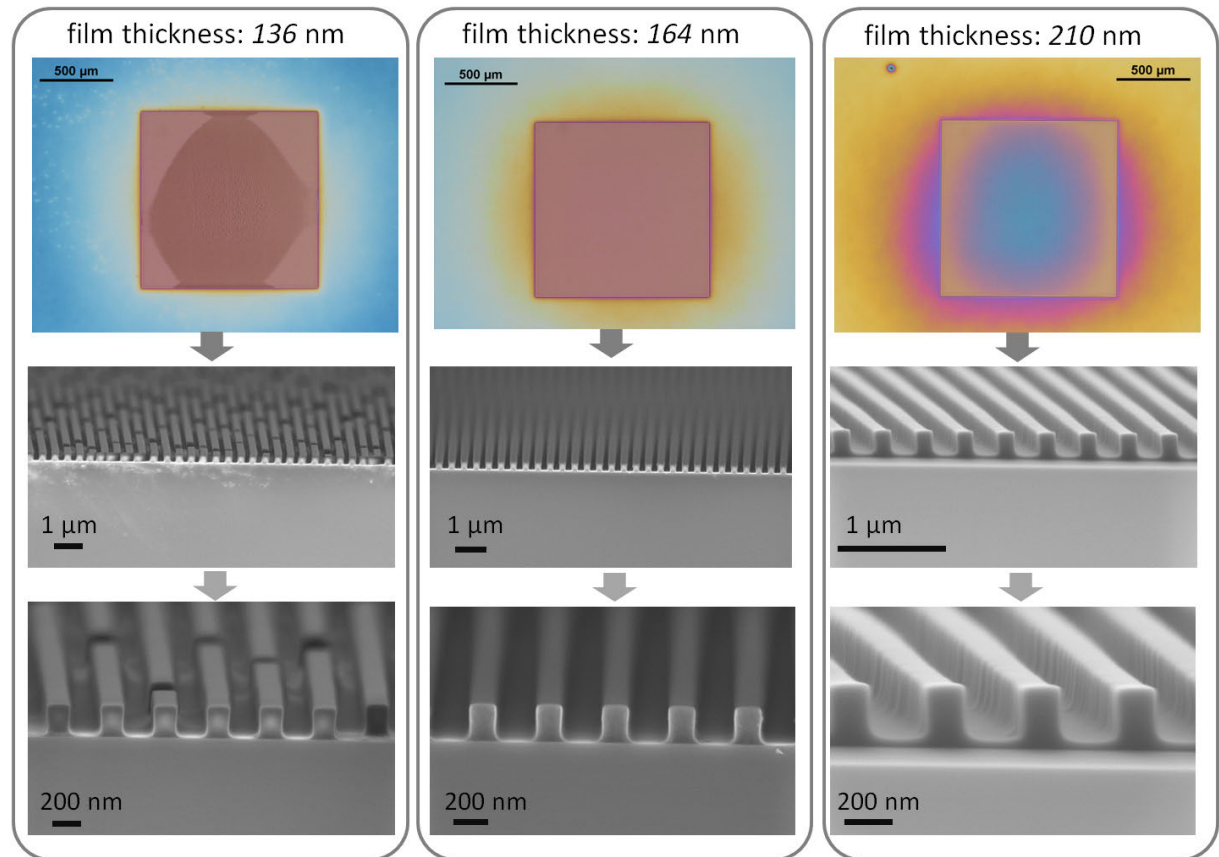


Figure 4.9: OrmoComp imprint on Si wafer with different initial layer thicknesses, which
are 136 nm, 164 nm, and 210 nm.

To optimize the imprint for low residue and fewer defects, the most important step is
to find the right initial layer thickness. As shown in Figure 4.9a, the film thickness (136
nm) is too thin for the stamp. The optical image shows dark region inside the imprint
area, indicating disruptive structures. The SEM images reveal the defects causing the
color change, which are discontinued filter lines. Interestingly, instead of obtaining an
overall thinner filter line, we have disrupted lines. The author considers it is an example
of capillary action playing a central role in filling the nano-cavities.

Thus, for filling structures in sub-micrometer range, the initial thickness has to be
matched correctly, as shown in Figure 4.9b. The optical image shows very homogeneous
color in the filter region, indicating flawless periodic structure, which is further confirmed
by the SEM images. There is also no residue to be visually identified by the SEM image.
For a thicker initial layer, stamp bending may occur like shown in Figure 4.9c. Color

gradient occurs at the center of the imprint area, which is shown to be residual layer in the SEM cross-section images. For all imprints regardless of the initial layer thickness, color gradient can be seen around the edge of the imprints, which indicates gradual height decrease and stamp bending around the protrusion area. This is to be addressed with the following passivation step.
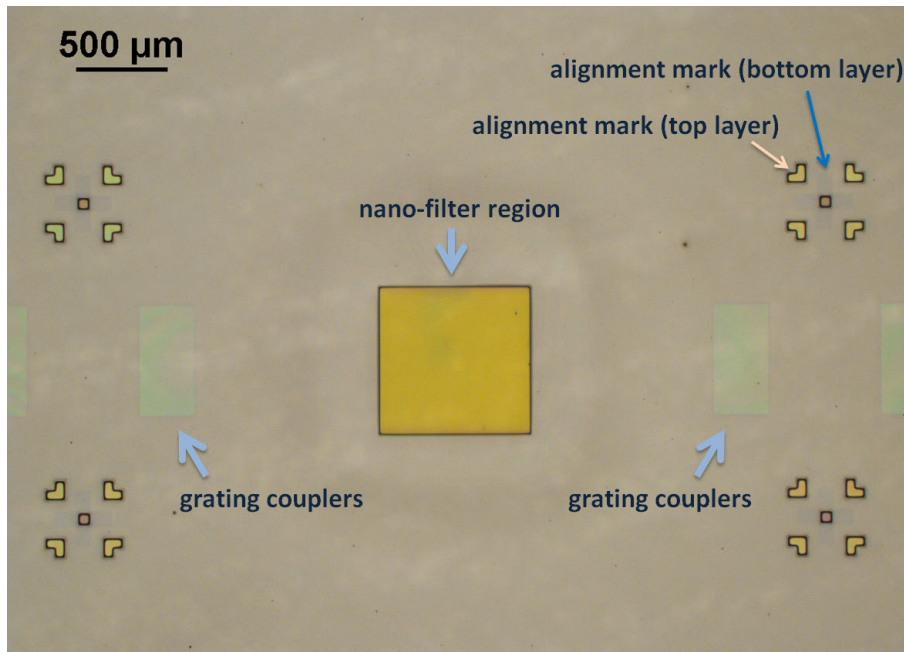


Figure 4.10: Optical image of the sensor after all fabrication steps. Annotations remark different areas of the sensor: grating couplers, nano-filter, and alignment marks.

The final passivation step defines the area of the nano-filter by applying a slightly smaller window defined in the lithography mask. In this way, the active length of the waveguide can be exactly defined and varied by different photo-masks. By applying the thick passivation layer, the inhomogeneity around the imprint area is eliminated. As shown in Figure 4.10, no color shift appears inside or outside the filter area. Furthermore, the final alignment marks are designed in the passivation layer and can be used for the final dicing step.

## 4.3 Electron beam lithography for imprint-stamp origination and meta-surface applications

In this thesis, most of the work has to deal with sub-micrometer structures. The fabrication of these structures requires delicate fabrication technique that is able to accomplish this resolution. Electron beam lithography (EBL) has been extensively used for this purpose for its extremely small beam size that is lower than the diffraction limit in most optical lithography[36]. In this section, the EBL system is introduced at first, followed by the routines developed for completing an E-beam writing on both conductive and non-conductive substrate. Furthermore, a strategy for high-throughput EBL is developed intending to maximize the speed for writing nano-dot array on a Si substrate for e.g. plasmonic color generation.

In our electron beam writing system (JEOL JBX-9500FS), the most relevant specifications for this work are given as follows:

- A ZrO/W thermal emitter is used to generate election beam.

- Acceleration voltage is 100 kV.

- Scan speed is up to 100 MHz.

- Minimal spot size of circa 4 nm at 1 nA and circa 10 nm at 10 nA

- Two deflectors are used. A large deflector for positioning (max. field size 1000 µm x 1000 µm, 20 bit) and a small deflector for scanning (field size circa. 4 µm x 4 µm, 12 bit with 1 nm min. grid size)

In EBL, the electron beam is focused and scanned over the target. The beam can be focused into a very small spot size (minimum 4 nm in our case), much smaller compared with conventional photo-lithography. The free space beam diameter depends on many parameters such as beam geometry (source size, numerical aperture of the lens), lens aberration, and beam diffraction. In our system, the beam size can be practically tuned by two parameters: beam current and aperture. The smallest beam size can be achieved by small beam current and small aperture. However, as to be shown later, small current also reduces the throughput. A trade-off between resolution and throughout is thus the central issue for any E-beam writing process. Moreover, what limits the resolution of EBL is not only the beam size but also the electron-substrate interaction as well as the resist property. What fundamentally enables the lithography process are the electrons (forward scattered, secondary or backward scattered) that either cross-link or de-cross-link the resist. Thus, a good combination of substrate type, resist of choice, and proper setting of E-beam writer is important to achieve high performance and high throughput, which is to be shown in the following sections.

## 4.3.1   Fabrication protocols

The fabrication protocol of a EBL process is similar to a photo-lithography process regarding sample handling . Here the author differentiates the process between a Si substrate and a quartz substrate, since they have different electrical conductivity and thus perform differently when exposed to electron beam.
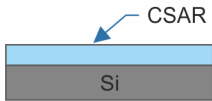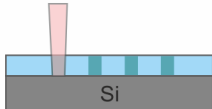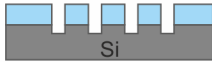
| Process | Procedure | Illustration |
|---|---|---|
| *1. E-beam lithography for stamp origination* | | |
| Spin-coat E-beam resist | E-beam resist CSAR is spin-coated onto a Si wafer. 190 nm is aimed. Prebake is done at 180°C for 5 min. |  |
| E-beam exposure | Electron beam lithography is carried out to define e.g. a nano-dot array. |  |
| Development | For CSAR resist, 1 min development in AR 600-546 is done. |  |
| Etching | Reactive ion etching is applied at -19°C with a combination of $SF_6$ and $C_4F_8$. After the etching, the depth is measured with a profilometer. |  |
| Removal of resist | $O_2$ plasma is used to remove the CSAR resist. |  |
| Anti-sticking treatment | FDTS is grafted onto the surface in gas phase by a molecular vapor deposition machine. |  |

Table 4.4: Fabrication protocol of a EBL process with Si substrate.

## 4.3.1.1  Imprint-stamp origination

A protocol of EBL on Si wafer is presented in Table 4.4. The process used for stamp origination is based on using E-beam resist CSAR to originate patterns, which is followed by an etching procedure to define the pattern for nano-imprint lithography. CSAR (AR-P 6200 (CSAR 62), AllResist GmbH) is a positive E-beam resist and is chosen because of the low clearing dose of 280 µC/cm$^2$ (190 nm thick) and its high resolution down to 10 nm[80]. As contrast, hydrogen silsesquioxane (HSQ), which is a high-resolution negative E-beam resist, has a clearing dose of 3000 - 50000 µC/cm$^2$. Therefore, pattering with reversed polarity, which can be made by changing positive resist to negative, is achieved here by using a lift-off process, which can saves a lot time. Lift-off with CSAR resist and Al mask is used in the next section for the meta-surface generation. In general, before the E-beam exposure, the following software preparation steps are to be done:

1. Generate pattern by CAD software or scripting. For most of the work done in this thesis, the drawings are done by directly scripting GDS file using gdsCAD library in Python 2.7[34].

2. Import GDS file to BEAMER software (GenISys GmbH, Germany) for conversion into .v30 file that JEOL requires.

3. A pattern healing step can be optionally carried out before the conversion, where overlapping patterns are merged into one layer to avoid double exposure.

4. Proximity effect correction has to be carried out. Proximity effect is caused by the back scattered electrons when the neighboring patterns are under exposure. For proximity effect correction, an electron beam tracing simulation has to be carried out at first. TRACER software from GenISys GmbH provides a good environment for Monte-Carlo simulation of the electron-substrate interaction. The point spread function obtained by the simulation is directly coupled into BEAMER software for proper correction. However, for a periodical pattern like nano-dot array, it is unnecessary to correct the whole pattern, as the correction dose will be the same every apart from the edge of the pattern.

   The routine developed here was to use a small dummy pattern with the same pattern density for the proximity effect correction to determine the dose offset level. Only the dose offset level in the center of the pattern is taken (representative for this particular pattern density), which is then applied to the original large pattern as overall dose modification instead of individual pattern correction. This method reduces the file size and total exposure time.

5. Fractionantion of the pattern into rectangles and trapezoids - the only formats that the E-beam writer can read. Details regarding fractionantion is discussed in section 4.3.2.

6. Determine the field size and writing order. The maximum filed size is 1 mm x 1 mm for our system. However, to avoid inhomogeneity which can occur at the edge of a field, smaller size of 500 µm x 500 µm or 250 µm x 250 µm is usually used.

7. Conversion into the v.30 file, which can be read by the E-beam computer.

## 4.3.1.2    Meta-surface generation
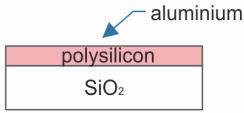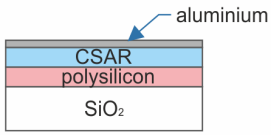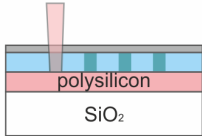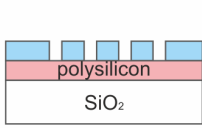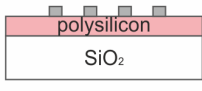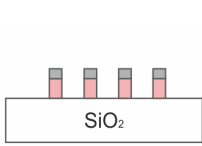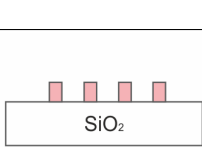
| Process | Procedure | Illustration |
|---|---|---|
| *1. E-beam lithography with lift-off for meta-surface application* | | |
| Si deposition on SiO$_2$ | Polycrystalline silicon (PolySi) is deposited on SiO$_2$ wafer (both sides) by LPCVD. One side is removed by reactive ion etching. | |
| Resist coating & Al layer deposition | CSAR resist is spin-coated. 20 nm aluminum layer is thermally evaporated for de-charging. | |
| E-beam exposure | Electron beam lithography is carried out to define e.g. a nano-dot array. Proximity effect correction is applied. | |
| Development | Al layer is removed with TMAH at first. CSAR is developed with AR 600-546. | |
| Al deposition for lift-off | Al layer is deposited with E-beam evaporator. 40 - 50 nm is enough for up to 500 nm PolySi etching. | |
| Lift-off | CSAR is removed by AR 600-71 or 1165 remover. | |
| Etching | Reactive ion etching is applied at 0°C with a combination of SF$_6$ and C$_4$F$_8$. Bosch process can also be used by alternating passivation and etching steps. | |
| Removal of Al | Al mask is removed by TMAH. | |

Table 4.5: Fabrication protocol of EBL for meta-surface generation with a glass susbtrate.

The fabrication protocol of fabrication of Si meta-surface of glass wafer is shown in

Table 4.5. As we can see, in comparison with Si substrate, glass substrate required more steps for de-charging of electrons. Even though a layer of polysilicon is present on top of the $SiO_2$, the layer thickness is rather low (200 nm), which cannot necessarily provide the sufficient conductivity. Thus, the standard procedure for non-conductive substrate is used with additional de-charging Al layer. Some remarks about the process are listed as follows:

- The Al de-charging layer has to be thermally evaporated or sputtered. E-beam evaporation has to be avoided because the underlying E-beam resist will be otherwise exposed.

- The Al deposition for lift-off mask should be done with E-beam evaporation when using positive resist. At this stage, the E-beam exposure during the deposition flood-exposes the resist and helps the cleavage during the lift-off.

- A proximity effect correction should carried out basing on $Si/SiO_2$ substrate.

- For a meta-surface exposure, where different dot sizes are mixed in a large pattern. A whole pattern proximity effect correction should be ideally carried out. However, it can easily take 20+ hours for a meta-surface pattern in centimeter scale which also generates 10+ gigabyte of extra data. Thus, a process is developed to simplify the correction. Here, dots are put into layers according to their sizes. A small scale proximity effect correction is carried out at first to show the dose variation needed for each dot size. This value is appointed as dose modification for all layers (with individual dot sizes) in the final exposure. In this way, dots with different sizes experience different doses, avoiding under- or over-exposure, while the data is kept slim. Results of using this technique is shown in Figure 4.11, where the smallest dot diameter is about 100 nm.
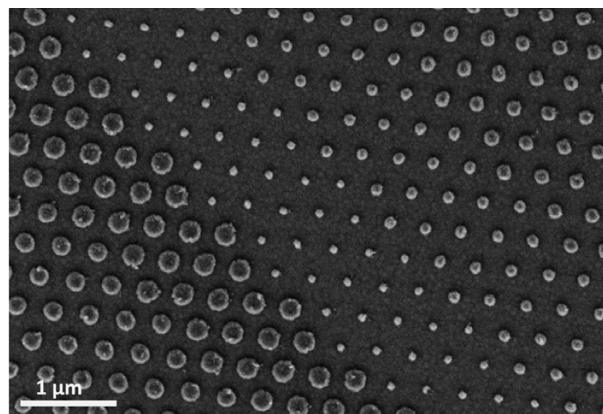


Figure 4.11: Aluminum disks on a $Si/SiO_2$ substrate for meta-surface application. Different doses are appointed to different layers containing in each unique disk diameter.

## 4.3.2  High-throughput EBL

Despite the high resolution of the E-beam system, the largest challenge of using EBL for large-scale patterning is in the economic aspect. Unlike conventional photo-lithography, EBL requires the beam sequentially expose the resist in a shot-by-shot manner. Many efforts have been done to enable fast writing such as the single-spot writing method developed in our group[50]. Here, the author expanded the model and introduced new aspects to enable fast and large-scale E-beam writing. The official writing time estimation of our JEOL JBX-9500FS system is shown in Figure 4.12.
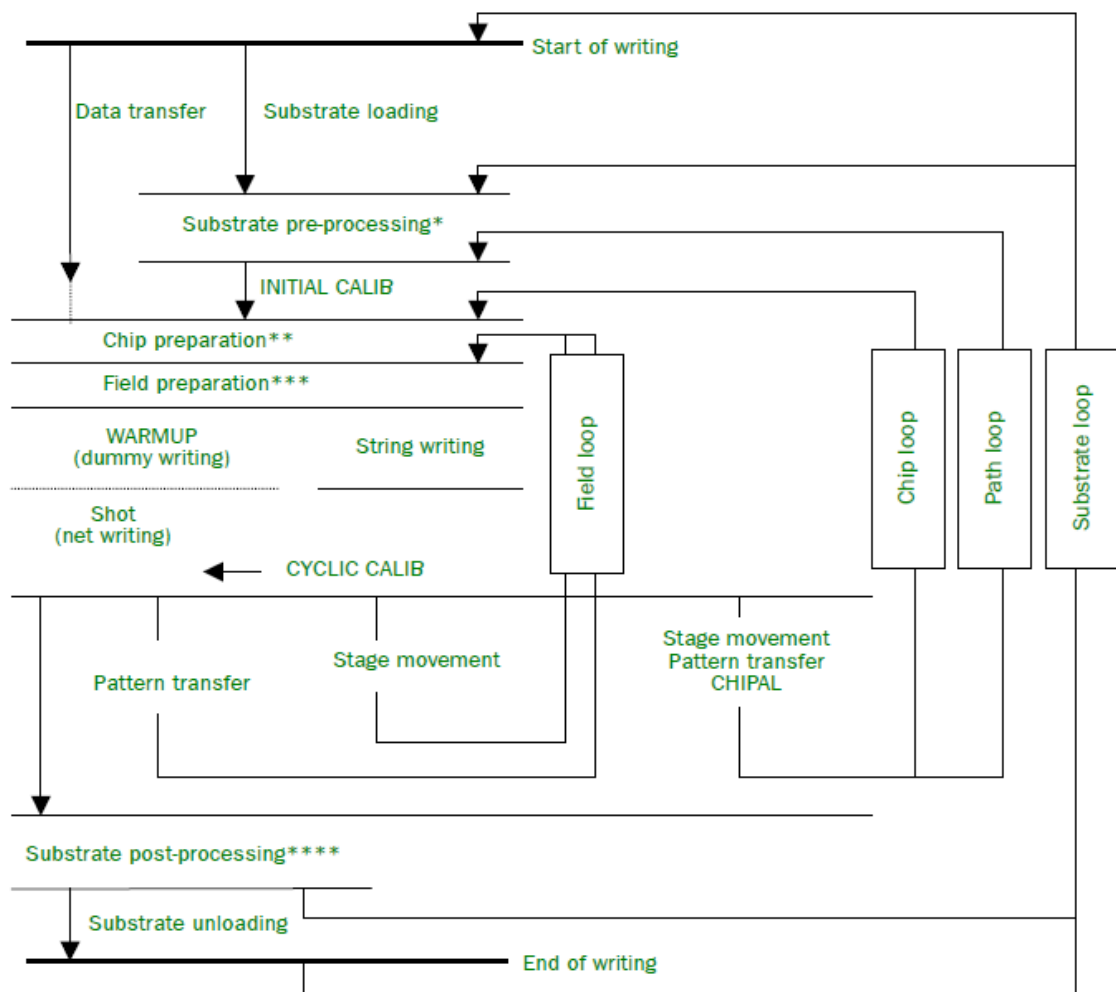


Figure 4.12: Writing-time estimation routine of JEOL JBX-9500FS. Reprint from the machine manual[52].

The routine is highly hierarchical and entangled, which makes it difficult to be described in a simple way. A simplified model that describes the most essential parts

can be expressed in the following way:

$$T_{total} = T_{exposure} + T_{stage\,movement} + T_{calibration} + T_{material\,transport}. \tag{4.2}$$

Here, $T_{total}$ is the total time, $T_{exposure}$ the exposure time, $T_{stage\,movement}$ the stage movement time, $T_{calibration}$ the calibration time, and $T_{material\,transport}$ the material transport time. For one wafer to be exposed, $T_{material\,transport}$ is constant of 15 min 30 s for JEOL JBX-9500FS. $T_{calibration}$ is composed of a initial calibration (always 4 min 10 s) and a cyclic calibration, which is approximately proportional to the total exposure time $T_{exposure}$, where the precise number of execution is dependent on more parameters like number of chips and fields. Furthermore, $T_{stage\,movement}$ is linear to the number of fields, of which the size is limited to 1000 µm x 1000 µm as shown previously. Thus, using a smaller writing field will give rise to larger stage movement time; however, the writing quality could be expected to be better because nonuniformity often occurs at the edge of each writing field[50]. It is not difficult to see that the most critical time section is the $T_{exposure}$.

As shown in Figure 4.12, for each field, the $T'_{exposure}$ can be expressed as follows:

$$T'_{exposure} = T_{field\,prep} + T_{shot,field} + T_{pattern\,transfer} + T_{stage\,movement}. \tag{4.3}$$

The field preparation time $T_{field\,prep}$ consists of the software and hardware setting time and height correction time, which are relatively fixed regardless of the pattern. The shot time $T_{shot,field}$, which is mostly discussed in literature[50, 70], can be described in a simplified way:

$$T_{shot,field} = \frac{DA_{field}}{I}, \tag{4.4}$$

where $D$ is the clearing dose of the E-beam resist, $A_{field}$ the total area in the writing field to expose, and $I$ the beam current. The shot time of a field can be further decomposed into individual shots:

$$T_{shot,field} = N_{shot}(T_{shot} + T_{settling}) + N_{fractures}T_{blank} \tag{4.5}$$

$$= N_{shot}\left(\frac{DA_{shot}}{I} + T_{settling}\right) + N_{fractures}T_{blank}, \tag{4.6}$$

where $N_{shot}$ is the total number of shots of the field, $T_{shot}$ the individual shot time of one single beam shot, $T_{settling}$ the settling time of the beam defelction, $N_{fractures}$ the total number of fractures, and $T_{blank}$ the blanking time. As shown in Figure 4.13, the beam is deflected to the starting position and unblanked for the exposure. Then, following the given shot pitch, the beam is deflected subsequently according to the path. The maximum frequency of beam deflection $F$ is given by JEOL for JBX-9500FS as:

$$F = \frac{I}{p^2 D} = \frac{A_{field}}{p^2 T_{shot,field}}, \tag{4.7}$$

where $p$ is the shot pitch. For JBX-9500FS, the maximum frequency which is also called scan rate, is 100 MHz, i.e. a minimum shot time of 10 ns. Usually, one wants to

minimize the shot pitch to increase the resolution of the writing, which automatically gives rise to higher $N_{shot}$, which is approximately equal $\dfrac{A_{field}}{p^2}$. This will increase the writing time due to the settling time $T_{settling}$ as shown in equation 4.6. However, since the whole deflection takes only 10 ns at 100 MHz, the settling time is expected to be almost negligible compared to the shot time. Thus, what remains in the $T_{shot,field}$ is the blanking time, which is linear to the total fracture number $N_{fractures}$. Furthermore, the term left in equation 4.3, which is the pattern transfer time $T_{pattern\,transfer}$, is also proportional to the number of the fractures, as shown in the following section.
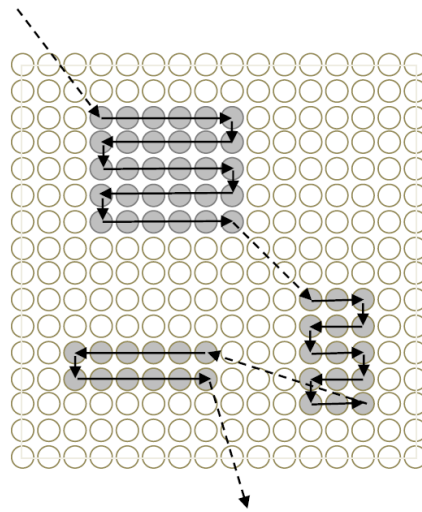


Figure 4.13: The way of exposure of JEOL JBX-9500FS. The beam is deflected at the location of the patterns and scans the area. Dashed lines indicate blanked beam while solid lines are unblanked exposure. Reprint from [70].

In Figure 4.14, the data transfer process is schematically shown. The board CPU-H has two processes called HSC and SPA. When the writing starts the stored pattern data are stored in W-buffer memory in HSC, where some of the data are even compressed. All data will be transferred to SPA as rectangles and trapezoids (fractures). The SPA partitions the data into scan regions for the sub-deflector. Thus, it is obvious, that the number of fractures can linearly increase the data transfer time.

Therefore, the author intend to study the relevance of the fracture number on E-beam writing speed. In order to show the time difference given by the number of fractures, a study is done with a typical exposure pattern of dot array. The pitch width of the dots are 200 nm x 200 nm. The pattern to be obtained at the end is circle (dot). The experiment is designed in the following way:

1. For the pattern design, three different shapes were drawn to represent the circle, as shown in Table 4.6 (1st column). Since all patterns in GDS format have to be polygons, there is no natural circle, a fine circle is defined with 64-sided polygon,
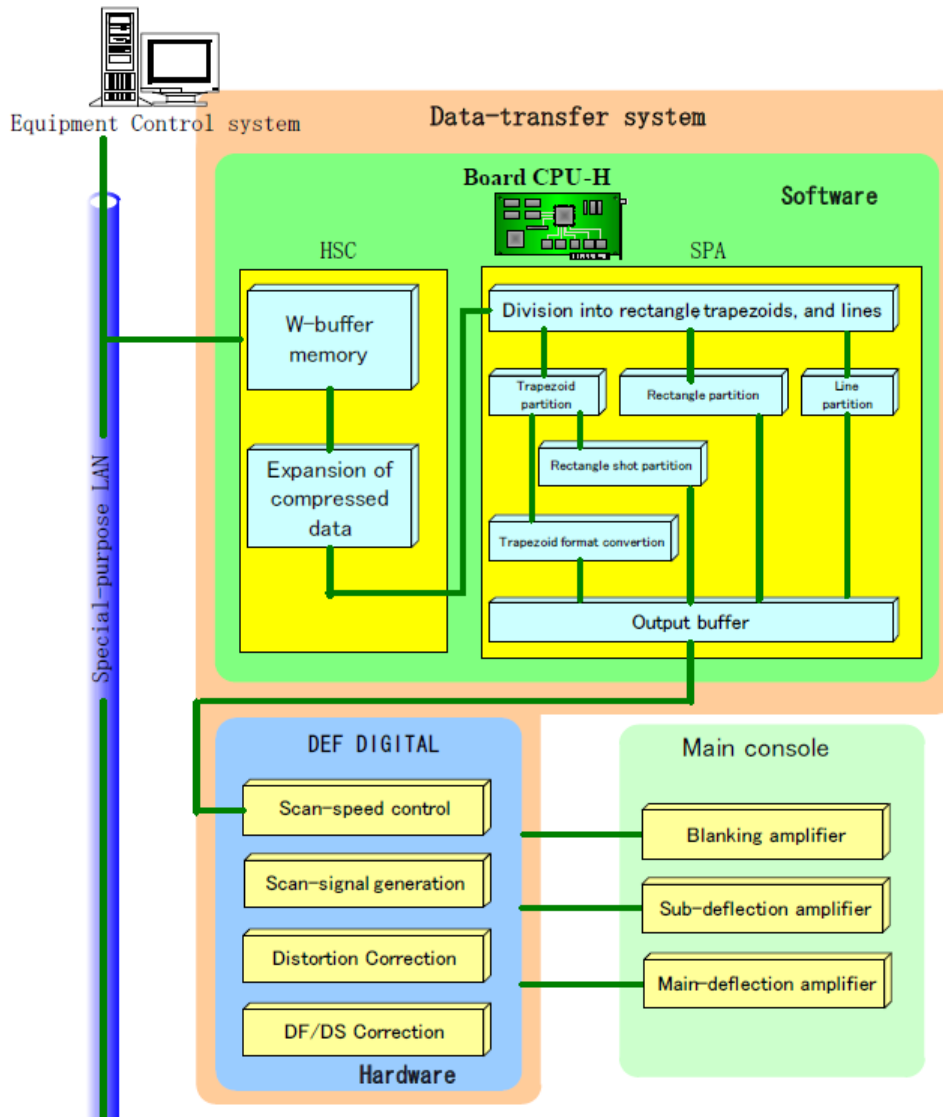
Figure 4.14: Data transfer system of JEOL JBX-9500FS. Reprint from the machine manual[52].

a simplified circle with 12 sides, and also a 'circle' with only 4 sides, which is effectively a square.

2. Fractionation algorithm is carried out in software BEAMER (GenISys GmbH, Germany) for different designs. The fracture resolution is set to be the highest to faithfully represent the designed structure. The result is shown in Table 4.6 (2nd column). Alternatively, if the resolution is set low, the 64-sided circle can be fractured into coarse pieces, which decreases the fracture number. Here, with the highest resolution, 49 fractures are generated for the 64-sided circle, while 5 fractures for the 12-sided counterpart and only one fracture for the 4-sided counterpart. The main reason is that the geometries that the data system SPA can
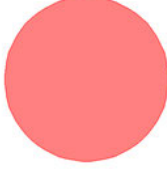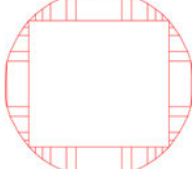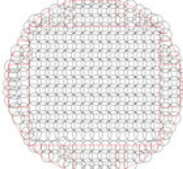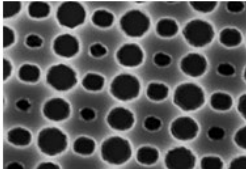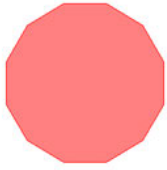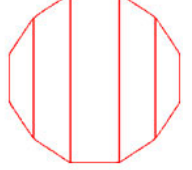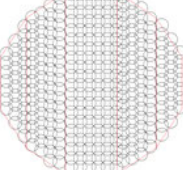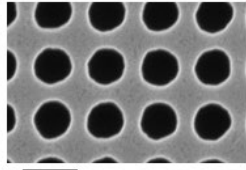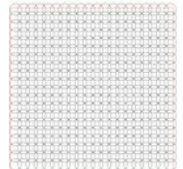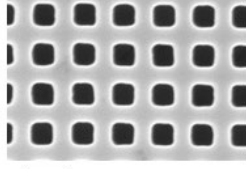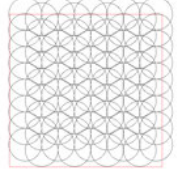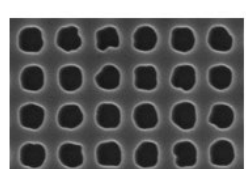
| original pattern unit | Fractured pattern unit | simulated shots | examples | exposure time |
|---|---|---|---|---|
| 64-sided circle | 53 fractures | beam size: 10 nm step size: 8 nm | 200 nm | *7h 48m* (current: 10 nA) |
| 12-sided circle | 5 fractures | beam size: 10 nm step size: 8 nm | 200 nm | *1h 20m* (current: 10 nA) |
| 4-sided circle | 1 fracture | beam size: 10 nm step size: 8 nm | 200 nm | *1h 0m* (current: 10 nA) |
| 4-sided circle | 1 fracture | beam size: 35 nm step size: 15 nm | 200 nm | *19m* (current: 44 nA) |

Table 4.6: Pattern fractionation for E-beam and its influence on writing speed.

read are rectangles and trapezoids. Thus all polygons have to be decomposed into those shapes. A fine circle naturally generates more delicate fractures. A square already fits into category rectangle and thus needs no further fractionation.

3. The next step of the E-beam writer takes is to fill the fractures with shots. The simulated shots are shown in Table 4.6 (3$^{rd}$ column). Here, the beam size and the step size are variables that the user can set. Two combinations are given here with a small beam of 10 nm (corresponding to a small current of around 10 nA) and a large beam of 35 nm (corresponding to a large current of around 44 nA). As shown in equation 4.7, the step size is limited to the maximum scan frequency of

the machine (100 MHz in our case). For the first three rows, 10 nm beam size and 8 nm step size are used. This parameter set is close to the situation of 10 nA beam current with 110 µm aperture in JBX-9500FS. Note that the filling algorithm of JEOL machine is defined by the vendor and differs from other conventional algorithms. The total number of shots in one single pattern is 276 for 64-sided circle, 280 for 12-sided circle, and 360 for 4-sided circle. Since the 4-sided circle has the same width as the diameter of the circle, the surface area is larger, which causes more shots for the filling. Furthermore, another set of beam size and beam step size was used for the 4-sided circle to simulate large current exposure. 35 nm beam size and 15 nm step size is close to 44 nA exposure with a aperture of 235 um. Here, as shown in the 4<sup>th</sup> row of Table 4.6, fewer shots are needed. In total there are 100 shots filled in a pattern unit.

4. Thereafter, the exposure time of all 4 parameter sets is calculated for the whole dot array with a clearing dose of 280 µC/cm$^2$. The dot array is composed of 25000 dots on both x and y direction, which gives a total number of $6.25 \cdot 10^8$ dots in a squared area (25 mm$^2$). The exposure time estimated is listed in the 5<sup>th</sup> column of Table 4.6, where examples of structures made with those parameter sets are plotted in the 4<sup>th</sup> column. It is obvious that the time is radically different in the four cases.

   - For the 64-sided circle with small beam size (row nr.1), we have a total time of 7 hours 48 minutes, which is extremely long.
   - For the 12-sided circle with small beam size (row nr.2), we have a total time of 1 hours 20 minutes, which is already 6 times shorter than the 64-sided circle, while the shot numbers have a difference of solely 2%.
   - For the 4-sided circle with small beam size (row nr.3), a total time of 1 hour is shown, which is shorter but similar to the 12-sided circle, while there are actually 28% more shots to be exposed than the 12-sided counterpart.
   - The by far shortest time is achieved by the large current and 4-sided design, which amounts to 19 minutes - only one third of the time achieved with 10 nA.

The shape of the circle after fabrication is shown in the 4<sup>th</sup> column of Table 4.6. Both 64-sided and 12-sided circle give very round shape. There is barely difference in shape quality to be identified. In case of the 64-sided sample, because of the asymmetric pattern distribution, some dots are elongated slightly towards direction of higher dose. A short range proximity effect correction can eventually solve this problem, which is however not applied for the sample shown in the image. Now, if we compare the result with the 4-sided circles, then there is a clear difference in the outcoming shape depending on the beam size. For a smaller current like 10 nA, one can still see the square shape, even the corners are not sharp (see 3<sup>rd</sup> row, 4<sup>th</sup> column in Table 4.6). For a larger beam current, the gaussian distribution of the beam is broader and causes more rounded shape, though some distortion can also be seen at the edge (see 4<sup>rd</sup> row, 4<sup>th</sup> column in Table 4.6).

In total, it can be concluded as follows:

- More fractures lead to longer writing time. Fractures lead to more beam blanking and extra data transfer time. By comparing the 64-sided and 12-sided circles, the author can estimate the time overhead for one extra fraction to be 0.77 µs. For a surface area of 1 cm$^2$ filled with dot array (pitch 200 nm), one extra fracture in the pattern will cost 32 minutes extra writing time, regardless of the beam current.

- Higher current leads to shorter exposure time. Ideally, the exposure time is inversely proportional to the beam current. In reality, due to different filling condition and overhead time like beam settling time, the exposure time is not strictly inversely proportional to the beam current. However, using higher current also helps generate round shape even with a square as the original pattern instead of circle with multiple sides.

- The fastest method for large-scale dot array generation is to use square as pattern to avoid additional fracture, which is paired with high current for short exposure time and rounded shape. 76 min/cm$^2$ is shown for 130-140 nm dots in 200 nm periodicity.

- In comparison to single-dot exposure method[50], where for each dot only one single shot (long exposure) is used, the method presented here is considered to be comparable or even better. Even though 100 shots are given instead of one, the overhead time inside one fracture is almost zero because of the fast deflection and nearly zero settling time. The only significant overhead is the fracture time from one dot to another, which is the 770 ns as calculated. Regarding the exposure time, for a single dot, 1143 ns total exposure time is required. However, in order for a single shot to achieve the same diameter as the 100 shots, the center part has to be highly overdosed because of the gaussian distribution of the beam - almost 3 times of the clearing dose is used[50]. The overdosed energy thus also causes wasted time. To achieve 130-140 nm dots in 200 nm period, about 70 min/cm$^2$ writing speed was reported for 42 nA and 30 µC/cm$^2$ clearing dose[50]. Our exposure time for the same periodicity and dot size is 76 min/cm$^2$ for 44 nA and 280 µC/cm$^2$ clearing dose. This clearing dose is almost 9 times higher than reported in [50]. If the same clearing dose is used as they reported, a nine-fold reduction in exposure time could be achieved.

- The last parameter that can be optimized is the resist thickness. In this thesis, the same resist formulation CSAR AR-P 6200.09 is used and a resist thickness of 190-200 nm is given. The clearing dose is around 280 µC/cm$^2$. However, using half of the thickness can lead to almost half of the dose required for positive tone resist, which thus leads to substantially shorter time. However, it's to be remarked that thinner resist also supports thinner etching depth when the resist is directly used as etching mask. For Si wafer, 200 nm resist can roughly support 400 nm Si etching (at -19°C)

# 4.4  Large scale nano-structured stamp replication
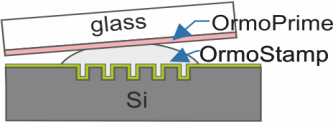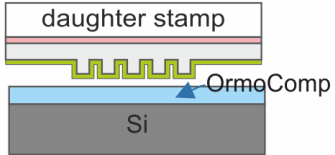
| Process | Procedure | Illustration |
|---|---|---|
| *1. Nano-imprint stamp replication* | | |
| Definition of master stamp | A Si stamp is processed by e.g. E-beam lithography and RIE etching. Nano-dot array is defined on the surface. | |
| Generation of daughter stamp | Ormostamp is cast imprinted onto a glass wafer coated with adhesion promoter OrmoPrime, which leads to the daughter stamp with reversed polarity. | |
| Imprint with daughter stamp | The daughter stamp is treated with anti-adhesion layer. A new Si wafer is spin-coated with OrmoComp. UV-nano-imprint is carried out. | |
| Separation | Using razor blade to separate the substrate with the daughter stamp. Polymer should stay on the new Si substrate. | |
| Etching | Reactive ion etching is applied to etch into the Si substrate, which defines nano-dots array with the same polarity as the master stamp (granddaughter stamp). | |

Table 4.7: Fabrication protocol for replication of a Si master stamp to a Si granddaughter stamp with the same pattern and polarity.

By using our high-throughput E-beam writing method, the author fabricated a large nano-dot array with a size 40 mm x 40 mm with a periodicity of 200 nm and diameter of 130 nm. The SEM image is shown as inserts in Figure 4.15. The imprint from this stamp can be used for plasmonic color generation, where a thin layer of aluminum is deposited to obtain local plasmon resonance[17, 95]. However, once the stamp is etched, the diameter of the nano-disks is fixed, which critically determines the resonance thus

the color[17]. However, there are many applications where a modification of the original stamp is necessary. For example, when another color is wished, a different disk size has to be achieved. This can be realized by e.g. oxidation of the original stamp, which is however not a reversible process. Furthermore, if one wants to use the pattern for injection molding as a mass production tool, one has to sacrifice the Si master to obtain the Nickel shim. In all these processes, the cost of the process is extremely high due to the irreversibility of the process. For a 40 mm x 40 mm nano-dot array, at least 25 hours of E-beam writing time are needed, which amounts to at least 10000 Euro. Therefore, it is of extremely high value if the master stamp can be replicated in a low-cost fashion, which will facilitate more customization or research possibilities. Here, the author presents a fabrication process using nano-imprint lithography for master origination, enabling low-cost cloning of the master original.

The fabrication protocol is listed in Table 4.7. At first, the original stamp is fabricated with EBL. In this case, nano-holes are defined inside the Si wafer. After anti-sticking treatment of the sample, it can be sued as an imprint stamp. Following the procedure of making transparent hybrid stamp, one can generate the daughter stamp with reversed polarity with OrmoStamp on glass wafer. Here, OrmoStamp daughter stamp reveals nano-disks. After the daughter stamp is treated with anti-sticking agent via covalent silane-bonding, it can be used to imprint on a new Si wafer coated with OrmoComp. UV-curing nano-imprint is applied with 6 bar pressure and 15 min imprint time. Since cured OrmoStamp polymer and the glass substrate all have high UV transparency, the UV-curing can take place through the imprint stamp and does not require the new substrate to be transparent. The nano-structure is thus replicated into the OrmoComp layer. Thereafter, one can apply reactive ion etching to transfer the pattern into the bulk Si. Finally, the remaining OrmoComp can be removed by e.g. RCA cleaning.

Images of the original 4 cm x 4 cm Si stamp and granddaughter stamp is plotted in Figure 4.15. In the optical images, we can see that after the imprint and before the removal of the OrmoComp polymer, there are some residues around the pattern. As mentioned earlier, spacers are used to keep a distance between the substrate and the stamp during vacuuming step of the UV-NIL, which avoid touching and inclusion of air pockets. The marks of the spacers can be vaguely seen in Figure 4.15b. Thereafter, the OrmoComp residue is removed by RCA cleaning, which includes

- 10 min bath at 70°C in solution of 30 vol. % $NH_4OH$, 30 vol. % $H_2O_2$, and 40 vol. % water

- 3 minutes quick rinse in water

- 30 seconds bath in buffer HF

- 10 min bath at 70°C in solution of 30 vol. % HCl, 30 vol. % $H_2O_2$, and 40 vol. % water

- 3 minutes quick rinse in water
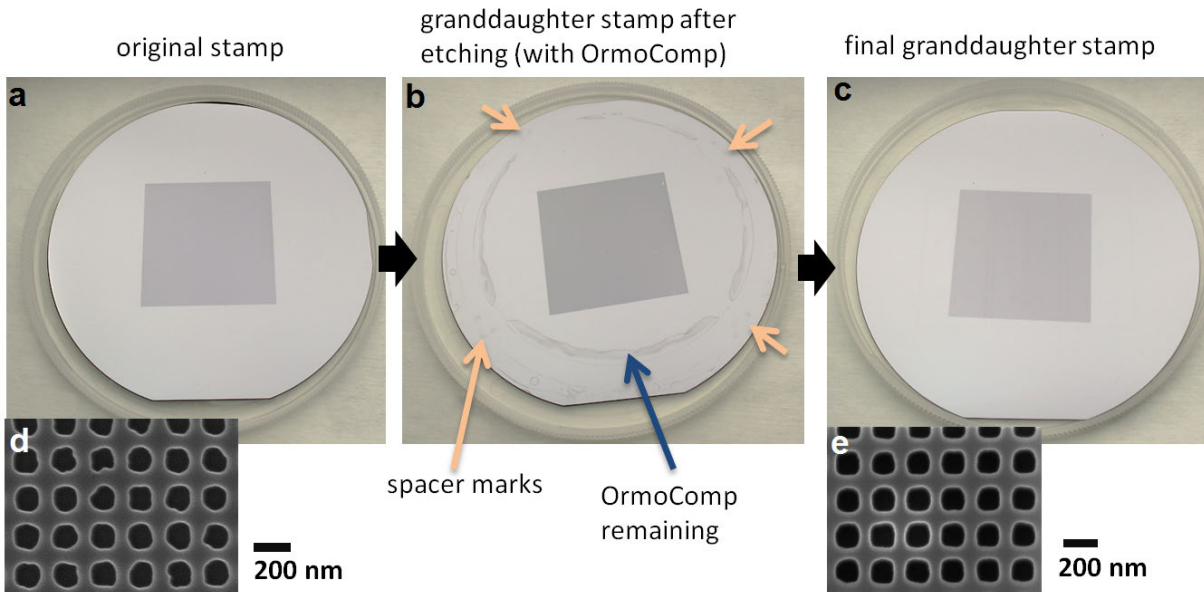
Figure 4.15: The process of master stamp origination. The original stamp (a) is used to make daughter stamps with OrmoStamp showing reversed polarity. A new Si wafer can be imprinted by the daughter stamp with OrmoComp, followed by a Si etching process, which yields the granddaughter stamp with the exact same pattern and polarity as the original master stamp (b). After removing the remaining OrmoComp, the granddaughter stamp can be used for further imprints (c). SEM images are inserted for the original stamp (d) and the granddaughter stamp (e).

- 30 seconds bath in buffer HF

- 5 minutes bubble rinse in water

Here, the author remarks that the RCA cleaning is a very thorough cleaning procedure, which is normally required for wafers before entering the furnaces for doping or annealing, where the least contamination is favored. According to the manufacture, OrmoComp can be removed by hot piranha with 3:1 $H_2SO_4$ and $H_2O_2$ at 70°C.

Looking at the shape of the nano-dots in SEM, as shown in Figure 4.15d-e, one can see that in the original stamp there are more small distortions around the edge of the circle. The reason is mainly due to the beam current fluctuation during the E-beam exposure especially if the exposure is extremely long like 25 hours in this process. However, as shown in the SEM images of the granddaughter stamp, those small distortions are not replicated. The reason is considered to be the rounding effect during the imprint process that is not able to replicate sharp changes in 10-20 nm range. The author considers this effect to be helpful for obtaining better plasmonic color generation after the imprint.

A crucial step of the stamp replication process is the etching process. Since the original stamp has a protrusion of only 50 nm, the replication into the OrmoComp

| Recipe | Nr.1 | Nr.2 | Nr.3 |
|---|---|---|---|
| $C_4F_8$(sccm) | 75 | 75 | 75 |
| $SF_6$(sccm) | *38* | *47* | *58* |
| Coil power (W) | 800 | 800 | 800 |
| Platen power (W) | 40 | 40 | 40 |
| Temperature (°C) | -19 | -19 | -19 |
| Process time (s) | 30 | 30 | 30 |
| Si etch depth (nm) | *60* | *86* | *140* |
| Dot diameter (nm) | *122* | *140* | *155* |

Table 4.8: Recipes of reactive ion etching of Si for granddaughter stamp generation.
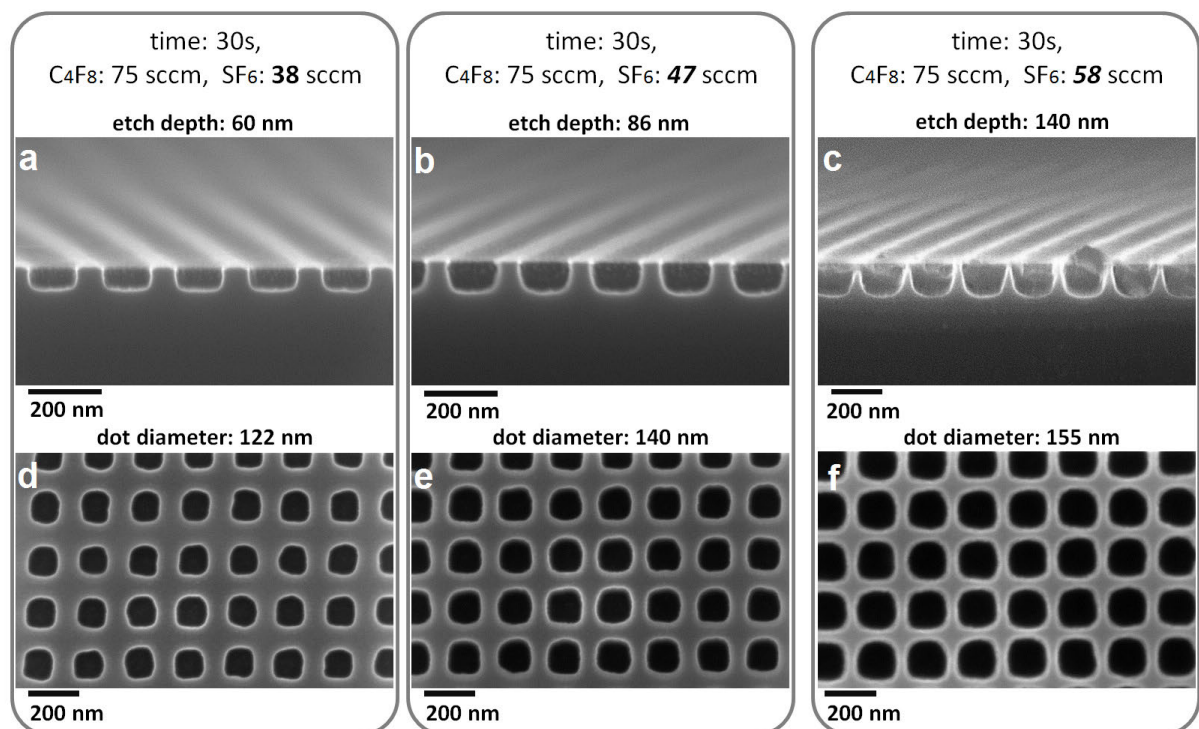


Figure 4.16: (a)-(c) SEM cross-section images and (d)-(f) SEM top side images of nano-dots etched with different recipes. 45 nm OrmoComp resist was used as etching mask.

polymer has only a height difference of about 45 nm (due to the volume shrinking after the UV curing). However, using 45 nm resist height to obtain 50-100 nm etching depth is challenging. For this purpose, different etching conditions are tested. The results are

shown in Figure 4.16. The reactive ion etching machine (Advanced Deep Reactive Ion Etching (DRIE) Pegasus, SPTS) is used for Si etching at -19°C, which gives the highest selectivity (resist/silicon etch ratio) - resist is less consumed for the same etching depth of Si. All relevant parameters are listed in Table 4.8. Most parameters are kept the same while the $SF_6$ proportion is being increased. In general, increasing $SF_6$ will increase the etching rate and isotropic profile, which can be seen from the cross-section in Figure 4.16a-c. By increasing the $SF_6/C_4F_8$ ratio from 0.5 to 0.6, more than 40% increase in etching depth is shown. The shape of the side wall also turns to slightly under-cutting, which can be helpful for plasmonic color generation, since Al will be deposited after the imprint and a continuous Al film (on top and around the nano-disk) will deteriorate the resonance condition. With further increased $SF_6/C_4F_8$ ratio (0.77), the etching depth further increases to 140 nm. However, the resist is also strongly attacked causing the boundary to be blurred out, which is not suitable for plasmonic color application.
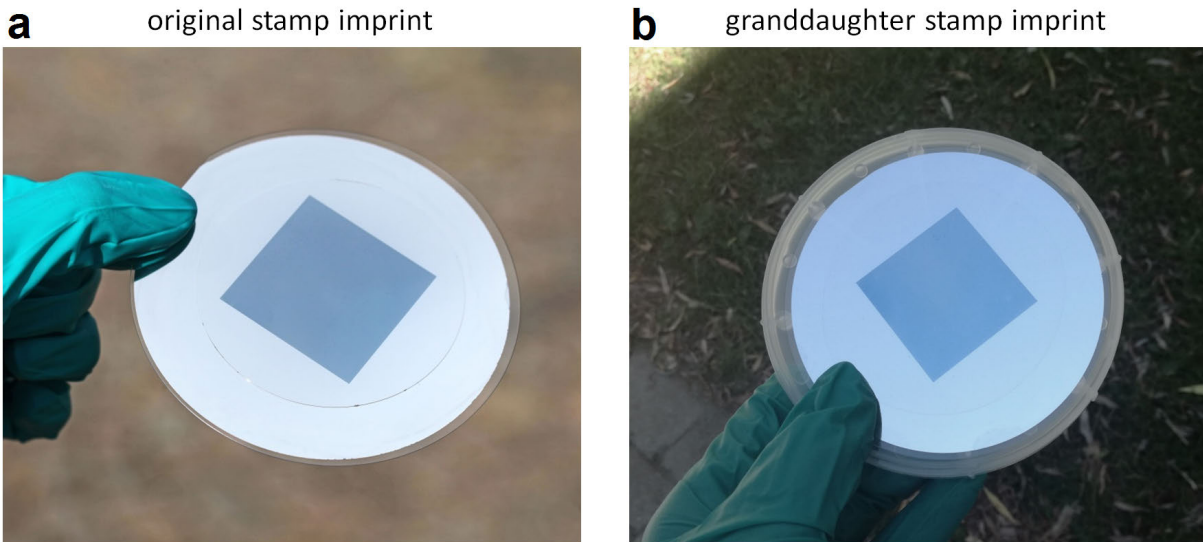


Figure 4.17: Images of imprints (OrmoComp) made with original stamp (a) and grand-daughter stamp (b). 15 nm aluminum was deposited on top of each wafer. The center area display blue color without diffraction effect, due to 200 nm sub-wavelength periodicity.

Subsequently, two imprints are made with the master and the granddaughter stamp. Those imprints are made with UV-cast imprint with OrmoComp on glass wafer. After-wards, 15 nm aluminum is E-beam evaporated on top. The local plasmonic resonance leads to absorption in different wavelength range. For 130 nm -140 nm disks, blue color should be observed, as shown in Figure 4.17, both original and granddaughter stamp give clear blue color. Under microscope, the color can be displaced more clearly, as shown in Figure 4.18. In the low magnification images on top, the writing fields of the E-beam writer can be clearly seen (200 µm x 200 µm). Note that plasmonic color generation is extremely sensitive to any size variation, thus slight change even in 5-10 nm range will still be visible. In the high magnification image below, one can see even finer splits,

which are the small scanning field of about 4 µm, which is exactly the way how the E-beam writer sequences the writing order. At the edge of the nano-structured field, there is a transition visible, showing slightly red-shifted color. The reason is the smaller dot size at the edge area due to the absence of proximity effect correction. As mentioned earlier, in order to maximize the writing speed, no proximity effect correction is carried out to avoid addition fractures or data transfer. Since the edge area is lower than 60 µm on a Si substrate, due to the scattering length of the beam, it is not critical for the visual color homogeneity.
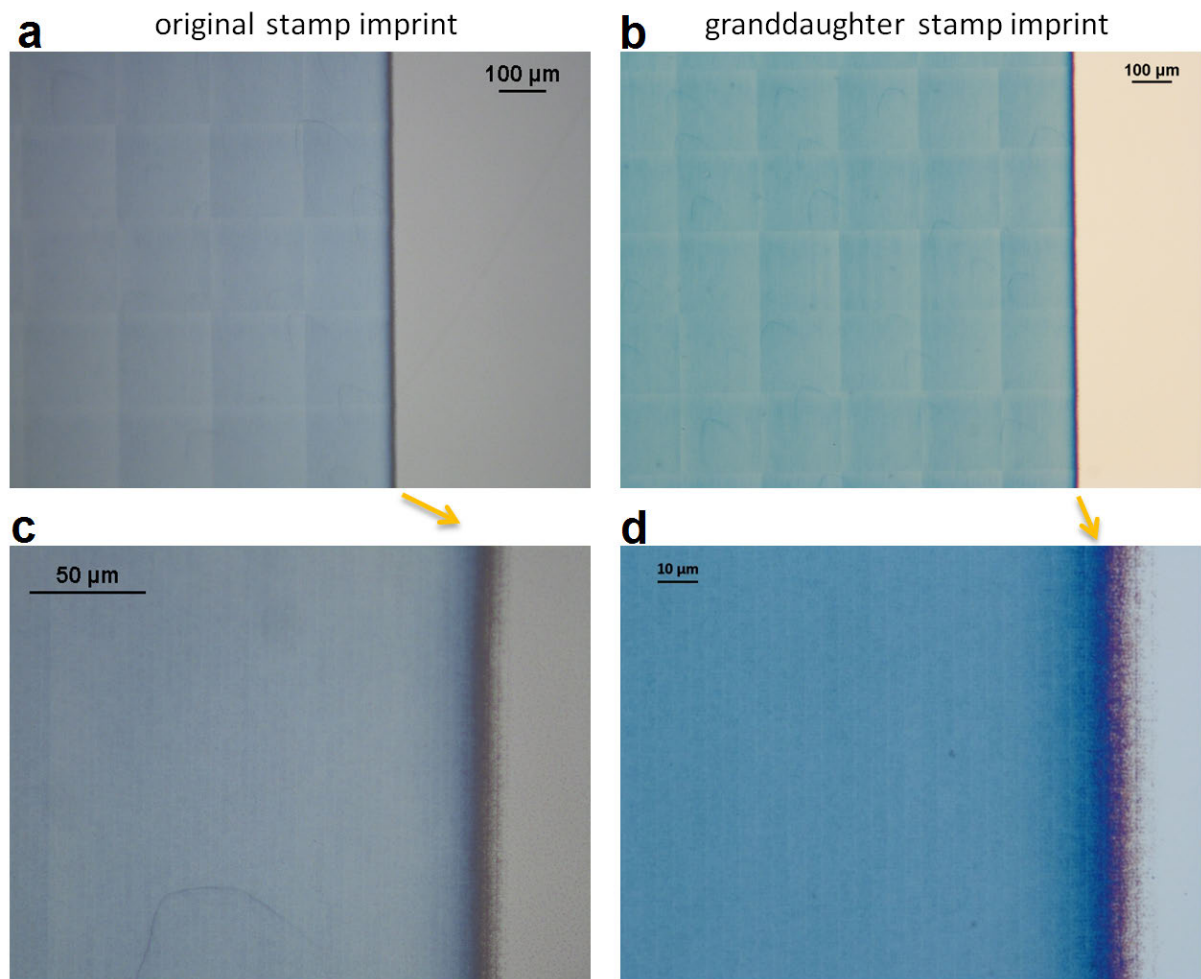


Figure 4.18: Microscope images of plasmonic color generated by original master stamp imprint (a)(c) and granddaughter stamp imprint (b)(d).

In conclusion, the granddaughter stamp can faithfully replicate the plasmonic color generated by the original stamp. The rounding effect of the replication process may contribute to even more homogeneous color generation.

# Device prototyping and sensor integration

## 5.1  Introduction

In this chapter, a device prototype is designed and manufactured for a second generation hemolysis sensor aiming at integration into Radiometer's ABL product family.
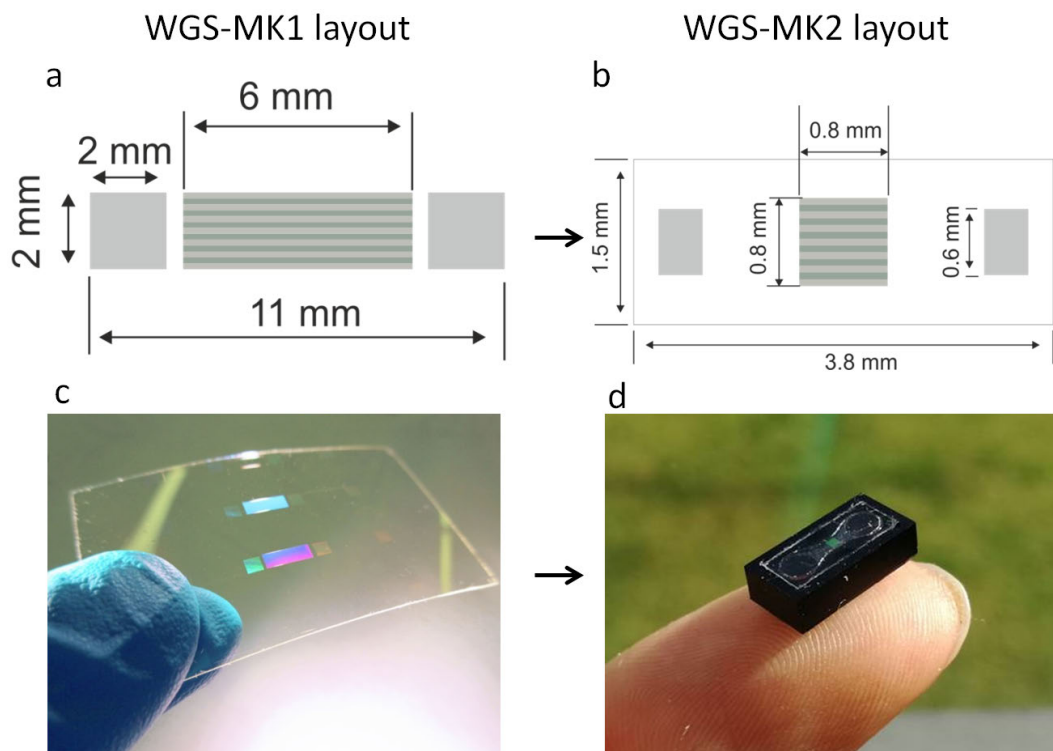


Figure 5.1: Requirement for the waveguide sensor mark 2 (WVG-MK2) (b) compared to the waveguide sensor mark 1 (WVG-MK1)(a). Smaller size is strongly reduced for better integration. (c) MK1 sensor is pictured on a flexible membrane cut from the wafer. (d) Packaged MK2 sensor in a PMMA sensor house for liquid in- and output.

After the development of the initial waveguide hemolysis sensor shown in Paper I, a

second generation of the waveguide hemolysis sensor is initiated with more strict space requirement for integration into Radiometer's sensor cassette system. The change in the layout design is shown in Figure 5.1. The main changes of the new design are the total footprint of the sensor and the active sensor area (filter area). In the first version, which is named as waveguide sensor mark I (WGS-MK1), the author adapted the design from a earlier project for the grating couplers. The size of the grating couplers area is 2 mm x 2 mm, which is large but not necessary. The active sensing area is 6 mm x 2 mm, where the critical propagation length of the waveguide is 6 mm, as shown in Figure 5.1a. The new requirement is however much smaller. A total footprint area of 3.8 mm x 1.5 mm is required for mounting into a dedicated sensor area in the outlet area of the ABL90 sensor cassette from Radiometer. Furthermore, the active area, which has contact to blood, should be reduced to a round window with a diameter of 1.2 mm. Thus, a square area of 0.8 mm x 0.8 mm is designed for the filter region to facilitate full contact with blood flow. There is also space for alignment tolerance. The grating couplers are reduced to 0.6 mm x 0.3 mm, where 0.3 mm is the grating length for in- and out-coupling. The specifications can be seen in Figure 5.1a-b.

In Figure 5.1c-d, pictures of the manufactured sensors (MK1 and MK2) are shown. Both MK1 and MK2 sensors are fabricated at first with a glass wafer and subsequently peeled off as a free-standing membrane of a thickness around 100 µm. For MK2 sensor in Figure 5.1d the sensor is already assembled into the sensor house where the in- and output of the flow is placed. The author remarks that the total footprint of the MK2 sensor is larger than the layout, which is shown in Figure 5.1b. The horizontal length of 3.8 mm is untouched while the vertical length is increased to 11 mm instead of 1.5 mm as indicated in Figure 5.1b. This change is solely meant to mechanically accommodate the flow, which comes vertically through the sensor. The extra vertical space eases the assembly and the design of the liquid ports by a lot. However, the final size requirement can definitely be met when more sophisticated design of the flow ports is made.

Another goal of the new sensor development is to create a setup prototype that can show potential of integration into the ABL90 blood gas analyzer of Radiometer, which means low cost, low space-requirement, and sufficient robustness. Furthermore, it should be able to be operated independently by a lab technician, and thus requires automated software operation matching the ABL90 operation routine as well as a large mechanical tolerance since one cannot align the sensor so precisely or avoid all environmental noises like in an optical laboratory with expensive equipment.

In the following sections, the optical, mechanical, electronic and software design of the setup prototype for waveguide sensor MK2 are presented. The final result is a stand-alone waveguide sensor system that can achieve waveguide absorption measurement with additional filtering ability. The sensors are packaged with the fluidic house and can be wired to the liquid section of the ABL90 blood gas analyzer. Finally, the sensor system is handed over to Radiometer and being tested with their staff.

## 5.2   Optical Design

The goal of the optical design is to find out the best solution for coupling broadband light (from multiple LEDs) into a single mode waveguide. The grating periodicity is kept the same and the angle of incidence is varied to match the grating condition. The main challenge is to find an optical system that 1) efficiently focuses the light from the LED element and 2) matches the angle condition given by the gratings. After the initial simulation and testings, a lens system was designed with individual aspheric condenser lens for each LED and a common focus lens, as shown in Figure 5.2a.
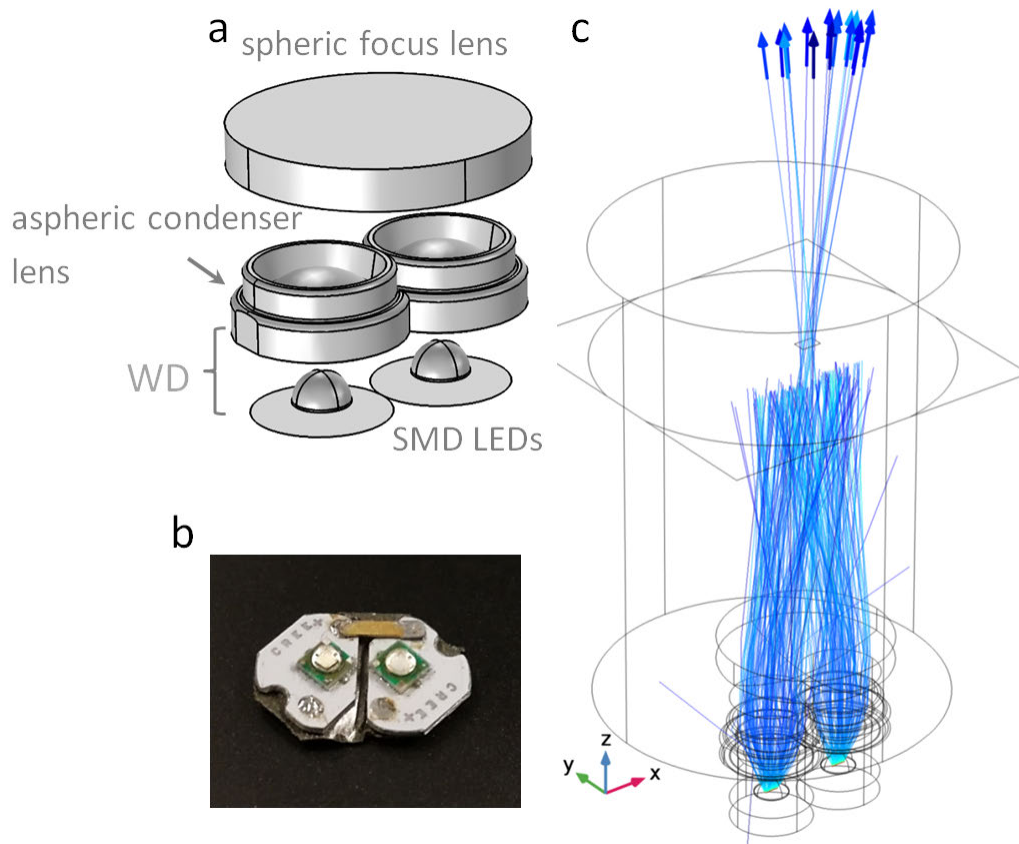


Figure 5.2: (a) Lens system for focusing two surface-mounted LED light sources into grating couplers. Two aspheric condenser lenses are used for each LED element. One large spherical focus lens is used to focus two light beams. The working distance (WD) of the aspheric lens is defined in the image. (b) Image of the surface-mounted LEDs. Two separate boards were modified to achieve small distance between the LEDs. (c) Ray tracing simulation of the two LED systems. An aperture was set in the middle plane to simulate the input aperture of the waveguide sensor. The transmitted rays are shown with arrows.

Two commercial surface-mounted-device (SMD) LEDs were used as light source as

shown in Figure 5.2b. The LEDs are acquired from Kiwi Lighting Inc.(Shenzhen, China) with a unit price of 1.5 US dollar, which matches very well the low-cost consideration of the design. The LEDs dies are manufactured by Epileds Technologies (Taiwan) and packaged in 3535 type (PCB size: 3.5 mm x 3.5 mm) with a maximal electrical power of 3 W. Central wavelength of 415 nm, 450 nm, and 480 nm are acquired. At a DC forward current of 650 mA, the forward voltage is about 3.6 V. The LEDs are soldiered on aluminum board for heat conduction. A semiphere silicone lens is included in the packaging, which has been taken into consideration for the simulation.

The aspheric condenser lens are made with molded plastics (CAY046-A, Thorlabs) with a focal length of 4.6 mm (0.4 NA). The use of plastic lens is not only because of the low cost but also because of the capability of mechanical rework. The lenses were ground down in diameter to match the distance of the LEDs, which is 6 mm. The spheric focus lens are plano-convex and made with N-BK7 glass.

Ray tracing simulations were carried out in COMSOL Multiphysics. The model is shown in Figure 5.2c. As we can seen, an aperture is placed 30 mm away from the plane of the LEDs with an opening of 1 mm x 1 mm to assimilate the grating couplers. All rays that do not pass through the aperture are eliminated. 55000 rays are released from each LED with a cone shape and a half angle of 35°. The length of the LED element (1.1 mm) is also considered where the ray release is homogeneous across the area.

Two important parameters, which have been studied, are the working distance (WD) of the aspheric condenser lens and the focal lens of the spherical focus lens. The results of the ray tracing simulation is shown in Figure 5.3. In the upper row, the WD is varied between the condenser lens and the LED plane. Here, the angle of incident is plotted on the x-axis and the ray count on the y-axis. The histogram is generated with a bin size of 0.5°. There are always two peaks shown in the positive and negative angle range, which come from the two LED light sources. A high ray count (y-axis) indicates a high intensity that reaches the aperture, which is desired for the optimization. The highest ray counts are achieved by a WD of 1.75 mm (see Figure 5.3b). With an increased or decreased working distance, the ray counts drop. The reason is that the condenser lens should ideally collimate the rays from the LED, which are to be focused through the second lens. If the WD is not matched with the ray condition, the ray will under-focus or diverge at the plane of aperture. However, one cannot simply take the WD given by the lens manufacture since the LED light source is not a point source and a silicone lens is embedded in the package. The ray tracing is thus very helpful in this case.

Another parameter of consideration is the focal length of the spherical focus lens (see Figure 5.3d-f). Unlike the condenser lens, which should have the highest NA for collecting a maximum range of angles, the focus lens can be chosen by freely. However, depending on the focal length (as well as NA) of the lens, different angle ranges will be achieved at the focus plane. For the grating couplers, one particular wavelength can be coupled with one particular angle. Ideally, the different wavelengths generated by a LED element
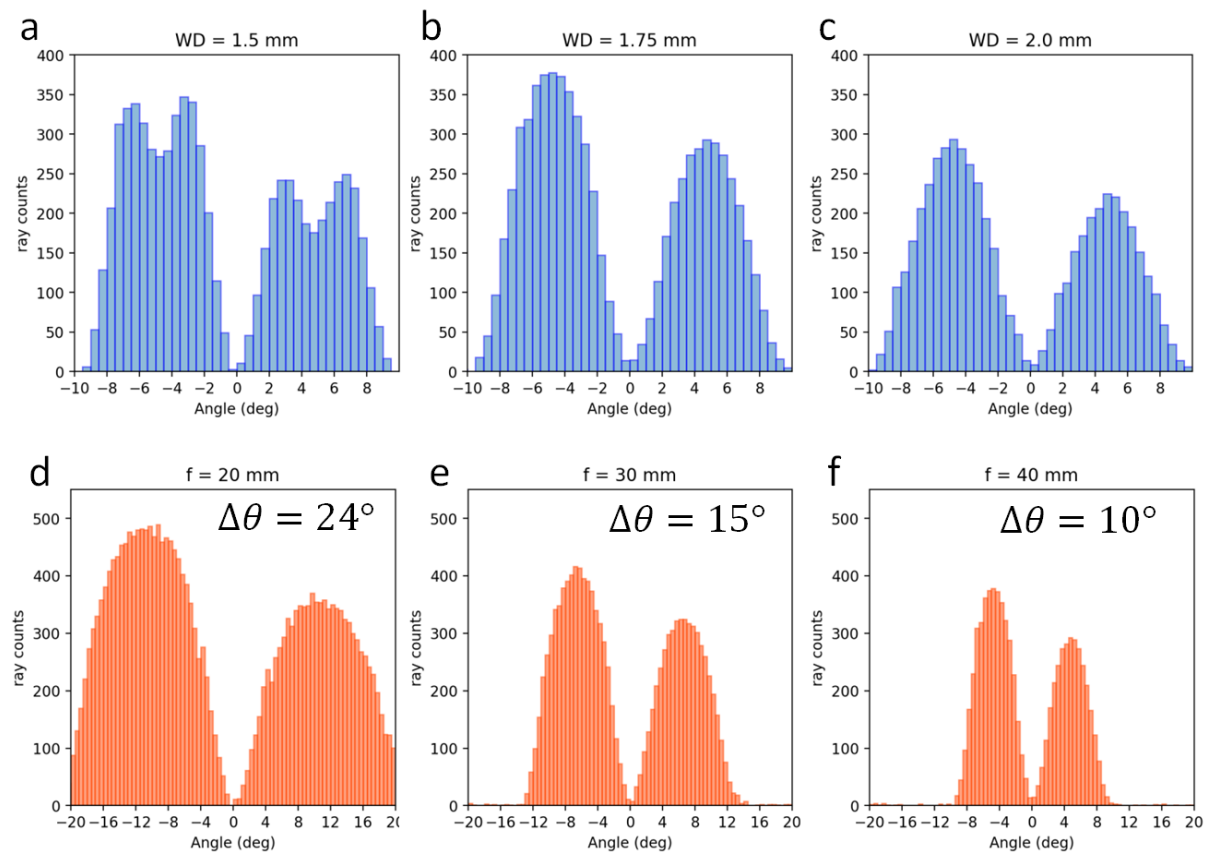
Figure 5.3: (a-c) Simulated histogram of the transmitted ray counts against the normal incident angles of the rays. Three different working distances of the aspheric condenser lens were used from 1.5 mm to 2.0 mm (a-c). Rays from the two LED sources are split into two areas (positive and negative). (d-f) Simulated histogram of the transmitted ray counts against the normal incident angles of the rays. Three different focal lengths of the spherical focus lens were used from 20 mm to 40 mm (d-f). The peaks of the two beams have an angle difference of $\Delta\theta$, which is annotated in each figure.

should be split in different angles and coupled into the grating coupler. However, this is not possible without an additional diffractive element. The best solution the author considers is to have the central wavelength of a LED matched with the corresponding coupling angle of the grating coupler. For a combination of 415/450 nm LEDs, the angle difference is about 7°. For 415/480 nm LEDs, it is about 12°. (415 nm is always needed for its relevance for hemoglobin absorption.) Thus, a focus length needs to be found to match the angle difference that is needed for different LED sources. As shown in Figure 5.3d-f, at 30 mm focal length, the angle difference $\Delta\theta$ is 15°, which is defined as the angle difference between the peaks of the two beams. In this case, one can use 415/480 nm LEDs as a combination. If 415/450 nm LEDs are used, then a higher focal length should be chosen. However, as we can see from Figure 5.3d-f, a larger focal length results in fewer rays reaching the aperture. The reason is that a small beam size (i.e. high ray

density) can be achieved by a high NA lens. Thus, increasing the focal length can help generating smaller angle spread but also decreases the absolute intensity. Therefore, a focal length of 30 mm is chosen with the 415/480 nm LED combination to achieve a balanced performance. Another possibility to reduce the angle spread while maintaining the intensity is to lower the distance between the LEDs. However, as shown in Figure 5.2b, the author has already tried to reduce the distance as much as possible. A possible improvement can be using customized LED packaging, which however requires much more resources to be spent.

## 5.3   Mechanical design

The mechanical design should provide the necessary degree of freedom to adjust and fix the LED light source system as well as the camera system for optical alignment. Furthermore, a sensor mounting platform should provide necessary fixture for the sensor house especially due to the changing flow in the liquid system.

The main system is illustrated in Figure 5.5. It mainly consists of three components: the light source system, the sensor mount, and the camera system. The light source and camera system should be aligned with a certain angle to the sensor to achieve the in-coupling condition as well as the output spectral readout. A flexure stage design
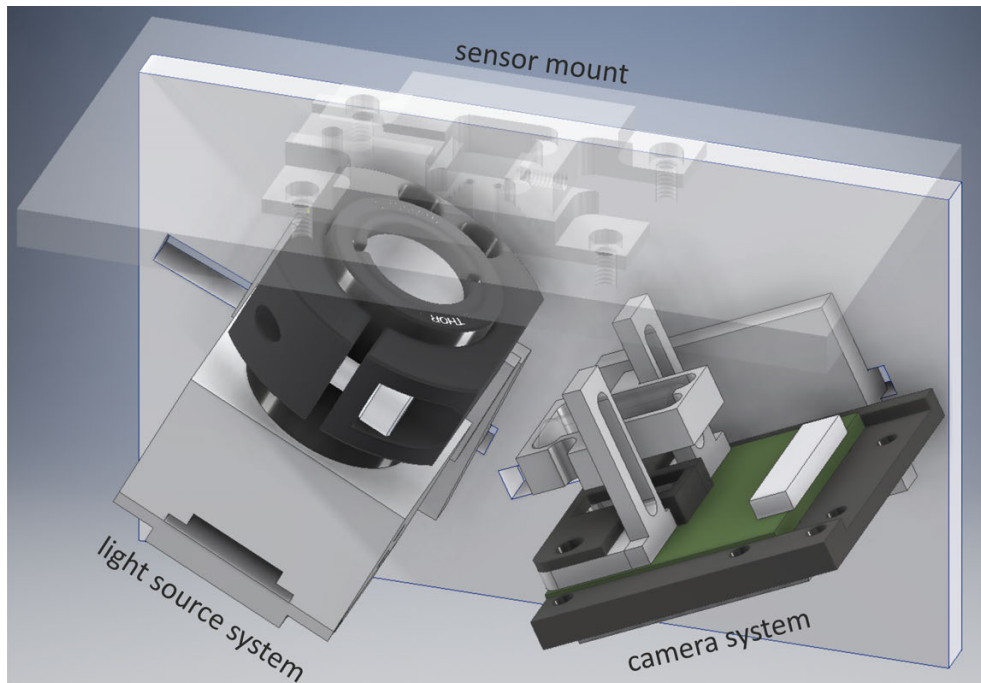


Figure 5.4: Illustration of optical system with integrated LED light source, optical system, and line camera readout.

is used to place the light source and camera system as a flexure mount on the stage.

With a pre-defined key-way on the ground plane, each component can slice relatively to the sensor position while maintaining the angle. To fix the components after the alignment, mounting cleats from Thorlabs can be used. The cleats can be seen in Figure 5.5. Those cleats are designed with one edge milled flat, making it possible to insert or remove a flexure mount without removing the clamp. By tightening the clamp screw, the positional fixture of the flexure mounts is enabled. Furthermore, black aluminum foil tape is used to isolate the input and output parts. This part is crucial for the waveguide sensor, as parasitic light that can leak to the camera is not wished.
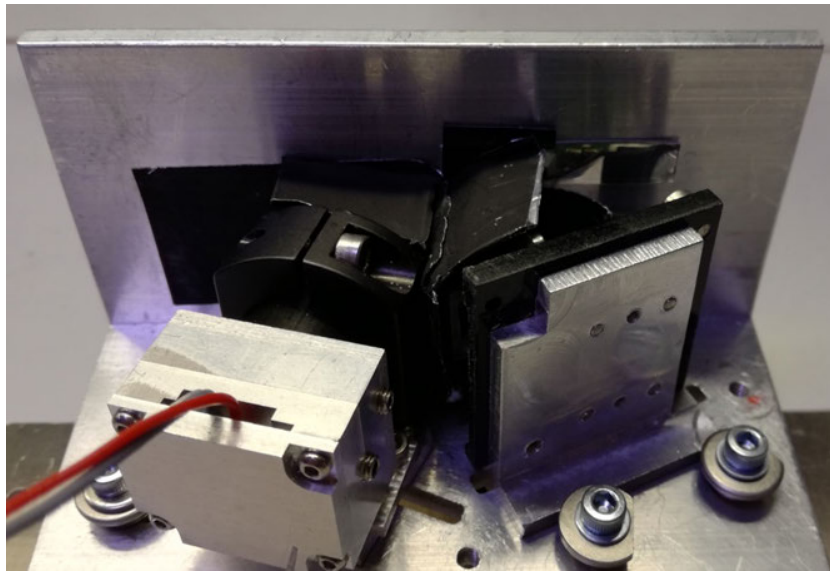


Figure 5.5: Image of the optical system for waveguide measurement. Both light source and camera system are movable through key-way mechanism.

## 5.3.1 Light source system

The light source system should implement what has been designed in the optical simulation with the sufficient degrees of freedom. In Figure 5.6, the components of the light source complex are shown. From right to left, the system is built with a LED board, a LED fixture, two aspheric condenser lens, a lens holder for the condenser lenses, a flexure adaptor, and a half inch lens tube hosting the spherical focus lens. The LED fixture is designed to directly clamp the LED elements (3.5 mm x 3.5 mm). Since the LEDs sit on different boards, which are further cut into smaller sizes, fixing the distance of the LEDs is a crucial step to guarantee the angle after focusing. Furthermore, the LED fixture also functions as aperture for beam cleaning, since the light from a LED element is very divergent (full angle: 140°), the fixture effectively narrows the beam angle range. Similarly, the lens holder fixes the two aspheric condenser lenses and creates a shape that can slip inside the flexure adaptor to vary the WD. The flexure adaptor provides on the one side the linear guide for the lens holder and LED fixture, which can be fixed by the

locking screws on the side. On the other side, the flexure adaptor provides slipping guide
for a standard half inch lens tube with a locking screw. Inside the lens tube, half inch
lenses can be mounted and adjusted in distance. After all components are mounted, the
back plate can be closed to the flexure adaptor via four screws. The back plate needs to
be glued with the SMD LED board through a thermal conducting tape. Furthermore,
a heat sink is glued to the outer side of the back plate to further dissipate the heat
generated by the LEDs.
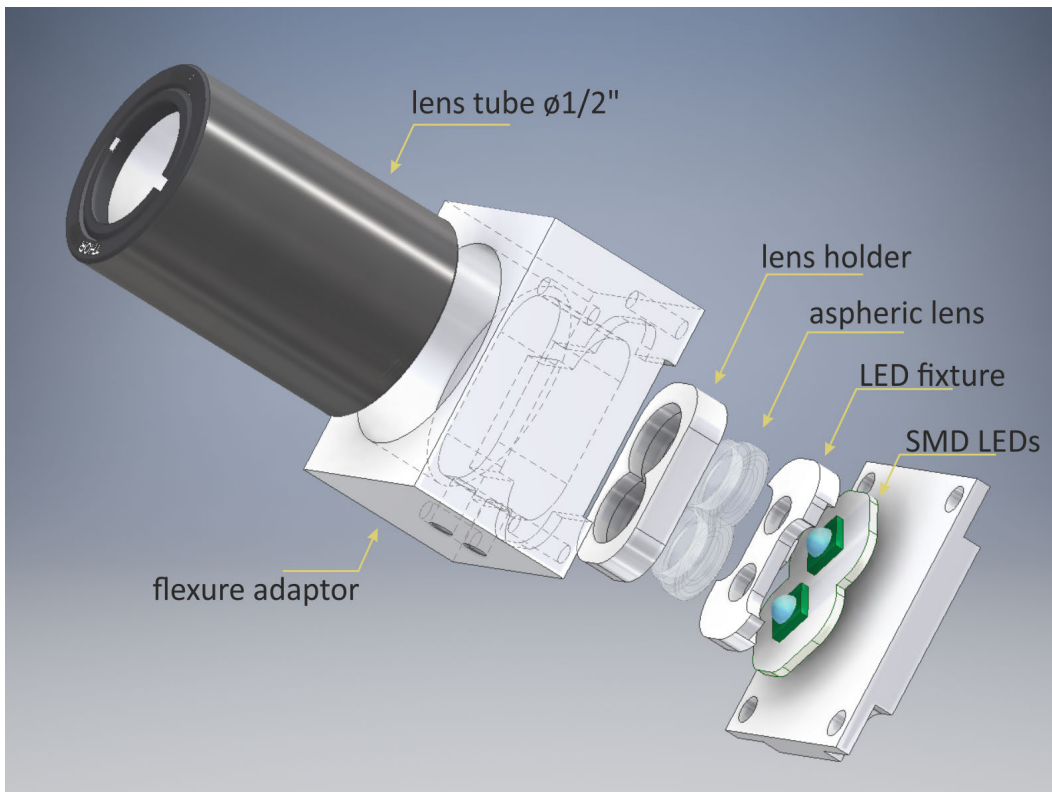


Figure 5.6: Illustration of the light source system for multi-LED light source and lens
system for optical focusing.

The light source system provides the focal length adjustment and fixture. However,
in order to have the best angle for the grating couplers, the incident angle should be
adjustable as well as the location of the focal point. This requires thus three degrees of
freedom. Thus, a mechanical design is made to facilitate the requirements, as shown in
Figure 5.7. The assembly consists of a slip ring, a rotation plate and a flexure mount
with key for sliding on the ground stage. The slip ring allows adjustment of the focal
plane relative to the sensor plane. The rotation plate holds the slip ring and can be
rotated around a screw (right) and fixed by another (left). A rotational range of 30° is
provided. Thus, one can easily align the light source to the grating coupler for achieving
the maximum coupling condition. Once the position is found, the whole system can
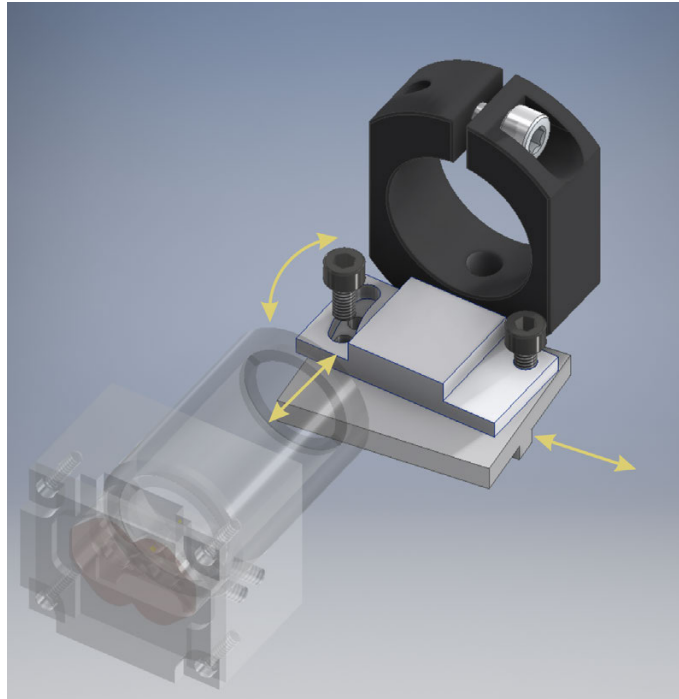
Figure 5.7: Illustration of the degree of freedom of the LED light source. XY-movement is enabled by a key-way and slip ring system. Yaw rotation is enabled with two screws as hinge and fixture.

be firmly locked by the designed locking mechanisms. The finished parts are shown in Figure 5.8a-b.
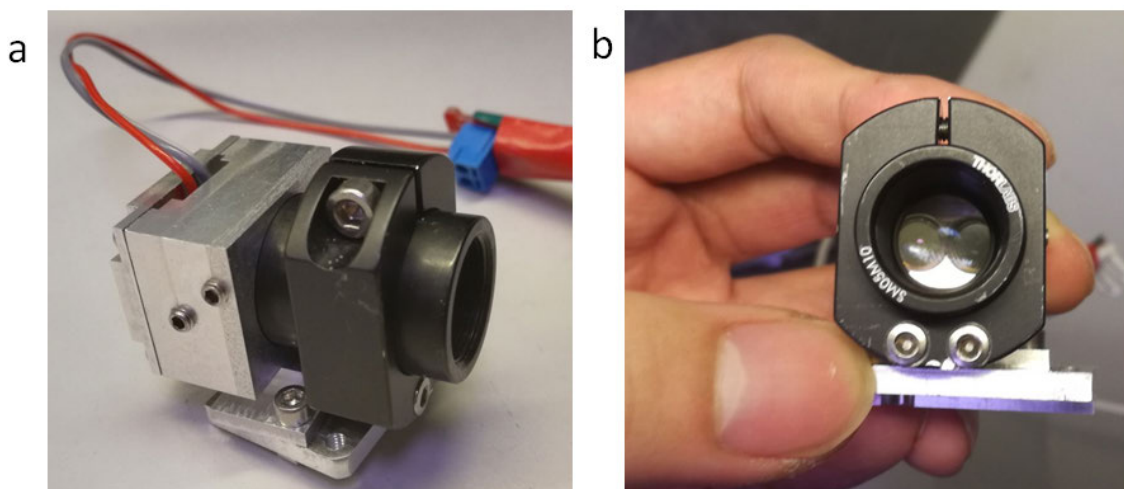


Figure 5.8: (a) Pictures of the mounted light source system.(b) Image of the LEDs through the lens system.

## 5.3.2   Camera system

In contrast to the light source system, the camera system has a lower requirement on the positional and angular precision. Since the camera itself should cover a broad range of spectrum, the main function of the camera system mechanics should be finding the maximum of the intensity out-coupled from the gratings. The design is shown in Figure 5.9.
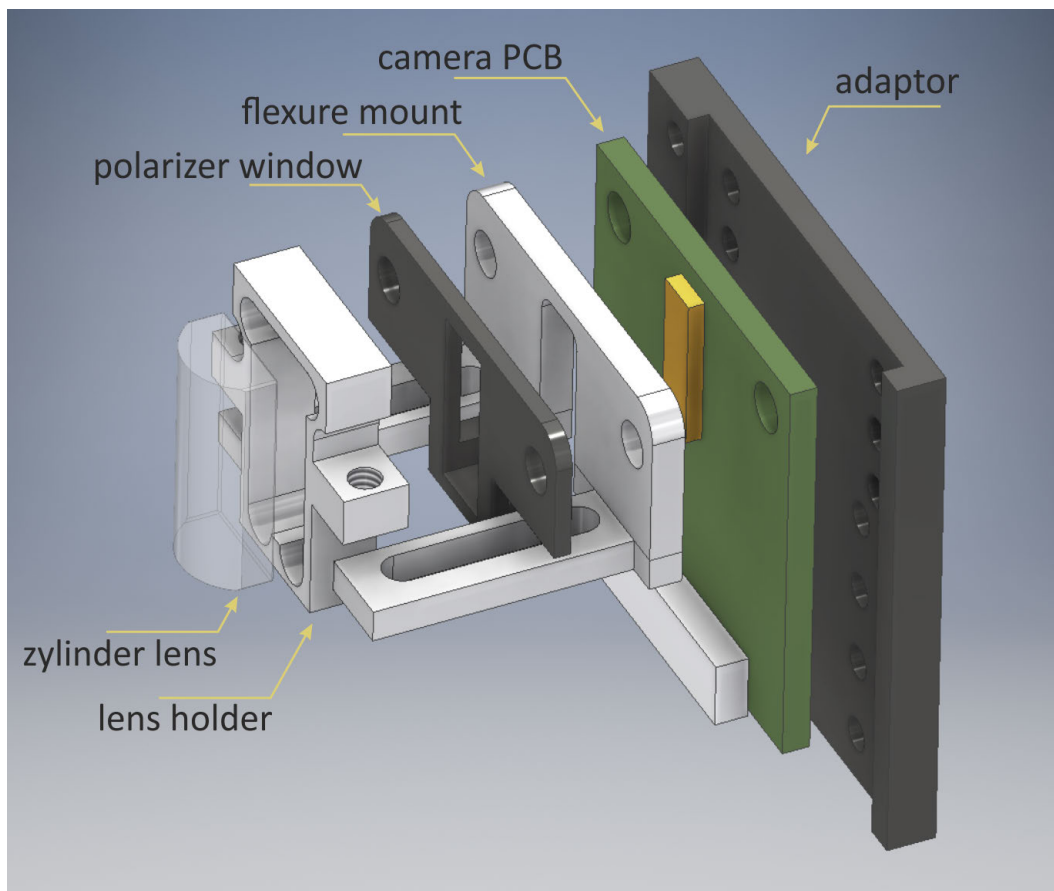


Figure 5.9: Illustration of the line camera system for spectral analysis. A cylinder lens is used for focusing and a linear polarizer is mounted before the light reaching the line camera.

The camera system consists of (from right to left) a adaptor plate, the camera PCB board, a flexure mount, a polarizer window, a lens holder, and a cylinder lens. The adaptor serves the fixture plate with threaded holes for the other components. The camera PCB can be mounted with two mounting holes. Figure 5.10a shows the camera PCB after soldering all components. The line camera is place in the middle of the board while the connector for the ribbon cable is placed on the other side. No electrical component is placed on the back side of the board. The flexure mount is fixed to the camera PCB while providing linear guides for the lens holder. The fixture of the

lens holder is accomplished by two locking screws on both sides. The cylinder lens (LJ1874L2-A, Thorlabs) is an important component for increasing the readout intensity by focusing/collecting the lateral light rays. Two factors are considered here:

- The grating couplers have a relatively large width of 0.6 mm. For the in-coupling, the beam can easily cover the whole grating area, due to the large beam focal size generated by the LEDs. Thus, one can assume that light also couples out in every lateral position of the out-coupling grating coupler, which is of 0.6 mm wide. On the other hand, the line camera pixels are only 63.5 µm wide. There is thus a mismatch in the size of a factor of 10. A cylinder lens can help focusing the light laterally to increase the intensity.

- The out-coupled rays broaden laterally. Since the in coupling involves a focal lens, the in-coupled light carries lateral momentum from the beginning. After the out-coupling, the light travels in free space with the initial lateral momentum, thus creating a large cone shape, which needs to be focused to increase the density.
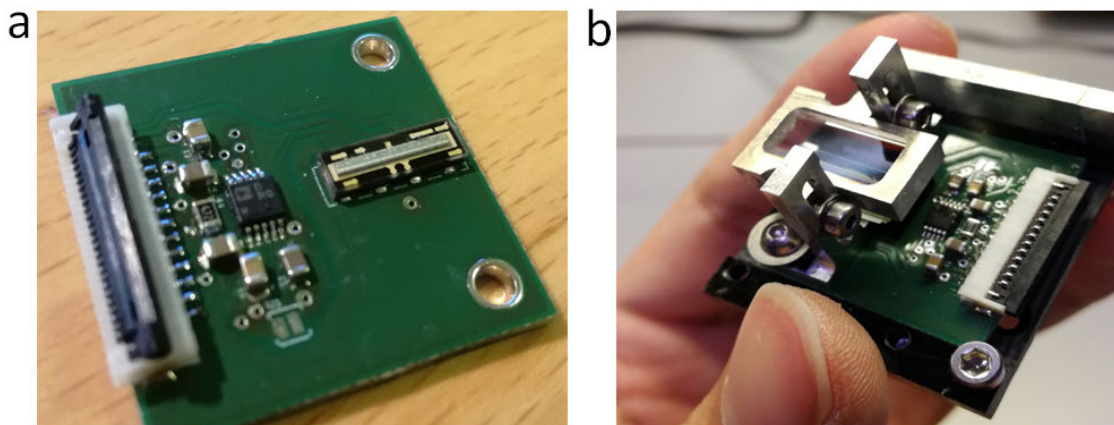


Figure 5.10: (a) Pictures of the PCB carrying the line camera and ADC.(b) Image of the camera system with adjustable cylinder lens and linear polarizer.

As Figure 5.10b shows, the cylinder lens can be adjusted vertically to find the maximum of the out-coupling energy. The intensity enhancement by a correctly positioned cylinder lens can be in 5-10 folds, which helps keeping the camera integration time low. Between the cylinder lens and the line camera a additional polarizer window is placed. A linear film polarizer (LPVISE2X2, Thorlabs) is used for this purpose. The film polarizer can be easily cut to the desired format and mounted to the polarizer window with adhesive. The polarizer film has low transmission under 400 nm, which has to be taken in consideration. The purpose of the polarizer is to distinguish the modes coupled out of the grating coupler. As discussed previously, a waveguide can support both TE and TM modes, which coupled out with slightly different angle. This effect leads to the overlapping signal if the polarization is not distinguished. Therefore, placing a polarizer either before the in-coupling or after the out-coupling is important. Note that, for a

fixed wavelength, one could have the waveguide core thickness designed exactly so that only TE mode is support (where TM mode is under the cut-off condition), as shown in Figure 3.3. However, this will not apply to a broadband coupling as the cut-off condition varies strongly with the wavelength. Thus, using polarizer is definitively constructive for obtaining distinct signal from a single mode.

### 5.3.3   Sensor mount

The sensor mount is designed in such a way that a sensor house can be interchanged and fixed. Figure 5.11 shows the illustration of the sensor mount.
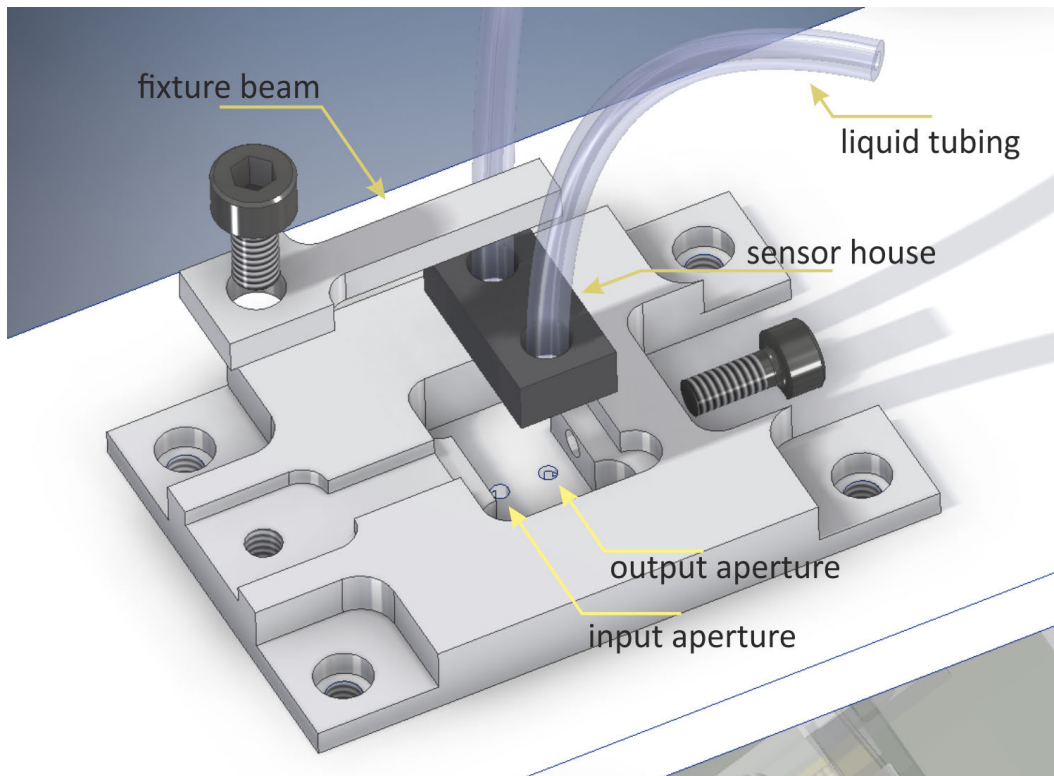


Figure 5.11: Illustration of the sensor mount for packaged waveguide sensor. The input and output apertures are illustrated. Tubing for liquid input and output are mounted from top. A fixture beam applies pressure from top and a screw from the right for fixing the sensor house.

The sensor house carries the sensor on the bottom side in the Figure. The top side is used to wire the liquid tubing. The most important aspect is to align the waveguide and grating couplers relative to the apertures shown in Figure 5.11. Both apertures are in round shape with a diameter of 1 mm. They are milled out from the top side at first; thereafter, a triangle is milled out layer-by-layer from the bottom side. The triangle gives larger opening at the bottom and gradually smaller opening towards the top side.

This design allows the light to be coupled with a higher angle up to 45°, which would be otherwise blocked by the material.

A locking screw (right in Figure 5.11) is used to fix the sensor house horizontally and a fixture beam is then applied with a second screw (left) for vertical pressure. The finished device is then wired to the liquid section of ABL90 as shown in Figure 5.14. Here, the aspiration was just taken from syringe containing human whole blood (on the right side), the blood is pumped to the sensor and being measured.
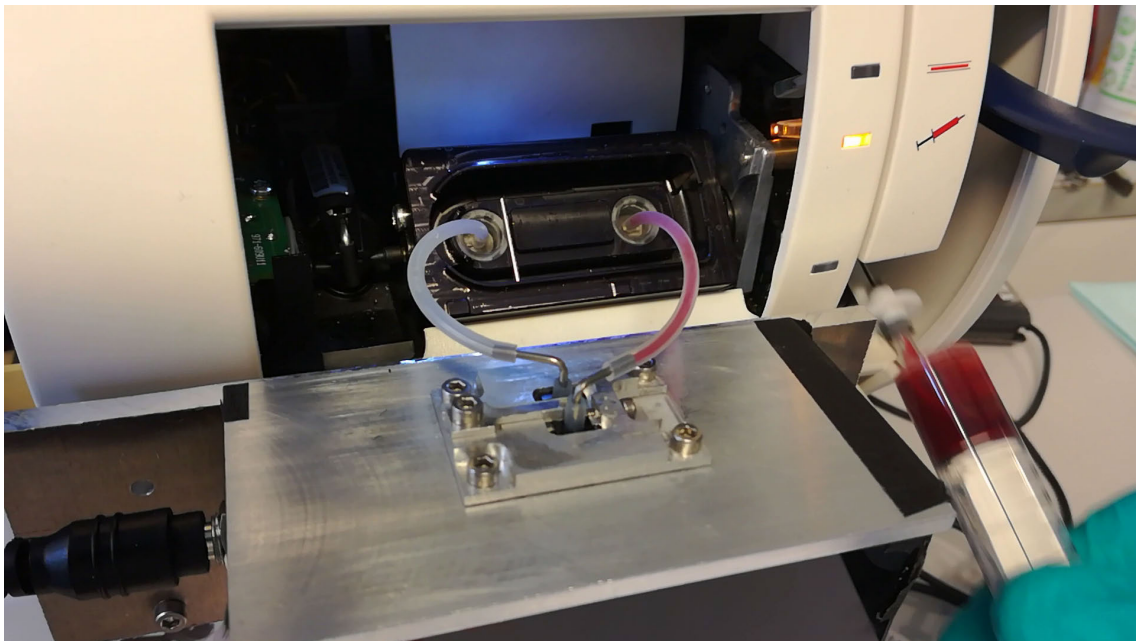


Figure 5.12: Picture of the sensor mount during a whole blood measurement carried out with a modified ABL90 blood gas analyzer.

## 5.3.4   Sensor packaging

The sensor packaging is done in multi-layer way as shown in Figure 5.13. The sensor house is the main mechanical support for the whole sensor as it provides a rigid body. Here, the sensor house is made with a black PMMA block, which also blocks the undesired environment light leaking into the output aperture. The sensor membrane is then fixed to the PMMA house by a double-sided adhesive film, which also defines the fluidic channel. The grating couplers are excluded from the liquid channel to avoid signal interference. Furthermore, permanent black ink from a mark pen is used to cover the top side of the grating coupler (the side towards the sensor house). This is important since the light couples out in both direction (upwards and downwards), while only the light propagating downwards through the aperture is of interest. By black-out the top side, refection from the light coupled upwards can be avoided.

As shown in Figure 5.13, the sensor membrane and the adhesive film are fit into
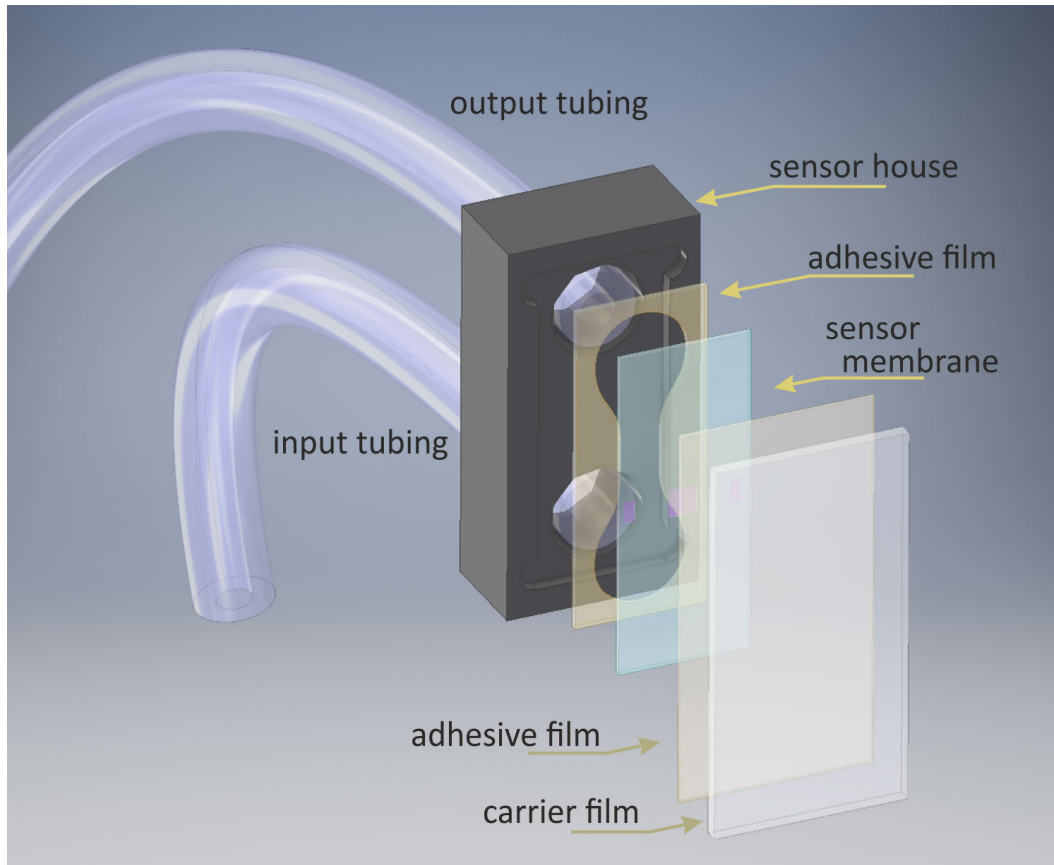
Figure 5.13: Illustration of the packaging of the waveguide sensor. The sensor sitting on a flexible membrane is mounted between the sensor house and the carrier film with two double-sided adhesive films. The sensor house functions as rigid element and liquid ports. The fluidic channel is defined by the adhesive film. The carrier film functions as mechanical support for the thin sensor membrane.

the insertion of the sensor house. Thus, after the assembly, the surface of the sensor membrane is at the same height of the bottom plane of the sensor house. This height matching is important since otherwise any pressure applied will cause compression of elongation of the adhesive and causing positional shift of the grating couplers, which is strictly to be avoided. When the sensor membrane sits in the insertion, it is much less prone to mechanical disturbance. The insertion also defines the lateral position of the sensor to the sensor house. Since the sensor house is the main target of fixation in the sensor mount, the alignment of the sensor membrane to the sensor house determines the alignment repeatability from sensor to sensor.

Moreover, due to the low thickness of the sensor membrane (100 µm), it will still bend when a large flow rate change takes places in the liquid channel. To avoid this influence, it is crucial to have a carrier film that can back the sensor membrane mechanically. This is accomplished with a 0.25 mm thick polystyrene film with an additional adhesive film

for bonding. The size of the carrier film is larger than the sensor membrane and cover
the whole footprint of the sensor house, which helps creating extra robustness. The
author remarks that a thicker and more rigid material can be better for this purpose, like
glass slices, which are however more difficult to cut. Also, the adhesive film can be re-
placed with liquid, curable adhesive which is more rigid after curing than an adhesive film.

The cutting of the sensor membrane is accomplished with a $CO_2$ laser. Here, the
intensity is found which is just enough to cut through the waveguide layer (OrmoCom-
p/OrmoClear/Efiron). The borosilicate glass wafer could be also cut with $CO_2$ laser
which requires much higher dose and also generated excessive heat. The cutting lines has
a smallest width of 150 µm by the machine used (Epilog Laser Mini). The alignment is
done by aligning with the alignment mark defined in the passivation layer. The sensors
after cutting are shown in Figure 5.14, where the filter areas show bright color due to
diffraction. Afterwards, individual sensors will be peel off from the glass wafer by a razor
blade and assembled to the sensor houses.
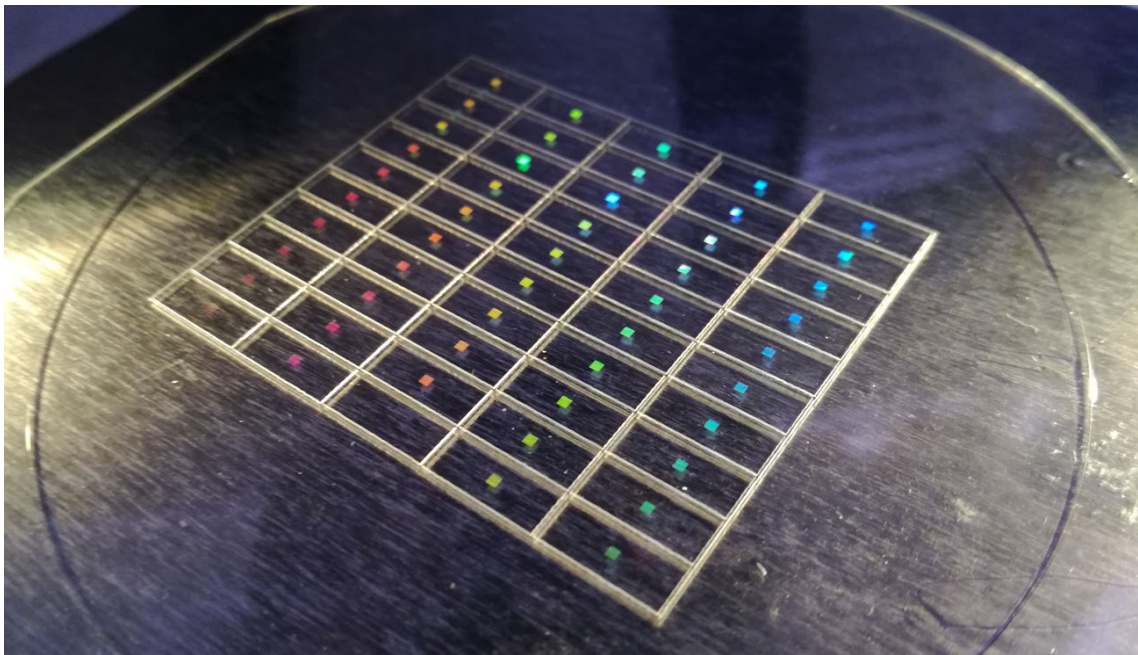


Figure 5.14: Picture of the sensor membrane after the $CO_2$ laser cutting. Diffraction by
the filter elements causes the different colors.

## 5.4   Electronic and software design

The electronic and software engineering plays an important role in this project, as the
sensor system should coordinate with ABL90 blood gas analyzer and be operated by users.
The electronic design has to fulfill the sensing functions like driving LED and reading
out signal from the line camera. It also needs to communicate with the ABL90 analyzer.

Furthermore, the software automation should be implemented for both hardware control and final data evaluation. The diagram shown in Figure 5.15 illustrates the whole system. The main components and their functions are discussed as follows:
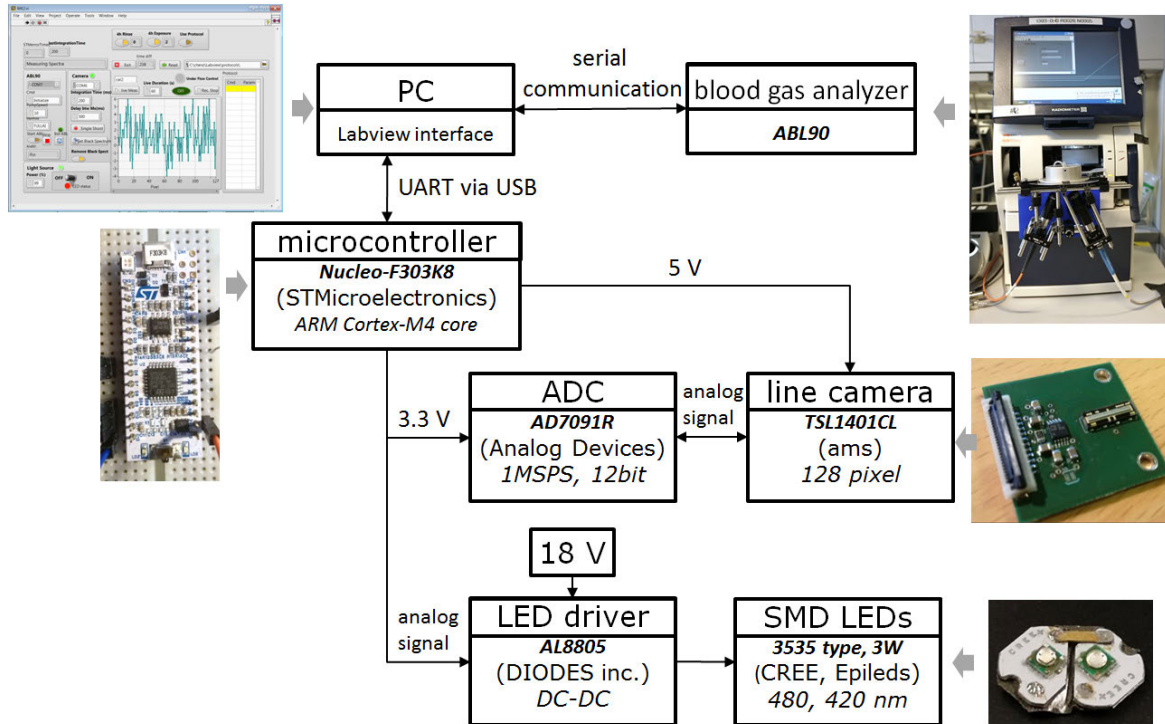


Figure 5.15: System diagram of the electronics and controlling chain of the waveguide sensor system.

- The micro-controller (MCU) is the central part of the waveguide sensor system and provides the interface from outside to the stand-alone waveguide sensor system. A development board (NUCLEO-F303K8) from STMicroelectronics is used to implement the system (see middle left insert of Figure 5.15). NUCLEO-F303K8 carries a ARM® Cortex®-M4 32-bit CPU with max 72 MHz operation frequency and digital signal processor (DSP) instruction. Three digital to analog converters (DAC) are also available. With a unit price of 5-6 US dollar, this MCU system suits well for our needs.

- The communication from the MCU board to PC is accomplished via the embedded ST-LINK/V2-1 programming tool on board, which provides a universal synchronous and asynchronous receiver-transmitter (USART) interface, which is used to address the MCU. Physically it is connected with a micro-USB cable, which also provides the 5 V power supply for the MCU as well as the external analog-to-digital converter (ADC) and the line camera.

- The communication to ABL90 can be done with serial communication via a COM port. The communication protocol is provided by engineers from Radiometer. The

author decided to use an additional PC (later on a laptop) to bridge the MCU and
the PC on ABL90. A Labview software was written to command both MCU and
ABL90 analyzer, which also provides the user interface for operators (see top left
insert of Figure 5.15). Eventually, the MCU can communicate to the on-board PC
of ABL90, where software like Labview can also run. This would simply the control
system and increase the integration level. However, running software on on-board
PC of ABL90 has more restrictions and thus was not implemented during the work.

- The camera control is commanded by the MCU. The analog signal coming from
  the line camera is converted by an external ADC to digital signal and transferred
  back to the MCU. The design of the camera board is shown later in detail.

- The LEDs are driven by a LED driver provided by Sparkfun Inc.(FemtoBuck LED
  Driver). The LED driver provides constant current that can be set by a on-board
  resist and external analog voltage input. The maximum current is set by the
  on-board resists. The current limit for all LEDs (connected serially) was set to be
  330 mA, which is lower than the nominal value given by the LED manufacture.
  This is due to consideration of heat management. At 330 mA, two LEDs will
  generate about 2 W energy, which needs to be dissipated by the heat sink. At 2 W,
  a moderate temperature increase is achieved to about 60°C in steady state. Higher
  power input will lead to more design requirement regarding heat dissipation. In
  addition to the hardware current setting by resist, the LED driver also provides
  adjustable software current setting via a DC voltage input, which will be discussed
  later. A 18 V DC power supply is used to power the LEDs, about 91% conversion
  efficiency can be reached by the DC-DC converter used in the LED driver (AL8805,
  DIODES Inc.). Thus, there is also heat generated in the driver board. This heat
  is managed by taping the driver to the aluminum housing by thermal conductive
  tape.

## 5.4.1  MCU board configuration

The configuration of the STM32F303 MCU is shown in Figure 5.16a. 6 pins are set as
general-purpose input/output (GPIO) ports and 3 as DAC outputs (green labels). The
GPIOs are used to communicate with the ADC and line camera. The DAC is used to
generate an analog voltage to set the current level of the LED driver. A voltage level
between 0.5 V and 2.5 V can set the current output of the LED driver from 25% to 100%
of the maximum. At 100%, 330 mA is fed to the LEDs as mentioned earlier. When the
control voltage is set at 0.5 V, an reduced current of about 82 mA is fed to the LEDs,
which reduces the heat generation. It serves as the stand-by mode.

In Figure 5.16b the connection of the pins of NUCLEO-F303K8 board and the con-
nection cable is shown. The circuit is implemented in a PCB to enable the connection to
the camera board. Here, a 12-wire ribbon cable is used, while, as shown in Figure 5.16b,
wire Nr. 2, 4, and 6 are all grounded. This is to avoid cross-talking the neighboring
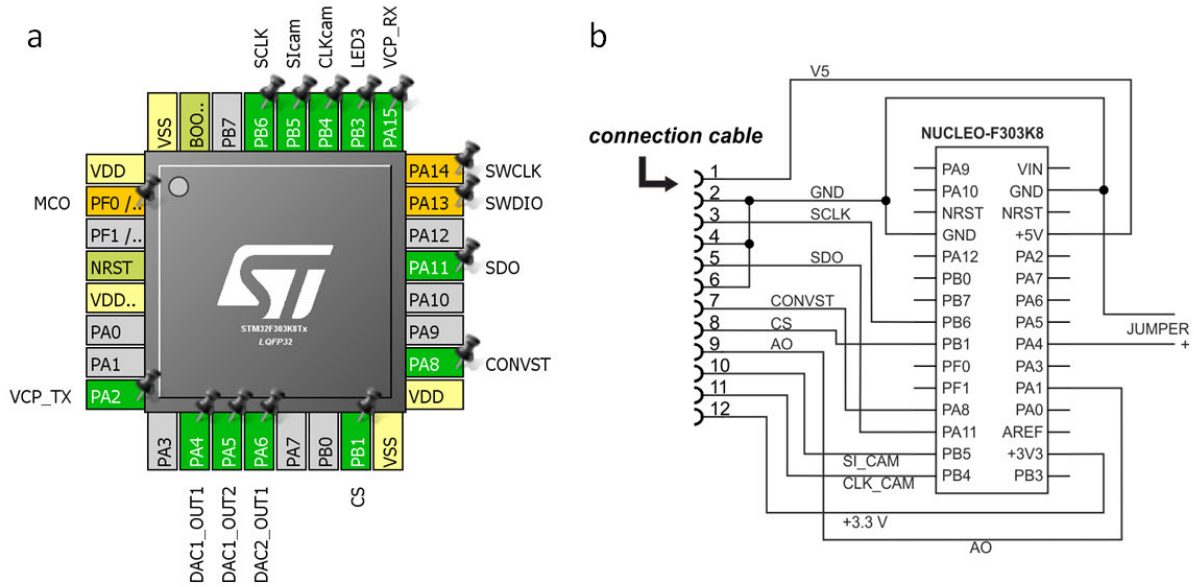
Figure 5.16: (a) Pin-out configuration of the STM32F303 MCU. (b) Electrical circuit of the adaptor board connecting NUCLEO-F303K8 pins to the connection cable.

signals, which could be left out to further reduce the space, since the system operates in a relatively low frequency range. For the final integration space is very limited inside ABL90 analyzer, the cable connector actually occupies the largest space on the board and thus should be optimized at first.

## 5.4.2 Camera board configuration

The camera board hosts the line camera and an ADC, which locally convert the analog signal from the camera to digital signal to be transferred via ribbon cable to the MCU. Consideration are as follows:

- The linear sensor array TSL1401CL from ams AG is used as the line camera. The main reason for choosing this model is because of the low unit price (under 5 US dollar), relatively simple operation and good functionality. It provides 128 pixels with a pixel size of 63.5 µm x 55.5 µm, where 63.5 µm is the width of each pixel and 55.5 µm is length in which direction all pixels are aligned. Thus, a total length of 8 mm is active for recording. Since different wavelengths are out-coupled at different angles, the distance of the camera to the grating couplers needs to be adjusted to span the relevant wavelength range. Here, a distance of 30 mm (from center of the line camera to grating couplers) is designed, which can cover 15° of the out-coupling angle, corresponding to a wavelength range of 400 nm to 500 nm. A closer distance will enable a broader wavelength range.
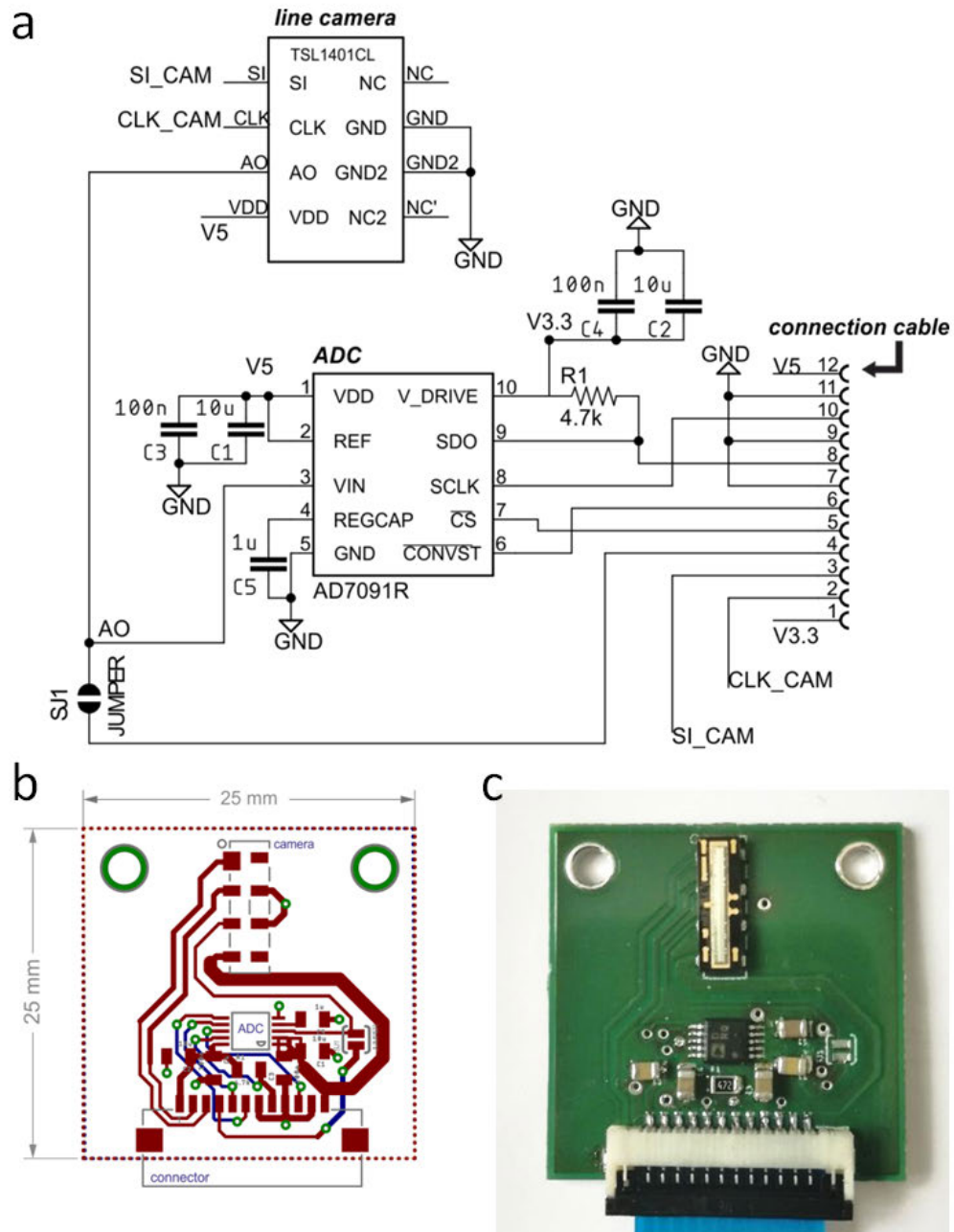
Figure 5.17: (a) Electrical circuit of the camera board carrying the line camera and the ADC. (b) Layout of the camera board. (c) Picture of the PCB after soldering all components

- A 12-bit ADC (AD7091) from ANALOG DEVICES Inc. is used to convert the analog signal to digital. With a unit price of 1.6 US dollar, the ADC is a cost-efficient solution with small space occupation (see Figure 5.17b-c). The reason for using an external ADC on the board is because the flexibility to separate the MCU and camera board. For the final integration, the space is very limited close to the

sensor. Thus, the camera board should be as small as possible and the MCU board should be placed remotely. However, if the distance is too large, the analog signal can gain noise easily due to the cable. Thus, converting the analog signal locally on board is a safe solution. Furthermore, the analog output signal of the line camera saturates at 4.8 V (when it is driven at 5 V like in our case) while the MCU has a conversion range up to 3.6 V for the integrated ADC. To avoid losing dynamic range, the author decided to use an external ADC (AD7091).
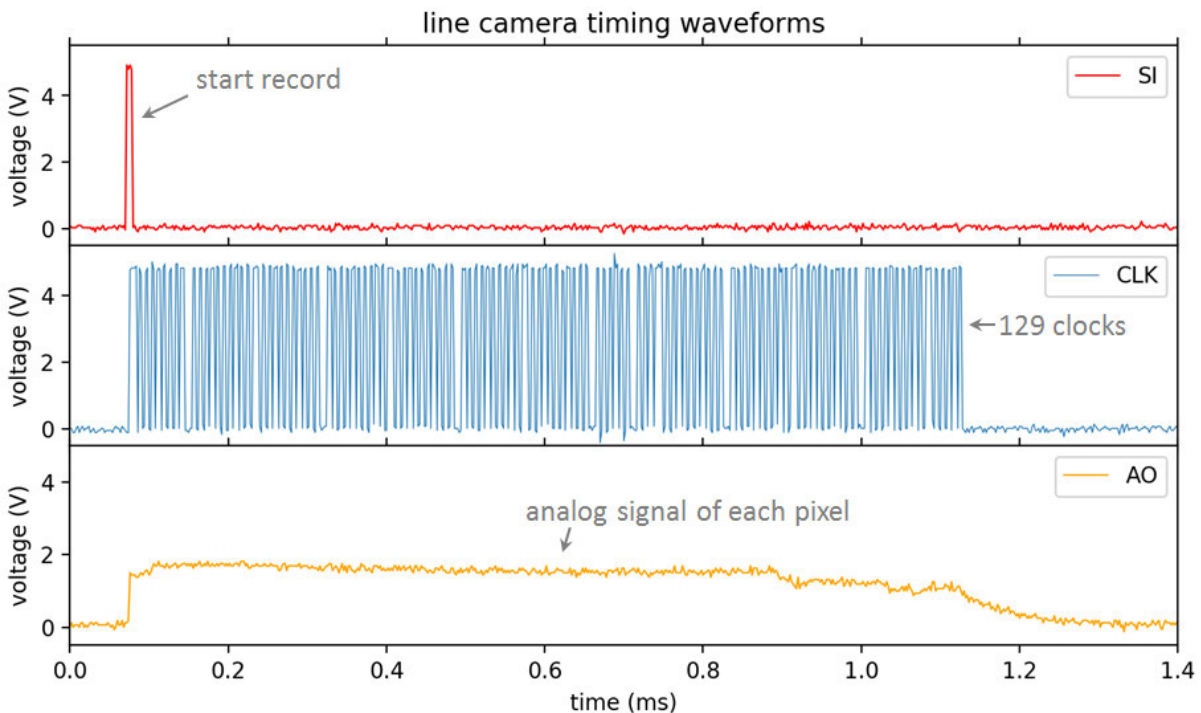


Figure 5.18: Waveform recorded by an oscilloscope for operating the line camera.

**Line camera configuration.** The electrical circuit and the layout for the line camera is shown in Figure 5.17. 5 V DC is used to drive the line camera to gain the largest dynamic range. The analog signal is connected via pin AO to the ADC on-board. An additional solder bridge (when soldered) also allows the analog to be transferred to the MCU through the ribbon cable. The timing waveform is shown in Figure 5.18. After one pulse at pin SI, the analog signal (AO) can be clocked out by signal at CLK. 129 clocks are required to obtain signal from all 128 pixels. The integration time is the same for all pixels and determined from the 19th clock prior to the SI pulse to the rising edge of the SI pulse. In our implementation, to obtain a defined integration time. A dummy interrogation cycle is used, where 129 clocks are quickly applied after a SI pulse, to clock out the indeterminate data that depends on the previous clocking condition. Thereafter, after waiting a certain time, which is given as the integration time (the time for the
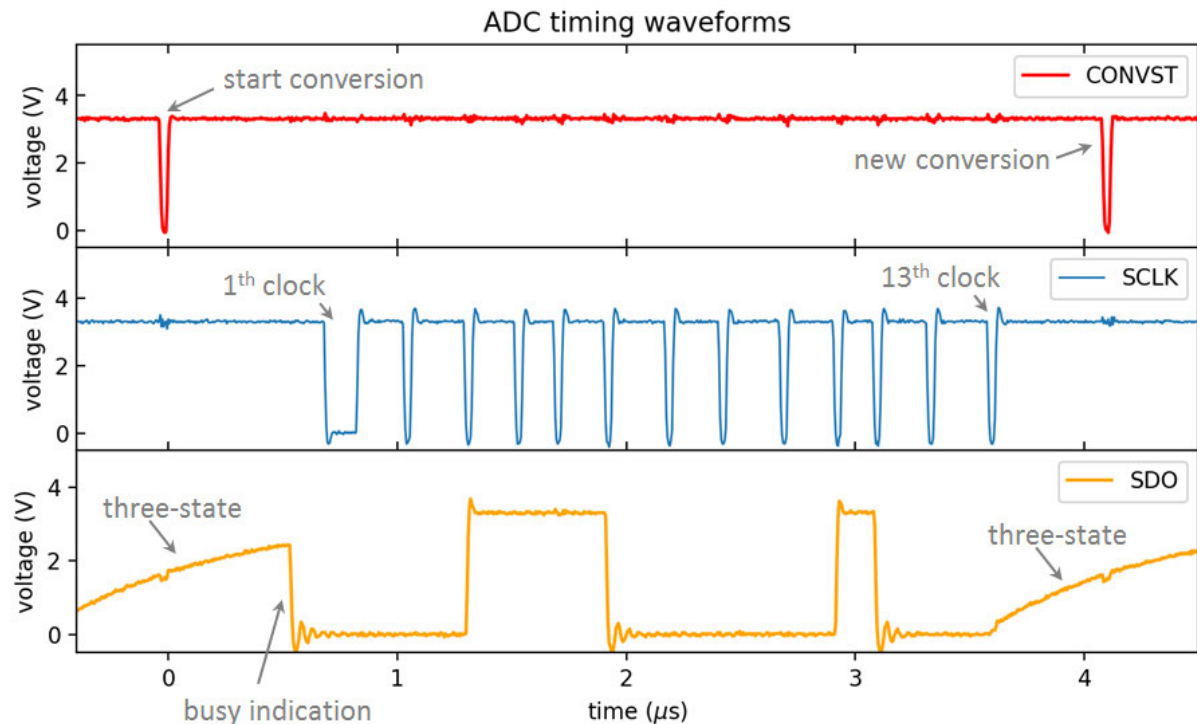
Figure 5.19: Waveform recorded by an oscilloscope for operating the ADC.

previous 110 dummy clocks, which counts as integration time, is also considered), the real signal is taken as shown in Figure 5.18.

**ADC configuration.**   3.3 V DC is used for $V_{DRIVE}$ of the ADC, which determines the operating voltage of the logic inputs and outputs, since the MCU operates at 3.3 V. However, 5 V is used for the power supply $V_{DD}$ and the reference voltage (REF), which makes the analog input range from 0 to 5 V. The timing waveform is shown in Figure 5.19. A conversion is started with a pulse at pin CONVST, followed by an internal conversion time of about 650 ns. After the conversion is finished, the output signal (SDO) will drop to logic zero state from the three-state which is a state between the logic zero and one. This function is used as busy indication. Thus, the falling edge at SDO is examined to determine the finish of the conversion and start the result reading, which is clocked out by 13 clocks (for 12 bits). As we can see in Figure 5.19, the signal shows low and high state at SDO, indicating the digital conversion result. The author remarks that the pull-up resist R1 in Figure 5.17a is very important for the busy indication function. Namely, R1 determines the recovery time for the three-state after the 13$^{th}$ clock. As shown in Figure 5.19, the falling edge after the three-state at 0.5 µs is clear, however, when the R1 is too high, like 100 KΩ suggested in the data-sheet, the recovery time of the three-state (to high voltage state) is very long and thus SDO remains low when the next conversion is initiated. In this case, a false detection of the busy indication can be

caused. The author changed R1 to 4.7 KΩ and there is no issue shown any more for continuous conversions.

## 5.5   Performance

The performance of the waveguide sensor MK2 with the new compact setup is shown in Figure 5.20. In Figure 5.20a, two lasers are used as light source instead of LEDs to examine the signal specificity and calibrate the wavelength projection on the line camera. Both 405 nm and 448 nm laser show good transmission through the waveguide and grating couplers. Importantly, around each signal peak, which is caused by the monochromatic laser light source, there is little noise such as sideband signal, i.e. the waveguide and grating couplers are able to project the spectral information to spatial information (pixel position). Ideally, each laser should only cause signal at one single pixel, given the relative large pixel width of 55 µm; however, in our case, 5 pixels were excited, which of course limits the spectral resolution. Two aspects can contribute to such signal broadening: 1) long grating couplers, which couple light out over a long distance thus causing beam broadening. This can be mitigated by e.g. a focal lens. 2) Surface roughness of the image sensor. The line camera TSL1401CL is encapsulated in a transparent polymer, presumably epoxy. The surface is rough (uneven structures in 10 µm range), which can cause signal contamination. Other image sensors with better encapsulation may also improve the performance like S10226-10 with 1024 pixels (Hamamatsu Photonics) or S10227-10 with 512 pixels (Hamamatsu Photonics), which however have a higher unit price in range of 10-20 US dollar.

Figure 5.20b shows the raw signal at the camera. Rinse liquid was measured at first, followed by the cal2 solution with 450 mg/dL tartrazine dye, which is rinsed away after the measurement. The signal shows clearly two areas representing two LED light sources. In the area around 445 nm between those two LEDs, there is nearly no intensity measured, which is in good agreement with the ray tracing simulation shown in Figure 5.3. Furthermore, a sudden drop can be seen at 470 nm with a small peak at 475 nm. This is attributed to the natural density filter applied on the lens holder, which is intended to damp the maximum signal from the second LED. At the same LED current, the LED at 480 nm generates almost five-fold intensity than that at 415 nm. Thus, the intensities of the two light sources are balanced to avoid saturation. However, a much more elegant solution would be using independent current control for each LED, which is not implemented within this work.

Figure 5.20c shows the absorbance measured with blood plasma, plasma with 100 mg/dL hemoglobin (plasma100), plasma with 100 mg/dL hemoglobin and 20 mg/dL bilirubin (bil.+plasma100), and cal2 (tartrazine 450 mg/dL). For comparison, the reference measurements taken with a photospectrometer are shown in Figure 5.20d. The doted areas in Figure 5.20c indicate regions where the intensity is low and thus high noise is
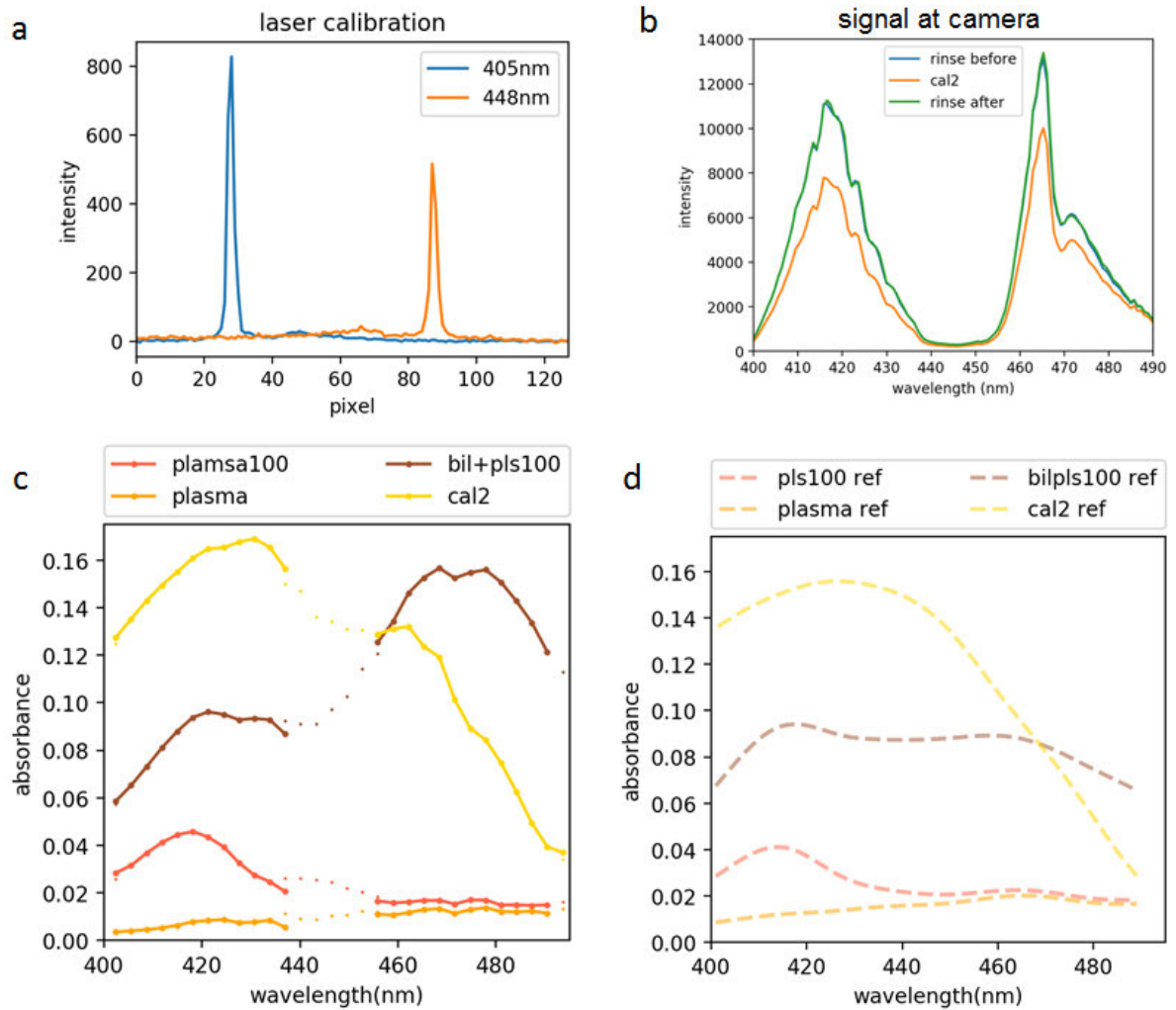
Figure 5.20: (a) Camera intensity when the waveguide is excited with two lasers. (b) Camera intensity measured with two LED as light source (central wavelength: 415 nm and 480 nm ). Signal of rinse and cal2 (tartrazine 450 mg/dL) solutions are shown. Rinse was applied before and after the cal2 measurement (c) Absorbance measured with blood plasma, plasma with 100 mg/dL hemoglobin (plasma100), plasma with 100 mg/dL hemoglobin and 20 mg/dL bilirubin (bil.+plasma100), and cal2 (tartrazine 450 mg/dL). (d) Absorbance measured with a photospectrometer as reference for comparison.

present. In general, line shapes of the MK2 measurements are similar to the reference. The absorption maximum of hemoglobin around 416 nm can be seen clearly in the waveguide measurement. The main difference is the absorption of bilirubin plasma sample at 480 nm. The absorption is much higher than the reference level. The cause is not fully clarified yet while it's suspected that the affinity of bilirubin to albumin plays an important role. The latter is present in high concentration in blood plasma and adheres to surface like polymer.

In conclusion, the performance of the MK2 sensor with the compact setup matches our expectation. The total sensitivity is about 30% to the MK1 sensor demonstrated in Paper I, while the optical length is only 13% of the previous version, i.e. the sensitivity per unit length is more than doubled in the MK2 version, which is mainly attributed to the waveguide thickness reduction from 220 nm to 140 nm. The filtering function and longterm stability are very close the MK1 sensor. The setup has also shown stable performance after being handed over to Radiometer.

# CHAPTER 6

# Results and Discussion

## 6.1  Summary of Paper I

In this work, an optofluidic sensor for inline detection of hemolysis on whole blood is demonstrated. Currently, there is no method to detect hemolysis in a fast and reliable way since the separation of red blood cells and plasma require time-consuming procedure such as centrifugation. The major innovations presented in this paper are as follows:
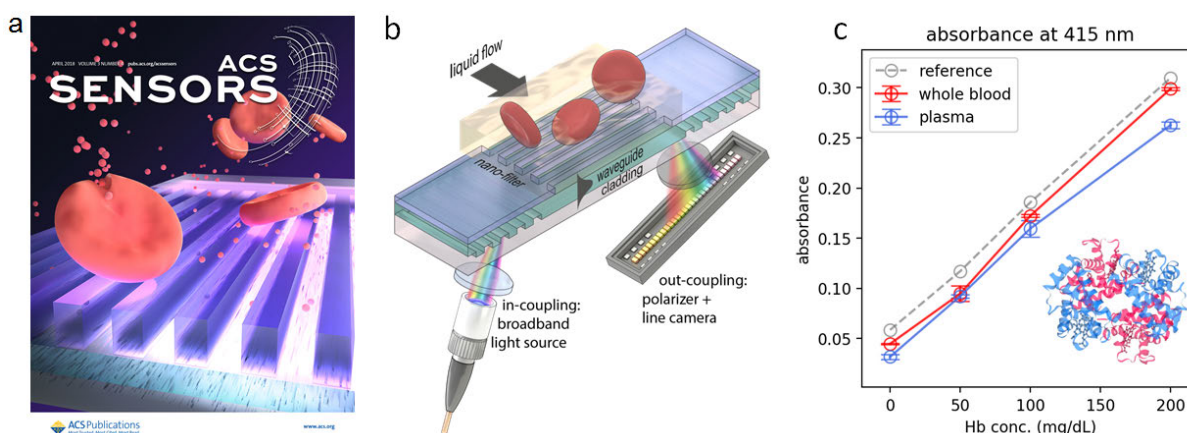


Figure 6.1: (a) The illustration of the sensor as the cover of the journal. Nano-filters block the red blood cells that are larger than the opening of the filters. (b) Optical setup of the sensor. Light is in-coupled from a fiber port with focusing lenses. Out-coupled light is evaluated by a line camera for spectral information. (c) Absorbance value of whole blood and plasma at 415 nm measured with the waveguide sensor. Reference measurements with photospectrometer are shown.

- Demonstration of a single-mode optical slab waveguide made of organic-inorganic hybrid polymer. Grating couplers are defined to enable in- and out-coupling of light. The fabrication is low-cost and suitable for industrial up-scaling.

- Innovative design of nano-ridge array on top of the waveguide, which provides additional local-filtering capability and doesn't compromise the the waveguiding property. The nano-filters can be chosen freely to match the size of the content to

be filtered. An illustration of the filtering principle is shown with the cover image selected by the journal in Figure 6.1a.

- Spectral analysis of the out-coupled light after the waveguide is accomplished with a line camera. The dispersion caused by gratings is evaluated by spatial information on the line camera. Thus, no additional spectrometer is required. Figure 6.1b shows the illustration of the setup.

- Testing of whole blood and blood plasma demonstrates the capability of filtering as well as the linearity of absorbance in the relevant hemolysis range(up to 200 mg/dL hemoglobin concentration), as shown in Figure 6.1c.

- Interference in blood plasma like bilirubin, which absorbs in the same wavelength range, can be distinguished by spectral analysis algorithm. A signal bias of 10% is shown with the presence of high concentration of bilirubin, which can be corrected when the bilirubin value from ABL90 blood gas analyzer is utilized.

- A detection limit under 5 mg/dL (0.05 g/L) hemoglobin is shown for whole blood hemolysis detection, which suffices the initial requirement of the project.

- Requirement on sample volume (<65 µL) is fulfilled with large budget. Detection time of 10 seconds, turn-around time 60 seconds, and sensor lifetime over a month are presented, which all fulfill the requirement of the project.

## 6.1.1   Further discussion

Here, some additional aspects will be discussed, of which some are requested by the reviewers of the paper during the publication process.

- The material usage cost for each single sensor would be less than 1 € in large production number. Since the process is based on nano-imprint lithography, the other major cost of the stamp fabrication through e-beam lithography. However, as one master stamp can be used thousands of times, the e-beam cost (3000 €) for each sensor would be around 0.06 € (assuming 1000 times imprint and 50 sensors per imprint). We are aware that the more cost is hidden in the production such as plasma treatment, stamp replication, and molecular coating. However, the estimation here demonstrates the essential costs and the potential for high volume fabrication of the sensor. Further optimization can also be envisaged to reduce the unit price of the sensor. Reducing the footprint of sensor can easily yield 500 sensors per wafer. Moreover, as the sensors are able to be peel-off from the wafer for packaging. The glass wafer can be potentially recycled, which reduces a large part of the cost raised in the fabrication.

- The temperature is also important for the sensor. A temperature change will induce change of the refractive indices of the polymers, which will change the coupling angle of grating couplers. It will cause a shift in the transmission spectra

| Cost items | per wafer (EUR) | per sensor (EUR) |
|---|---|---|
| glass wafer | 30 | 0.6 |
| polymer and solvent | 6 | 0.12 |
| E-beam cost | 3 | 0.06 |
| total cost | 39 | 0.78 |

Table 6.1: Cost estimation of the sensor fabrication. It's assumed that 50 sensors are carried per wafer.

on the line camera, which can be however compensated by algorithm. Nevertheless, maintaining the temperature is important for consistent measurement results. In the commercial version of ABL90 FELX blood gas analyzer from Radiometer, the sensors are kept at 37°C, which will also benefit our sensor performance.

- Hemoglobin in blood can have different forms: oxyhemoglobin, deoxyhemoglobin, carboxyhemoglobin, and methemoglobin and they all have different absorption spectra[96]. However, in normal cases when fresh blood sample from human or bovine are extracted and has contact to air, most of the free hemoglobin is in the oxygenated form[64]. Thus, for all analysis, the oxyhemoglobin spectrum is used.

## 6.2   Summary of Paper II

In this work, an optofluidic waveguide Young interferometer is demonstarted, which is composed of a sensing waveguide with nano-filters on top and a reference waveguide, as illustrated in Figure 6.2a. The major innovations are considered to be as follows:

- A highly compact Young interferometer is presented with grating couplers for light coupling. In comparison to butt or endfire coupling, where the waveguide has to be cut for coupling from the cross-section. The grating couplers enable 2D parallelization of the sensors on a single substrate, which can potentially be used as the bottom of a microtiter plate.

- Simultaneous detection of liquid refraction and absorption in the visible wavelength range is demonstrated. The refraction is measured with the phase shift of the interferogram while the absorption is measured with the attenuation of the signal. The detection of bulk refractive index change shows a limit of detection in $10^{-5}$.

- The nano-filters on top of the sensing waveguide enable size dependent exclusion of particles and impurities from the liquid. Nano-beads from 100 nm to 500 nm are
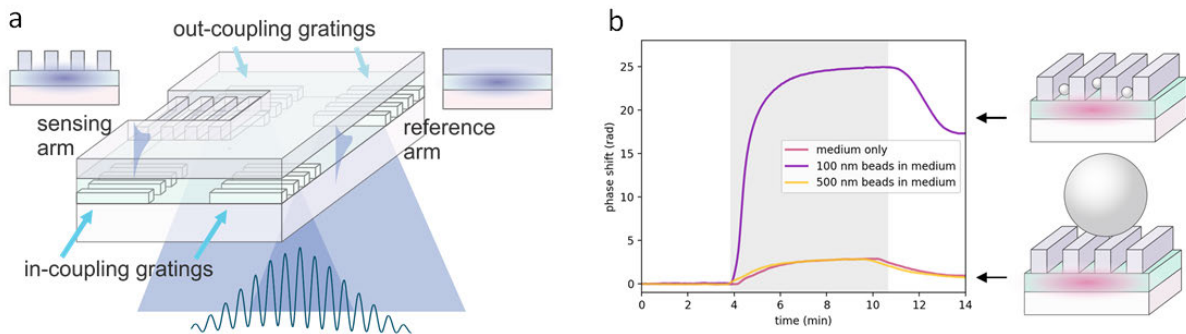
Figure 6.2: (a) Illustration of the waveguide interferometer. A sensing and a reference waveguide are placed beside each other. A sensing window with nano-filters is exposed to the liquid. The guided light in both waveguides is out-coupled and generates an interference pattern on the line camera. (b) Time-resolved phase shifts measured with contact to nano-beads suspensions. 100 and 500 nm polystyrene beads were used, where a strong reaction in phase shift is observed with 100 nm beads. The original medium is isolated by centrifugation and measured as well. Little difference is shown between the original medium and the 500 nm beads suspension due to the size exclusion function.

measured for their contribution to the liquid refractive index. Figure 6.2b shows the results of the measurement.

- Fluorescent excitation is demonstrated with size-exclusive feature. Fluorescent nano-beads from 100 nm to 500 nm

The results of the work provide valuable guidelines for designing optical sensors dealing with complex turbid media especially in PoC applications.

# Conclusion

In this thesis, different waveguide sensors are developed for PoC applications.

A hemolysis waveguide sensor is demonstrated for fast and reliable hemolysis detection. The sensor shows capability of working with whole blood with no requirement of additional sample preparation like centrifugation. The innovative nano-filter on top of the waveguide enables local blocking of species out of the evanescent field and allows independent choice of light wavelength and filtration size. It is shown that a spectrometer-less analysis of spectral extinction of molecules can be successfully achieved by employing out-coupling gratings as a dispersive element and a line camera for readout. it is further demonstrated that the portable optical setup is capable of being integrated into a commercial blood gas analyzer (ABL90, Radiometer Medical ApS, Denmark). Tiny sample volume (65 µL) is required. Fast measurement time (< 10 s) as well as fast turn-around time (<1 min) is demonstrated. Long-term tests up to 7 weeks were also carried out to demonstrate the high repeatability and reliability of the hemolysis sensor measuring whole blood samples even with the presence of strong interference from bilirubin.

For the next stage of sensor integration, a second generation of the hemolysis sensor was developed with smaller sensor footprint and broader bandwidth of detection. The final sensors are cut into flexible membrane and packaged into individual devices with liquid interfaces. A tailored setup was designed and fabricated with fully stand-alone electronic control, which allows fully automated operation of hemolysis detection together with an ABL90 blood gas analyzer. The cost of all components in the setup is also minimized to demonstrate the potential of commercial up-scaling of the product.

Furthermore, methods and techniques developed during the hemolysis sensor have also leaded to further innovations. Nano-structure transfer method is demonstrated by nano-imprint lithography. The residue-free imprint method is utilized to make low-cost copies of expensive E-beam written imprint stamps. A reliable, low-cost, and large-scale pattern transfer method was shown for master origination targeting at plasmonic color generation and meta-surface applications.

Moreover, a multi-functional waveguide interferometer sensor is demonstrated with the size-exclusion technology developed for hemolysis detection. Here, an integrated optical Young interferometer is developed for sensing both refraction and absorption of a liquid sample. The refraction is determined by the phase shift of the interferogram while

the absorption is measured by the signal attenuation. Nano-filters are integrated to the sensing waveguide so that size-exclusive detection can be demonstrated. Nano-beads of different diameters (100 nm to 500 nm) are measured by phase shift as well as fluorescent emission.

# 7.1   Outlook

The hemolysis sensor has been demonstrated to a high stage of development. Nevertheless, there are some points require further improvement and investigation:

- The signal measured with MK2 sensor with the integrated setup has more noise in the spectra than MK1. The absorbance spectrum shows harmonics which has to be filtered. The author considers the line camera sensor can be the cause of those harmonics. Better variations should be tested such as S10226-10 with 1024 pixels (Hamamatsu Photonics) or S10227-10 with 512 pixels (Hamamatsu Photonics).

- Better configuration of LED light source is needed. A narrow arrangement of the SMD LEDs can generate smaller angle spread, which is desired for seamless broadband coupling. Furthermore, individual control of the LEDs is needed. Since the quantum efficiency varies a lot for LEDs at different wavelength, different forward currents are needed for different LEDs so that the intensities can be balanced to avoid saturation.

- The elevated sensitivity of bilirubin with the second LED at 480 nm needs more investigation, ideally by seamless broadband coupling. Furthermore, signal drop with the 480 nm LED has been observed during the long-term test at Radiometer. The reason can be the bandwidth supported by the thin waveguide. The sensor is only 140 nm thick, which may cut off the high wavelength above 500 nm.

The master origination method by nano-imprint lithography can be further exploited for more specific applications:

- New resists can be tested for pattern transfer method. Here, OrmoComp polymer is used for pattern transfer due to its good adhesion to Si substrate and its compatibility to OrmoStamp in the stamp release process. However, it is not the only feasible candidate. When other pure organic resists are investigated for dilution and spin-coating thickness, they could replace OrmoComp. The advantage of pure organic resist lies mainly in the removal step, where, unlike OrmoComp, they can be cleaned with oxygen plasma with ease.

- Different etching recipes can be used to yield different dot diameters, which can be used to generate different plasmonic color.

- Further modifications like oxidation of the nano-holes can also yield different diameters, which can be utilized to generate more sophisticated patterns.

The Young interferometer sensor can also be further developed and exploited as follows:

- Surface fictionalization can be envisaged to enable binding of e.g. protein, extracellular vesicles. Size exclusion can be used to further amplify the specificity of the detection and eventually study the size distribution of the particles.

- Assays can be developed to enable unique detection capability. For instance, drug dissolution dynamics can be studied by the interferometer.

- Embedding the sensors to a microtiter plate can enable a sensing platform with unique multi-functionality.

# Appendix

## A.1 Paper I

# Optofluidic Sensor for Inline Hemolysis Detection on Whole Blood

Chen Zhou,[†] Mehdi Keshavarz Hedayati,[†] Xiaolong Zhu,[†] Frank Nielsen,[‡] Uriel Levy,[¶] and Anders Kristensen*,[†]

[†]Department of Micro- and Nanotechnology, Technical University of Denmark, DK-2800 Kongens Lyngby, Denmark
[‡]Radiometer Medical ApS. DK-2700 Brønshøj, Denmark
[¶]Department of Applied Physics, Hebrew University of Jerusalem, Jerusalem, Israel

**S** *Supporting Information*

**ABSTRACT:** Hemolysis is the rupture of red blood cells and constitutes the most common reason for unsuitable blood samples in the clinic. To detect hemolysis, one has to separate the hemoglobin in blood plasma from that in red blood cells. However, current methods entail centrifugation for cell-plasma separation, which is complex, time-consuming, and not easy to integrate into point-of-care (PoC) systems. Here, we demonstrate an optofluidic sensor composed of nanofilters on an optical waveguide, which enables evanescent-wave absorption measurement of hemoglobin in plasma with the capability of real-time inline detection on whole blood without extra sample preparation like centrifugation. Long-term testing with inline integration in a modified, commercial blood gas analyzer shows high reliability and repeatability of the measurements even with the presence of interference from bilirubin. We envision that the present work has large potential in improving diagnosis quality by enabling PoC hemolysis detection in blood gas analyzers and can also lend unique sensing capabilities to other applications dealing with complex turbid media.

**KEYWORDS:** hemolysis sensor, Point-of-Care, whole blood, optofluidics, nanowells, waveguide sensor, nanoimprint, in vitro diagnostics
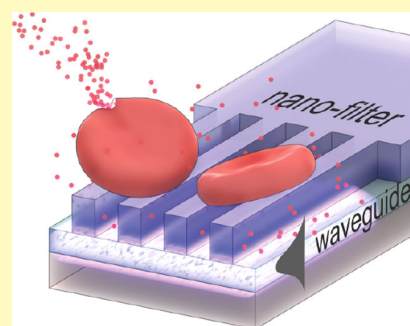
Hemolysis is the rupture of the red blood cells (RBCs) and the release of their contents into blood plasma.[1] It is the largest preanalytical error source in health care facilities and clinical laboratories around the world, accounting for 39−69% of all the unsuitable samples—about five times higher than the second leading cause.[2] Hemolysis can originate from both *in vivo* conditions, such as sickle cell disease and infections, as well as *in vitro* conditions, such as traumatic blood draw and sample mishandling; the possibility of both occurring complicates identification of the source of hemolysis. Furthermore, the presence of hemolysis interferes with the detection of important vital parameters like $K^+$ and $Ca^+$ concentration in the blood.[1] In other situations like cardiac surgery undergoing cardiopulmonary bypass (CPB), hemolysis is nearly ubiquitous,[3] eventually causing acute kidney injury.[4] The state-of-the-art hemolysis detection protocols require centrifugation steps to separate blood plasma and cells, which is time-consuming, resource demanding, and prone to cause additional preanalytical errors. Centrifugation protocols are not easy to integrate into PoC platforms.

In this paper, we present a PoC hemolysis sensor combining evanescent absorption detection and local plasma separation without the need of any sample preparation. The plasma separation is achieved with an integrated nanofilter comprising an array of nanowells. So far, waveguide absorption spectroscopy has been demonstrated for sensing pH value,[5] protein,[6−9] and molecules.[10−15] Separation of blood plasma and RBCs is achieved by either active methods, such as magnetic,[16,17] dielectrophoretic,[18,19] and acoustic,[20,21] or passive methods, such as hydrodynamic,[22−24] sedimentation,[25,26] and filtration.[27−30] Our optofluidic strategy is based on an innovative dual function of nanofilters that act as a component of the waveguide as well as a functional filter for RBCs. The nanofilters enable light propagation without diffraction and scattering while effectively blocking cells or platelets with short diffusion length and time, as shown schematically in Figure 1a. Grating couplers are integrated to couple broadband LED light into—and spectrally disperse light out of—the waveguide sensor, enabling spectral analysis without using an extra spectrometer or monochromator. The wavelength range of the LED light source is adjusted to the highest optical absorption of Hb, as shown in Figure 1b (highlighted area). The absorbance measured with the optofluidic sensor is compared with photospectrometer reference data. The sensor was integrated into a modified, commercial blood gas analyzer (ABL90 FLEX, Radiometer Medical ApS, Denmark), as shown in Figure 1c, to assess its repeatability, reliability, and durability.

## ■ RESULTS AND DISCUSSION

**Sensor Design and Optical Simulation.** The sensor is designed to have dual-function: a waveguide and a filter for RBCs. The waveguide is made by the assembly of a cladding
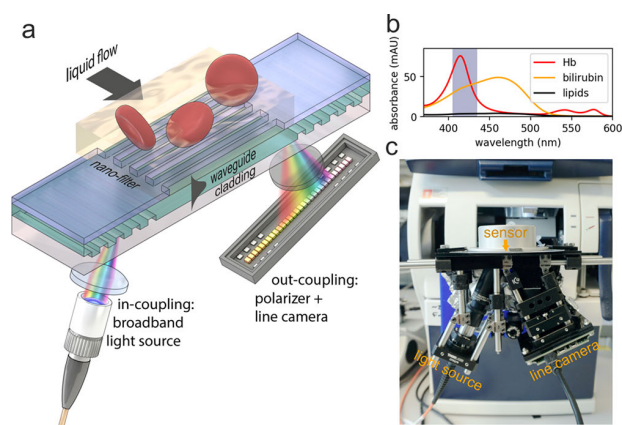
**Figure 1.** (a) Illustration of the hemolysis sensor comprising waveguide, cladding, and nanofilter for cell/plasma separation. Gratings functioning as dispersive element enable spectral analysis with a line camera as readout. (b) Reference absorption spectra of main components in blood plasma: Hb, bilirubin, and lipids. The wavelength of LED light used is highlighted at the background. (c) Portable setup attached to a state-of-the-art blood gas analyzer for automated measurements.

layer, a waveguide core layer, and a structured top layer for filtering. To effectively and reliably eliminate the absorption from the RBCs (smallest feature size of about 1−2 $\mu$m), these nanofilters have a pitch width of 400 nm and an opening of 200 nm for blood plasma/light interaction. Only species smaller than the size of the filter opening are allowed to diffuse downward and thus interact with the guided light, as illustrated

in Figure 2a. The small dimension prevents cells clogging the filter. The nanofilters are aligned parallel to the light propagation direction without interruption to enable the wave propagation without diffraction and scattering. The cladding layer on top of grating couplers is not structured in order to prevent coupling conditions being influenced by changes of refractive index (RI) in the liquid sample. According to Lambert−Beer's law, we determined the sensitivity $S$ in our system with relation to other parameters of the sensor as follows (derivation in Supporting Information)

$$S = \eta \varepsilon l \tag{1}$$

where $\eta$ denotes the mode-field overlap with the analyte.[31] $\eta$ is defined as the energy ratio of the evanescent field interacting with the liquid to the total energy flow. $\varepsilon$ is the extinction coefficient of the detection target; $l$ the length of the light/ sample interaction. If the length of the sensor is fixed by a given specification, the mode-field overlap becomes the major optimization parameter. Mode analysis was performed using COMSOL Multiphysics to optimize the mode-field overlap and thus the sensitivity (rf. Materials and Methods). Mode analysis of the fabricated ridge waveguide is shown in Figure 2b, where transverse electric (TE) and transverse magnetic (TM) modes indicate horizontal and vertical electrical field distribution, respectively. In this configuration, the TM mode shows higher mode-field overlap than the TE mode, as Figure 2b (right panel) depicts. The height of the filter and the thickness of the waveguide were swept in simulation for sensitivity optimization. In Figure 2c, the mode-field overlap ratio of the TE mode is plotted. With decreasing waveguide thickness, the overlap ratio increases because of less confinement. On the other hand, with larger thickness, the waveguide supports the guiding of higher-
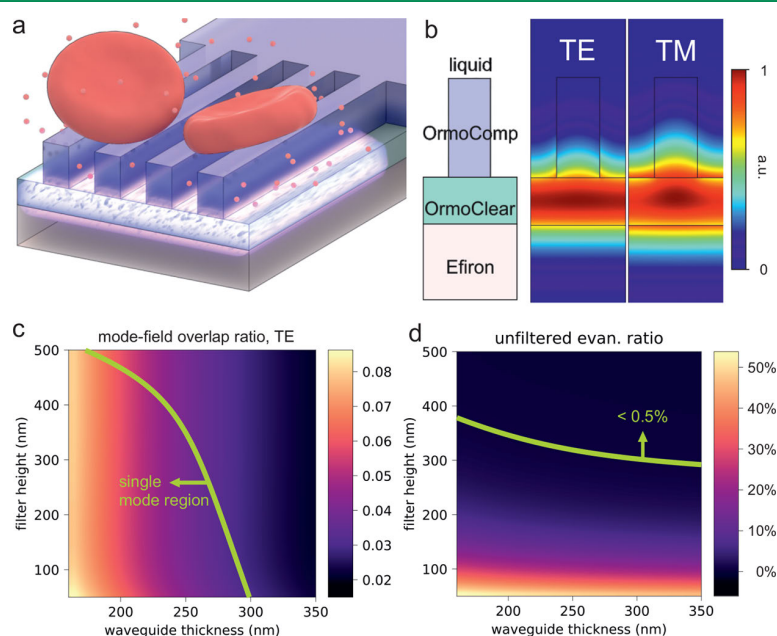


**Figure 2.** (a) Illustration of the working principle of the waveguide sensor with nanofilters. Large components in blood like cells and platelets are blocked out of the evanescent field of the waveguide. Small molecules like Hb are measured with evanescent absorption spectroscopically. (b) Mode analysis simulation (electrical field norm) of the fabricated waveguide. Different waveguide layers are illustrated on the left; TE and TM polarizations are shown with their field distribution on the right. (c) Evanescent overlap ratio with TE polarization for varying filter height (OrmoComp) and waveguide thickness (OrmoClear), revealing different sensitivities. The desired region with single mode operation is highlighted. (d) Ratio of the evanescent energy distributed outside the filter range is plotted agaisnt filter height (OrmoComp) and waveguide thickness (OrmoClear). The desired region with <0.5% is highlighted.
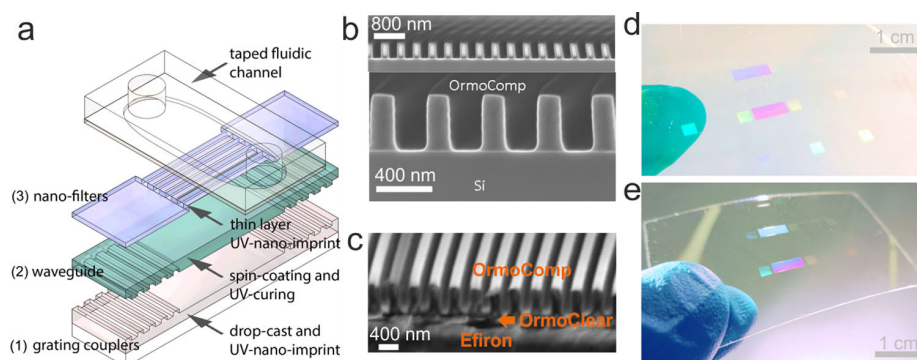
**Figure 3.** (a) Illustration of the fabrication steps of the sensor utilizing multiple UV-nanoimprint steps. Fluidic channel is easily defined with taped channels. (b) Cross-sectional SEM images of nanofilters fabricated on Si in which the filter height and width can be seen on the bottom panel. The high uniformity is shown on the top panel. (c) Cross-sectional SEM images of the fabricated waveguide with OrmoComp as filters, OrmoClear as waveguide, and Efiron as cladding. (d) Fabricated sensor on a glass wafer. (e) Fabricated sensor on a free-standing membrane.
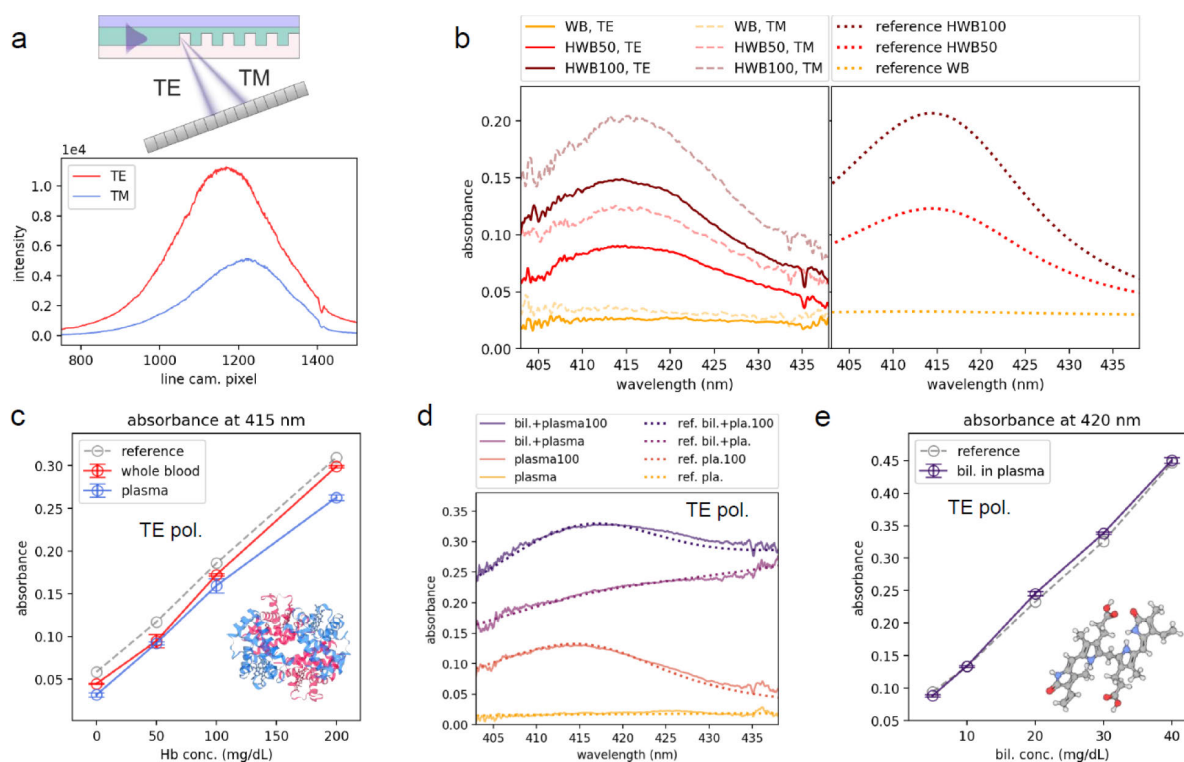


**Figure 4.** (a) Projection of TE and TM mode on the line camera. (b) Absorption spectra measured with whole blood (WB) and hemolyzed whole blood (HWB, 50 and 100 mg/dL) samples with TE and TM modes (left). The photospectrometer reference measurements taken with 1 cm cuvettes are show on the right. (c) Measurements of different Hb concentrations in whole blood and plasma. The photospectrometer reference spectra are scaled and plotted at the background. (d) Absorption spectra of plasma, plasma with 100 mg/dL Hb and their bilirubin-interfered (20 mg/dL) counterparts. (e) Absorption measured with different concentrations of bilirubin mixed into nonhemolyzed plasma.

order modes. The border where the first order mode occurs is marked in Figure 2c. The higher order modes were excluded for their leaky behavior which would compromise data analysis.

The height of the filters plays an important role in filtration of the RBCs. The area above the filters can be accessed by RBCs causing nonspecific absorption, and must be minimized. Figure 2d shows the unfiltered ratio which is defined as the proportion of the propagating mode energy flow above the filter to the corresponding total energy flow in the liquid. 0.5% is set to be the threshold, which is derived from the desired Hb detection limit of 20 mg/dL and the Hb concentration in RBCs

of about 3600 mg/dL. The dividing line shown in Figure 2d marks the 0.5% limit. The waveguide thickness of 180 nm and the filter height of 400 nm were chosen to compromise high sensitivity and reliable filtration. Our fabricated device (filter height 420 nm, filter width 180 nm, waveguide thickness 190 nm) fairly matches the designed values from the simulation, in which case the mode-field overlap ratio, $\eta$ is 7.0% (TM) and 6.0% (TE), and a unfiltered ratio is lower than 0.5%.

The grating couplers have a periodicity of 368 nm to enable the coupling of broadband light with wavelengths between 405 and 435 nm into the waveguide at an incidence angle of 20−

28°. There is no lateral confinement in the waveguide, whereas a width of 2 mm is designed for the grating couplers and the filters. The large dimension is chosen deliberately in order to use commercial LEDs as a light source, which provides broadband illumination and a large focal spot size. Here, the broadband light is coupled with different incident angles. For a 30 nm bandwidth centered at 420 nm, an incident angle range of 5.8° is needed to couple the light in, leading to a very low numerical aperture (i.e., 0.05). The focus is strongly limited because of the high beam divergence of the commercial available LED light source. To harvest the maximal energy of the light source, the angles are matched for coupling with a single convex lens and the beam size is controlled to be several millimeters. Note that multilayer gratings can increase the broadband coupling efficiency;[9] however, it leads to higher costs and complexity during fabrication.

**Sensor Fabrication and System Integration.** The sensor is fabricated in multiple nanoimprint steps that provide a sub-200 nm resolution with up-scalable production capacity. Figure 3a shows the entire fabrication sequence. At first, a drop-cast polymer (Efiron, Luvantix, South Korea) is imprinted with UV-curing to define the grating couplers. A second layer (OrmoClear H101, micro resist technology GmbH, Germany) is then spin-coated on top to serve as the core of the waveguide. The final layer featuring the nanofilters (OrmoComp, micro resist technology GmbH, Germany) is also fabricated with UV-nanoimprint using an organic–inorganic hybrid polymer stamp (OrmoStamp, micro resist technology GmbH, Germany). With the methods developed here, we successfully demonstrated (i) large scale structural homogeneity up to 6 × 2 mm², (ii) sub-200 nm resolution with an aspect ratio (AR) of 2.5, (iii) very low imprint residual left to the layer underneath, (iv) very low cost per device, and (v) nearly 100% fabrication yield. The imprint residual—the thin layer of polymer left on the supporting substrate after the imprint[32]—must be minimized because it directly decreases the sensitivity. This is achieved by introducing an organic–inorganic hybrid polymer mold replicated from an E-beam written Si stamp. Demonstrations of the imprinted nanofilters on a Si substrate and on a waveguide are shown in Figure 3b and c, respectively, where the imprint residual layer thickness is below 20 nm. The combination of the materials allows the final device to be flexible and detachable, as the sensor can be simply peeled off the glass substrate. The detached, free-standing, and flexible membrane can be cut into individual sensors, as shown in Figure 3d and e. This flexibility grants the unique capability of one-step integration into an existing platforms such as a sensor cassette containing other sensors. In comparison with other highly sensitive evanescent sensors,[33−38] our sensor can achieve very short turnaround time (<60 s) with high specificity toward Hb in blood plasma. It can measure blood samples with a variable hematocrit (e.g., from 0% to 45%) and is insusceptible to any cell clogging. The separation is immediate and invulnerable to varying flow rate caused by peristaltic pumping, which is hard to achieve by any microfluidic separation methods.[21−24]

**Sensor Performance.** Using the output grating coupler as the dispersive element, different wavelengths can be resolved from a waveguide by a line camera, as demonstrated by Mendes et al.[9] The use of a single mode waveguide is important because higher order modes can contaminate the spectrum due to the different out-coupling angles of these modes. In this work, we used a linear polarizer to distinguish the TE and TM polarized

light because there is around 2° difference when they are coupled out of the waveguide. As shown in Figure 4a, the peaks in the spectra of these two modes deviate in position on the camera. In the present configuration, both TE and TM modes are excited by the wide-angle in-coupling. The spectrum on the camera is determined with two lasers with different wavelengths (details in Supporting Information). To compare with reference absorption measurements with a photospectrometer, the spectral sensitivities of the waveguide were taken into account to correct the line shapes.

We tested the sensor with whole blood (WB), both human and bovine. The left panel of Figure 4b shows the absorption spectra of WB and hemolyzed whole blood (HWB) spiked with 50 and 100 mg/dL Hb. The concentration of 100 mg/dL is an important threshold as it causes about +7% and −24% interference in clinically relevant $K^+$ and total bilirubin concentration in the blood, respectively.[39] These limits are also close to the values of the allowable errors recommended by Clinical Laboratory Improvement Amendments.[40] As shown in Figure 4b, the difference between 0, 50, and 100 mg/dL is highly distinctive in both TE and TM polarized incidences, which confirms that the sensitivity is sufficiently high. The maximum of the absorption is visible at 415 nm, in good agreement with the line shape of the photospectrometer reference measurements shown on the right panel.

Figure 4c shows the measurements of WB samples (red line) and their plasma counterparts (blue line) as well as the photospectrometer reference measurements with 1 cm cuvettes (gray dashed line), where the latter is scaled in amplitude for comparison. The maximum Hb concentration used is 200 mg/dL, which corresponds to about 0.7% hemolysis—close to the level recommended by European Directorate for the Quality of Medicines (EDQM) for maximum acceptable level of hemolysis in blood products for transfusion.[41] Each data point is based on three measurements. At 0 and 100 mg/dL Hb concentrations, the coefficients of variation (CoV) are 1.65% and 0.86%, respectively, showing excellent repeatability of the sensor. Although for the clinical use the hemolysis level from 0 to 200 mg/dL is the most interesting range, the present sensor can perform in larger extent ranging from 0 to 1000 mg/dL. On the other hand, comparing the whole blood and plasma measurements, we observed very good overlaps which shows that filtration is highly effective. The absorbance of the WB samples is slightly higher than that of the plasma, which can be attributed to the unspecific scattering of the light which can be absorbed by RBCs in the bulk.

In field applications, however, whole blood can be more complex than just hemoglobin in free plasma. There, the presence of bilirubin is a main source of interference. We examined the interference by adding high concentration of bilirubin into the hemolyzed and nonhemolyzed plasma samples. 20 mg/dL (corresponding to 340 mmol/L) bilirubin was added, which is a threshold for neonatal hyper-bilirubinaemia that can lead to neurological dysfunction.[42] As Figure 4d shows, the bilirubin addition increases the absorption for both the sensor and reference measurements. However, the exact amount of Hb and bilirubin can be determined by multivariate regression with the reference spectra. The addition of high concentration bilirubin can increase the overall sensitivity by 18%, which is consistent throughout the measurements over long period and thus can be calibrated. The sensitivity shift is caused by two factors: first, the large difference in molecular weight of Hb and bilirubin, which are
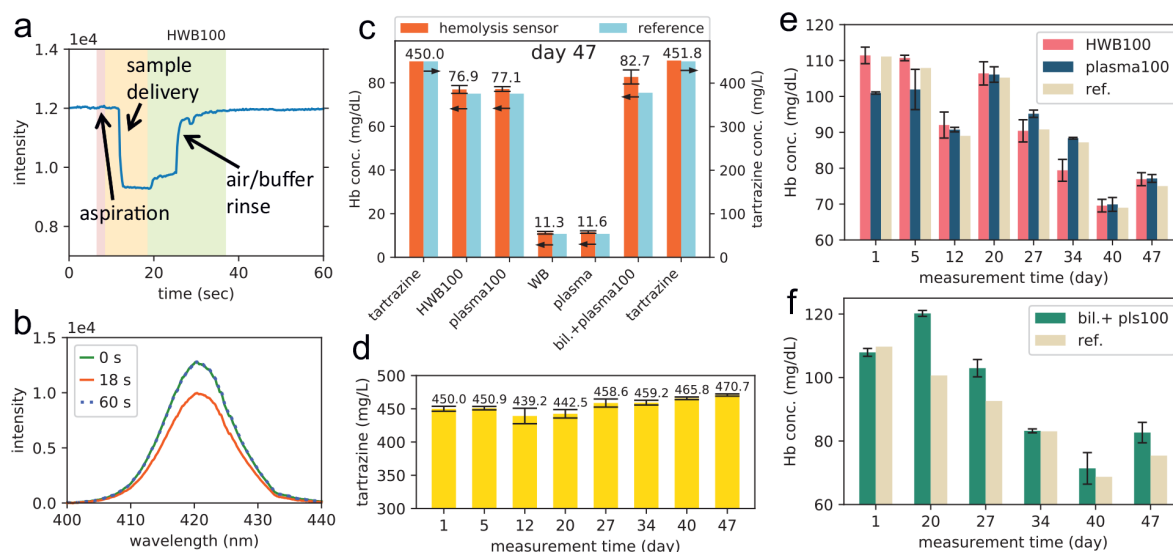
**Figure 5.** (a) Time-resolved absorption signal at 420 nm wavelength for measurement of hemolyzed whole blood (HWB) with 100 mg/dL Hb. Different sections of the measurements are highlighted and annotated. (b) Spectral information during a measurement for buffer signal at 0 and 60 s and HWB at 18 s. (c) Measurement protocol on 47th measurement day. The values from our sensor are annotated on top and to be compared with references. (d) Sensitivity development with tartrazine calibration liquid for 47 days. (e) Comparison of hemolyzed whole blood (Hb 100 mg/dL, HWB100) and their plasma counterparts (plasma100) together with reference values.(f) Comparison of hemolyzed whole blood (100 mg/dL Hb) with bilirubin addition (bil.+pls100) with reference values of the Hb concentration.

16 kDa and 0.58−0.76 kDa (unconjugated and conjugated), respectively. The small protein can access the waveguide surface more easily, to which albumin is bound, owing to its high affinity. We observed the same with tartrazine dye solution (534 g/mol). Second, 99.9% of unconjugated bilirubin is bound to albumin in the plasma,[43] while plasma albumin also adheres to the sensor surface, where the evanescent field is strongest. Different bilirubin concentration mixed into plasma was measured without hemolysis as shown in Figure 4e. Here, we observed no change in the sensitivity in high concentration range, which shows that the change of bilirubin/albumin binding ratio in high concentration is not relevant.[44] Other nonspecific binding to the sensor surface is not critical for two reasons: (1) The sensor surface is passivated by albumin from the blood plasma. (2) As far as a molecule not absorbing significantly in the 400−430 nm range, it will not interfere with our absorption measurement, since we analyze the absorption fingerprint of a molecule rather than the refractive index change. In summary, we showed the capability of detecting Hb on whole blood and distinguishing bilirubin as interference with a single LED light source. However, additional LEDs with different wavelengths can also be integrated to yield a broader spectrum for other applications.

**Long-Term Performance.** One of the most important features for the hemolysis sensor is the long-term performance. We tested our optical hemolysis sensor rigorously for 7 weeks with a weekly repetition of the test series, while the sensor was integrated as an inline component in the modified ABL90 FLEX blood gas analyzer. A single measurement flow is shown in Figure 5a, where we see the drop of the signal due to the absorption of plasma hemoglobin and its fast recovery after the rinse. The spectra at three different time points are shown in Figure 5b, where no drift or remaining absorbency can be observed.

A daily test protocol is shown in Figure 5c, where it starts and terminates with a 450 mg/L tartrazine dye solution for

calibration of the sensitivity. As fresh bovine blood is used for the preparation of the rest of the reagents, fluctuations in Hb concentration are inevitable and the dye calibration can thus better quantify the long-term change. Hemolyzed whole blood samples with about 100 mg/dL Hb concentration (HWB100) are tested with 5 runs, followed by its centrifuged plasma counterparts (plasma100). WB and its plasma counterpart (plasma) are prepared in the same way. To test for interference, bilirubin (20 mg/dL) is mixed into the plasma sample with 100 mg/dL Hb. According to Figure 5c, very little change in sensitivity happens before and after carrying out the measurement series as tartrazine deviates only 0.4%. Very small concentrations of Hb around 10 mg/dL in nonhemolyzed samples can be resolved. Only slight deviation is present under high bilirubin concentration.

Observing the whole test period of 47 days, we can find a high daily repeatability and a small drift in the sensitivity, as shown in Figure 5d, where the tartrazine absorption is shown. The results show only a overall drift is 4.7% after 47 days, which can be attributed to detachment of the nanofilters or slight change in material optical property as the sensor is kept in liquid (even in the standby phase). The results of HWB and the plasma counterparts are plotted in Figure 5e. Variation in sample Hb concentration is present as the reference Hb measurements fluctuate between 68 to 115 mg/dL, which helps evaluating the sensor performance upon concentration variations. The pooled standard deviations ($S_p$) are 2.6 and 2.3 mg/dL for whole blood and plasma samples, respectively, showing similar and very good repeatability. From these values, we can calculate the limit of detection to be 4.3 mg/dL for free hemoglobin sensing in whole blood. Note that the bias to the reference is not considered. The bias between WB and plasma samples is however larger (up to 10%). It might originate from the scattered light, which is not guided but still projected onto the camera, and the camera background correction that took place between the HWB and plasma measurements.

Furthermore, the influence of additional bilirubin in plasma is evaluated. Figure 5f shows the evaluated Hb in plasma with bilirubin interference; the $S_p$ of 2.7 mg/dL is almost the same as that without bilirubin. An overall positive bias with respect to the reference (7.0% CoV in average) can be seen, indicating slightly elevated absorption with the coexistence of bilirubin and Hb. In general, we observed no performance deterioration after 7 weeks, confirming the durability of the hemolysis sensor with the long-term exposure to blood and rinse.

## ■ CONCLUSIONS

In summary, we demonstrated an optofluidic waveguide sensor for in-line hemolysis detection on whole blood with unique, integrated cell/plasma separation ability. The arrangement of nanofilters on top of the waveguide enables local blocking of species out of the evanescent field and allows independent choice of light wavelength and filtration size. The fabrication process can be easily scaled up for industrial production with low cost and high production yield. The sensor can be used as a flexible, standalone device or can be easily integrated into existing PoC platforms. It is shown that a spectrometer-less analysis of spectral extinction of molecules can be successfully achieved by employing out-coupling gratings as a dispersive element and a line camera for readout. We demonstrate here that the portable optical setup is capable of being integrated into a commercial blood gas analyzer. Long-term tests up to 7 weeks were also carried out to demonstrate the high repeatability and reliability of the hemolysis sensor subject to whole blood samples even with the presence of strong interference from bilirubin. We envisage large potential for the sensor to be used inline in blood gas analyzers for hemolysis detection as well as in other fields related to turbid media measurements.

## ■ MATERIALS AND METHODS

**Sensor Fabrication and Materials.** To fabricate the hemolysis sensor, a borofloat wafer was used as substrate a substrate. The polymer Efiron (Luvantix, South Korea) was drop-cast and imprinted with the silicon master stamp, which is treated with perfluorodecyltrichlorosilane (FTDS). The polymer was cured by UV exposure in an $N_2$ atmosphere, followed by manual separation with a razor blade. The waveguide layer made of OrmoClear H101 was spin-coated on the Eifron surface treated with oxygen plasma and baked to evaporate solvent. OrmoClear H101 was diluted with propylene glycol methyl ether acetate (PGMEA) to yield the desired thickness. The UV curing of OrmoClear H101 was done by UV curing in $N_2$ atmosphere. The waveguide stack was oxygen plasma treated before spin-coating with OrmoComp, which was diluted in the same way as OrmoClear H101. After the evaporation of the solvent, the waveguide was aligned with the organic−inorganic hybrid imprint stamp to define the nanofilters. Imprinting was done by applying 6 bar pressure for 20 min with subsequent UV exposure in a UV-imprinter (CNI v 2.0, NIL Technology, Denmark). A thick layer of OrmoComp can be optionally used to passivate the surface outside of the filter region, which was done with UV-photolithography with a mask aligner (Karl Süss MA6 contact aligner, Germany). Finally, a fluidic channel can be applied by a double-adhesive tape (tesa 62571, Germany) with a cover formed by laser-cut PMMA. Fabrication of the organic−inorganic hybrid imprint stamp started with oxygen plasma treatment of a borofloat glass wafer, followed by spin-coating of an adhesion layer OrmoPrime08. Around 150 $\mu$L OrmoStamp was suspended on top of the wafer and imprinted with the FTDS-treated master stamp while UV exposure was applied to cure the OrmoStamp, followed by hard-baking at 130 °C for 15 min. The stamp was finished by treating with FTDS for antisticking property. Here, OrmoPrime08, OrmoStamp, OrmoClear H101,

OrmoComp, PGMEA are acquired from micro resist technology GmbH, Germany.

**Optical Simulations.** The mode analysis simulations were carried out with COMSOL (COMSOL Multiphysics). Unit cells were defined with Floquet periodicity. Real and imaginary refractive index were acquired by spectroscopic ellipsometry measurements (M-2000, J.A. Woollam) of each material deposited as a thin film onto silicon wafers. OrmoComp ($n_{OrmoComp}$ = 1.537 @420 nm), OrmoClear H101 ($n_{OrmoClear}$ = 1.629 @420 nm), and Efiron ($n_{OrmoComp}$ = 1.414 @420 nm) were modeled for the geometry we obtained. The evanescent overlap was defined by the ratio of power immersed in the liquid to the total power in the waveguide. Unfiltered ratio was defined as power in the area higher than the top of the filter region to the total power in the liquid.

**Blood Sample Preparation.** Hemolyzed whole blood was prepared by mixing completely hemolyzed fresh whole blood from human or bovine to fresh whole blood, of which the total hemoglobin concentration was measured with a blood gas analyzer in advance (ABL90 FLEX, Radiometer Aps, Denmark). The completely hemolyzed whole blood was obtained by freezing the blood sample in −20 °C for at least 3 h. Part of the prepared whole blood sample was centrifuged to obtain the plasma sample. Bilirubin interfered plasma samples were prepared by adding concentrated bilirubin base solution into plasma from the centrifuged whole blood sample containing 100 mg/dL Hb. The bilirubin base solution was prepared by mixing bilirubin powder (Sigma-Aldrich, USA) into 0.1 M NaOH solution with a concentration of 10 g/L. Tartrazine calibration liquid was prepared by mixing tartrzine (450 mg/L) into the Cal. Two solution from a Radiometer solution pack (REF 944−157, Radiometer Aps, Denmark).

**Absorption Characterization.** An LED light source (M420L3, Thorlabs) with a peak wavelength of 420 nm was used for the Hb absorption test. The light was collimated into a multimode fiber with a core diameter of 200 $\mu$m. The output light was collimated and focused with a plano-convex lens with a focal length of 50 mm. The sensor was placed on a platform with two apertures fitting the size of the grating couplers (2 × 2 mm). The out-coupled light was filtered through a linear polarizer and captured by a CMOS linear image sensor (S11639−01, Hamamatsu, Japan). For the calibration of the sensor, 405 and 450 nm laser diode modules (CPS405, CPS450, Thorlabs) were used to define the spectral locations. During the measurement phosphate buffered saline (PBS) or rinse solution from Radiometer solution pack (REF 944−157, Radiometer ApS, Denmark) were used to rinse the surface of the sensor. Scattering signals on the linear camera were corrected by linear subtraction of signal tails before the absorbance is calculated.

**Reference Absorption Measurement.** All biological samples were diluted with phosphate buffered saline (PBS) solution according to their concentrations. The following mixing ratios were used for samples in this work: nonhemolyzed plasma 1:3, plasma with 100 mg/dL Hb 1:6, plasma with 100 mg/dL Hb and 20 mg/dL bilirubin 1:12, tartrazine calibration solution with 450 mg/L tartrazine: 1:12. UV-transparent 1 cm cuvettes were used for characterization with a UV photospectrometer (UV-1800 Shimadzu Corp., Japan). A spectral range from 330 to 700 nm was used to characterize the samples for reference.

**Long-Term Measurement.** During the long-term measurements the optical setup was attached to a modified ABL90 FLEEX blood gas analyzer(Radiometer ApS, Denmark). Two ports were wired through silicone tubing to the in- and outlet of the analyzer. The samples were always acquired through the sample inlet of the analyzer. Each acquisition took around 70 $\mu$L of the sample, which was delivered to the sensor by the internal peristaltic pump of the analyzer. Five seconds were set to allow the sample in touch with the sensor before the rinse protocol is carried out, which was a modified version of the commercial version of the analyzer, including 5 times air and rinse alternating purge and a final liquid rinse. Recording of the camera was carried out with 2−12 ms integration time subject to the intensity transmitted. 250 ms sampling interval was used for real-time recording, which terminated after 20 s after the rinse protocol. The calculation of

the different components in the blood was made afterward by nonlinear least-squares fitting with reference spectra. Daily measurement protocol included 5 times repeated HWB 100 and the rest samples were measured 3 times apart from the tartrazine calibration liquid which was measured once before and after all other measurements. Tartrazine (450 mg/dL) was measured once before and once after the blood and plasma measurements. The evaluation of the long-term sensitivity change was done by observing tartrazine absorption over days, while it was calibrated with the measurements on the first day to 450 mg/dL. Bovine blood was used during the long-term test, which was acquired from Statens Serum Institute, Denmark. After the sample measurements, the analyzer was automated to perform a rinse protocol every 4 h for circulation and purge.

## ■ ASSOCIATED CONTENT

**Ⓢ Supporting Information**

The Supporting Information is available free of charge on the ACS Publications website at DOI: 10.1021/acssensors.8b00030.

   System modeling and calculations (PDF)

## ■ AUTHOR INFORMATION

**Corresponding Author**
*E-mail: anders.kristensen@nanotech.dtu.dk.
**ORCID** Ⓞ
Anders Kristensen: 0000-0001-9567-1656
**Notes**
The authors declare no competing financial interest.

## ■ ACKNOWLEDGMENTS

## ■ REFERENCES

(1) Lippi, G.; Cervellin, G.; Favaloro, E. J.; Plebani, M. *In Vitro and In Vivo Hemolysis - An Unresolved Dispute in Laboratory Medicine*; DeGruyter: Germany, 2012.

(2) Lippi, G.; Guidi, G. C. Risk management in the preanalytical phase of laboratory testing. *Clin. Chem. Lab. Med.* **2007**, *45*, 720−727.

(3) Vercaemst, L. Hemolysis in cardiac surgery patients undergoing cardiopulmonary bypass: a review in search of a treatment algorithm. *Journal of Extra-corporeal Technology* **2008**, *40*, 257−67.

(4) Mamikonian, L. S.; Mamo, L. B.; Smith, P. B.; Koo, J.; Lodge, A. J.; Turi, J. L. Cardiopulmonary Bypass is Associated with Hemolysis and Acute Kidney Injury in Neonates, Infants and Children. *Pediatr Crit Care Med.* **2014**, *15*, 111−119.

(5) Gupta, R.; Goddard, N. J. Broadband absorption spectroscopy for rapid pH measurement in small volumes using an integrated porous waveguide. *Analyst* **2017**, *142*, 169−176.

(6) Wiederkehr, R. S.; Mendes, S. B. Extension of the broadband single-mode integrated optical waveguide technique to the ultraviolet spectral region and its applications. *Analyst* **2014**, *139*, 1396−1402.

(7) Sakota, D.; Takatani, S. Plasma surface reflectance spectroscopy for non-invasive and continuous monitoring of extracellular component of blood. *Proc. SPIE* **2012**, *8439*, 1−6.

(8) Bradshaw, J. T.; Mendes, S. B.; Saavedra, S. S. Accelerated Article A Simplified Broadband Coupling Approach Applied to Chemically Robust Sol-Gel, Planar Integrated Optical Waveguides A Simplified Broadband Coupling Approach Applied to Chemically Robust Sol-Gel, Planar Integrated Optical Waveguides. *Anal. Chem.* **2002**, *74*, 1751−1759.

(9) Mendes, S. B.; Li, L.; Burke, J. J.; Lee, J. E.; Dunphy, D. R.; Saavedra, S. S. Broad-Band Attenuated Total Reflection Spectroscopy of Waveguide. *Langmuir* **1996**, *12*, 3374−3376.

(10) Cadarso, V. J.; Llobera, A.; Puyol, M.; Schift, H. Integrated photonic nanofences: Combining subwavelength waveguides with an enhanced evanescent field for sensing applications. *ACS Nano* **2016**, *10*, 778−785.

(11) Ryckeboer, E.; Bockstaele, R.; Vanslembrouck, M.; Baets, R. Glucose sensing by waveguide-based absorption spectroscopy on a silicon chip. *Biomed. Opt. Express* **2014**, *5*, 1636−1648.

(12) Gupta, R.; Bastani, B.; Goddard, N. J.; Grieve, B. Absorption spectroscopy in microfluidic flow cells using a metal clad leaky waveguide device with a porous gel waveguide layer. *Analyst* **2013**, *138*, 307−314.

(13) Zhang, L.; Wang, P.; Xiao, Y.; Yu, H.; Tong, L. Ultra-sensitive microfibre absorption detection in a microfluidic chip. *Lab Chip* **2011**, *11*, 3720.

(14) Prabhakar, A.; Mukherji, S. Microfabricated polymer chip with integrated U-bend waveguides for evanescent field absorption based detection. *Lab Chip* **2010**, *10*, 748.

(15) Mogensen, K. B.; Friis, P.; Hubner, J.; Petersen, N. J.; Jorgensen, A. M.; Telleman, P.; Kutter, J. P. Ultraviolet transparent silicon oxynitride waveguides for biochemical microsystems. *Opt. Lett.* **2001**, *26*, 716−718.

(16) Kim, P.; Ong, E. H.; Li, K. H. H.; Yoon, Y. J.; Ng, S. H. G.; Puttachat, K. Low-cost, disposable microfluidics device for blood plasma extraction using continuously alternating paramagnetic and diamagnetic capture modes. *Biomicrofluidics* **2016**, *10*, 024110.

(17) Han, K.-H.; Frazier, A. B. Paramagnetic capture mode magnetophoretic microseparator for high efficiency blood cell separations. *Lab Chip* **2006**, *6*, 265−273.

(18) Nakashima, Y.; Hata, S.; Yasuda, T. Blood plasma separation and extraction from a minute amount of blood using dielectrophoretic and capillary forces. *Sens. Actuators, B* **2010**, *145*, 561−569.

(19) Jung; Kwak, H.-Y. Separation of Microparticles and Biological Cells Inside an Evaporating Droplet Using Dielectrophoresis. *Anal. Chem.* **2007**, *79*, 5087−5092.

(20) Lenshof, A.; Ahmad-Tajudin, A.; Järås, K.; Swärd-Nilsson, A.-M.; Åberg, L.; Marko-Varga, G.; Malm, J.; Lilja, H.; Laurell, T. Acoustic Whole Blood Plasmapheresis Chip for Prostate Specific Antigen Microarray Diagnostics. *Anal. Chem.* **2009**, *81*, 6030−6037.

(21) Petersson, F.; Nilsson, A.; Holm, C.; Jönsson, H.; Laurell, T. Separation of lipids from blood utilizing ultrasonic standing waves in microfluidic channels. *Analyst* **2004**, *129*, 938−943.

(22) Prabhakar, A.; Kumar, Y. V. B. V.; Tripathi, S.; Agrawal, A. A novel, compact and efficient microchannel arrangement with multiple hydrodynamic effects for blood plasma separation. *Microfluid. Nanofluid.* **2015**, *18*, 995−1006.

(23) Kersaudy-Kerhoas, M.; Kavanagh, D. M.; Dhariwal, R. S.; Campbell, C. J.; Desmulliez, M. P. Y. Validation of a blood plasma separation system by biomarker detection. *Lab Chip* **2010**, *10*, 1587.

(24) Mach, A. J.; di Carlo, D. Continuous scalable blood filtration device using inertial microfluidics. *Biotechnol. Bioeng.* **2010**, *107*, 302−311.

(25) Zhang, X. B.; Wu, Z. Q.; Wang, K.; Zhu, J.; Xu, J. J.; Xia, X. H.; Chen, H. Y. Gravitational sedimentation induced blood delamination for continuous plasma separation on a microfluidics chip. *Anal. Chem.* **2012**, *84*, 3780−3786.

(26) Sun, M.; Khan, Z. S.; Vanapalli, S. a. Blood plasma separation in a long two-phase plug flowing through disposable tubing. *Lab Chip* **2012**, *12*, 5225−5230.

(27) Aran, K.; Fok, A.; Sasso, L. A.; Kamdar, N.; Guan, Y.; Sun, Q.; Ündar, A.; Zahn, J. D. Microfiltration platform for continuous blood plasma protein extraction from whole blood during cardiac surgery. *Lab Chip* **2011**, *11*, 2858.

(28) Thorslund, S.; Klett, O.; Nikolajeff, F.; Markides, K.; Bergquist, J. A hybrid poly(dimethylsiloxane) microsystem for on-chip whole blood filtration optimized for steroid screening. *Biomed. Microdevices* **2006**, *8*, 73−79.

(29) Kang, T. G.; Yoon, Y.-J.; Ji, H.; Lim, P. Y.; Chen, Y. A continuous flow micro filtration device for plasma/blood separation using submicron vertical pillar gap structures. *J. Micromech. Microeng.* **2014**, *24*, 087001.

(30) Shim, J. S.; Ahn, C. H. An on-chip whole blood/plasma separator using hetero-packed beads at the inlet of a microchannel. *Lab Chip* **2012**, *12*, 863.

(31) Mortensen, N. A.; Xiao, S.; Pedersen, J. Liquid-infiltrated photonic crystals: enhanced light-matter interactions for lab-on-a-chip applications. *Microfluid. Nanofluid.* **2008**, *4*, 117−127.

(32) Bhushan, B. E., Ed. *Springer Handbook of Nanotechnology*, 3rd ed.; Springer: Berlin Heidelberg, 2010; Chapter 9, pp 271−312.

(33) Mauranyapin, N. P.; Madsen, L. S.; Taylor, M. A.; Waleed, M.; Bowen, W. P. Evanescent single-molecule biosensing with quantum-limited precision. *Nat. Photonics* **2017**, 1−6.

(34) Shao, L.; Jiang, X.-F.; Yu, X.-C.; Li, B.-B.; Clements, W. R.; Vollmer, F.; Wang, W.; Xiao, Y.-F.; Gong, Q. Detection of Single Nanoparticles and Lentiviruses Using Microcavity Resonance Broadening. *Adv. Mater.* **2013**, *25*, 5616−5620.

(35) Zhu, J.; Ozdemir, S. K.; Xiao, Y.-F.; Li, L.; He, L.; Chen, D.-R.; Yang, L. On-chip single nanoparticle detection and sizing by mode splitting in an ultrahigh-Q microresonator. *Nat. Photonics* **2010**, *4*, 46−49.

(36) He, L.; Özdemir, a. K.; Zhu, J.; Kim, W.; Yang, L. Detecting single viruses and nanoparticles using whispering gallery microlasers. *Nat. Nanotechnol.* **2011**, *6*, 428−432.

(37) Baaske, M. D.; Foreman, M. R.; Vollmer, F. Single-molecule nucleic acid interactions monitored on a label-free microcavity biosensor platform. *Nat. Nanotechnol.* **2014**, *9*, 933−9.

(38) Baaske, M. D.; Vollmer, F. Optical observation of single atomic ions interacting with plasmonic nanorods in aqueous solution. *Nat. Photonics* **2016**, *10*, 733−739.

(39) Koseoglu, M.; Hur, A.; Atay, A.; Cuhadar, S. Effects of hemolysis interference on routine biochemistry parameters. *Biochemia Medica* **2011**, 79−85.

(40) U.S. Department of Health and Human Services, Public Health Service, Centers for Disease Control, P. H. P. O. *CLIA '88 Focus on Clinic and Office Laboratories*, 1988.

(41) EDQM, *Guide to the preparation, use and quality assurance of blood components, Recommendation No. R (95) 15*.

(42) Provan, D. *Medicine*; **2009**; Vol. *98*; Chapter 12, p 920.

(43) Roca, L.; Calligaris, S.; Wennberg, R. P.; Ahlfors, C. E.; Malik, S. G.; Ostrow, J. D.; Tiribelli, C. Factors affecting the binding of bilirubin to serum albumins: Validation and application of the peroxidase method. *Pediatr. Res.* **2006**, *60*, 724−728.

(44) Ardakani, S. B.; Dana, V. G.; Ziaee, V.; Ashtiani, M.-T. H.; Djavid, G. E.; Alijani, M. Bilirubin/Albumin Ratio for Predicting Acute Bilirubin-induced Neurologic Dysfunction. *Iranian Journal of Pediatrics* **2011**, *21*, 28−32.

## A.2 Manuscript of Paper II

# Multifuntional waveguide interferometer sensor: simultaneous detection of refraction and absorption with size-exclusion function

**CHEN ZHOU,**[1] **MEHDI KESHAVARZ HEDAYATI,**[1] **AND ANDERS KRISTENSEN**[1,*]

[1]*Department of Micro- and Nanotechnology, Technical University of Denmark, DK-2800 Kongens Lyngby, Denmark*
*[*]anders.kristensen@nanotech.dtu.dk*

**Abstract:** A waveguide Young interferometer is presented with simultaneous detection of liquid refraction and absorption(i.e. complex refractive index). The real part of refractive index change (refraction) is detected by tracing phase shifts of the interferogram generated by a sensing and reference waveguide. The imaginary part of refractive index (absorption) is determined by the attenuation of the transmitted signal at certain wavelength. Furthermore, nano-filters are fabricated atop the sensing waveguide, which enables size-exclusion filtering of species to the evanescent field. It shows capability of distinguishing small and large particles from 100 nm to 500 nm in diameter, which is further confirmed by fluorescent excitation experiments. The present sensor could find broad application in optical characterization of complex turbid media with regard to their complex refractive index.

**OCIS codes:** (130.5460) Polymer waveguides; (120.3180) Interferometry, (280.4788) Optical sensing and sensors.

## References and links

1. P. Kozma, F. Kehl, E. Ehrentreich-Förster, C. Stamm, and F. F. Bier, "Integrated planar optical waveguide interferometer biosensors: A comparative review," Biosens. Bioelectron. **58**, 287–307 (2014).
2. K. Schmitt, K. Oehse, G. Sulz, and C. Hoffmann, "Evanescent field sensors based on tantalum pentoxide waveguides - A review," Sensors. **8**, 711–738 (2008).
3. S. Aikio, J. Hiltunen, J. Hiitola-Keinänen, M. Hiltunen, V. Kontturi, S. Siitonen, J. Puustinen, and P. Karioja, "Disposable photonic integrated circuits for evanescent wave sensors by ultra-high volume roll-to-roll method," Opt. Express **24**, 2527 (2016).
4. M. Hofmann, Y. Xiao, S. Sherman, U. Gleissner, T. Schmidt, and H. Zappe, "Asymmetric MachâĂŞZehnder interferometers without an interaction window in polymer foils for refractive index sensing," Appl. Opt. **55**, 1124 (2016).
5. A. Ksendzov and Y. Lin, "Integrated optics ring-resonator sensors for protein detection," Opt. Lett. **30**, 3344 (2005).
6. Y. Xiao, S. A. Mendez, M. Hofmann, M. Gauch, H. Ehlers, D. Ristau, C. Mueller, and H. Zappe, "Sensitivity enhancement of polymeric MachâĂŞZehnder interferometers by use of thin high-index films," Sensors Actuators, A: Phys. **265**, 181–186 (2017).
7. M. Hiltunen, J. Hiltunen, P. Stenberg, J. Petäjä, E. Heinonen, P. Vahimaa, and P. Karioja, "Polymeric slot waveguide at visible wavelength," Opt. Lett. **37**, 4449 (2012).
8. N. Nilius, T. M. Wallis, and W. Ho, "Influence of a Heterogeneous Al 2 O 3 Surface on the Electronic Properties of Single Pd Atoms," Opt. Express **25**, 2–5 (2003).
9. L. Ahmadi, M. Hiltunen, P. Stenberg, J. Hiltunen, S. Aikio, M. Roussey, J. Saarinen, and S. Honkanen, "Hybrid layered polymer slot waveguide Young interferometer," Opt. Express **24**, 10275 (2016).
10. M. Hiltunen, J. Hiltunen, P. Stenberg, S. Aikio, L. Kurki, P. Vahimaa, and P. Karioja, "Polymeric slot waveguide interferometer for sensor applications," Opt. Express **22**, 7229 (2014).
11. M. Wang, J. Hiltunen, C. Liedert, S. Pearce, M. Charlton, L. Hakalahti, P. Karioja, and R. Myllylä, "Highly sensitive biosensor based on UV-imprinted layered polymeric-inorganic composite waveguides," Opt. Express **20**, 20309 (2012).
12. P. G. Hermannsson, K. T. Sørensen, C. Vannahme, C. L. Smith, J. J. Klein, M.-M. Russew, G. Grützner, and A. Kristensen, "All-polymer photonic crystal slab sensor," Opt. Express **23**, 16529 (2015).
13. M. Häyrinen, M. Roussey, A. Säynätjoki, M. Kuittinen, and S. Honkanen, "Titanium dioxide slot waveguides for visible wavelengths." Appl. optics **54**, 2653–7 (2015).

14. C. Zhou, M. Keshavarz Hedayati, X. Zhu, F. Nielsen, U. Levy, and A. Kristensen, "Optofluidic Sensor for Inline Hemolysis Detection on Whole Blood," ACS Sensors **3**, 784–791 (2018).
15. B. T. Cunningham, P. Li, S. Schulz, B. Lin, C. Baird, J. Gerstenmaier, C. Genick, F. Wang, E. Fine, and L. Laing, "Label-free assays on the BIND system," J. Biomol. Screen. **9**, 481–490 (2004).
16. K. Schmitt, B. Schirmer, C. Hoffmann, A. Brandenburg, and P. Meyrueis, "Interferometric biosensor based on planar optical waveguide sensor chips for label-free detection of surface bound bioreactions," Biosens. Bioelectron. **22**, 2591–2597 (2007).
17. D. R. Lide, "CRC Handbook of Chemistry and Physics," eBook. p. 3485 (2003).
18. K. Sørensen, C. Ingvorsen, L. Nielsen, and A. Kristensen, "Effects of water-absorption and thermal drift on a polymeric photonic crystal slab sensor," Opt. Express **26**, 5416–5422 (2018).
19. C. Stamm, R. Dangel, and W. Lukosz, "Biosensing with the integrated-optical difference interferometer: dual-wavelength operation," Opt. Commun. **153**, 347–359 (1998).
20. W. Lukosz, C. Stamm, H. Moser, R. Ryf, and J. Dübendorfer, "Difference interferometer with new phase-measurement method as integrated-optical refractometer, humidity sensor and biosensor," Sensors Actuators B: Chem. **39**, 316–323 (1997).
21. A. Brandenburg, "Differential refractometry by an integrated-optical Young interferometer," Sensors Actuators B: Chem. **39**, 266–271 (1997).
22. M. Wang, S. Uusitalo, C. Liedert, J. Hiltunen, L. Hakalahti, and R. Myllylä, "Polymeric dual-slab waveguide interferometer for biochemical sensing applications," Appl. Opt. **51**, 1886 (2012).
23. D. J. Rowe, D. Smith, and J. S. Wilkinson, "Complex refractive index spectra of whole blood and aqueous solutions of anticoagulants, analgesics and buffers in the mid-infrared," Sci. Reports **7**, 1–9 (2017).
24. A. Bavali, P. Parvin, S. Z. Mortazavi, M. Mohammadian, and M. R. Mousavi Pour, "Red/blue spectral shifts of laser-induced fluorescence emission due to different nanoparticle suspensions in various dye solutions," Appl. Opt. **53**, 5398 (2014).
25. W. M. b. M. Yunus, "Refractive index of dye solution," Appl. Opt. **28**, 4268 (1989).

## 1. Introduction

Optical waveguides have been widely used as efficient sensors for detection of refractive index (RI) change by probing near surface region of the sample with the evanescent field [1,2]. Recently, polymer waveguides have gained great attention owing to their interesting properties including high transparency in the UV-visible range, versatile process-abilities, cost effectiveness, and mechanical flexibility [3,4]. Different designs including ring resonators [5], interferometers [6–11] and guided mode resonance filters [12] have been demonstrated. In order to enhance the sensitivity of the polymeric sensor, various strategies have been demonstrated. Organic-inorganic polymer slot waveguides have been developed to enable large light-liquid interaction [7, 9, 13]. Some polymer waveguides have shown enhanced sensitivity by incorporating additional high RI material like $TiO_2$ and $Ta_2O_5$ at the interface to the liquid, [2, 6, 8, 9]. However, simultaneous measurement of both real and imaginary component of refractive index has been less explored. Here, we addressed this issue and present a sensor that is able to detect real and imaginary part of refractive index at the same time using a Young interferometer. Furthermore, we added additional size-exclusion sensing functionalities, which has been demonstrated in our previous work for detection of hemolysis in whole blood [14]. The multi-functionality can significantly expands the applicability of the sensor in to areas dealing with complex turbid medium.

The interferometer sensor presented in this work is comprised of two waveguides (sensing and reference) with individual grating couplers for both in- and out-coupling. The sensing waveguide has nano-filters atop with an opening of 200 nm that enable local exclusion to the evanescent field, enabling size dependent detection. With help of the grating couplers, the finished sensors are highly integrated and can be individually addressed and measured without need of dicing [3,7,9,11]. This feature enables a compact parallelization of the sensor, which is applicable in various sensing platforms such as embedding to the bottom of a microtiter plate [15]. We measured ethanol water mixture to calibrate the bulk RI sensitivity as well as a dye solution for absorption measurement. Here, both the phase shift due to the real part of RI ($n$) and the absorption due to the imaginary part ($k$) can be obtained. Size-exclusion function was verified by measuring solutions containing polystyrene nanoparticles of different sizes. Moreover, we use

the waveguide evanescent field for fluorescent excitation to excite fluorescent nanoparticles with different sizes, which further proves the size-selectivity of the waveguide.
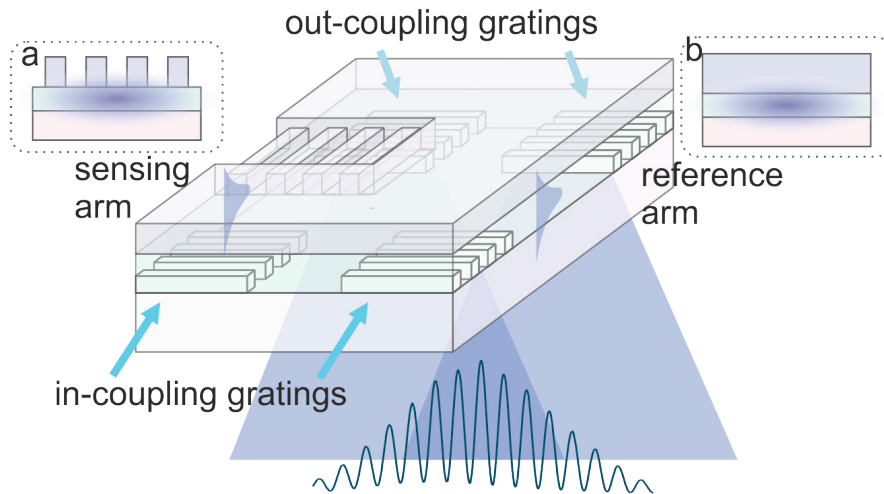


Fig. 1. Illustration of the waveguide interferometer. A sensing and a reference waveguide is placed beside each other. A sensing window with nano-filters is exposed to the liquid, where the rest of the sensor is passivated by a thick layer of polymer. The light is coupled by the in-coupling gratings into the waveguides, while the guided light is out-coupled by the out-coupling gratings and generates an interference pattern on the line camera. Insets (a-b) in dashed windows show the cross section of the sensing and reference arm

## 2. Design and fabrication of the interferometer with size-exclusion filters

### 2.1. Design of a grating-coupled Young interferometer

The schematic image in Figure 1 illustrates the design of the device. We aimed to generate a Young interferometer with two slab waveguides with grating couplers for in- and out-coupling. Instead of using a Y-splitter to generate two waveguides from one [10, 11], we used two grating couplers to define two slab waveguides. The latter avoids lateral confinement and simplifies the fabrication process. A gap of 200 $\mu$m between the grating couplers defines the distance between the fringes of the interferogram. The total propagation length of the waveguide on the chip is 3.4 mm. The active sensing length is given by the area where the waveguide is exposed to the liquid, as shown in the sensing arm of the Figure 1. This length is 800 $\mu$m in our design, where a longer distance can further amplify the total phase shift, as will be discussed later. For the light source, a laser module with 450 nm wavelength (CPS450, Thorlabs) is used. The laser beam is linear polarized and focused with a single convex lens (focal length 100 mm). The large focal length gives a low numerical aperture which is preferred for coupling into an equidistant grating coupler for its narrow acceptance angle. The beam size is chosen large enough to be able to couple into the two grating couplers (for sensing and reference arms) at the same time, which eliminates the need of additional beam splitter. The out-coupled light can scatter laterally to generate an interferogram to be captured by a line camera as shown in Figure 2a. The Fourier transformed signal is shown in Figure 2b, where a sharp frequency appears, shows the efficiency of the grating coupled Young-interferometer even without any additional slits as used in other works [16].
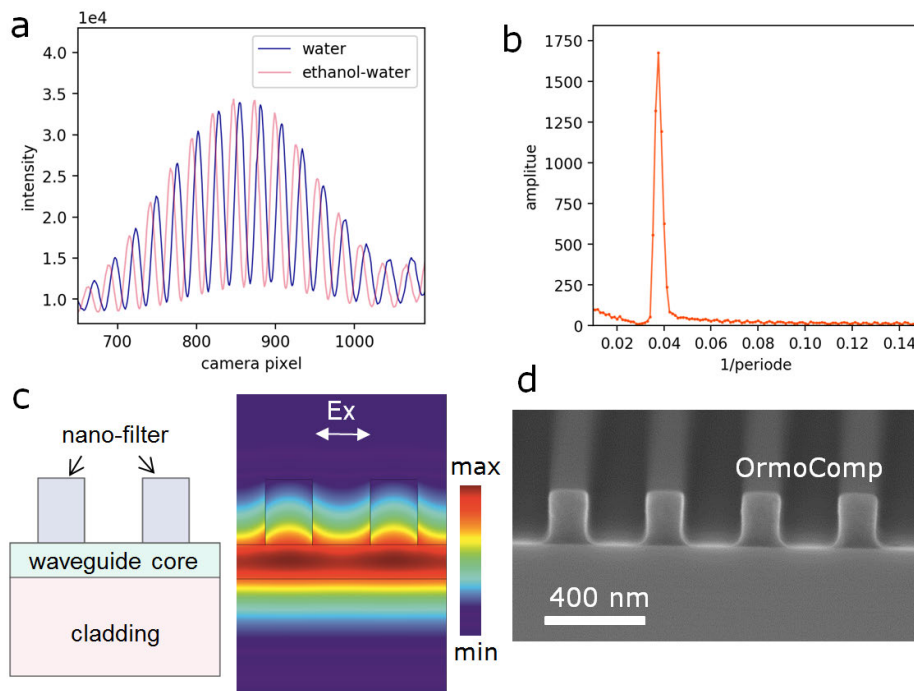
Fig. 2. a) The interferograms captured by the line camera of water and an ethanol-water solution. b) The amplitude of the Fourier transformed interferogram. c) illustration and the optical simulation of the TE mode of the waveguide. The mode is confined underneath the top of the filters to avoid interference from the bulk. d) SEM image of imprinted nano-filters (OrmoComp) on a Si substrate. Little imprint residue can be seen.

## 2.2. Design of the waveguide with nano-filters

The sensitivity of the interferometer sensor is contributed by the mode overlap of the guided light with the liquid. Slot waveguides are widely used for their large mode overlap as the guided mode can reside in the low refractive index medium [9]. For the sensing arm, we aim to achieve high sensitivity while maintaining the functionality as local filters. UV-nanoimprinted OrmoComp (micro resist technology GmbH, Germany) ridges atop the waveguide core function as filters, as shown in Figure 2c. Here, we did waveguide mode analysis with COMSOL Multiphysics (COMSOL Inc., Sweden). A 800 nm unit cell with periodic boundary condition is created. The transverse electric (TE) mode, which is horizontally aligned, is shown in Figure 2c. It is clear that the mode is strongly confined under the top of the nano-filters. The strongest mode intensity is inside the waveguide core. In the middle of a nano-well, the energy density of the fundamental TE mode is only 2.3% at the top (250 nm high) compared to the bottom. Since the evanescent field is confined under the ridges, large species in the bulk liquid are not interacting with the guided light, enabling size exclusive detection. To enable the confinement for the device, we chose a high RI polymer (OrmoClear H101, micro resist technology GmbH, Germany) as the waveguide core. The material is doped with $ZrO_2$ to achieve high RI (1.63 at 450 nm) while being highly transparent in the visible range [12]. The material for the nano-filters (OrmoComp) and the cladding (Efiron, Luvantix, South Korea) exhibit a RI of 1.54 and 1.43 at 450 nm, respectively. The contrast from OrmoComp cover material to the waveguide core as well as cladding has to be chosen carefully as the grating coupler areas are made of the same materials. A low contrast in

RI will also lead to lower coupling efficiency, as the gratings are covered in OrmoComp material, as shown in Figure 1. The thickness of the waveguide core is chosen to be low (130 nm) in order to enable the maximal evanescent mode overlap with liquid. The effective refractive index of the waveguide with nano-filters is 1.485 (TE mode, horizontally polarized), while the reference waveguide has a $n_{eff}$ = 1.533.

## 2.3. Fabrication

The sensor is fabricated with the following steps: 1) we drop-cast the Efiron polymer onto the glass substrate and the grating couplers are extruded from the surface by UV nanoimprint lithography. The Si stamp is made by E-beam lithography with etched gratings (390 nm in pitch). 2) Core material OrmoClear H101 is spin-coated onto the surface of the cladding material. By adjusting the dilution and spin-coating velocity, the core thickness is controlled. 3) A thin layer OrmoComp (140 nm) is spin-coated to the cured OrmoClear H101 surface, followed by a UV-nanoimprint step to define the nano-filters. 4) A thick layer of OrmoComp layer (8 $\mu$m) is spin-coated, followed by a photolithography step for opening the sensing windows, leaving the reference waveguide isolated. The challenge is to obtain a residue free imprint of the nano-filter(cf. Figure 2d), since a residual layer will decrease the sensitivity of the waveguide. We use a stamp made of OrmoStamp (micro resist technology, Germany) to enable a homogeneous imprint with low stamp bending and low residual layer. The OrmoStamp stamp is a replica of the E-beam written Si stamp and grafted with perfluorodecyltrichlorosilane (FDTS) for anti-sticking surface. A molecular vapor deposition process was used by subsequently applying $O_2$ plasma and FDTS (MVD 100, Applied Microstructures Inc. , USA). A demonstration of the nano-filter imprint is shown in Figure 2d, where it is made on Si wafer for better SEM imaging. The pitch of the filters is 400 nm and the width is 180 nm, which leaves an opening of 220 nm for the liquid interaction.
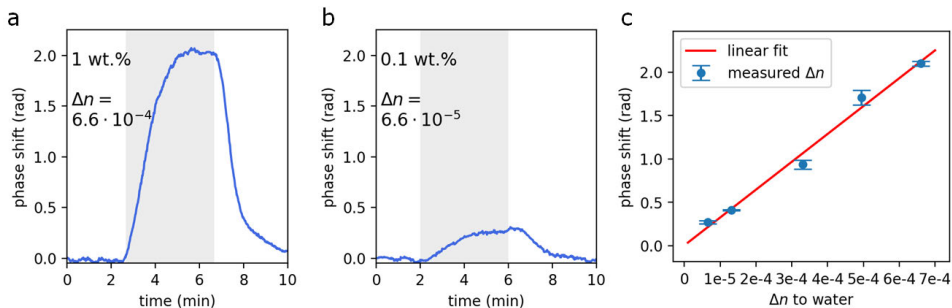


Fig. 3. a) and b) Time-resolved phase shifts recorded for applying ethanol-water solution with different weight concentration to water. The gray areas indicate the influx of ethanol-water solution. c) Plot of measured the phase shifts from different ethanol-water solution. The RI change is calculated and plotted on the x axis. The linear fit shows the linearity of the phase shift to the bulk RI change.

## 3. Performance of the interferometer sensor

### 3.1. Measurement of ethanol-water mixture

To verify the sensitivity of the sensor we performed a series of measurements with ethanol-water mixture. A laser at 450 nm was used, while a CMOS line camera (S11639-01, Hamamatsu, Japan) captures the signal in a second interval for time-resolved measurement. A PMMA housing is taped onto the sensor to define the fluidic path on the interferometer. We mixed ethanol-water

solutions of various concentrations (0.1 %, 0.2%, 0.5%, 0.75%, 1% by weight). The RI change of the medium $\Delta n_c$ of different ethanol-water is calculated as $\Delta n_c = 6.6 \cdot 10^{-4} \cdot C_{eth}$ where the percentage by weight of ethanol in water is $C_{eth}$. Here, we have adapted the empirical value to our working wavelength at 450 nm [17]. Prior to the experiments with ethanol-water solution, we prepared the sensor by filling the channel with DI water for at least 4 hours to saturate the water absorption of the polymer [11, 18].

The phase change is calculated by monitoring the spatial displacement of the interference fringes. The frequency domain of the original spatial signal is calculated by a fast Fourier transform (FFT) algorithm. The peak of the amplitude in the frequency domain corresponds to the fringes that are generated by the waveguide interference, as shown in Figure 2b. With the knowledge of the relevant frequency, the argument at that frequency can be used to calculate the time-dependent phase shifts. In Figure 3a,b, the phase shifts of the 1 and 0.1 wt.% ethanol-water solution are plotted. The first two minutes, the sensor is exposed to DI water followed by exposure to ethanol-water mixture (with gray background). Then, the sensor is rinsed with DI water again. The smallest concentration we measured is $\Delta n$ of $6.6 \times 10^{-5}$, where three measurements showed a standard deviation of 0.0175 rad. The limit of detection is $1.7 \times 10^{-5}$ by LoD = $3\sigma$. Note that the sensor has an effective length of 0.8 mm, which limits the phase shift since the phase shift is given as follows [19]:

$$\Delta\phi = 2\pi L \frac{\Delta\widetilde{n}_{eff}}{\lambda} = 2\pi L \frac{\Delta n_{eff,sen} - \Delta n_{eff,ref}}{\lambda}, \tag{1}$$

where $\Delta\phi$ denotes the phase shift to be measured, $L$ the length of the sensing waveguide (exposed to the liquid), $\lambda$ the operation wavelength, $\widetilde{n}_{eff}$ the total difference in the effective RI, which is defined as the difference between the RI of the sensing arm $\Delta n_{eff,sen}$ and $\Delta n_{eff,ref}$. In order to achieve a lower detection limit, a strategy is to increase the length of the sensor. The largest length, i.e. phase shift per RI unit, that can be used is only limited to the loss of the sensor. By using a short wavelength laser (450 nm), a large increase in phase shift is realized in comparison to most of previous works [4, 6, 7, 10, 13, 18, 20, 21], which operates with a laser above 630 nm. The sensitivity for homogeneous bulk RI sensing of this sensor is comparable to those made by only polymers [4, 11, 22]. We remark that approaches like coating with high RI dielectrics can be employed to enhance the LoD [6, 9]. However, it may compromise the size-exclusion functionality of the sensor. The dynamic range of the real refractive index sensing by the waveguide sensor is determined by the cut-off wavelength of the waveguide. In our case, a real refractive index between 1.0 and 1.52 can be measured which is determined by the refractive index of the filter material used (1.54, OrmoComp).

### 3.2. Measurement of both real and imaginary part of the refractive index

Since we can adjust the relative intensity of the sensing and reference waveguide, an interferogram with both intensity and phase shift information can be easily generated, as shown in Figure 4a. In this case the intensity of the light transmitted through the sensing waveguide (relative to the reference waveguide) is increased in order to obtain more intensity information. As we can see from Figure 4a, the high frequency waveform has en envelope of a base signal, where the latter is used to evaluate the transmitted intensity. We prepared a dye solution with 100-600 mg/dL tartrazine in water. Tartrazine has a absorption maximum around 435 nm, while the laser is operating at 450 nm. In Figure 4a, both intensity attenuation and phase shift are shown. The former is caused by the tartrazine absorption - the imaginary part of the refractive index ($k$), while the latter is caused by the real part of the refractive index ($n$). However, the original signal involves both phase shift and intensity change and is not ideal for extraction of the atteuation. In order to obtain solely the intensity signal, the interferogram is low-pass filtered by cutting off high
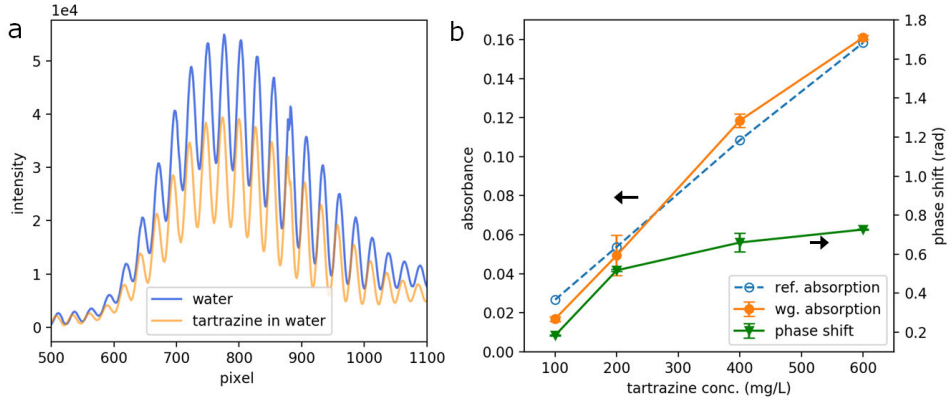
Fig. 4. a) Interferogram of water and a dye solution. The overall intensity is decreased when the sensor is exposed to the tartrazine dye solution. b) Plot of the absorbance (left axis) and phase shift (right axis) measured with the interferometer sensor. Different tartrazine concentrations were mixed into water. The reference absorbance of the dye solutions at the same wavelength (450 nm) is also plotted. The phase shift is evaluated with the same interferogram, which gives the real part of the refractive index.

frequency signal after the Fourier transformation, as shown in Figure 5 a, b. The spatial signal that is generated by the interference is thus eliminated, as shown in Figure 5 c, d. Then, the low-pass filtered signal can be integrated over the whole range to obtain the total transmitted intensity. The absorbance of the solution is then calculated by $a = -\log_{10}(I_{sample}/I_{water})$, where $I_{sample}$ and $I_{water}$ denote the total intensity measured with the sample and rinse, respectively. The absorbance $a$ is linear correlated to the imaginary part, $k$, of the RI [23]. For the waveguide absorption the relation can be described in the following form:

$$k = \frac{\lambda a}{4\pi \eta d \log_{10} e},$$ (2)

where $\lambda$ and $d$ are the wavelength and optical path length, respectively, $\eta$ is the fraction of evanescent energy flux compared to the whole waveguide. Here, we assume zero absorption by the water and use it as the reference signal. In Figure 4b the absorbance is plotted against the reference measurement taken with 1 cm cuvette and a photospectrometer (UV-1800 Shimadzu Corp., Japan). The reference absorbance is linearly scaled to fit the absorbance level of the waveguide. The scale factor $f$ can be used to obtain the evanescent energy factor $\eta$ by $\eta = f \frac{d_{cuvette}}{d_{waveguide}}$, where $d_{cuvette}$ and $d_{waveguide}$ denote the optical path length of the cuvette and waveguide. The LoD of the absorption measurement is determined to be $3.5 \cdot 10^{-3}$ absorbance, which corresponds to 13 mg/L tartrazine in water. The phase shift of the signal is also plotted to the right axis of Figure 4b. In contrast to the absorbance signal, the phase shift is not linear to the concentration of the dye, which is typical for dye solutions [24, 25]. By using the calibration data obtained from the ethanol-water solution, we can determine $\Delta n$ caused by 600 mg/L tartrazine dye addition to water to be $2.3 \cdot 10^{-4}$.

### 3.3. Characterization with nano-beads

One of the special of the present waveguide sensor is the ability to distinguish between small and large objects. We demonstrated the capability by measuring polystyrene nano-beads with different diameters. Two different sizes of 100 and 500 nm (Nanosphere™ Size Standards, Thermo Scintific) were used. A size distribution (standard deviation) of 7.8 and 7.9 nm is given
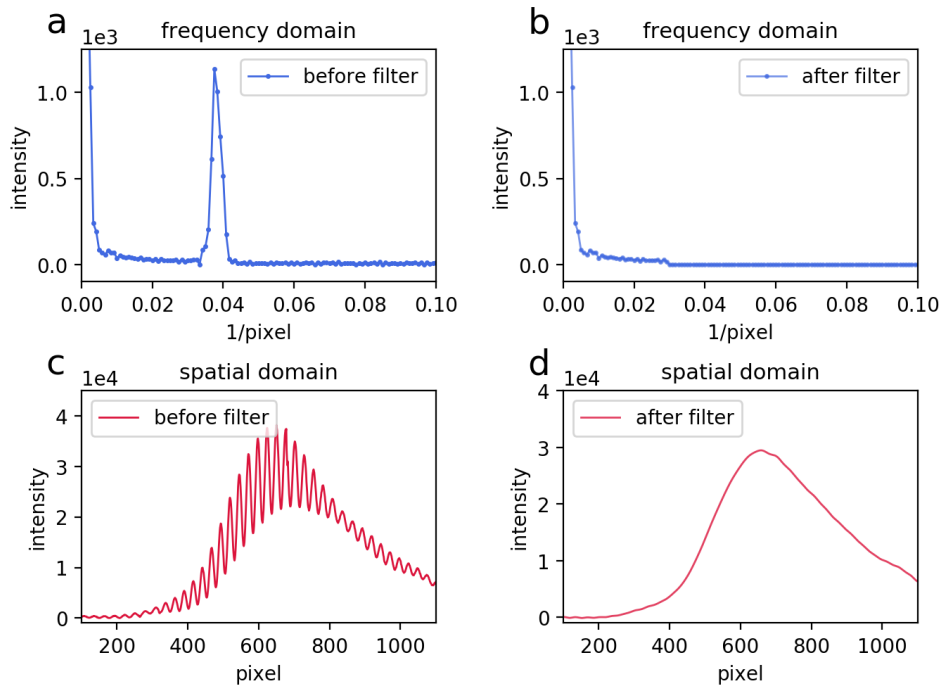
Fig. 5. a) Amplitude of the Fourier-transformed interferogram with a peak which is caused by the waveguide interference. b) Low-pass filtered Fourier-transformed interferogram. The amplitude of the signal that is caused by the interference is set to zero, leaving only bias signal given by the total transmission. c) Interferogram with increased intensity for the sensing waveguide, generating elevated bias signal. d) Inverse Fourier-transformed signal after low-pass filtering. Fringes caused by the interference are eliminated, which can be used to evaluate the attenuation due to absorption.

for the 100 and 500 nm nano-beads, respectively. We know that polystyrene has a RI of 1.61 at 450 nm. We diluted the original suspension of the nano-beads from the manufacture to DI water with a volume ratio of 1:1. Then, we centrifuged part of the 500 nm suspension to obtain the pure carrier medium. To measure the phase shift caused by the nano-beads, we use water as rinse and flush 100 nm and 500 nm beads solution as well as the centrifuged medium. The results are shown in Figure 6. As illustrated, the small beads (100 nm) are able to diffuse into the trenches of 200 nm, while the 500 nm beads are kept outside the evanescent field. Therefore, we observed similar phase shift between the 500 nm beads and the medium. The small change in phase (i.e. the increase in phase shift in the gray area for 500 nm beads) is attributed to the additives given in the original liquid suspension, like surfactants for keeping beads from aggregation. The result demonstrates the ability of the size-exclusion of the sensor. It allows measurement of tiny RI change even with the presence of large impurities, like the 500 nm nano-beads, which renders the liquid completely foggy and intransparent. The threshold of the size-exclusion can be engineered by adjusting the distance of the filers. In comparison to a slot waveguide [7, 9, 13], which also confine the field between high RI ridges, the advantage of our sensor is the flexibility in choosing size threshold as an extra degree of freedom, whereas the gap of a slot waveguide cannot be selected freely. As Figure F5 shows, the 100 nm solution triggered strong phase shift in the waveguide (see the violet curve). After the rinse, the phase shift does not recover to the original level, which is attributed to the fact that some of the particles are immobilized in between the
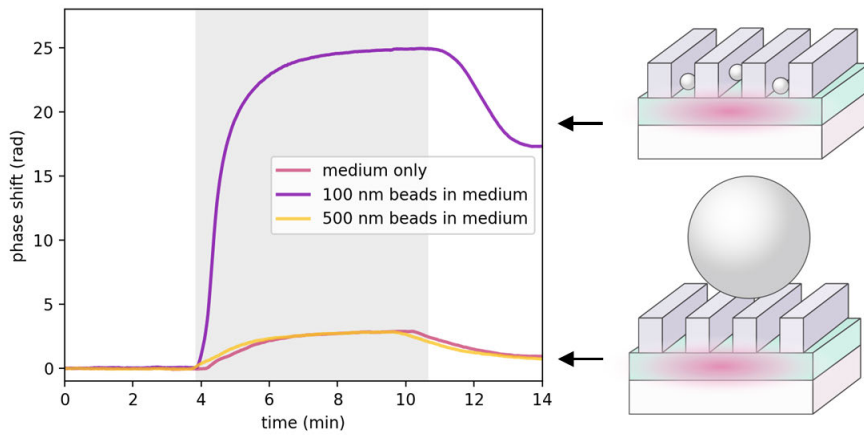
Fig. 6. Time-resolved phase shifts measured with contact to nano-beads suspensions. 100 and 500 nm polystyrene beads were used, where a strong reaction in phase shift is observed with 100 nm beads. The original medium is isolated by centrifugation and measured as well. Little difference is shown between the original medium and the 500 nm beads suspension due to the size exclusion function. The effect of size-exclusion is illustrated schematically on the right side of the graph.

nano-filters even after the rinse, which cause the raise in the RI to the pure water. Thus, this feature can be utilized to physically immobilize nano-spheres. On the other hand, a hydrophilic surface treatment can be used to both waveguide and nano-beads, in order to avoid immobilization of particles, which is beyond the scope of this study.

### 3.4. Characterization with fluorescent excitation

The waveguide can also be utilized for fluorescent excitation with size-exclusion ability. By placing a microscope objective underneath the sensor, the fluorescent signal can be obtained. In our experiment, a 20x microscope objective is used, while a long-pass filter is used before the camera. As demonstrated in Figure 7a-b , both sensing and reference waveguides are lightened by the laser light. In Figure 7b, the guided light ray is visible due to the auto-fluorescence of the polymers, where in the area of nano-filters there is higher intensity due to scattering. Furthermore, we used three green fluorescent nano-beads with different diameter to visualize the size-exclusive excitation (44 nm, 100 nm and 500 nm). For the images in Figure 7c-e, the integration time is kept the same at 20 ms. It is clear that both 100 nm and 44 nm nano-beads were strongly excitation in the filter area. The contrast between the intensities of sensing and reference waveguide also proves the viability of the passivation. We note that we used different sensors for each experiment since the small beads can get stuck in the filter thus contaminates the following measurements. Therefore, small variations in the intensity profile can be observed, which is due to the fact that the coupling condition is slightly different in those experiments. On the other hand, we did not observe significant excitation with the 500 nm beads sample. Only small signal increase can be observed which is mainly due to the scattered light in the liquid. Note that the integration time of the auto-fluorescent experiment is the same as the rest, the maximal intensity is under 50 counts as shown in Figure 7b, while the highest intensity achieved by the 100 nm fluorescent beads is at 2250 counts.
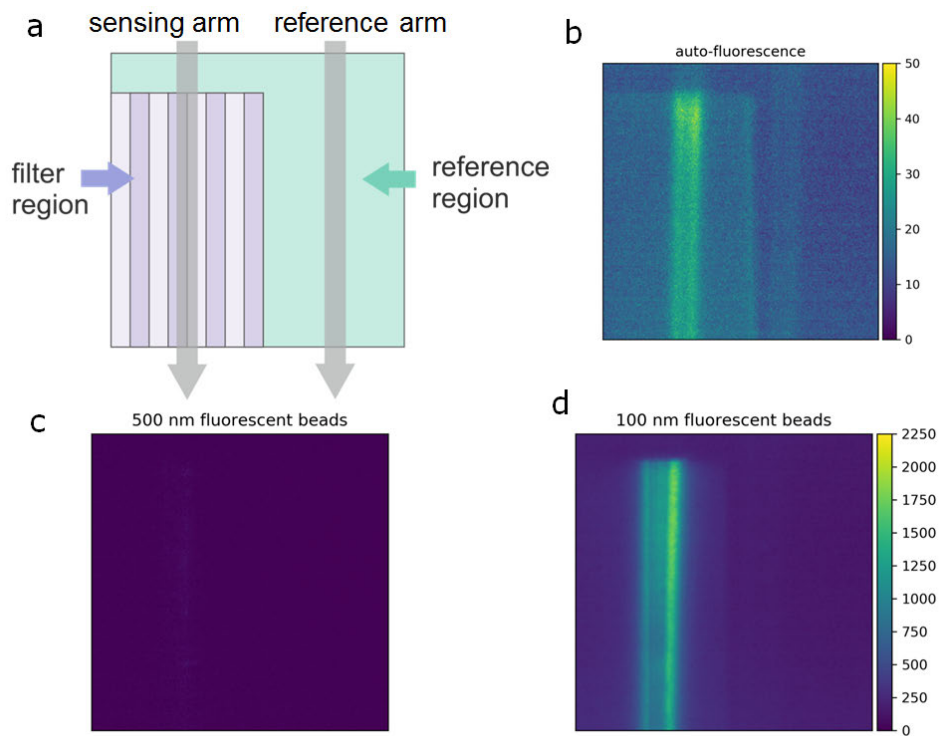
Fig. 7. Fluorescent excitation using waveguide interferometer. a) Illustration of the positions of the sensing and reference waveguide as well as the area of the nano-filters. b) The auto-fluorescence of the waveguide caused by the 450 nm laser excitation. The colorbar used is shown on the right. c-d) Two fluorescent beads ( 100 nm and 500 nm) are measured with the color bar scaled to the maximum intensity. The integration time remains the same for all measurements.

## 4. Conclusion

In this work we developed a highly sensitive waveguide interferometer sensor that is capable of detecting both refraction and absorption which is realized by evaluating the phase shift of the interference fringes and attenuation of the total transmitted signal. It is additionally paired with size-exclusion functionality to enable optofluidic measurement in complex turbid media. We utilize the confinement of the guided light in the waveguide in which nano-filters atop the waveguide that enables exclusion of larger particles in the liquid. A homogeneous bulk RI detection with a LoD in $10^{-5}$ is shown. Moreover, we used nano-beads to verify the ability of size exclusion by means of phase shift and fluorescent excitation. We envision that the sensor can be adopted for various optical detection applications involving small molecules or particles in complex turbid media.

## Acknowledgements

# Bibliography

[1] Nóra Adányi, Krisztina Majer-Baranyi, Mária Berki, Béla Darvas, Baomin Wang, István Szendrő, and András Székács. "Development of immunosensors based on optical waveguide lightmode spectroscopy (OWLS) technique for determining active substance in herbs". In: *Sensors and Actuators, B: Chemical* 239 (2017), pages 413–420.

[2] Leila Ahmadi, Marianne Hiltunen, Petri Stenberg, Jussi Hiltunen, Sanna Aikio, Matthieu Roussey, Jyrki Saarinen, and Seppo Honkanen. "Hybrid layered polymer slot waveguide Young interferometer". In: *Optics Express* 24 10 (2016), page 10275.

[3] Sanna Aikio, Jussi Hiltunen, Johanna Hiitola-Keinänen, Marianne Hiltunen, Ville Kontturi, Samuli Siitonen, Jarkko Puustinen, and Pentti Karioja. "Disposable photonic integrated circuits for evanescent wave sensors by ultra-high volume roll-to-roll method". In: *Optics Express* 24 3 (2016), page 2527.

[4] Ismail E Araci, Sergio B Mendes, Nasuhi Yurt, Seppo Honkanen, and N Peyghambarian. "Highly sensitive spectroscopic detection of heme-protein submonolayer films by channel integrated optical waveguide." In: *Optics express* 15 9 (2007), pages 5595–5603.

[5] Edikan Archibong. "Optofluidic Spectroscopy Platform for Detection of Hemolysis". PhD thesis. University of South Florida, 2015, page 82.

[6] Edikan Archibong, Justin Stewart, and Anna Pyayt. "Optofluidic spectroscopy integrated on optical fiber platform". In: *Sensing and Bio-Sensing Research* 3 (2015), pages 1–6.

[7] Susanna Aura, Ville Jokinen, Mikko Laitinen, Timo Sajavaara, and Sami Franssila. "Porous inorganic–organic hybrid material by oxygen plasma treatment". In: *Journal of Micromechanics and Microengineering* 21 12 (2011), page 125003.

[8] BASF. *Irgacure TPO - Technical Data Sheet.* Technical report March. 2013, pages 4–7.

[9] John Thomas Bradshaw, Sergio B. Mendes, Neal R. Armstrong, and S. Scott Saavedra. "Broadband coupling into a single-mode, electroactive integrated optical waveguide for spectroelectrochemical analysis of surface-confined redox couples". In: *Analytical Chemistry* 75 5 (2003), pages 1080–1088.

[10]    John Thomas Bradshaw, Sergio B Mendes, and S Scott Saavedra. "Accelerated Article A Simplified Broadband Coupling Approach Applied to Chemically Robust Sol - Gel , Planar Integrated Optical Waveguides A Simplified Broadband Coupling Approach Applied to Chemically Robust Sol-Gel , Planar Integrated Optical Waveguides". In: *Acs Symposium Series* 74 8 (2002), pages 1751–1759.

[11]    Albrecht Brandenburg, Ralf Krauter, Christa Künzel, Monika Stefan, and Heinrich Schulte. "Interferometric sensor for detection of surface-bound bioreactions". In: *Applied Optics* 39 34 (2000), page 6396.

[12]    Victor J. Cadarso, T. Kiefer, V. Auzelyte, H. Atasoy, Gabi Gruetzner, and Jürgen Brugger. "Direct imprinting of organic–inorganic hybrid materials into high aspect ratio sub-100 nm structures". In: *Microsystem Technologies* 20 10-11 (2014), pages 1961–1966.

[13]    CAvity Modelling FRamework (CAMFR). *http://camfr.sourceforge.net/index.html.*

[14]    L. Chan, M. Pineda, J. Heeres, P. Hergenrother, and B. Cunningham. "A general method for discovering inhibitors of protein-DNA interactions using photonic crystal biosensors." In: *ACS Chem Biol* 3 7 (2008), pages 437–448.

[15]    Leo L. Chan, Saujanya L. Gosangari, Kenneth L. Watkin, and Brian T. Cunningham. "A label-free photonic crystal biosensor imaging method for detection of cancer cell cytotoxicity and proliferation". In: *Apoptosis* 12 6 (2007), pages 1061–1068.

[16]    Leo L. Chan, Saujanya L. Gosangari, Kenneth L. Watkin, and Brian T. Cunningham. "Label-free imaging of cancer cells using photonic crystal biosensors and application to cytotoxicity screening of a natural compound library". In: *Sensors and Actuators, B: Chemical* 132 2 (2008), pages 418–425.

[17]    Jeppe S. Clausen, Emil H??jlund-Nielsen, Alexander B. Christiansen, Sadegh Yazdi, Meir Grajower, Hesham Taha, Uriel Levy, Anders Kristensen, and N. Asger Mortensen. "Plasmonic metasurfaces for coloration of plastic consumer products". In: *Nano Letters* 14 8 (2014), pages 4499–4504.

[18]    I. R. Cooper, S. T. Meikle, G. Standen, G. W. Hanlon, and M. Santin. "The rapid and specific real-time detection of Legionella pneumophila in water samples using Optical Waveguide Lightmode Spectroscopy". In: *Journal of Microbiological Methods* 78 1 (2009), pages 40–44.

[19]    Kaspar Cottier, Max Wiki, Guy Voirin, Hui Gao, and Rino E. Kunz. "Label-free highly sensitive detection of (small) molecules by wavelength interrogation of integrated optical chips". In: *Sensors and Actuators, B: Chemical* 91 1-3 (2003), pages 241–251.

[20]    C. M. Cripps. "Rapid method for the estimation of plasma haemoglobin levels." In: *Journal of clinical pathology* 21 1 (1968), pages 110–112.

[21]    Graham H. Cross, Yitao Ren, and Neville J. Freeman. "Young's fringes from vertically integrated slab waveguides: Applications to humidity sensing". In: *Journal of Applied Physics* 86 11 (1999), pages 6483–6488.

[22]   Brian Cunningham, Peter Li, Bo Lin, and Jane Pepper. "Colorimetric resonant reflection as a direct biochemical assay technique". In: *Sensors and Actuators, B: Chemical* 81 2-3 (2002), pages 316–328. arXiv: `arXiv:1011.1669v3`.

[23]   Stefania Dante, Daphné Duval, Borja Sepúlveda, Ana Belen González-Guerrero, José Ramón Sendra, and Laura M. Lechuga. "All-optical phase modulation for integrated interferometric biosensors". In: *Optics Express* 20 7 (2012), page 7195.

[24]   Johanna Davila, Delphine Toulemon, Tony Garnier, Aurélie Garnier, Bernard Senger, Jean Claude Voegel, Philippe J. Mésini, Pierre Schaaf, Fouzia Boulmedais, and Loïc Jierry. "Bioaffinity sensor based on nanoarchitectonic films: Control of the specific adsorption of proteins through the dual role of an ethylene oxide spacer". In: *Langmuir* 29 24 (2013), pages 7488–7498.

[25]   Henry Dietrich. "One Poke or Two: Can Intravenous Catheters Provide an Acceptable Blood Sample? A Data Set Presentation, Review of Previous Data Sets, and Discussion". In: *Journal of Emergency Nursing* 40 6 (2014), pages 575–578.

[26]   Goce Dimeski, Alan E. Clague, and Peter E. Hickman. "Correction and reporting of potassium results in haemolysed samples". In: *Annals of Clinical Biochemistry* 42 2 (2005), pages 119–123.

[27]   Yunhong Ding, Christophe Peucheret, and Haiyan Ou. "Ultra-high-efficiency apodized grating coupler using a fully etched photonic crystal". In: *Pacific Rim Conference on Lasers and Electro-Optics, CLEO - Technical Digest* 38 15 (2013), pages 2732–2734.

[28]   Maria B. Dühring and Ole Sigmund. "Improving the acousto-optical interaction in a Mach-Zehnder interferometer". In: *Journal of Applied Physics* 105 8 (2009).

[29]   Patrick Dumais, Claire L Callender, Julian P Noad, and Christopher J Ledderhof. "Integrated optical sensor using a liquid-core waveguide in a Mach-Zehnder interferometer." In: *Optics express* 16 22 (2008), pages 18164–18172.

[30]   Robin Fahraus and Torsten Lindqvist. "THE VISCOSITY OF THE BLOOD IN NARROW CAPILLARY TUBES". In: *Am J Physiol – Legacy Content* 96 3 (1931), pages 562–568.

[31]   V. F. Fairbanks, S. C. Ziesmer, and P. C. O'Brien. "Methods for measuring plasma hemoglobin in micromolar concentration compared". In: *Clinical Chemistry* 38 1 (1992), pages 132–140.

[32]   Mathew Foley, Nizar Kifaieh, and William K Mallon. "Financial impact of emergency department crowding." In: *The western journal of emergency medicine* 12 2 (2011), pages 192–7.

[33]   "Free hemoglobin concentration in severe sepsis: methods of measurement and prediction of outcome." In: *Critical care (London, England)* 16 4 (2012), R125.

[34]   gdsCAD. *https://pypi.org/project/gdsCAD/*.

[35]   Bradley C. Gehrs and Richard C. Friedberg. "Autoimmune hemolytic anemia". In: *American Journal of Hematology* 69 4 (2002), pages 258–271.

[36]   George R. Brewer. *Electron-Beam Technology in Microelectronic Fabrication.* Academic Press, Inc., 1980.

[37]   OrmoPrime08 micro resist technology GmbH. *https://www.microresist.de/en/ product/hybrid-polymers-4.*

[38]   H. Schift. *NaPANIL – Library of Processes.* third edit. NaPANIL-consortium, 2014.

[39]   Karl-Heinz Haas and Herbert Wolter. "Synthesis, properties and applications of inorganic–organic copolymers (ORMOCER®s)". In: *Current Opinion in Solid State and Materials Science* 4 6 (1999), pages 571–580.

[40]   M. Harboe. "A method for determination of hemoglobin in plasma by near-ultraviolet spectrophotometry". In: *Scandinavian Journal of Clinical and Laboratory Investigation* 11 1 (1959), pages 66–70.

[41]   "Harmonization in hemolysis detection and prevention. A working group of the Catalonian Health Institute (ICS) experience". In: *Clinical Chemistry and Laboratory Medicine* 52 11 (2014), pages 1557–1568.

[42]   Markus Häyrinen, Matthieu Roussey, Antti Säynätjoki, Markku Kuittinen, and Seppo Honkanen. "Titanium dioxide slot waveguides for visible wavelengths." In: *Applied optics* 54 10 (2015), pages 2653–7.

[43]   R. G. Heideman, R. P H Kooyman, and J. Greve. "Performance of a highly sensitive optical waveguide Mach-Zehnder interferometer immunosensor". In: *Sensors and Actuators: B. Chemical* 10 3 (1993), pages 209–217.

[44]   R. G. Heideman, R. P.H. Kooyman, and J. Greve. "Development of an optical waveguide interferometic immunosensor". In: *Sensors and Actuators: B. Chemical* 4 3-4 (1991), pages 297–299.

[45]   "Hemolytic anemia". In: *American Family Physician* 69 11 (2004), pages 2599–2606.

[46]   Pétur G. Hermannsson, Kristian T. Sørensen, Christoph Vannahme, Cameron L.C. Smith, Jan J. Klein, Maria-Melanie Russew, Gabi Grützner, and Anders Kristensen. "All-polymer photonic crystal slab sensor". In: *Optics Express* 23 13 (2015), page 16529.

[47]   Marianne Hiltunen, Jussi Hiltunen, Petri Stenberg, Sanna Aikio, Lauri Kurki, Pasi Vahimaa, and Pentti Karioja. "Polymeric slot waveguide interferometer for sensor applications". In: *Optics Express* 22 6 (2014), page 7229.

[48]   Marianne Hiltunen, Jussi Hiltunen, Petri Stenberg, Jarno Petäjä, Esa Heinonen, Pasi Vahimaa, and Pentti Karioja. "Polymeric slot waveguide at visible wavelength". In: *Optics Letters* 37 21 (2012), page 4449.

[49]   Roland Himmelhuber, Marion Fink, Karl Pfeiffer, Ute Ostrzinski, Anna Klukowska, Gabi Gruetzner, Ruth Houbertz, and Herbert Wolter. "Innovative materials tailored for advanced micro-optic applications". In: *Proc. of SPIE, Photonics Packaging, Integration, and Interconnects VII* 6478 February 2007 (2007), 64780E–1–12.

[50]   Emil Højlund-Nielsen, Tine Greibe, N. Asger Mortensen, and Anders Kristensen. "Single-spot e-beam lithography for defining large arrays of nano-holes". In: *Micro-electronic Engineering* 121 (2014), pages 104–107.

[51]   Jiri Homola, Sinclair S. Yee, and Günter Gauglitz. "Surface plasmon resonance sensors: review". In: *Sensors and Actuators B* 54 1-2 (1999), pages 3–15.

[52]   JEOL Ltd. *Instruction manual JBX-9500FSZ electron beam lithography system.* 2011.

[53]   S. E. Kahn, B. F. Watkins, and E. W. Bermes. "An evaluation of a spectrophoto-metric scanning technique for measurement of plasma hemoglobin". In: *Annals of Clinical and Laboratory Science* 11 2 (1981), pages 126–131.

[54]   Namsoo Kim, In Seon Park, and Woo Yeon Kim. "Salmonella detection with a direct-binding optical grating coupler immunosensor". In: *Sensors and Actuators, B: Chemical* 121 2 (2007), pages 606–615.

[55]   Mehmet Koseoglu, Aysel Hur, Aysenur Atay, and Serap Cuhadar. "Effects of hemolysis interference on routine biochemistry parameters". In: *Biochemia Medica* (2011), pages 79–85.

[56]   Peter Kozma, Florian Kehl, Eva Ehrentreich-Förster, Christoph Stamm, and Frank F. Bier. "Integrated planar optical waveguide interferometer biosensors: A comparative review". In: *Biosensors and Bioelectronics* 58 (2014), pages 287–307.

[57]   S. Kurunczi, A. Hainard, K. Juhasz, D. Patko, N. Orgovan, N. Turck, J. C. Sanchez, and R. Horvath. "Polyethylene imine-based receptor immobilization for label free bioassays". In: *Sensors and Actuators, B: Chemical* 181 (2013), pages 71–76.

[58]   P. V. Lambeck. "Remote opto-chemical sensing with extreme sensitivity: Design, fabrication and performance of a pigtailed integrated optical phase-modulated Mach-Zehnder interferometer system". In: *Sensors and Actuators, B: Chemical* 61 1 (1999), pages 100–127.

[59]   Giuseppe Lippi and Gian Cesare Guidi. "Risk management in the preanalytical phase of laboratory testing". In: *Clinical Chemistry and Laboratory Medicine* 45 6 (2007), pages 720–727.

[60]   MicroVacuum Ltd. *http://www.owls-sensors.com/company.*

[61]   W. Lukosz, Ch. Stamm, H.R. Moser, R. Ryf, and J. Dübendorfer. "Difference inter-ferometer with new phase-measurement method as integrated-optical refractometer, humidity sensor and biosensor". In: *Sensors and Actuators B: Chemical* 39 (1997), pages 316–323.

[62]   H. Ma, A. K.Y. Jen, and L. R. Dalton. "Polymer-based optical waveguides: Mate-rials, processing, and devices". In: *Advanced Materials* 14 19 (2002), pages 1339–1365.

[63]   Robert Magnusson, Debra Wawro, Shelby Zimmerman, and Yiwu Ding. "Resonant photonic biosensors with polarization-based multiparametric discrimination in each channel". In: *Sensors* 11 2 (2011), pages 1476–1488.

[64] Richard A. Malinauskas. "Plasma Hemoglobin Measurement Techniques for the In Vitro Evaluation of Blood Damage Caused by Medical Devices". In: *Artificial Organs* 21 12 (1997), pages 1255–1267.

[65] Lara S Mamikonian, Lisa B Mamo, P Brian Smith, Jeannie Koo, Andrew J Lodge, and Jennifer L Turi. "Cardiopulmonary Bypass is Associated with Hemolysis and Acute Kidney Injury in Neonates, Infants and Children". In: *Pediatr Crit Care Med* 15 3 (2014), pages 111–119. arXiv: `NIHMS150003`.

[66] Dietrich Marcuse. *Theory of Dielectric Optical Waveguides, Second Edition.* Academic Press, 1991, pages 1–58.

[67] Euan J. McCaughey et al. "Current methods of haemolysis detection and reporting as a source of risk to patient safety: A narrative review". In: *Clinical Biochemist Reviews* 27 4 (2016), pages 143–151.

[68] S B Mendes, L Li, J J Burke, J E Lee, and S S Saavedra. "70-Nm-Bandwidth Achromatic Waveguide Coupler". In: *Applied optics* 34 27 (1995), pages 6180–6186.

[69] Sergio B Mendes, Lifeng Li, James J Burke, John E Lee, Darren R Dunphy, and S Scott Saavedra. "Broad-Band Attenuated Total Reflection Spectroscopy of Waveguide". In: *Langmuir* 7463 8 (1996), pages 3374–3376.

[70] Shinji Okazaki. "High resolution optical lithography or high throughput electron beam lithography: The technical struggle from the micro to the nano-fabrication evolution". In: *Microelectronic Engineering* 133 (2015), pages 23–35.

[71] Marc Papenheim, Christian Steinberg, Khalid Dhima, Si Wang, and Hella-Christin Scheer. "Flexible composite stamp for thermal nanoimprint lithography based on OrmoStamp". In: *Journal of Vacuum Science & Technology B, Nanotechnology and Microelectronics: Materials, Processing, Measurement, and Phenomena* 33 6 (2015), 06F601.

[72] George A. Porter. "Spectrophotometric method for quantitative plasma hemoglobin resulting from acute hemolysis". In: *The Journal of Laboratory and Clinical Medicine* 60 2 (1962), pages 339–348.

[73] Amit Prabhakar and Soumyo Mukherji. "Microfabricated polymer chip with integrated U-bend waveguides for evanescent field absorption based detection". In: *Lab on a Chip* 10 6 (2010), page 748.

[74] F. Prieto, B. Sepúlveda, A. Calle, A. Llobera, C. Domínguez, A. Abad, A. Montoya, and L. M. Lechuga. "An integrated optical interferometric nanodevice based on silicon technology for biosensor applications". In: *Nanotechnology* 14 8 (2003), pages 907–912.

[75] Drew Provan. "Oxford Handbook of Clinical Haematology". In: *Medicine.* Volume 98. 6. 2009. Chapter 12, page 920.

[76] Zhi Mei Qi, Naoki Matsuda, Jose Santos, Kiminori Itoh, Akiko Takatsu, and Kenji Kato. "A study of molecular adsorption of bromothymol blue by optical waveguide spectroscopy". In: *Langmuir* 19 2 (2003), pages 214–217.

[77]    Daisuke Sakota, Yuki Kani, Ryo Kosaka, Masahiro Nishida, and Osamu Maruyama. "Simultaneous determination of hemolysis and hematocrit in extracorporeal circulation by plasma surface reflectance spectroscopy." In: *Conference proceedings: Annual International Conference of the IEEE Engineering in Medicine and Biology Society. IEEE Engineering in Medicine and Biology Society. Conference* 2013 (2013), pages 6764–7.

[78]    Muhammad Rizwan Saleem, Seppo Honkanen, and Jari Turunen. "Thermo-optic coefficient of Ormocomp and comparison of polymer materials in athermal replicated subwavelength resonant waveguide gratings". In: *Optics Communications* 288 (2013), pages 56–65.

[79]    Helmut Schift and Anders Kristensen. "Nanoimprint Lithography – Patterning of Resists Using Molding". In: *Springer Handbook of Nanotechnology.* Edited by Bharat Bhushan. 3rd. Springer, 2010. Chapter 9, pages 271–312.

[80]    M. Schirmer, B. Büttner, F. Syrowatka, G. Schmidt, T. Köpnick, and C. Kaiser. "Chemical Semi-Amplified positive E-beam Resist (CSAR 62) for highest resolution". In: October 2013 (2013), page 88860D.

[81]    Ethan Schonbrun, Gert Blankenstein, Josef Kerimo, and Hansong Zeng. *Patent: US20170336385A1 (Evanescent hemolysis detection).* 2017.

[82]    Juan Segurola, Norman S. Allen, Michele Edge, Adam McMahon, and Stephen Wilson. "Photoyellowing and discolouration of UV cured acrylated clear coatings systems: Influence of photoinitiator type". In: *Polymer Degradation and Stability* 64 1 (1999), pages 39–48.

[83]    B. Sepúlveda, G. Armelles, and L. M. Lechuga. "Magneto-optical phase modulation in integrated Mach-Zehnder interferometric sensors". In: *Sensors and Actuators, A: Physical* 134 2 (2007), pages 339–347.

[84]    George Y. Shinowara, Dolores M. Johnston, Marilyn J. Herritt, and E. Phyllis Lorey. "Spectrophotometry Studies on Blood Serum and Plasma: The Physical Determination of Hemoglobin and Bilirubin". In: *American Journal of Clinical Pathology* 24 6 (1954), pages 696–710.

[85]    Ana-Maria Simundic, Elizabeta Topic, Nora Nikolac, and Giuseppe Lippi. "Hemolysis detection and management of hemolyzed specimens". In: *Biochemia Medica* 20 2 (2010), pages 154–159.

[86]    Johan Söderberg, P. Andreas Jonsson, Olof Wallin, Kjell Grankvist, and Johan Hultdin. "Haemolysis index - An estimate of preanalytical quality in primary health care". In: *Clinical Chemistry and Laboratory Medicine* 47 8 (2009), pages 940–944.

[87]    C Stamm, R Dangel, and W Lukosz. "Biosensing with the integrated-optical difference interferometer: dual-wavelength operation". In: *Optics Communications* 153 4-6 (1998), pages 347–359.

[88]    András Székács, Nóra Adányi, Inna Székács, Krisztina Majer-Baranyi, and István Szendrő. "Optical waveguide light-mode spectroscopy immunosensors for environmental monitoring". In: *Applied Optics* 48 4 (2009), B151–B158.

[89] Dirk Taillaert, Frederik Van Laere, Melanie Ayre, Wim Bogaerts, Dries Van Thourhout, Peter Bienstman, and Roel Baets. "Grating couplers for coupling between optical fibers and nanophotonic waveguides". In: *Japanese Journal of Applied Physics, Part 1: Regular Papers and Short Notes and Review Papers* 45 8 A (2006), pages 6071–6077.

[90] Leen Vercaemst. "Hemolysis in cardiac surgery patients undergoing cardiopulmonary bypass: a review in search of a treatment algorithm". In: *The journal of extra-corporeal technology* 40 4 (2008), pages 257–67.

[91] Meng Wang, Sanna Uusitalo, Christina Liedert, Jussi Hiltunen, Leena Hakalahti, and Risto Myllylä. "Polymeric dual-slab waveguide interferometer for biochemical sensing applications". In: *Applied Optics* 51 12 (2012), page 1886.

[92] R. E. Wenk. "Mechanism of interference by hemolysis in immunoassays and requirements for sample quality". In: *Clinical Chemistry* 44 12 (1998), page 2554.

[93] Rodrigo S Wiederkehr and Sergio B Mendes. "Extension of the broadband single-mode integrated optical waveguide technique to the ultraviolet spectral region and its applications." In: *The Analyst* 139 6 (2014), pages 1396–1402.

[94] Aurel Ymeti, Johannes S Kanger, Jan Greve, Paul V Lambeck, Robert Wijn, and Rene G Heideman. "Realization of a multichannel integrated Young interferometer chemical sensor." In: *Applied optics* 42 28 (2003), pages 5649–60.

[95] Xiaolong Zhu, Christoph Vannahme, Emil Højlund-Nielsen, N. Asger Mortensen, and Anders Kristensen. "Plasmonic colour laser printing". In: *Nature Nanotechnology* (2015), pages 1–6.

[96] W. G. Zijlstra and A. Buursma. "Spectrophotometry of hemoglobin: Absorption spectra of bovine oxyhemoglobin, deoxyhemoglobin, carboxyhemoglobin, and methemoglobin". In: *Comparative Biochemistry and Physiology - B Biochemistry and Molecular Biology* 118 4 (1997), pages 743–749.

[97] A. Zwart, O. W. Van Assendelft, B. S. Bull, J. M. England, S. M. Lewis, and W. G. Zijlstra. "Recommendations for reference method for haemoglobinometry in human blood (ICSH standard 1995) and specifications for international haemiglobincyanide standard (4th edition)". In: *Journal of Clinical Pathology* 49 4 (1996), pages 271–274.

DTU Nanotech
Department of Micro- and Nanotechnology